

University of Southampton Research Repository ePrints Soton

Copyright © and Moral Rights for this thesis are retained by the author and/or other copyright owners. A copy can be downloaded for personal non-commercial research or study, without prior permission or charge. This thesis cannot be reproduced or quoted extensively from without first obtaining permission in writing from the copyright holder/s. The content must not be changed in any way or sold commercially in any format or medium without the formal permission of the copyright holders.

When referring to this work, full bibliographic details including the author, title, awarding institution and date of the thesis must be given e.g.

AUTHOR (year of submission) "Full thesis title", University of Southampton, name of the University School or Department, PhD Thesis, pagination

UNIVERSITY OF SOUTHAMPTON

FACULTY OF NATURAL AND ENVIRONMENTAL SCIENCES

CHEMISTRY

MULTISCALE MODELLING OF CELLULAR
CALCIUM SIGNALLING

BY

DANIEL JOHN MASON

THESIS FOR THE DEGREE OF DOCTOR OF PHILOSOPHY

SEPTEMBER 2012

Supervisors: Prof. Jonathan Essex and Prof. Hans Fangohr

Advisor: Prof. Jeremy Frey

UNIVERSITY OF SOUTHAMPTON
ABSTRACT

FACULTY OF NATURAL AND ENVIRONMENTAL SCIENCES

Chemistry

Doctor of Philosophy

**MULTISCALE MODELLING OF CELLULAR CALCIUM
SIGNALLING**

By Daniel John Mason

The ability to design effective medicines that treat disease requires a detailed knowledge of the associated natural processes. These natural processes operate on a range of complex spatio-temporal scales. Computational modelling allows us to investigate such processes, however these often provide detail only at a single spatio-temporal scale. Multiscale modelling aims to combine or link these scales represented by computational models, such that information is passed between different types of simulation. The aim of this investigation is to develop a multiscale model of cellular calcium signalling through extension of existing models. The pancreatic acinar cell was chosen for this treatment, owing to the polarised structure, range of signalling events, and disease states that are characteristic of this cell type.

Published models, that use networks of Ordinary Differential Equations (ODE), were implemented to gain understanding of the complex dynamics exhibited by cellular systems. ODE-based biological network models reduce the complexity of a system by making assumptions about the spatio-temporal properties. A model of the calcium dynamics of the pancreatic acinar cell was coupled to a model of the mitochondria, and the resulting collection of ODEs was extended to hypothetically simulate the onset of acute pancreatitis; a disease state whose mechanism is not yet fully understood. The entire model was then reformulated into one that uses the Finite Element Method (FEM) to solve the diffusion equation of species around the system, as well as to distribute spatially the contributing factors to cellular calcium signalling, such as associated calcium pumps. This provided a more physical representation of the cell, compared to the ODE model.

However, some of the results found in the original published material relating to model behaviour could not be reproduced fully in the FEM implementation. The issues encountered during this study highlight the challenges faced when modelling complex systems that have incomplete data, and instead rely on heavily fitted parameters. Despite this, the results demonstrate behaviour consistent with many experimental observations, due to the sophistication of FEM over ODE models. These include insight into the distribution of mitochondria, calcium tunnelling in the endoplasmic reticulum (ER), and mitochondrial calcium accumulation as a mechanism of acute pancreatitis onset. These findings represent the unique paths that may be followed while constructing a multiscale model, and a platform from which further research may continue.

Contents

List of figures	vii
List of tables	xiii
List of accompanying material	xviii
Authors declaration	xix
Acknowledgements	xxi
1 Introduction	1
1.1 Introduction	1
1.2 Overview	3
2 Modelling Complexity at the Cellular Level	5
2.1 What is a multiscale model?	5
2.1.1 Multiscale modelling approaches	6
2.2 Cellular level models of calcium signalling	8
2.2.1 Considerations	8
2.2.2 Obtaining models	10
2.2.3 Components applicable to most models at the cellular level	12
2.3 Overview of cellular model types	19
2.3.1 Compartmental ODE network models	19
2.3.2 Diffusional PDE models	23
2.4 Modelling tools	25
2.4.1 ODEs in Python using Odeint	26
2.4.2 FEM in Python using FEniCS/DOLFIN	28
2.5 Summary	33
3 Biological Background	37
3.1 Calcium	37
3.2 Mitochondria	38

3.2.1	Motility	39
3.3	The Pancreatic Acinar Cell	40
3.3.1	Structure and Function	41
3.3.2	Mitochondria in the Pancreatic Acinar Cell	46
3.3.3	Pancreatitis	47
3.3.4	Notable computer models of pancreatic acinar cell calcium dynamics	49
3.4	Modelling scope	50
3.5	Summary	52
4	Biological network modelling at the cellular level using ODEs	55
4.1	Implementation of literature models	55
4.1.1	The Bondarenko et al. Model of the Cardiac Myocyte	55
4.1.2	The Sneyd et al. Model of the Acinar Cell	62
4.1.3	The Bertram et al. Model of Mitochondria	68
4.2	Extension of literature models: the coupled acinar cell and the simplified mitochondria	71
4.2.1	Coupling of the Acinar cell and the Mitochondria	73
4.2.2	Sensitivity to BA and FAEE	84
4.3	Summary	88
5	Biological Finite Element Modelling	91
5.1	Finite element modelling of the pancreatic acinar cell in two dimensions	91
5.1.1	Considerations	91
5.1.2	Preliminary code development	115
5.1.3	Error and numerical stability	116
5.1.4	Simulation method	118
5.1.5	Steady State	121
5.2	Summary	122
6	Results and Discussion I: ODE model of the coupled acinar cell and the mitochondria	125
6.1	The effects of stimulation by IP ₃ on the coupled ODE model	126
6.1.1	Single pulse on unstimulated steady-state system	126
6.1.2	Constant concentration of IP ₃ in the cell	128
6.2	Onset of acute pancreatitis induced by BA or FAEE-like molecules	129
6.3	Summary	134

7	Results and Discussion II: FEM model of the coupled acinar cell and the mitochondria	137
7.1	The 'natural' model cell	138
7.1.1	Apical and basal calcium responses to stimulation by IP3 . . .	139
7.1.2	Apical and basal mitochondrial responses to stimulation by IP3	152
7.1.3	ER concentration changes	156
7.1.4	Comparison to the ODE implementation	160
7.2	Removal of the mitochondrial firewall	166
7.2.1	Apical and basal calcium responses to stimulation by IP3 . . .	166
7.2.2	ER concentration changes	175
7.3	The model cell and mitochondrial motility	177
7.4	Simulations carried out with redistributed mitochondria	182
7.4.1	Apical and basal calcium responses to stimulation by IP3 . . .	183
7.4.2	Apical and basal mitochondrial responses to stimulation by IP3	190
7.5	Onset of acute pancreatitis induced by BA or FAEE-like molecules . .	194
7.5.1	ER response to BA exposure	194
7.5.2	Cytosol response to BA exposure	195
7.5.3	The mitochondrial response to BA-induced calcium dynamics	199
7.5.4	Usefulness as a model of acute pancreatitis onset	199
7.6	Summary	201
8	Conclusions	203
8.1	Lessons learned from multiscale modelling	203
8.1.1	Concluding remarks on model results	206
8.1.2	Future extension and improvement to the multiscale model of the pancreatic acinar cell	209
	Glossary	215
	Bibliography	219

List of Figures

2.1	Hierarchy of multiscale scales below the cellular scale.	6
2.2	Plot showing Hill functions used for controlling pump rate.	15
2.3	Schematic of the RyR channel Markovian model.	16
2.4	State transitions of the activated RyR Markovian model.	18
2.5	Schematic of common pool and local control models of the cell. . . .	20
2.6	Schematic of a spatially compartmentalised model.	22
2.7	Tomography reconstruction of a mitochondrion and adjacent CaRU in 3D.	24
2.8	Sample code to model a Lotka-Volterra style predator-prey system. .	28
2.9	Predator-prey example output.	29
2.10	Sample code of a FEM simulation using FEniCS/DOLFIN. Any terms not declared in the code are automatically imported from DOLFIN. .	35
2.11	The change in distribution of matter during the example FEM simu- lation.	36
3.1	The location of pancreatic acinar cells in the body.	42
3.2	Schematic of the arrangement of organelles in the pancreatic acinar cell.	42
3.3	The distribution and quantification of mitochondria in the pancreatic acinar cell.	46
4.1	Schematic of the fluxes in an ODE model of the cardiac cell.	57
4.2	Plots showing the results from implementation of the cardiac cell model	60
4.3	Schematic of the common pool pancreatic acinar cell ODE model fluxes.	63
4.4	Plots showing results from the implementation of the common pool ODE model of the pancreatic acinar cell at a fixed concentration of IP3.	65
4.5	Plots showing results from the implementation of the common pool ODE model of the pancreatic acinar cell at a decaying concentration of IP3.	67
4.6	Schematic of the simplified ODE model of the mitochondria.	69
4.7	Plots showing the results from implementation of the mitochondria ODE model.	70

4.8	Schematic of the fluxes in the combined pancreatic acinar cell with simplified mitochondria.	73
4.9	Plot showing the behaviour of the mitochondria model in the environment it was designed for.	76
4.10	Plot showing the behaviour of the mitochondria model in an environment where the homeostatic calcium concentration is too low.	77
4.11	Plot showing the behaviour of the mitochondria model in an environment where the homeostatic calcium concentration is too low, with the J_{NaCa} fluxes scaled by 0.1.	77
4.12	Plot showing the behaviour of the mitochondria model in an environment where the homeostatic calcium concentration is too low, with both J_{NaCa} and J_{uni} fluxes scaled by 0.1.	78
4.13	Plot showing the behaviour of the mitochondria model in an environment where the homeostatic calcium concentration is too low, with both J_{NaCa} and J_{uni} fluxes scaled by 0.65.	80
4.14	Plot showing the behaviour of the mitochondria model in an environment where the homeostatic calcium concentration is too low, with both J_{NaCa} and J_{uni} fluxes scaled by 0.03.	82
4.15	Plot showing the behaviour of the mitochondria model in an environment where the homeostatic calcium concentration is too low, with J_{NaCa} and J_{uni} , and also J_{F1F0} and J_{ANT} fluxes scaled by 0.03.	82
4.16	Schematic of the modified RyR Markovian model, sensitive to BA . . .	85
4.17	Schematic of the modified IPR Markovian model, sensitive to BA . . .	86
5.1	Geometry of the FEM model of the pancreatic acinar cell.	92
5.2	Schematic of the 'layers' explanation used to explain the FEM model.	94
5.3	Distribution of the RyR and IPR channel agents	96
5.4	Distribution of the SERCA and PMCA pumps, and SOC channel agents	97
5.5	Distribution of the mitochondrial agents	98
5.6	Format of the array used to store agent information. The coordinates and closest mesh cell index are always stored at the beginning of the array slice, and the degrees of freedom follow.	102
5.7	Plots of the time steps considered for use in the FEM model.	103
5.8	Plots showing FEniCS code performance over time.	105
5.9	Plots showing the FEM model performance over time.	106
5.10	Plots showing a single channel and pump controlling concentration in the FEM environment	109
5.11	Contour and gradient plots showing the effect of a single channel and pump changing concentration in the cytosol over time.	110

5.12	Plots showing a high density of pumps and channels controlling concentration in the FEM environment	112
5.13	Contour and gradient plots showing a high density of pumps and channels changing concentration in the cytosol over time.	113
5.14	Plot showing altered channel activation properties upon slight increase in pump density.	114
6.1	Plots showing stimulation of the combined acinar-mitochondria ODE model with a decaying concentration of 30 μM IP3	127
6.2	Plots showing stimulation of the combined acinar-mitochondria ODE model with a fixed concentration of 3 μM IP3	130
6.3	Plots showing stimulation of the combined acinar-mitochondria ODE model with a fixed concentration of 25 μM BA	133
7.1	Plots showing calcium peak data in response to 3 μM IP3 for the model.	141
7.2	Plots showing calcium peak data in response to 30 μM IP3 for the model.	142
7.3	Plots showing peak calcium concentration and time to peak relationship to IP3 for the model.	144
7.4	Plots showing approximate time to peak calcium concentration data obtained from published material by Sneyd et al. (2002).	146
7.5	Plot showing approximate apical peak calcium concentration data obtained from published material by Giovannucci et al. (2002).	147
7.6	Plots showing the relationship between average basal RyR activity with peak apical calcium concentration and IP3 for the model.	149
7.7	Plots to compare the different peak concentrations and rise times, and corresponding wave speeds for 3 and 30 μM IP3 in the model.	150
7.8	Plot showing the wave speeds obtained for a range of IP3 concentrations in the model.	151
7.9	Plot showing the apparent wave speeds observed both experimentally and computationally, obtained from Sneyd et al. (2002), for a range of IP3 concentrations (approximate).	152
7.10	Plots showing the response of mitochondrial calcium and membrane potential to cell stimulation, for a range of IP3 concentrations in the model.	154
7.11	Contour plots showing the typical distribution of intracellular calcium and ATP in the model	155
7.12	Plots showing the effect of cell stimulation by 30 μM IP3 on the ER. .	158

7.13	Time evolution of the calcium concentration gradient in the ER, and calcium tunnelling during stimulation of the model cell with 30 μM IP3.	159
7.14	Plots showing the total change in calcium in the coupled acinar and mitochondria FEM model.	162
7.15	Plots showing the total change in calcium in the coupled acinar and mitochondria ODE model.	163
7.16	Plots showing the total change in calcium in the implementation of the Sneyd et al. (2002) ODE model.	163
7.17	Plots showing the total change in calcium the coupled acinar-mitochondria ODE model and each mitochondrial agent in the FEM multiscale model.	164
7.18	Plots showing calcium peak data in response to 3 μM IP3 for the model without the mitochondrial firewall.	168
7.19	Plots showing calcium peak data in response to 30 μM IP3 for the model without the mitochondrial firewall.	169
7.20	Plots showing peak calcium concentration and time to peak relationship to IP3 for the model without the mitochondrial firewall.	170
7.21	Plots showing the relationship between average basal RyR activity with peak apical calcium concentration and IP3 for the model without the mitochondrial firewall.	172
7.22	Plots to compare the different peak concentrations and rise times, and corresponding wave speeds for 3 and 30 μM IP3 in the model without the mitochondrial firewall.	173
7.23	Plot showing the wave speeds obtained for a range of IP3 concentrations in the model without the mitochondrial firewall.	174
7.24	Plot showing the open fraction of all RyR channels in the model cell with disabled mitochondria and stimulation by 30 μM IP3. The difference in colour is used to provide contrast between the plots of the many RyR channel agents. Light orange indicates RyRs closer to the apex of the cell, while darker red indicates RyRs closer to the base of the cell. The first group of peaks that are also the largest are the RyRs contained in the apical region. As these initial agents begin to deactivate, RyRs further away are activated by the calcium diffusing from the apical region, propagating the wave over the cell via CICR.	175
7.25	Plots showing the effect of cell stimulation by 30 μM IP3 on the ER in the model without the mitochondrial firewall.	176
7.26	Automated redistribution of mitochondria from random positions.	179
7.27	Automated redistribution of mitochondria from the cell boundary.	180
7.28	Automated redistribution of mitochondria from inferred locations.	181

7.29	Final positions of the redistributed mitochondria that began at the cell boundary, ready for IP ₃ stimulation.	182
7.30	Plots showing calcium peak data in response to 3 μ M IP ₃ for the model with redistributed mitochondria.	184
7.31	Plots showing calcium peak data in response to 30 μ M IP ₃ for the model with redistributed mitochondria.	185
7.32	Plots showing peak calcium concentration and time to peak relationship to IP ₃ for the model with redistributed mitochondria.	187
7.33	Plots showing the relationship between average basal RyR activity with peak apical calcium concentration and IP ₃ for the model with redistributed mitochondria.	188
7.34	Plot showing the wave speeds obtained for a range of IP ₃ concentrations in the model with redistributed mitochondria.	189
7.35	Plots showing the response of mitochondrial calcium and membrane potential to cell stimulation, for a range of IP ₃ concentrations in the model with redistributed mitochondria.	191
7.36	Plots showing the effect of cell stimulation by 30 μ M IP ₃ on the ER in the model with redistributed mitochondria.	192
7.37	Plot showing the effect of stimulation by 25 μ M BA on the total ER calcium concentration of the FEM model.	195
7.38	Plots showing calcium peak data in response to 25 μ M BA for the model.	197
7.39	Plots showing total calcium change in the cytosol in response to 25 μ M BA for the model.	198
7.40	Plot showing the response of mitochondrial calcium to 25 μ M BA in the model.	200
7.41	Plot showing the response of mitochondrial calcium to 50 μ M BA in the model.	200

List of Tables

2.1	Table of rate constants used in the Markovian RyR model.	16
5.1	Agent densities used in simulations for distribution of IPR, RyR and SERCA on the ER surface, and PMCA and SOC on the cell membrane, in the acinar cell FEM model.	100
5.2	Table showing the total and compartmental change in moles of calcium over the time course of 10 s.	117
5.3	Table showing the total and compartmental change in moles of ATP and ADP over the time course of 10 s.	117
5.4	Table showing the total and compartmental change in moles of calcium over the time course of 10 s, when stimulated with 6 μM IP3. . .	118
5.5	Table showing the total and compartmental change in moles of ATP and ADP over the time course of 10 s, when stimulated with 6 μM IP3.	118

Accompanying material

The work during this study was performed on computer. The programming code spans many thousands of lines altogether, and is therefore not particularly useful when printed to paper. Model code has been written to disk and is included with this thesis. One directory contains the ODE based models detailed in Chapter 6 ('Code/ODE/'), consisting of the implemented acinar cell, mitochondria and cardiac cell models, and the extended acinar-mitochondria model. The multiscale FEM model code detailed in Chapter 5 is included in a separate directory ('Code/FEM/):

- `simconf (.py)` - Simulation configuration file that controls the model.
- `simlib (.py)` - The main model code library.
- `simulation (.py)` - The script that is executed to initiate a simulation, subject to the parameters in `simconf`.
- `plotter (.py)` - The script that produces custom plots of the data.
- `coordinate_setup (.py)` - The script that controls agent distribution.
- `units (.py)` - The script that handles the definition of units in the model.
- `test_diffusion (.py)` - A test script that looks at diffusion.
- `test_FindBest_dt (.py)` - A test script that looks at time steps.
- `test_integration (.py)` - A test script that looks at integration.
- `test_agentMovement (.py)` - A test script that looks at mitochondrial motility.
- `testconf (.py)` - A script containing parameters to control some tests.
- `multiResult_plotter (.py)` - A script that extracts and plots data from simulations

The other scripts included in this directory are `'su_units (.py)`, and a folder named `'si_units/'`, which is code created by the University of Southampton Engineering Department (authored by Dr. Thomas Fischbacher, Prof. Hans Fangohr, and Dr. Matteo Franchin). The folder `'simdata/'` contains the initial conditions used to produce the results detailed in Chapter 7.

In a separate folder are animated videos that were produced from regular snapshots of the multiscale simulations, which are useful for visualising the model behaviour:

- `ATPi contour map (.avi)` - Video showing the distribution and change in ATP in the cytosol over time, represented as dynamic contour lines (units in μM).

- CaER colour map (.avi) - Video showing the distribution and change in ER calcium over time, represented as a stationary colour map (units in μM).
- CaER contour map (.avi) - Video showing the distribution and change in ER calcium over time, represented as dynamic contour lines (units in μM).
- CaER normalised quiver (.avi) - Video showing the direction of the concentration gradient of calcium in the ER over time.
- Cai colour map (.avi) - Video showing the distribution and change in cytosolic calcium over time, represented as a stationary colour map (units in μM).
- Cai contour map (.avi) - Video showing the distribution and change in cytosolic calcium over time, represented as dynamic contour lines (units in μM).
- Cai normalised quiver (.avi) - Video showing the direction of the concentration gradient of calcium in the cytosol over time.

The videos contained on this disk ('Videos/') are the same for each group of simulations, for consistency and comparison, and accompany the results and discussion sections:

- Natural cell
 - 3 and 30 μM IP3 stimulation
- Mitochondrial firewall removal
 - 3 and 30 μM IP3 stimulation
- Mitochondrial redistribution
 - 3 and 30 μM IP3 stimulation
- BA exposure
 - 25 and 50 μM BA exposure

In addition to this, a selection of relevant videos has been made publicly available on YouTube*.

*<http://www.youtube.com/user/DMmultiscale> (accessed 22/9/12)

Declaration of authorship

I, Daniel John Mason declare that the thesis entitled 'Multiscale Modelling of Cellular Calcium Signalling' and the work presented in the thesis are both my own, and have been generated by me as the result of my own original research. I confirm that:

- this work was done wholly or mainly while in candidature for a research degree at this University;
- where any part of this thesis has previously been submitted for a degree or any other qualification at this University or any other institution, this has been clearly stated;
- where I have consulted the published work of others, this is always clearly attributed;
- where I have quoted from the work of others, the source is always given. With the exception of such quotations, this thesis is entirely my own work;
- I have acknowledged all main sources of help;
- where the thesis is based on work done by myself jointly with others, I have made clear exactly what was done by others and what I have contributed myself;
- none of this work has been published before submission.

Signed:

Date:

Acknowledgements

I would like to thank my supervisors Professor Jonathan Essex and Professor Hans Fangohr for their combined support, enthusiasm, and guidance provided throughout the project. I feel that under their supervision, this project has provided me with many skills in both the research and implementation of ideas. Thank you Hans for your patient guidance with Python, particularly when I had problems with the code, as this proved invaluable. I also would like to thank Marijan Beg for his work on the scripts that helped me with finite element modelling, and the EPSRC for funding this project.

Members of the group, past and present, have contributed to a friendly working environment that has been a pleasure to be part of, and I wish everyone the best for the future.

I would like to thank my friends and family for being supportive, understanding, and for putting up with me in general (especially at times when my mind probably wandered into solving project-related problems!). Thank you to my family, for ensuring that I was properly fed and watered during the final few of months of study - I think that I owe more than a fair few cups of tea! A final thank you goes to my parents for being very supportive of my interests and decisions in life, both financially and emotionally, as well as giving me the opportunity to attend university as it has been a marvellous experience.

Chapter 1

Introduction

1.1 Introduction

Prior to reading this sentence, the most likely action you performed was to turn to this page, but you probably thought nothing of it at the time. When you turned the page, a signal travelled from your brain to move your fingers, hand, and arm, in a coordinated movement that lasted a couple of seconds. The events that occurred during those couple of seconds can be separated into a number of spatial and temporal scales.

At the smallest spatio-temporal scales, reaction and diffusion of ions and small molecules has taken place to transfer a signal within, and between cells. At a larger spatio-temporal scale than this, molecule-protein level interactions took place that translated the signal into a chain of events, such as the increased production of chemical energy. Larger still, protein-protein level interactions pulled contractile fibres together, and this resulted in contraction at the cellular level. Multiple units of skeletal muscle cells contracting at the same time in different muscle sets eventually translated to movement of the skeletal system.

The events and interactions that occur at each spatio-temporal scale are complex and dynamic. For example, signals in the cell that involve ions such as calcium, sodium, and potassium, may differ by frequency (temporal), location within the cell (spatial), and magnitude of transient concentration. The outcome of a sig-

nalling event may be dependent on a particular combination of these differences, and problems with these signals may result in problems for cellular organelles such as the mitochondria and the nucleus. Malfunctioning organelles may result in malfunctioning cells, and these may result in a disease state at the scale of an organ. Undoubtedly, this causes a problem for the organism.

As intelligent organisms, we are interested in solving problems and have created machines to use as tools that help us. Complex systems can be represented mathematically as a collection of simple equations that change the properties of a system over time, and computers are becoming increasingly capable of solving these equations, thus enabling more complex problems to be solved. Methods exist to solve problems at an appropriate level of detail for each of the scales previously mentioned. Quantum mechanical (QM), molecular mechanical (MM) and coarse-grained (CG) modelling can capture the detail appropriate to scales between ions, molecules and proteins; but capturing larger scale cell or organelle behaviour is for the most part too computationally intractable for these techniques. Instead, ordinary differential equations (ODE) and finite element methods (FEM) are used to capture the behaviour of fluxes and diffusion that exist in systems at this scale. However, as simulations represent increasingly large spatio-temporal scales, an increasingly large number of assumptions are made about the processes occurring in the scales below, to ensure the simulation is computationally tractable.

Returning to the example of simulating a system at the cellular level, suppose the desire is to investigate the effect of a compound, known to reduce the binding affinity of a particular protein to calcium, on the calcium dynamics of the entire cell; clearly a method must be chosen which captures the detail required. The QM, MM, and CG methods can capture detailed molecular interactions, but not the whole-cell dynamics. On the other hand, ODE and FEM methods can capture the larger scale behaviour, but offer little detail on molecular dynamics. Instead the system must be broken down into appropriately modelled levels of detail, and have the relevant information passed between these methods. This allows observation of the

effect a molecular scale event can have on a much larger cellular scale and above. This approach is termed multiscale modelling, and is a multidisciplinary field that requires a combination of biophysics, mathematics and programming.

This study concerns the construction of a multiscale model of the pancreatic acinar cell, which was achieved by combining ODE models of the cell and the mitochondria with the FEM modelling technique. Construction of this model allowed detail encoded in the ODE version of the cell to emerge, and the resulting cellular dynamics to be analysed. This offered insight into the natural and diseased-state processes that occur in the pancreatic acinar cell, and ultimately serves as a platform for incorporation of further scales of simulation in the future.

1.2 Overview

In the following chapters, an introduction to modelling complexity at the cellular level is provided. The subject of multiscale modelling, and the approaches that can be taken when constructing such a model, is discussed. Next, features common to most types of model at the cellular level is discussed, before moving onto a more detailed review on the types of model that exist, with examples. Following this, an overview on the biology of calcium, the mitochondria, and the pancreatic acinar cell is provided as background knowledge to the systems that were implemented.

The process of implementing and extending ODE models of the cell and mitochondria is explained, along with the issues that were encountered. Implementation of the FEM multiscale model is described, which was based upon the ODE implementation where the mitochondria and acinar cell were combined. Finally, the outcome of the ODE and FEM models is discussed, and future directions considered.

Chapter 2

Modelling Complexity at the Cellular Level

2.1 What is a multiscale model?

In order to understand and develop treatments for disease, the relationship between chemistry, the cell, the organ, and the organism need to be considered. Each of these scales is a complex system that reacts to changes in the level(s) above and/or below. On the cellular level, the dynamics of a system are very closely linked to events occurring at the atomic scales below (Figure 2.1), and the environment the cell exists in at the scales above^[1,2]. Each scale has a range of specialised modelling techniques that provide detail appropriate for that particular scale.

As we are interested in developing drugs that treat disease on a molecular level it would be desirable to model the entire cell using detailed atomistic techniques, but this is not currently possible. Instead, the problem needs to be approached by simulating multiple scales of detail using the methods appropriate for each, and linking them together. This enables events at the smallest scales to have an impact on the largest, without need for computationally intractable simulation of the entire cell. Reduction of complexity in this manner is known as multiscale modelling.

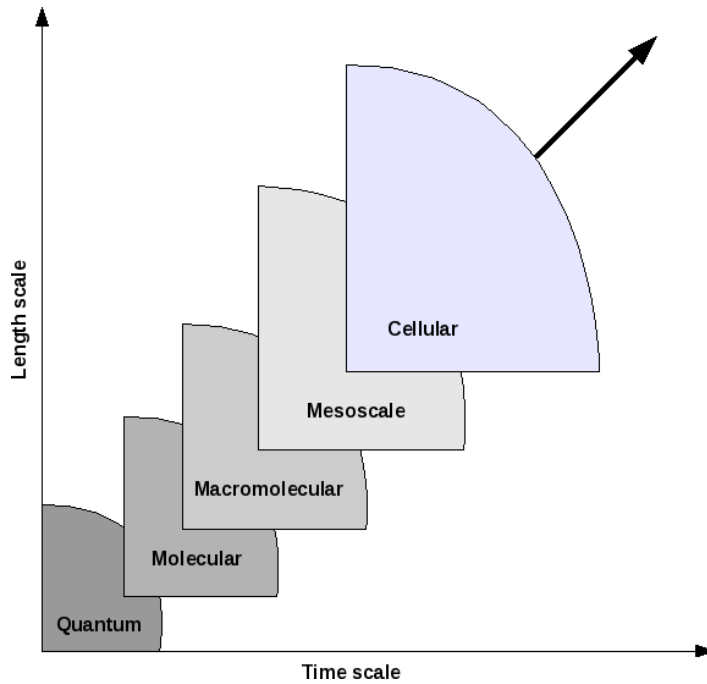


Figure 2.1: Example of the scales below the cellular level that could be used in a multiscale model^[1,2]. A number of methods are available to perform simulations at each scale, often in isolation or independently of each other. Multiscale modelling links simulations between these scales.

2.1.1 Multiscale modelling approaches

Systems can be modelled from a top-down or bottom-up perspective, depending on the information available^[3,4]. A top-down approach would look at a higher level scale such as a tissue and how it behaves, then form a model which captures this behaviour in order to feed back information to a lower scale. A bottom-up approach would involve modelling a detailed process, and extracting parameters from this in order to change the behaviour of a system that relies on this parameter at a higher level. Gabdoulline et al. (2003) applied Brownian dynamics simulations to a protein structure for the estimation of an undetermined kinetic parameter^[5]. This allowed the association rate constant of superoxide binding to peroxidase to be fed into a network model that produced oscillatory behaviour required for a physiological response. To move up the scale one further notch from a cellular model, several of the same type of network model may be coupled together to form a tissue, which could be used to study the propagation of action potential of cells linked by gap junctions^[6]. Multiscale modelling may also allow a middle-out approach, where

a particular scale is chosen for modelling with a view to eventually linking scales above and/or below.

Linking scales in a multiscale model is achieved by coupling methods in either a hierarchical or hybrid manner^[2,3]. The hierarchical modelling approach takes information from one scale of simulation for use in another, by passing data between independently running simulations. The hybrid approach relies on two or more different representations of the system being embedded in a single simulation, such that different parts of the system are modelled at a different resolution. At the molecular level, an example of this is combination of quantum-mechanical and molecular-mechanical (QM/MM) methods, that allow critical portions of an enzyme and substrate to be captured in QM detail (such as a protein-ligand binding pocket) whilst the rest of the protein and solvent is represented in a less computationally demanding way using MM^[1]. Alternatively, atomistic/coarse-grained (AT/CG) approaches may be used on systems of a much larger scale^[7].

Mathematical models at the cellular level may investigate chains of reactions involving genes and proteins in a biological pathway that, starting from different cellular genetic make-up (genotype), result in altered properties of the living system (phenotype)^[8]. These models allow the investigation of the relationship between expression of a gene, such as one that is mutated, and a resulting disease state. Another type of cellular model investigates the physical dynamics of a system, often involving the uptake and release of chemical species into cellular compartments using a mixture of rate constants and chemical reactions coupled to diffusion (such as ODE and PDE/FEM models). Ultimately, the information provided by these simulations could be used for designing therapeutic strategies.

One could envisage a multiscale model of the cell as a physical representation that draws on from molecular level simulations, directed by a biological pathway model that identifies a therapeutic target. For example; the effectiveness of a particular drug on an ion channel or protein, that has been identified by a genotype-phenotype model, could be simulated by an AT/CG method to provide rate con-

starts for use in a physical model of the cell, and these rate constants have an effect on the spatio-temporal dynamics. The effect of these dynamics on the behaviour of the cell may alter the properties of multiple cells, joined as a tissue in a higher level model.

The cellular scale is therefore an attractive level at which to begin construction of a multiscale model. It is at a level close enough to glean information from more detailed molecular simulations at the scales below, and can provide information as a building block to higher level simulations. Modelling the cell in a physical manner enables the coupling of movement and reaction of multiple species over time with associated rate constants, and this can provide insight into the mechanism of cellular signalling. The cellular signalling molecule of choice in this project was chosen to be calcium (for more information, see Section 3.1).

2.2 Cellular level models of calcium signalling

2.2.1 Considerations

At the cellular level, the dynamics of a system are usually modelled as a set of rules or equations that contribute to the change in a component of that system, such as concentration. These individual contributions may be a relatively simple representation of a subsequent complex process and, depending on the rules that they must abide by, the outcome may be deterministic or stochastic.

Cellular level models are usually represented by a deterministic collection of ODEs that represent compartmental concentrations of the cell, channel states, and membrane potentials. The combination of contributions to each ODE gives rise to complexity; starting from a relatively simple set of equations or rules, emergent behaviour may arise that can yield an otherwise unpredictable result from minor subsequent changes. This minor change could be an altered parameter that represents a disease state, such as a slower rate constant that disrupts the kinetics of an ion channel, or an altered model of the channel altogether^[9].

Two models of a cell that achieve similar results could contain very different parameters, depending on the approach used to fit with experimental data. In an ODE-based network model, for example, a peak calcium concentration in the cytosol that results from stimulation could be formed by multiple fluxes of matter flowing into and out of a compartment. In a similar model of the same cell, those same fluxes could potentially be constructed from very different parameters, or be an entirely different collection of fluxes altogether. Additionally, the compartments into which the cell is divided as a coarse representation of cell geometry could differ in number, size, and function.

Another consideration with models at the cellular level is where the data used for parameters is sourced from. Although an ever growing body of experimental data are being made available for the kinetics of cellular processes as science progresses, it is unlikely a modeller will find experimental data that apply solely to the particular cell in question. If suitable parameters are found for the same cell type, it is also unlikely that these measurements were taken from cells of the same species of organism. While this may be attributed to difficulties in obtaining certain parameters from some cell types or species, it could also be that the parameter has been characterised to a high enough standard previously that there is little need for characterisation in another cell type.

The use of parameters taken from different species and cell types is common among computational models of the cell, but perhaps more so for large and more complex systems. Data that is missing or incomplete in a model requires parameters to be fitted to closely related experimental data, if this is not available, then parameters are used from similar systems. Modelling every single aspect of a system is a huge task, and there needs to be consideration into what actually needs simulation for the required conclusions to be made. A recent publication on a whole cell computational model states that over 900 publications, and over 1900 experimentally observed parameters were used in construction of the system^[8]. If the supplementary data associated with model construction and parameters are viewed, referenced

publications for different cell types can be found.

Many cell models assume a 'well-mixed' environment, where the concentration of a particular species is homogeneous throughout each compartment. This great simplification is made possible by encoding the spatial and temporal effects on diffusion through the parameters that control fluxes. In reality there may be large concentration gradients throughout the cell, regions which are protected from concentration gradients by a firewall, and areas of privileged communication between organelles; the latter is referred to as a microdomain^[10-12]. An example of a microdomain is the space between L-type and RyR channels in the cardiac cell, known as the diadic cleft. This region experiences much steeper concentration gradients during stimulus than the rest of the cytosol, due to the spatial distribution of channels and pumps that contribute to calcium flux. These lead to a variety of calcium release events observed in different cell types known as sparks, sparklets, blinks, scintillas, and puffs, and result in different physiological responses^[10]. The existence of such complex behaviour can be lost in models that are too simplistic.

2.2.2 Obtaining models

Biological models of the cell rapidly evolve as more is understood about these systems. Projects such as CellML* aim to standardise, store and exchange computer-based mathematical models. At the time of writing, around 600 models are available in the CellML repository. The CellML language allows models to be shared as XML files for use by a variety of tools and editors, although it has been recognised that different results and large variations in computational performance may occur between these tools^[13]. This highlights the possibility of a 'black-box' element of using such packaged software, where the modeller may observe different results than are expected, and not necessarily be able to deduce why from a software methodology perspective.

In theory, the author is responsible for model validity and the ability of the file

*<http://www.cellml.org/> (accessed 7/9/12)

to reproduce published data. However, models available in the CellML repository are curated and validated to a different extent, and these actions are not necessarily performed by the original authors. The measure of curation status in CellML is signified through a four tier star system. As stated on the website*; level 0 (no stars) means the model is not curated, level 1 (one star) requires the model will load and run in a simulation environment, level 2 (two stars) requires the model to provide results that are qualitatively similar to those published for the model, and level 3 (three stars) requires the model to be quantitatively and qualitatively verified as providing identical results to those of the originally published model. The website also states that, from experience, to get to level 2 from level 1 there is a need to “adjust the published model description” due to the frequent errors introduced into the model during the publication process.

A strength of CellML is that it requires every quantity in a model to have units associated with it, which provides good practice for model developers and moves toward standardising these models. However, dimensional consistency is not required for a model to be considered valid by CellML standards, and therefore many models in the repository could potentially be considered incorrect (at levels 1 and 2). Validation of CellML models by dimensional analysis is possible using tools such as JSim[†] and Cellular Open Resource[‡] (COR), which can also cope with mixtures of dimensionally consistent but incorrect units to parameters, such as micro- and millimolar (μM and mM). These tools will not however recognise undeclared scaling factors inherited from the original published equations that are commonly used for conversion between milli- and micro- metric prefixes, such as 0.001 or 1000. In addition to incorrect units and unexplained scaling factors, published models may contain typographical errors, fail to disclose all parameters, or fail to mention stimulation routines. Any one of these issues makes reproduction of published data difficult or impossible, and these problems are magnified by model complexity.

*<http://www.cellml.org/getting-started/tutorials/cellml-model-curation> (accessed 7/9/12)

[†]<http://physiome.org/jsim/> (accessed 7/9/12)

[‡]<http://cor.physiol.ox.ac.uk/> (accessed 7/9/12)

Similar to CellML, another model repository which stands out is Simtk*. Simtk aims to provide a selection of physics-based open-source tools to biomedical researchers. As such, a range of projects are currently in progress in specialist fields ranging from molecular dynamics, joint load analysis, and multiscale modelling of the musculoskeletal system.

Irrespective of where a model is obtained from, each aims to simulate a system based upon physical processes. These physical processes have assumptions made of them, in order to simulate a system at an appropriate level of detail.

2.2.3 Components applicable to most models at the cellular level

Although a wide range of approaches may be taken in modelling the cell, many possess the same underlying principles or components that represent physical processes. The cause, effect, and detail of cellular signalling events may be lost in some models or methods that do not consider the geometric arrangement of cellular architecture. An example of this is the comparison of single-pool, local control, and higher dimensional models. The following sections provide an overview on commonly used types of model and the limitations each present, starting with some of the common principles each of these types share.

Fluxes

The flow or transport of material in a system from one region to another is known as flux. Fick's first law of diffusion shows us that flux is the amount of matter passing through a unit area per unit time, and is equal to the diffusion coefficient multiplied by the concentration gradient^[14] (Equation 2.1, where D ; diffusion coefficient, N ; number density of matter per unit volume, z ; directionality).

$$J = -D\left(\frac{dN}{dz}\right) \quad (2.1)$$

*<http://simtk.org> (accessed 7/9/12)

This tells us that a system with a non-homogeneous distribution of matter, presented as a concentration gradient, will tend toward equalising this distribution by diffusion. Modelling techniques that solve the diffusion equation in continuum keep track of the distribution of concentration in space, and provide the change over time by Fick's second law of diffusion (Equation 2.2). This tells us that if the concentration is raised at a coordinate in space, this distribution will again equalise through diffusion, but do so for the entire domain. In both Equations 2.1 and 2.2 the change in concentration over time is greatest when (and where) the concentration gradient is largest.

$$\frac{\partial N(z, t)}{\partial t} = D \frac{\partial^2 N(z, t)}{\partial z^2} \quad (2.2)$$

Techniques such as ODE based network models may encode this information by separating regions of the cell into compartments linked by fluxes and controlled by specific rate constants, while assuming that the concentration in each compartment is homogeneous. This effectively reduces the number of dimensions and complexity of the model. Equation 2.3 is an example of such a flux that links two compartments containing different molar concentrations of calcium; A and B , where τ is the time constant for transfer in seconds, and the units of flux are M s^{-1} . If the concentration in compartment A is higher than B the flux will be positive, which means transfer of concentration from A to B will occur, and vice versa. The time constant τ encodes information about distance or obstructions between the compartments that ensure this flux is not instantaneous.

$$J = \frac{[\text{Ca}^{2+}]_A - [\text{Ca}^{2+}]_B}{\tau} \quad (2.3)$$

Equation 2.3 demonstrates the physical process of diffusion that equalises a concentration gradient. However, many processes in the cell actively transport matter from a compartment of low concentration to one of high concentration, against a gradient. This enables the cell to accumulate matter inside an organelle such as the

endoplasmic reticulum (ER) to prime the system for signalling events. These processes are carried out by cellular pumps and are often modelled in the form of a Hill function, which still has units of flux but does not abide by Fick's first law since it is an active process. Equation 2.4 is an example of such a function, where v is the maximal rate of flux in M s^{-1} , K_m is the half-saturation constant with units of M , $[\text{Ca}^{2+}]$ is the concentration of the compartment pumping from in M , and n is the dimensionless Hill cooperativity factor.

$$J = v \frac{[\text{Ca}^{2+}]^n}{K_m^n + [\text{Ca}^{2+}]^n} \quad (2.4)$$

This function produces a curve dependent on $[\text{Ca}^{2+}]$ that rises from zero toward a maximal value of 1 at $[\text{Ca}^{2+}] = 2K_m$, which is used to scale v . The steepness of the curve is dependent on n , and typically has a value of 2. The most important feature of this representation of a pump is that it does not allow the rate of flux to increase indefinitely since pumps can only work up to their maximal capacity (Figure 2.2). This is different to the form of flux in Equation 2.3 that will increase as a function of the magnitude of concentration gradient.

Fluxes are summed with respect to the compartment they are flowing into or out from and are scaled by the appropriate volume ratio between compartments. Returning to the previous example of a diffusive flux, if compartment A in Equation 2.3 has twice the volume of compartment B , the inward flux of compartment B will be scaled by a factor of 2. This ensures that the flow of matter causes a greater change in the smaller compartment than it does the larger, owing to the differences in volume.

Markovian models

In addition to pumps, many models also feature excitable channels which are controlled by multi-state Markovian models. Models of this type are built from a collection of ODEs and present the fraction of channels in the model that are in a particular state, which is often changed upon exposure to an agonist (such as calcium).

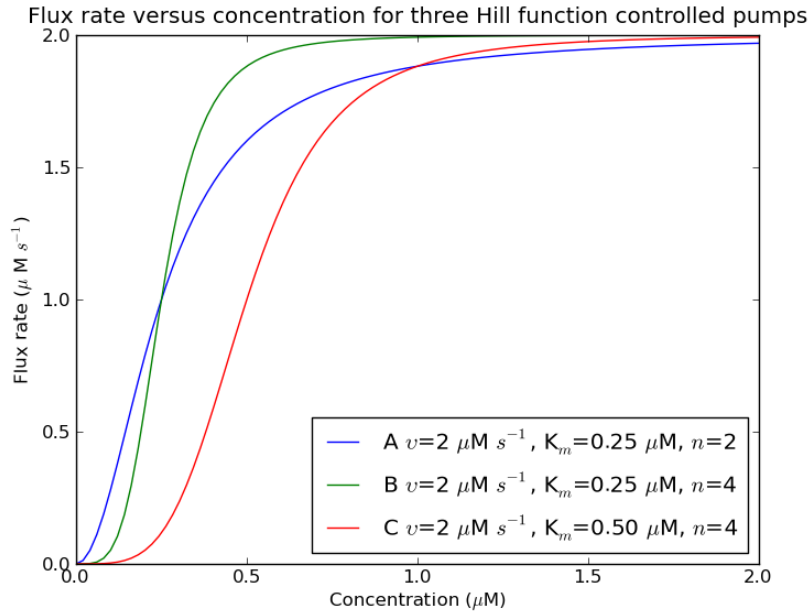


Figure 2.2: Hill functions for pumps that show fluxes reaching a maximal rate determined by v , with a steepness of curve determined by n , at a concentration determined by K_m . Pumps A and B both show they reach 50% maximal pump rate at a concentration of $0.25 \mu\text{M}$, with a steeper function for pump B due to the higher Hill cooperativity factor, n . Pump C has a higher half saturation constant than pumps A and B at $0.5 \mu\text{M}$.

The types of state in these Markovian models include closed, inactive, active and open, each of which may have more than one instance, depending on the complexity of channel activation kinetics. Throughout a simulation, the sum of populations in these states is equal to 1, and transition between each state is controlled by rate equations.

A relatively well-known Markovian model in the field of cellular modelling is the Keizer-Levine Ryanodine Receptor channel (RyR)^[15], and was originally developed to mimic calcium-induced calcium release (CICR) in cardiac cells. CICR is a mechanism through which a small, localised, increase in the calcium concentration is translated into further release of calcium from a cellular store, and is important in the propagation of cellular signals. The Keizer-Levine RyR model contains four states; $C1$, $C2$, $O1$ and $O2$, where C and O denote respectively the fraction of channels in the closed and open states.

A schematic of the Markovian RyR channel models is shown in Figure 2.3, and is presented as a collection of ODEs in Equations 2.6 to 2.9, that describe the change in

populated states over time. These equations show that the only interface with their surrounding environment is calcium concentration in theoretical compartment B .

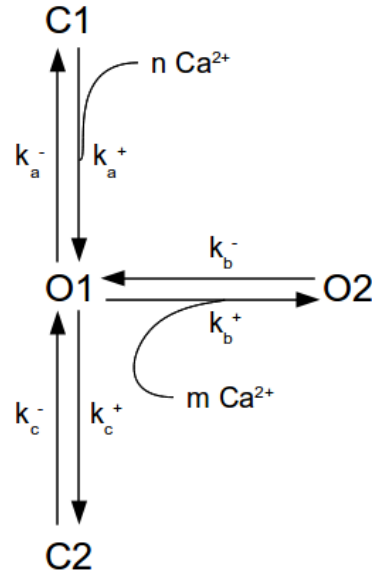


Figure 2.3: Schematic of the RyR channel Markovian model, adapted from Keizer-Levine (1996)^[15], showing transition between states (C; closed state, O; open state, k ; rate constant, m and n are the number of ions that bind to the channel and Ca^{2+} is calcium concentration. Steps a and b are concentration-dependent and step c is not).

$$O1 + O2 + C1 + C2 = 1 \quad (2.5)$$

$$\frac{dO1}{dt} = [\text{Ca}^{2+}]_B^4 k_a^+ C1 + k_c^- C2 + k_b^- O2 - k_a^- O1 - k_c^+ O1 - [\text{Ca}^{2+}]_B^3 k_b^+ O1 \quad (2.6)$$

$$\frac{dO2}{dt} = [\text{Ca}^{2+}]_B^3 k_b^+ O1 - k_b^- O2 \quad (2.7)$$

$$\frac{dC1}{dt} = k_a^- O1 - [\text{Ca}^{2+}]_B^4 k_a^+ C1 \quad (2.8)$$

$$\frac{dC2}{dt} = k_c^+ O1 - k_c^- C2 \quad (2.9)$$

$$J_{RyR} = v_{channel}(O1 + O2)([\text{Ca}^{2+}]_A - [\text{Ca}^{2+}]_B) \quad (2.10)$$

k_a^+	$1500 (\mu\text{M})^{-4} \text{ s}^{-1}$	k_a^-	28.8 s^{-1}	k_b^+	$1500 (\mu\text{M})^{-3} \text{ s}^{-1}$	k_b^-	385.9 s^{-1}
k_c^+	1.75 s^{-1}	k_c^-	0.1 s^{-1}	$v_{channel}$	4.5 ms^{-1}		

Table 2.1: Table of rate constants used in the Keizer-Levine^[15] RyR Markovian model.

At any point in time, the fraction of channels in the open state is found by the

sum $O1 + O2$, and this dimensionless value is used to scale the diffusive flux linking compartments A and B in Equation 2.10, where $v_{channel}$ is the maximum channel permeability. This means that channel flux only occurs when the sum of states $O1$ and $O2$ are greater than zero, and a concentration gradient exists between the compartments A and B , to satisfy Fick's equations. Upon channel activation by elevated calcium levels in compartment B , Equation 2.10 will result in release of calcium from compartment A into B , further elevating compartment B . This is an example of CICR.

Figure 2.4 shows an example where the model changes from closed to an open state in response to increase in $[Ca^{2+}]_B$, before returning to the closed state. In this example, the concentration of calcium in compartment B is manually held fixed at $0.1 \mu\text{M}$ and not affected by any resulting fluxes. When the concentration of calcium is held fixed at a concentration of $0.5 \mu\text{M}$, the RyR quickly switches from a closed to an open state fraction of approximately 0.6, or 60% (Figure 2.4, top). After the maximal peak of openness, the fraction declines to a partially open state of approximately 0.07 (7%), and remains at this value until the concentration of calcium in compartment B returns to the original value of $0.1 \mu\text{M}$. This secondary open state remains so due to faster rate constants in steps a and b compared to step c (see Table 2.1 and Figure 2.3).

While the concentration of calcium is low, closed state $C1$ is mostly populated and thus primed for transitioning to open state $O1$ when $[Ca^{2+}]_B$ increases, due to the large rate constant k_a^+ (Figure 2.4, bottom). Increase in the population of open state $O1$ results in subsequent transition of population to open state $O2$. While $O1$ and $O2$ are populated, the rate constant k_c^+ causes accumulation of population in closed state $C2$, and this is lost very slowly to $O1$ again, due to the magnitude of rate constant k_c^- . This results in $C2$ being the most populated after the peak channel open state while the concentration compartment B is held, and the $O1$ state is second most populated.

Representation of channel kinetics in this manner is by no means the only way to

do so. Alternatives exist that are more simplistic or more elaborate, however the majority of models examined during this study involved Markovian representations.

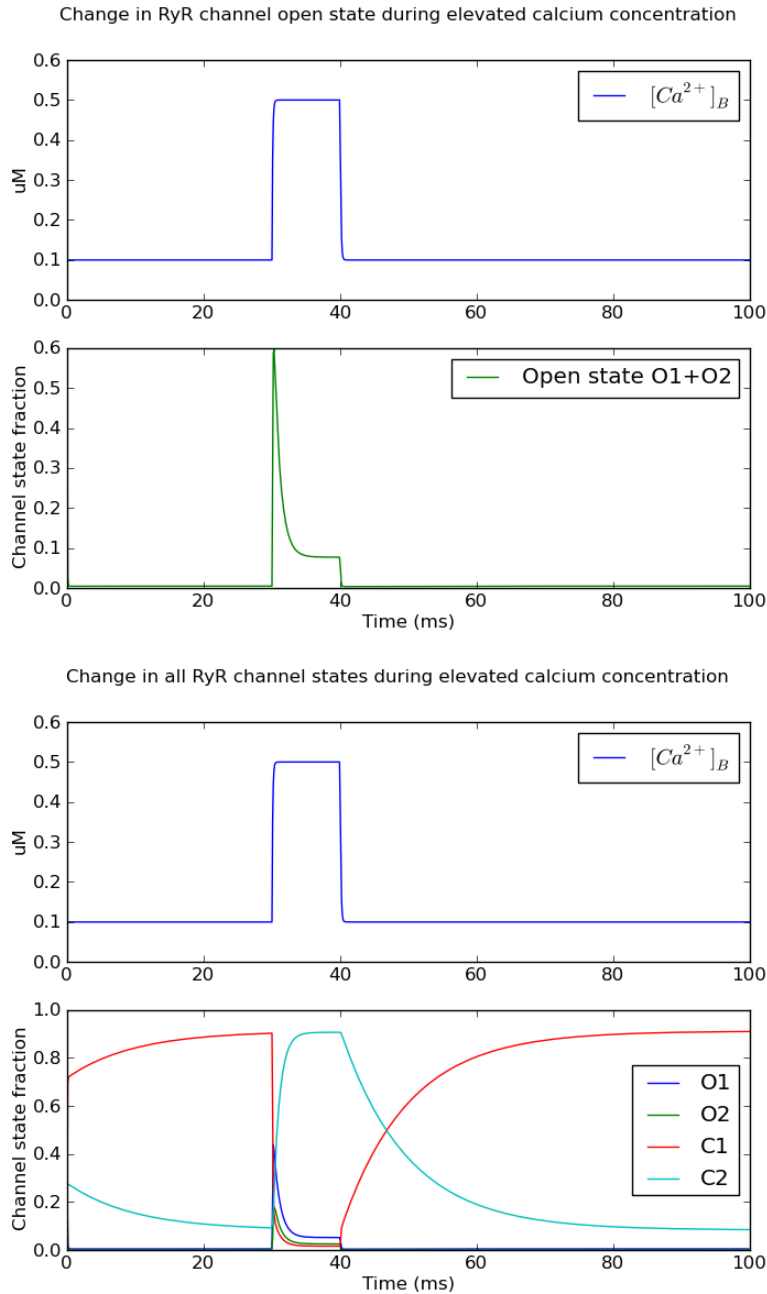


Figure 2.4: Change in states in the Keizer-Levine Markovian model of the RyR channel^[15] during activation by a temporarily fixed calcium concentration in compartment *B*. Top; the change in fixed calcium concentration over time compared to the sum of open states *O1* and *O2* that react to the change. An initial maximal open state occurs, followed by a secondary open state that is a result of the rate equations combined with the calcium concentration in compartment *B* held fixed. Bottom; the change in calcium concentration compared to all of the model states.

2.3 Overview of cellular model types

A fully detailed overview of all the many different cell models and techniques in systems biology is beyond the scope of this thesis. Instead this section provides classification of models, accompanied with a relevant example, where appropriate. The approach taken in modelling the cell is by no means limited by these classifications

2.3.1 Compartmental ODE network models

As previously mentioned, a challenge of simulating cellular processes may be overcome by compartmentalisation of the cell. Each compartment represents organelles inside the cell, whose individual concentration of species changes dynamically over time according to the behaviour of fluxes that link compartments. Fluxes simply add to or subtract from concentration of species in a compartment, meaning that concentration throughout the entire volume of this compartment is assumed to be uniform (also referred to as 'well-mixed'). While compartmentalisation with respect to functional organelles is a logical approach, ODE network models can overlook important localised transients, that occur inside a compartment, collectively known as microdomains. Those which do not consider microdomains are known as common pool models, and those which do are known as local control models^[16-18] (Figure 2.5).

To help explain the significance of these two types, examples can be drawn from models of the cardiac ventricular myocyte. The RyR channel model described in previous sections reacts to an elevated calcium concentration in the compartment it senses, transitioning from a closed to an open state. In the cardiac cell, this elevation results primarily from the L-type calcium channel (LCC), located on the cell membrane. The LCC (for which Markovian models also exist) is voltage gated and activates after depolarisation of the cell membrane, resulting in a small influx of calcium from an extracellular source, that subsequently activates the RyR channels

via CICR. The RyR then release a far greater amount of calcium from the Sarcoplasmic Reticulum (SR), which flows into the cytosol, activating further processes such as muscle-fibre contraction. The elevated calcium concentration returns to normal shortly afterwards, as the SR is refilled by SERCA pumps or removed by extracellular fluxes on the cell membrane.

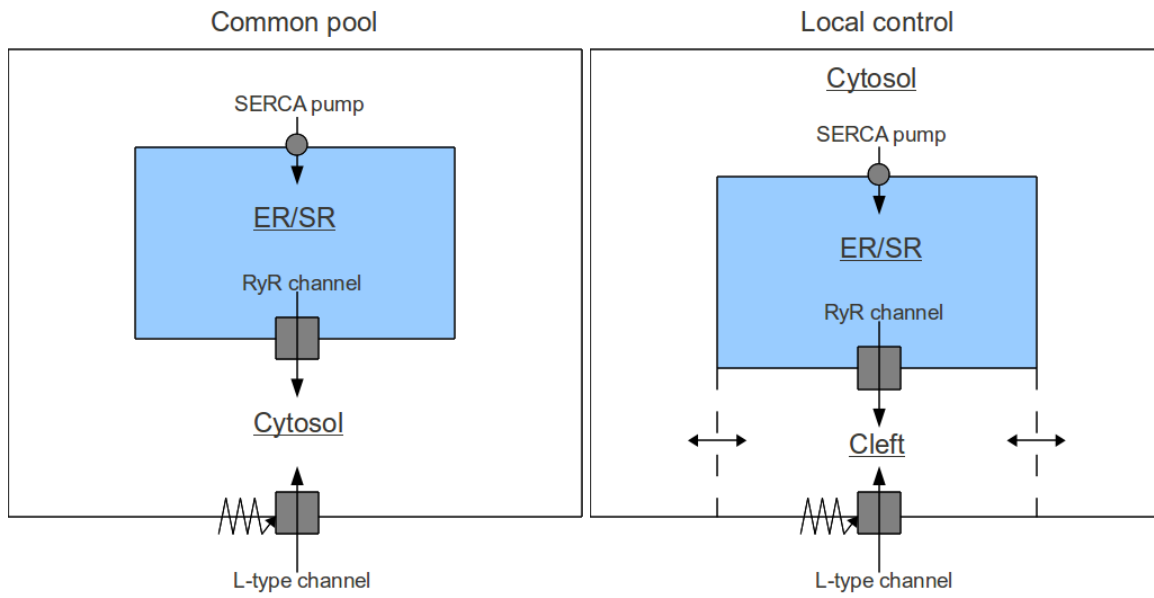


Figure 2.5: Simplified schematic of the cardiac cell, showing two categories of ODE network models of the cell. A common pool model links all fluxes involving CICR directly to the cytosol, while a local control model further compartmentalises the cell such that CICR fluxes communicate via an additional cleft compartment.

Common pool

A common pool modelling approach would represent the cardiac cell as two effective compartments; the SR and the cytosol, where CICR of the RyR channel depends on calcium concentration transients in the cytosol (Figure 2.5, left). Common pool models can reconstruct and predict cellular mechanisms, hence their extensive use in computational science. However, they can fall short when it comes to reconstruction of the cardiac action potential, which is controlled by the time evolution of ionic concentration in the cytosol.

While the common pool approach is theoretically the correct mechanism for CICR, the RyR is exposed to any other fluxes that contribute to concentration change

in the 'well mixed' cytosol as a consequence. This potentially can lead to initiation of CICR via an unrelated mechanism, or result in unrealistic behaviour. An additional issue to consider involves calcium injected by the LCC directly into the cytosolic compartment, where the large volume of the cytosolic compartment requires a greater calcium influx before activation of RyR can occur. In reality, the response of RyR to LCC is more sensitive to activation, and this is due to the spatial arrangement of channels in this microdomain of the cell. Clusters of RyR and LCC are in fact closely opposed to one another^[19].

Existing common pool models of the cardiac cell are typically from around the time of early model development in the field, such as that by Hilgemann and Noble^[20] and Luo and Rudy^[21]. As more was understood about cellular function, cardiac cell models were incrementally improved toward taking into account the spatial arrangement of features in this particular cell type. This was achieved through further compartmentalisation to provide regions of local control.

Local control

The L-type and RyR channels are physiologically located opposite to one another, in a region known as the diadic cleft^[17,22,23]. Local control models include this region as an additional compartment between the SR and the cytosol (Figure 2.5, right), which allows more private communication between the channels^[24,25], and/or a more graded trigger response of RyR to the LCC flux^[26]. This is made possible by the decreased volume of the diadic cleft requiring a smaller input from the LCC to achieve CICR, in comparison to common pool models that instead involve the cytosolic volume.

Taking this idea of local control even further is the coupling of RyR and LCC gating models into a calcium release unit (CaRU)^[27]. The CaRU model ensures that a direct relationship between RyR and LCC activity is maintained, providing a more graded calcium release response of the RyR from LCC action.

Local control models add further degrees of freedom, and an effective spatial res-

olution not offered by common pool models, that enhance predictive capability. The cardiac cell is an example of a model which requires specific concentration changes in ionic species for control of the action potential, which is important in cardiovascular research. Depending on the nature of the study, ODE models of other cell types may not benefit from local control, being adequate as common pool models. On the other hand such models could be classed as early developments in the field of the cell type, as early common pool cardiac cell models could, and future research may conclude that the spatial arrangement of features in the cell is significant.

Spatially compartmentalised

Another category of ODE network model are those which are spatially compartmentalised. This involves splitting the cytosol into several compartments that are linked by diffusive flux terms. The example in Figure 2.6, shows an example where the pancreatic acinar cell was split into 50 compartments along the x axis of the cell, and rate constants that control the model were altered depending on the region of the cell that they represent^[28].

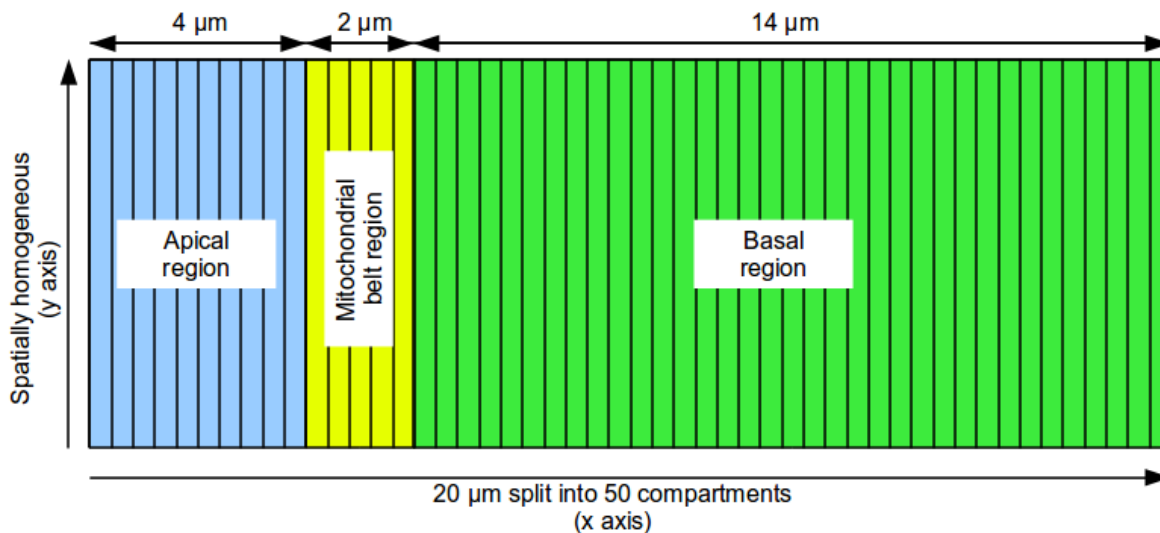


Figure 2.6: Diagram showing an example of a spatially compartmentalised ODE network model of the pancreatic acinar cell, adapted from Sneyd et al.^[28]. The cell is split into 50 compartments along the x axis, while it is assumed that the concentration gradient is spatially homogeneous along the y axis, thus treating each compartment as a common pool model.

The concentration in each compartment along the y axis of this model is assumed

to be homogeneous, while the concentration between compartments along the x axis are heterogeneous. Each compartment has the same, or similar, contributions to concentration, and so each compartment along the x axis is effectively a common pool model. While this method can theoretically model diffusion across multiple dimensions, this type of model is more suited to finite element methods.

2.3.2 Diffusional PDE models

Compartmental ODE models can provide a lot of information, owing to the fact they are relatively simple to construct and fast to compute, and thus are an important tool for investigating biological systems. However, due to the simplifications and assumptions that compartmental ODE models make of cellular spatio-temporal resolution, there is a significant amount of detail in biological systems that these cannot model sufficiently. Further detail can be extracted from models of a biological system that use more sophisticated physical techniques, at the cost of computational speed and the complexity of construction.

The finite element method

The finite element method (FEM) splits a simulation domain into individual elements called a mesh, which may then have PDEs solved for at the nodes of the mesh. In terms of cellular calcium dynamics, we are interested in a solution to PDEs in the form of the diffusion equation. In order to obtain more accurate calculations it is possible to increase the density of the mesh in specific regions of the domain. Imaging techniques have advanced to a point where it is possible to reconstruct the 3D structure and location of complex organelles from 2D images, and fluorescence labelling techniques can provide insight into the location and dynamics of cellular species^[23,29–33] (Figure 2.7). From these reconstructions it is possible to model a realistic 3D mesh on which boundary conditions can be applied, and around which diffusion can be modelled.

FEM has been used to model complex systems in the past. An example of using

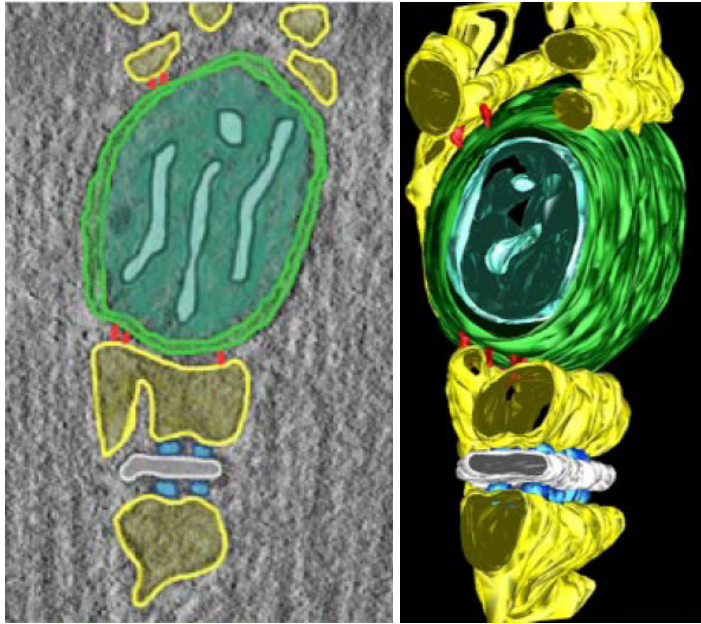


Figure 2.7: Tomography (left) and 3D reconstruction (right) of a mitochondrion and adjacent CaRU in skeletal muscle of the mouse. (Adapted, and reproduced with permission from Boncompagni (2009)^[33]. SR; yellow, T-tubule; white, outer and inner mitochondrial membrane; green and blue, tethering structures between mitochondria and SR; red).

such a method is analysis of synaptic transmission in the neuromuscular junction (NMJ)^[34–36]. The extent and timecourse of acetylcholine (ACh) diffusion modelled in continuum, was examined for effect by acetylcholinesterase (AChE) and acetylcholine receptor (AChR) density, different neurotransmitter release models, and complex and realistic NMJ geometry. The results supported experimental observations, and allowed predictions to be made, such as secondary postsynaptic cleft folds serving purposes other than to bind or remove ACh in the NMJ. Similarly, Means et al.^[37] used the FEM approach to model the reaction-diffusion dynamics of calcium diffusing through channels on the ER membrane of a mast cell for different sized clusters of channels, using both realistic and simplified geometries.

Simplification of cellular structure is often achieved through treating organelles as explicitly separate compartments, but in reality the ER/SR has a complicated structure and forms an extended network throughout cytoplasm. A method known as homogenisation uses the FEM approach, and simplifies a structurally complex system by assuming it can be represented by periodic repetition of a smaller reference cell. In other words, this is a microscopic description of a macroscopic structure

that can be used to build up the complex structure of the SR or ER^[38]. Effective diffusion coefficients for ionic species are derived by a homogenisation process, which depends on the microscopic properties of structure^[39].

FEM offers a flexible technique for modelling detailed cellular calcium dynamics, that cannot be provided by the ODE techniques previously discussed.

2.4 Modelling tools

Modelling tools that have so far been mentioned include Jsim and COR, which are related to CellML, and also Simtk as a collection of tools for a range of fields in biology. Another tool of note is the Stochastic Pi Machine* (SPiM) that uses a method known as pi-calculus to model systems using kinetic theory of physical chemistry.

Many modellers use tools such as these, that are specifically designed for biological systems, because they simplify the task of constructing a model. However, many prefer the use of a programming language such as FORTRAN, Python or C++ to handle integration routines and plotting instead. The use of a programming language in preference to a modelling tool allows more control over the system, extraction of specific data, and leaves room for modifications or extensions to the code which would not otherwise be possible using a software package.

The implementations carried out in this project use the Python programming language, which has a large user base and a growing body of scientific tools that can be imported in a modular fashion. In addition to this, Python is a high-level, interpreted language that interfaces well with other programming languages, and has an emphasis on readability. These are all traits useful for future extensions of a multiscale model, which may require integration with other specialised software, different to that which tools such as Simtk may be capable of integrating with.

As construction of a biological network model from scratch is beyond the scope and resources of this project, implementation of published ODE models of cellular

*<http://research.microsoft.com/en-us/projects/spim/default.aspx> (accessed 7/9/12)

calcium dynamics was carried out with a view to modelling a disease state. Extension of these models was then achieved by modifying and coupling them together. Where possible, original source code was obtained from authors of the models that were implemented.

2.4.1 ODEs in Python using Odeint

The Odeint (`scipy.integrate.odeint`) package, part of the SciPy* module for Python, integrates a system of ODEs using LSODA from the FORTRAN library ODEPACK. Odeint uses a nonstiff method to solve systems initially and, by dynamically monitoring data as it is solved, has the ability to switch to a stiff method (i.e. the integrator can switch between fixed and flexible time steps to solve a system of ODEs). Odeint has an advantage over the more commonly used Euler or fourth-order Runge-Kutta (RK4) methods, in that it uses several previous solutions of the function in question to assist in determining the new value, as opposed to only using a single previous value. Odeint reduces error resulting from a numerically unstable equation by evaluating the function more thoroughly at points in time where greater rates of change are found. The integrator introduces efficiency by not examining solutions between time steps if it can predict what the result at each time step will be, based upon previous results.

These features provide an efficient integration tool which dynamically selects the most appropriate method for solving a function, with the ability to use variable step sizes depending on the rate of change found. This does however present a caveat if a system of ODEs reaches some kind of equilibrium, whereby the degrees of freedom present little or no predictable change over a simulation period. If the system involves a non-analytical input such as adding $1\mu\text{M}$ of calcium to stimulate CICR at time t , the system may not experience this addition if the integrator has taken to predicting the result at each time step, and does not fall on time t . Fortunately, a list of important points in simulation time can be passed into the integrator to ensure

*<http://www.scipy.org> (accessed 7/9/12)

they are analysed.

Example system

The `Odeint` function requires three pieces of data; an array of the degrees of freedom (the variables in which we are interested), an array setting out the timespace and the right-hand side function containing the ODEs needed to solve the variables. Consider the somewhat non sequitur, yet simple, example system in Figure 2.8. This is a modified version of the Lotka-Volterra tutorial from the SciPy cookbook* that describes the predator-prey interaction between rabbits and foxes, and is intended as a simple analogy to ODE cell modelling.

When the simulation runs, Python steps into `'__main__'`, sets up arrays providing the timespace `ts` and initial variables `y0`, and passes these into the `odeint` function along with the name of the right-hand side function that contains the ODEs, `rhs`. `Odeint` then solves the function for each time point provided by `ts`, returning all results as a 2D array to `ys`. The result of this particular problem is a system of fluctuating rabbit and fox populations that dynamically react to one another (Figure 2.9). This simple system may be increased in complexity through the addition of other factors, such as a disease that kills the animals at a certain constant rate, or other organisms that interact with the rabbits and foxes. An assumption in this example is that there is a rich food source for the rabbits, which is always available no matter what the rabbit population is. By adding a depletable food source, this could decrease the rate in which rabbits breed and impart an effect on the fox population.

The same principles seen here are true for modelling cellular dynamics. The concentration of ionic species changes over time and these are dependent on the processes that regulate them, such as pumps, channels and buffers. Assumptions about the system can be made, such as the constant supply of cellular energy, which simplifies the simulation. The addition of further processes to the system may potentially perturb any steady state that was present beforehand, causing the system

*<http://www.scipy.org/Cookbook/LotkaVolterraTutorial> (accessed 7/9/12)

```

import pylab as p
from scipy.integrate import odeint

def rhs(y,t):
    # extract the current population
    rabbits,foxes = y[0],y[1]
    # calculate the change in population during time step
    d_rabbits_dt = (rabbits*rabbitBreedRate)-\
                   (rabbits*rabbitEatenRate*foxes)
    d_foxes_dt = (foxBreedRate*rabbitEatenRate*rabbits*foxes)-\
                 (foxes*foxStarveRate)
    # pass back result for timestep
    return np.array([d_rabbits_dt, d_foxes_dt])

if __name__ == '__main__':
    rabbitBreedRate = 1.
    rabbitEatenRate = 0.1
    foxStarveRate = 1.5
    foxBreedRate = 0.75
    ts=np.arange(0,20,0.001) # start, stop, step size
    y0 = np.array([10,5])   # start with 10 rabbits and 5 foxes
    ys = odeint(rhs,y0,ts)  # pass system, initial conditions and
                            # times to the odeint function

    # Plotting
    rabbits,foxes = ys[:,0],ys[:,1] # extract results
    p.figure()
    p.title('Rabbit and fox population change over time')
    p.plot(ts,rabbits,'r',label='rabbits')
    p.plot(ts,foxes,'g',label='foxes')
    p.xlabel('time')
    p.ylabel('population')
    p.show()

```

Figure 2.8: Sample code to model a Lotka-Volterra style predator-prey system.

to behave differently, and this presents a problem when extending models.

2.4.2 FEM in Python using FEniCS/DOLFIN

FEM approximates physical problems that may be applied to an object as partial differential equations (PDE) or integral equations. Objects may be built up and divided into simple shapes as a mesh, providing a solution to these equations at the mesh nodes. This process of breaking up an object into smaller chunks increases accuracy of the calculation, and allows the mesh to be refined in regions that require further

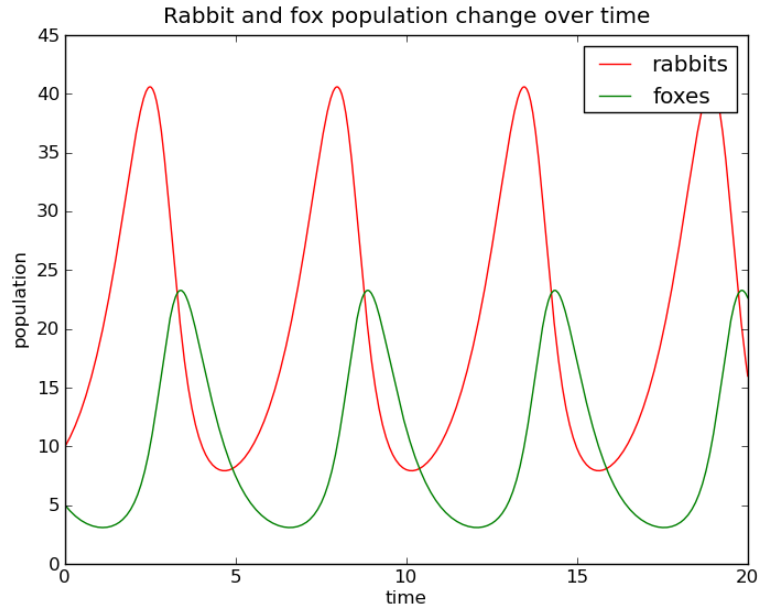


Figure 2.9: Predator-prey example output.

accuracy (at computational cost). Some applications that FEM may be used for include analysing the stresses, aerodynamics and thermodynamics of objects. In the context of this research, the ability to model the spatio-temporal diffusion of species is of interest, and the following solution to the diffusion equation as our PDE is explained with reference to the FEniCS project^[40]. FEniCS is essentially a collection of tools that can be imported into Python as libraries, and the tool that was used most during this study is DOLFIN*. The general principles of this technique are applicable to other research involving FEM, however the tools used determine the exact approach taken.

The diffusion equation in terms of FEM

The flux in a solution is presented by Fick's laws, where $J(\vec{r}, t)$ is flux, $u(\vec{r}, t)$ is concentration at position and time, and D is a diffusion constant:

$$\vec{J}(\vec{r}, t) = -D\nabla u(\vec{r}, t) \quad (2.11)$$

To ensure stability and simplicity, convection and the existence of an electrical

*<http://fenicsproject.org/> (accessed 7/9/12)

field in the system are neglected, and mass conservation is assumed. The diffusion equation used in the FEM simulations of this study is shown in Equation 2.12:

$$\frac{\partial u(\vec{r}, t)}{\partial t} = D\Delta u(\vec{r}, t) \quad (2.12)$$

Where Δ represents the system as Euclidean space (Equation 2.13):

$$\Delta = \frac{\partial^2}{\partial x^2} + \frac{\partial^2}{\partial y^2} + \frac{\partial^2}{\partial z^2} = \nabla^2 \quad (2.13)$$

This defines how the system changes concentration over time, but to fully represent the problem we need boundary conditions. To represent the cell membrane in our model, we require Neumann boundary conditions to ensure nothing may enter or leave the system on the boundary of the domain, to ensure mass conservation.

Equation 2.12 can be re-written such that the change in concentration of our system over time depends on the diffusion constant D , concentration Δu , plus a function f . If Ω represents the domain, the problem is defined inside the boundary in Equation 2.14 and on the boundary in Equation 2.15:

$$\frac{\partial u}{\partial t} = D\Delta u + f \text{ in } \Omega, \text{ for } t > 0 \quad (2.14)$$

$$\frac{\partial u}{\partial t} = 0 \text{ on } \partial\Omega \quad (2.15)$$

At $t = 0$, we must have an initial distribution, I , of concentration defined as a function of space (such as a gaussian distribution relative to a position in the domain, or a uniform concentration), and this is represented in Equation 2.16:

$$u = I \text{ at } t = 0 \quad (2.16)$$

Finite element solution to the diffusion equation

To solve the diffusion equation using the finite element approach, a mesh is constructed representing the domain Ω and the time derivative is discretised by a finite difference approximation^[40]. If superscript n denotes sampling in time at t_n , a sample of the diffusion equation at time n is:

$$\frac{\partial}{\partial t}u^n = \Delta u^n + f^n \quad (2.17)$$

Backward finite difference approximation (assuming a known previous solution $n - 1$ to the equation) where dt is a time discretisation parameter, yields a time-discrete version of the diffusion PDE:

$$\frac{\partial}{\partial t}u^n \approx \frac{u^n - u^{n-1}}{dt} \quad (2.18)$$

If an initial value $u_0 = I$ is known, reordering of the previous equation such that our solution u^n only appears on the left hand side provides us with a recursive set of stationary problems that can be solved for at the nodes of the mesh, for $n = 1, 2, \dots$:

$$u^n - dt\Delta u^n = u^{n-1} + dt f^n \quad (2.19)$$

Time integration with FEniCS/DOLFIN

The finite element method in FEniCS/DOLFIN requires our diffusion problem to be expressed in terms of a bilinear and a linear (functional) form; a and L , respectively^[40]. This is achieved by multiplying our initial concentration function u , by a test function v , for some function space \hat{V} , and integration of second derivatives by parts over the spatial domain. Where $a(u, v) = L(v)$, and dx is the infinitesimal distance between nodes of the mesh, at $t = 0$ this yields:

$$a_0(u, v) = \int_{\Omega} uv dx \quad (2.20)$$

$$L_0(v) = \int_{\Omega} I v dx \quad (2.21)$$

Thereafter, when $t > 0$:

$$a(u, v) = \int_{\Omega} (uv + dt \nabla u \cdot \nabla v) dx \quad (2.22)$$

$$L(v) = \int_{\Omega} (u^{n-1} + dt f^n) v dx \quad (2.23)$$

With the relevant functions and parameters defined, FEniCS will solve the diffusion equation to profile all of trial function u in trial space V for all of test function v in test space \hat{V} . The automated approach of FEniCS in solving PDEs, coupled with the readability of Python, means a FEM simulation that solves the diffusion equation can be set up with relative ease.

An example of such a simulation is shown in Figure 2.10, and follows the previous description. A mesh is set up using the `Rectangle` function, which requires information on the dimensions of the simulation domain starting from x_0, y_0 to l_x, l_y , with $N_x \times N_y$ nodes upon which the diffusion equation is solved. The function space V and initial condition \mathbb{I} are initialised, and used for construction of the initial distribution of concentration `u_prev`. The boundary condition `bc` is set up for the function space, and the trial and test functions `u` and `v` are declared. Following this, `a` and `L` are defined in terms of the diffusion equation, using the time step `dt` and diffusion constant `D`. After declaration of variables that enable switching between previous and current solutions of `u`, a while loop is entered that will solve the diffusion equation over time `t+dt` until `T` is reached. Using the command `u.vector()[i]`, where `i` is an integer representing the array index of a node on the mesh, the value at this point can be observed or changed. The location at this index can be used as an input for a pump flux or used for local activation of a channel at this position.

When the profile of concentration is a Gaussian distribution that originates from the centre of a function space, using a modified version of the previous FEniCS sam-

ple code in Figure 2.10, the simulation will provide the resulting plot in Figure 2.11. Initially, the centre of this profile of concentration has a value of $1.5 \mu\text{M}$, which decreases to approximately $0 \mu\text{M}$ at the edges of the profile. After each step that the diffusion equation is solved for, the system moves closer toward a homogeneous distribution of matter across the profile. The centre peak of the profile reduces in concentration, while the concentration at the edges of the profile rise and, eventually, the difference in concentration between each sample of the profile essentially does not change as the simulation progresses. During the entire redistribution of matter in this example with natural boundary conditions, total concentration does not change to a degree more significant than numerical precision.

This process of concentration smoothing out across the system is a visual representation of Fick's second law. In terms of this process in a cellular environment, one can imagine a cellular store releasing a quantity of some species at a position in space, and the immediately surrounding areas experiencing a higher concentration gradient than areas further away. The geometry, localisation of pumps and channels, and other proteins that interact with the species in question impart an additional effect on the distribution of matter over time. Further details on FEM model construction, including examples of interaction between pumps and channels, is detailed in Section 5.1.1.

2.5 Summary

Biological systems at the cellular level present a wealth of complexity that requires simplification and approximation in order to be computationally tractable. An appropriate method should be used to obtain the detail required from the system, and construction of a system using well characterised and simple physical processes enables emergent behaviour to arise.

If the dynamic concentration change of a species in response to channel activation is required, one might use an ODE network model, which will provide these

changes with respect to compartments in the cell. If more detail on the spatial nature of concentration change within compartments is required, one might use FEM to represent these compartments in multiple dimensions. Processes that occur on the smallest time scales do impart an effect on those at larger time scales, and while there are methods of simulation for many different system scales, these are often used in isolation of each other and so do not have an effect on neighbouring scales. Multiscale modelling can be used to link these together.

Before choosing an appropriate method for simulation, detail on the physiology of the biological system is required. Novel modelling opportunities may present themselves along with potential research routes for the future, while keeping in mind models which have already been produced.

```

from dolfin import *
# Based upon code in the FEniCS manual
class Boundary(SubDomain): # define the Dirichlet boundary
    def inside(self, x, on_boundary):
        return on_boundary
# Set up mesh with dimensions
lx, ly, Nx, Ny = 10, 10, 100, 100
mesh = Rectangle(0,0,lx,ly,Nx,Ny)
# Set up function space of elements
V = FunctionSpace(mesh, 'Lagrange', 1)
# Define an initial concentration
I = Constant(1.5)
# Previous value of u is initial distribution I
u_prev = interpolate(I,V)
# Find the boundary, apply conditions
bc = Dirichlet(V,u_prev,Boundary)
u = TrialFunction(V)
v = TestFunction(V)
dt = 0.1 # Time step
D = 10 # Diffusion constant
# Left hand side equation
a = u*v*dx + dt*D*inner(nabla_grad(u), nabla_grad(v))*dx
# Right hand side equation
L = u_prev*v*dx
# The associated time-dependent matrix from non
# time-dependent 'a', used during time looping
A = assemble(a)
# Our right hand side function, corresponding to L
b = assemble(L)
# Our new unknown at the new time level
u = Function(V)
T = 10 # Simulation length
t = 0 # Initial time
i = 20 # Position in the array we wish to observe
while t<=T: # Main loop over time
    # Reassemble the right hand function
    b = assemble(L, tensor=b)
    # Apply boundary conditions
    bc.apply(A, b)
    # Solve the diffusion equation, as u
    solve(A, u.vector(), b)
    # Sample concentration at mesh index i
    concentration_i = u.vector()[i]
    # Change concentration at mesh index i
    u.vector()[i]
    # Assign new solution to the previous result
    u_prev.assign(u)
    t += dt # Increment time

```

Figure 2.10: Sample code of a FEM simulation using FEniCS/DOLFIN. Any terms not declared in the code are automatically imported from DOLFIN.

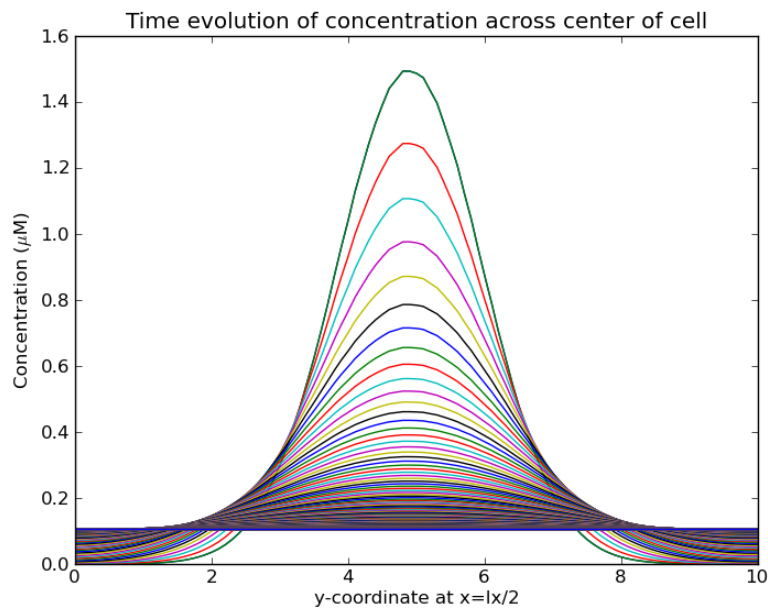


Figure 2.11: Plot showing the time evolution of an initial Gaussian distribution of concentration across the centre of a layer or cell, which diffuses over time to form a homogeneous distribution of matter. Each line represents the profile of concentration at each step, where the centre of the profile decreases with each subsequent step.

Chapter 3

Biological Background

3.1 Calcium

Calcium is a ubiquitous ion in biological systems, acting as a second messenger in signal transduction pathways. With a highly regulated concentration in cells, calcium interacts with a wide range of proteins, such as those which buffer or transport the ions into cellular stores. Once stored, calcium may be released in response to signals from other messengers or, in the case of CICR, in response to calcium itself. Calcium also plays a part in regulating the membrane potential of the organelle in which it is stored, similar to other ions found in the cell^[41].

Calcium transients usually present themselves as small oscillations, perhaps local to a particular region of the cell, but may also present themselves as a cell-wide 'global' wave of elevated concentration. The information encoded into these signals is so complex that, in the case of cardiac muscle cells, normal operation may continue under conditions where the frequency of oscillations is consistent but arrhythmic oscillations may result from defective calcium channels^[42]. Arrhythmic oscillations may result in an irregular heartbeat, with potentially fatal consequences. Abnormal calcium dynamics in other cell types can result in different physiological responses that also result in disease states. The complex characteristics exhibited by calcium dynamics in the cell make this ion important for understanding cellular processes and research into disease.

3.2 Mitochondria

The mitochondria are effectively cellular batteries. These organelles generate the majority of ATP in the cell, which is a source of chemical energy used by many cellular processes. A mitochondrion contains both an inner and outer membrane, that forms two internal compartments. The outer membrane contains many copies of the transport protein porin, which is permeable to many molecules and small proteins^[41]. The inner membrane is highly impermeable and selective to what it imports, particularly ions. The matrix is the space inside the inner membrane that, as a result of this selectivity, has a highly concentrated and specialised collection of enzymes and substrates required for production of ATP.

To summarise the process of ATP production, pyruvate and fatty acids entering the mitochondria are broken down and the products are metabolised by the citric acid cycle. This produces a source of electrons in the form of NADH and FADH₂. Electrons from these products are passed along an electron transport chain, to drive a proton gradient across the inner membrane that drives phosphorylation of ADP to ATP by ATP-synthase. One molecule of ATP is then exported from the mitochondria in exchange for one molecule of ADP from the cytosol^[41].

Calcium is taken up by the mitochondria from the local environment via the electrogenic calcium uniporter on the inner membrane, and is removed by the mitochondrial sodium-calcium exchanger. Elevated mitochondrial calcium activates rate limiting enzymes of the citric acid cycle, increasing the rate of ATP synthesis. During sustained elevations in mitochondrial calcium concentration, due to elevated intracellular calcium concentrations, formation and opening of the mitochondrial permeability transition pore (MPTP) occurs^[43]. This pore increases the normally low inner mitochondrial membrane permeability, causing mitochondrial membrane depolarisation and loss of the proton gradient that drives ATP production^[44] (a schematic of these processes is shown in Figure 4.6). Damage to the cell may occur if a high mitochondrial calcium level is combined with increased oxidative stress arising from the respiratory chain, where the mitochondria may initiate

the apoptotic programme of cell death^[45].

Being such an important organelle combined with the ability to initiate cell death, the mitochondria are related to a number of diseases including epilepsy, dementia and cancer^[46,47]. Mitochondria have DNA of their own (mtDNA), that is separate to nuclear DNA, and is usually inherited from the mother during sexual reproduction. Mutations to mtDNA typically affect the mitochondrial respiratory chain, and this in turn has greatest effect on tissue with high ATP requirements. Mutations to mtDNA and mitochondrial damage may also result from disease and ageing^[46]. Additionally, the mitochondria possess proteins thought to be involved in the control of fat storage in response to hormones and temperature, and regulate insulin secretion from pancreatic beta cells in response to blood glucose levels, making the mitochondria also important in obesity and diabetes^[47]. This organelle is therefore an important target for treatment of disease.

3.2.1 Motility

In many cells, the mitochondria are very dynamic; changing shape, undergoing fusion and fission, and relocation^[48]. Mitochondria spend the majority of their time undergoing brownian diffusion, but do perform bursts of directed movement approximately 6% of the time along microtubules or actin filaments that exist throughout the cell^[49,50]. The molecular motor kinesin pulls the mitochondria away from the centre of the cell (toward the plus end of a microtubule), and the molecular motor dynein pulls mitochondria toward the centre (toward the minus end of a microtubule). Movement toward or away from the centre of the cell is known as retrograde or anterograde transport, respectively.

It is unclear how the opposing motor forces are controlled to avoid a continual tug-of-war, but it is most likely that a directional programme to favour one motor over the other is required^[51]. This programme is thought to be initiated by cellular signalling molecules, mediated by the protein miro GTPase^[51,52]. These signalling molecules are thought to include protein kinase C (PKC, a family of proteins thought

to decode calcium signals^[53]), and calcium itself.

In addition to signalling molecules, there is also evidence of the functional state of the mitochondrion in controlling bi-directional transport^[51]. The functional state of mitochondria themselves is interesting, as it is thought to enable removal of defective mitochondria away from sites of high energy demand^[54]. Evidence for this is based on the fact that mitochondria exhibiting a low membrane potential have been observed in neurons to be transported away from areas of metabolic intensity, while others with high membrane potential were transported in the opposite direction, toward the area of energy demand^[55]. Mitochondria exhibiting a high membrane potential in addition to ATP depletion have been observed in cases of chronic pancreatitis^[56].

In addition to signals in the cell controlling the directionality of mitochondria, it has been shown that mitochondrial movement is effectively halted during calcium spikes in the cytosol, followed by full recovery of motility when the calcium concentration returns to homeostatic levels. Complete arrest of motility in the region of a concentration spike between 1-2 μM is thought to support recruitment of mitochondria to enhance local calcium buffering and ATP production in the region of the cell that requires such an enhancement^[57]. This may explain the existence of mitochondrial subpopulations in different cells instead of a uniform distribution^[58,59]. In contrast, cardiac muscle cells have a more crystalline arrangement of mitochondria, in order to provide ATP efficiently to the site of need. Disorganised and abnormally small mitochondria may be found in many cases of disease^[48,60].

3.3 The Pancreatic Acinar Cell

This report has so far discussed the complex nature of calcium signalling, and the importance of this ion in healthy and diseased cells. Also discussed is the importance of the mitochondria in providing services to the cell such as calcium buffering and ATP supply, and the role of this organelle in disease.

An interesting cell type from a modelling perspective, that combines previously discussed aspects of signalling with mitochondrial distribution and function, is the pancreatic acinar cell. The structural and functional relationship of cellular features in this cell result in a spatial pattern of events that require modelling efforts at different time scales. In addition to this, the pancreatic cell does not appear to have been modelled as extensively as other cells, such as the cardiac myocyte, which provides more scope for advancing knowledge in this area of biology. From a medical point of view, the pancreatic acinar cell is involved in pancreatitis, for which there are a lack of specific treatments^[61], and existing data that suggests an increasing trend in cases^[62].

The next section will discuss the biology of the pancreatic acinar cell, and finish with a short recap on what could be modelled as an extension of other modelling attempts.

3.3.1 Structure and Function

The pancreatic acinar cell is found in the exocrine tissue of the pancreas and is responsible for secretion of digestive enzymes. Figure 3.1 shows the location of the pancreas in the human body, and the location of acinar cells in the pancreas.

Acinar cells are described as both structurally and functionally polarised, and may be regarded as having two parts; the apical and basal regions^[63–65]. The regions differ in the number, type, and molecular function of the cellular organelles they contain, and these differences may be related to functional requirements.

The majority of the pancreatic acinar cell is considered to be the basal region, and contains typical cellular organelles such as the nucleus, ER, golgi apparatus, and mitochondria (Figure 3.2). The ER extends from the dense tubular network it consists of in the basal region through to a collection of rod-like extensions in the apical region of the cell, where it is held in position by microtubules^[65,66]. The apical region has a distinguishable boundary formed by a band of mitochondria, and contains zymogen granules (ZG) that store digestive enzymes in an inactive

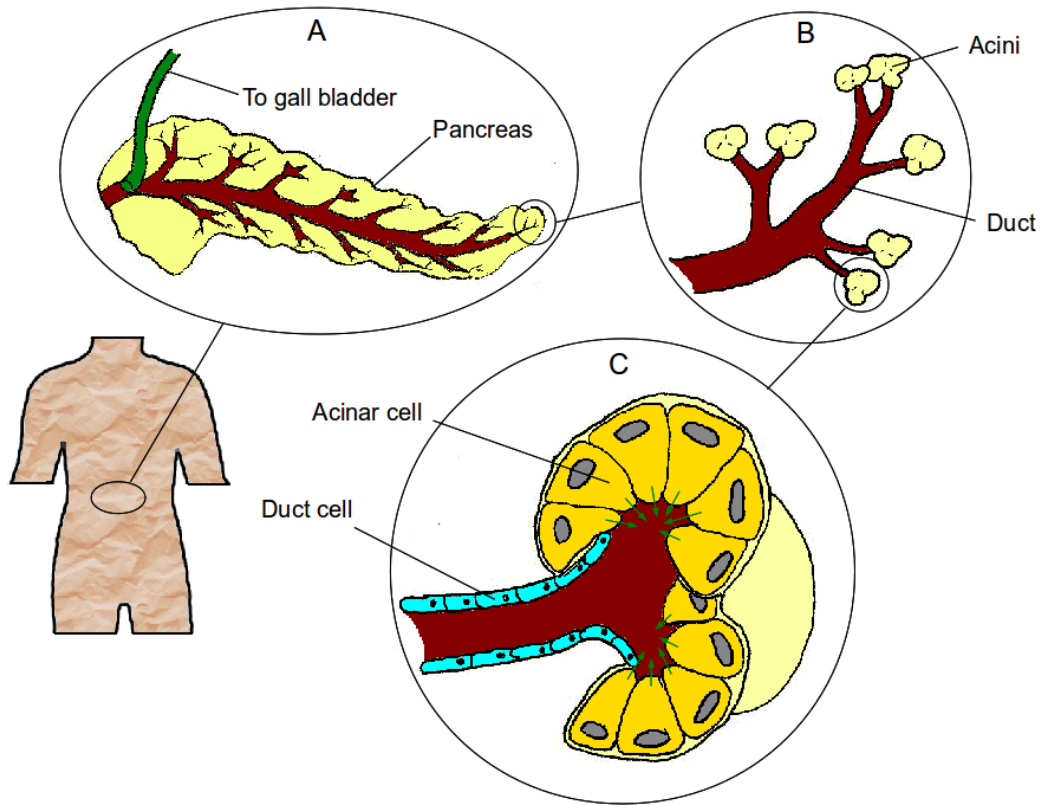


Figure 3.1: Schematic of the location of pancreatic acinar cells. The pancreas (A) is part of the human digestive system, inside the pancreas, the pancreatic duct branches out and ends at acini (B). Acini are clusters of cells, and the acinar cells contained in these (C) secrete digestive enzymes to break down food in the small intestine.

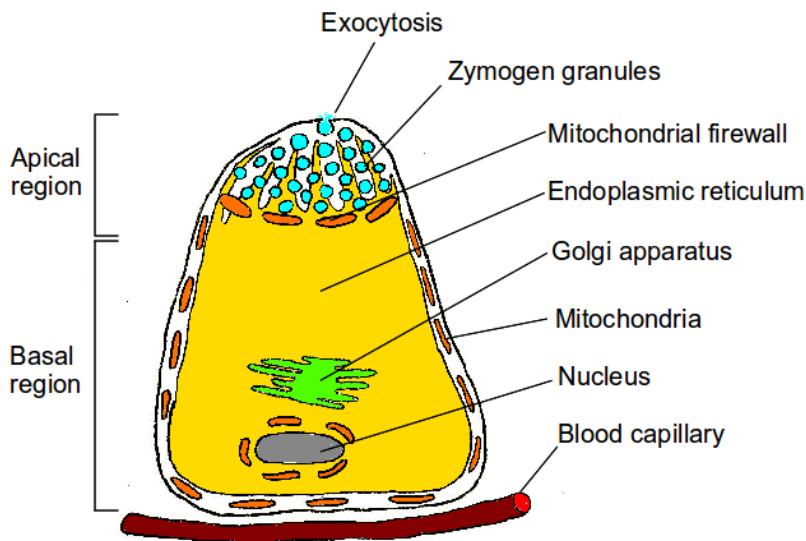


Figure 3.2: Schematic of the arrangement of organelles in the pancreatic acinar cell.

pro-enzyme form, ready for exocytosis through the apical cell membrane.

This polarised distribution of cellular components gives rise to a range of spatiotemporal calcium oscillations. These oscillations result in, or from, signals of other cellular messengers, usually mediated by cyclic release and uptake from cellular calcium stores. The main calcium store in the pancreatic acinar cell is the ER, but calcium may also be stored or buffered by the nucleus, mitochondria, golgi apparatus and ZGs^[66].

The primary purpose of calcium signals in the pancreatic acinar cell is to initiate the secretion process of digestive enzymes, and so the majority of these signals take place in the apical region. However, these 'local' oscillations may not be confined to the region in which they are initiated. Under certain conditions, a calcium transient initiated in the apical region may propagate into the basal region via CICR forming a 'global' wave of elevated concentration^[28,67].

The function of these 'global' calcium waves is thought to be for communication with organelles in the basal region, perhaps as a notification that apical secretion has taken place, in order to coordinate other functions of the cell in response^[66]. Calcium signals in the pancreatic acinar cell may be initiated by a range of molecules that activate calcium channels, but the main signalling molecule studied for this cell type is the messenger inositol (1,4,5)-triphosphate (IP3)^[63,66].

IP3 activates an IP3-sensitive calcium channel (IPR) located on the ER membrane, and the IPR channel oscillates between open and closed states that involve a negative feedback mechanism from the calcium that is released. Propagation of the IPR initiated calcium signal from the apical region toward the basal region is carried out by CICR of the RyR channels, which are also located on the ER membrane. The spatial localisation of IPR and RyR channels provides a calcium signalling system that may be controlled by a single messenger, and changes signal in response to availability of the molecule^[68].

Multiple isoforms of IPR and RyR exist in the pancreatic acinar cell on the ER membrane, with the density of these channels dependent on the region of the cell.

The apical region contains a high density of both channels and a sub-region of IPR channels with higher affinity to IP₃, known as the 'trigger zone'^[69]. The basal region contains IPR channels with a lower affinity for IP₃, and a higher density of RyR channels^[66]. Separating the apical and basal regions of the cell is a band of mitochondria, thought to buffer apical calcium transients and provide ATP to this region of higher metabolism (see Section 3.3.2).

The effect of this distribution of channels and mitochondria is that the apical region reacts to lower physiological concentrations of IP₃ to enable production of local oscillations. In contrast, higher concentrations of IP₃ may elicit a global wave through activation of IPR channels in the basal region that have a lower affinity for IP₃, in addition to a large calcium transient propagating across the cell, originating from the apical region via CICR.

Through a combination of channel inhibition and activation, Straub et al. (2000)^[67] controlled the contribution of either the RyR, IPR or mitochondria to calcium transients experimentally. The study found that CICR of the RyR channels, by waves initiated from the apical region, is modulated by the ability of the apical boundary mitochondria to buffer calcium. Inhibition of mitochondrial calcium uptake results in CICR of RyRs toward the basal region due to the altered dynamics of calcium clearance in the apical region. Inhibition of the RyRs with ryanodine prevents a CICR wave at low concentrations of IP₃, but higher concentrations result in a global calcium wave due to increased activation of the lower density IPR channels in the basal region. A combination of activated basal IPR channels and mitochondrial fire-wall breaching by calcium transients in the apical region was found to be responsible for wave propagation at high concentrations of IP₃.

In a similar study, Giovannucci et al. (2002)^[70] investigated experimentally the cytosolic calcium dynamics resulting from stimulation of pancreatic acinar and parotid cells after stimulation with IP₃. Through near-instantaneous and spatially uniform flash photolysis of caged IP₃, a transient rise in calcium was found in both cell types. The transient is described as a spatially localised signal in a discrete por-

tion of the apical region of the cell, where concentrations of IP₃ above a threshold induce a global calcium signal with characteristics of a propagating wave. They found that initial concentrations of IP₃ above 10 μ M are enough to induce an 'apparent wave' by significantly activating IPR channels throughout the cell, and subsequently CICR.

In order to return the cytosolic calcium concentration back to homeostatic levels, there are two main calcium transporters in this cell type; the sarco-endoplasmic reticulum ATPase (SERCA), for replenishment of the ER, and the plasma membrane ATPase (PMCA), for extrusion of calcium to the extracellular space. The density of calcium pumps in the cell is high due to their relatively slow mode of action. The PMCA pumps are localised mainly on the apical membrane in order to lower the concentration between calcium oscillations. The SERCA pump is found all over the ER membrane, close to calcium release sites, and is thought to provide high-affinity buffering of calcium ions that enforces localisation of calcium waves^[66].

The apical portion of the ER is losing calcium by frequent activation of IPR and RyR during normal operation, yet the ER does not seem to entirely deplete. The reason behind this is a phenomenon known as ER 'tunnelling'^[71,72]. Calcium that is lost in the apical region from the ER (and removed from the cell by PMCA) is replenished by an extracellular source via store-operated channels (SOC) at the basal membrane, which has been proposed to be activated by either depletion of the ER or direct activation of IP₃^[66]. Independent of the mechanism of entry, this influx of calcium at the base of the cell is required at the apical region, and is transported by the ER through absorbing calcium released by SOC at the basal membrane, and transporting it to the region of low concentration inside the ER by diffusion. This way the ER has a replenished calcium concentration in the apical region, without significantly raising the concentration in the cytosol or producing additional signals^[65]. In addition to immediate uptake of the ER, calcium entering from the basal membrane may be taken up by nearby mitochondria, or diffuse into the cytoplasm and accumulate in other cellular organelles such as the nucleus, golgi, or eventually

the ZGs, before being removed by PMCA or exocytosis^[66].

3.3.2 Mitochondria in the Pancreatic Acinar Cell

Mitochondria are present in the acinar cell, in three distinct subpopulations; perinuclear, perigranular and subplasmal or peripheral^[58,58,59,63,67] (Figure 3.3). These three sub populations of mitochondria respond to cytosolic calcium signals in their immediate environment by locally regulating calcium homeostasis and energy supply^[59], and are possibly recruited to these areas by a regulated cellular transport mechanism^[49,57].

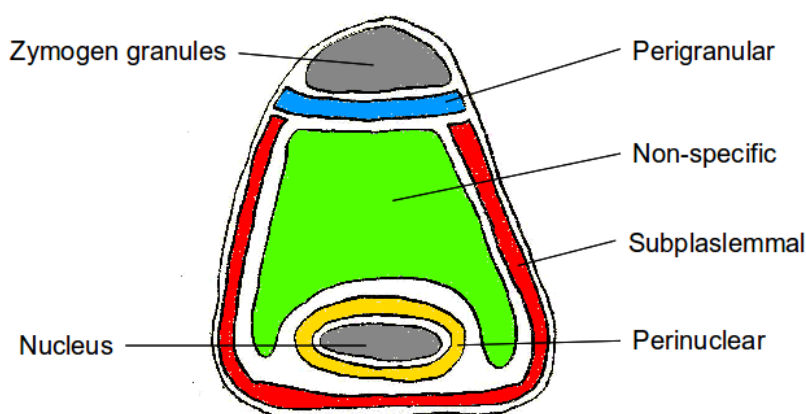


Figure 3.3: The distribution and quantification of mitochondria in the pancreatic acinar cell.

Perinuclear mitochondria are thought to interact with the nucleus by adjusting ATP supply through privileged communication via nuclear calcium signals, or by being available for initiation of apoptosis after receiving the associated signals. In addition to these roles, perinuclear mitochondria may also ensure protection from elevated intracellular calcium^[58,59], which could be damaging to the nucleus.

Subplasmal mitochondria are thought to locate themselves close to areas of calcium entry around the plasma membrane. Here, calcium transients stimulate ATP production, which is required by the ER and plasma membrane ATP-dependent uptake machinery in response to elevated calcium.

Perigranular mitochondria surround the ZGs in the apical region of the cell, which are also described as being a mitochondrial firewall, boundary, or belt^[11,58,63].

The function of this firewall is thought to confine calcium oscillations to the granular region, as well as stimulate enhanced local ATP production that is used for processes leading to exocytosis^[59].

3.3.3 Pancreatitis

Pancreatitis is the inflammation of the exocrine pancreas, and may be classified as either chronic or acute. The disease usually develops either as a result of gallstones moving into the pancreas, or moderate to heavy ethanol consumption. Mortality rates for the disease are around 5-10%, with this number increasing to around 30% if complications develop. The multiple pathobiological pathways activated during acute pancreatitis means there are lack of specific treatments for the disease, and this is the reason for such a high mortality rate^[61].

One of the earliest events in acute pancreatitis is premature activation of digestive enzymes inside the ZGs of the pancreatic acinar cell by trypsin, that subsequently lead to autodigestion of the host cell. Although the specific cause of trypsin activation is still unknown, it is thought to be related to sustained acinar cell stimulation over the time course of 15-20 minutes, with almost complete emptying of ER calcium^[64,73].

Non-physiological and sustained increases in intracellular calcium concentration lead to increased consumption of ATP in the cell, as ATP-dependent pumps work harder to remove calcium from the cytosol^[56,61]. Bile acids (BA) and fatty acid ethyl esters (FAEE) may activate IPR and RyR channels of the ER, stimulate release of calcium from the ZGs and activate SOCs, all of which abnormally increase the intracellular calcium concentration. In addition to this, BA may also inhibit restoration of homeostasis by deactivating the ATP dependent SERCA and PMCA pumps^[61,64,74]. Sustained elevation in intracellular calcium may cause ATP depletion due to mitochondrial dysfunction^[75], since calcium accumulation leads to depolarisation of mitochondrial membrane potential and, eventually, opening of the mitochondrial permeability transition pore^[76]. Additionally, calcium accumulation in the mito-

chondria leads to initiation of apoptosis or necrosis. The pancreas does seem to have evolved a defense against the development of the disease. At the initial stages of pancreatitis the secretion of pancreatic fluid is greatly increased, which suggests a possible 'wash-out' mechanism. Failure of this defence is thought to allow reflux of BA in the presence of gallstones that block the pancreatic ducts^[61,64].

As sustained elevation of calcium concentration is a key aspect of the disease at a cellular level, a potential therapeutic strategy is likely to involve reduction of these elevated levels in order to promote ATP production of the dysfunctional mitochondria. A possible way to achieve this is to deliver encapsulated ATP directly to the affected cells in order to kick-start ATP dependent pumps and return calcium homeostasis, which may restore mitochondrial function^[61].

Gallstones are very common and associated with a number of risk groups, such as those who have cirrhosis of the liver, are obese, are female, or those who have recently lost weight. Of the adult population in England, it is estimated that 1 in 10 have gallstones, and there is a 1 in 50 chance of gallstones causing symptoms*. According to statistics gathered by the National Health Service Information Centre for health and social care (NHS IC), the total number of alcohol-related NHS admissions per year in England has more than doubled between 2002 and 2010, from 510,800 to 1,057,000^[62]. Contributing to these totals, the number of admissions wholly attributable to alcohol-induced chronic pancreatitis has also more than doubled from 3,100 to 7,000, while the number of admissions partly attributable alcohol-induced acute and chronic pancreatitis has shown an increase from 3,300 to 3,900. While it could be argued there is a social problem underlying such trends, the data suggests that cases of alcohol-related pancreatitis are likely to increase in number in the future.

Better understanding is required of physiological processes in the cell, in order to understand diseases such as pancreatitis and ultimately develop therapeutic medicine. Computational modelling can aid understanding of such processes,

*<http://www.nhs.uk/Conditions/Gallstones/Pages/Introduction.aspx> (accessed 7/9/12)

and could ultimately be used to assess and further develop the approach taken to develop such treatments.

3.3.4 Notable computer models of pancreatic acinar cell calcium dynamics

The Sneyd et al. model of calcium waves in pancreatic and parotid acinar cells

Sneyd et al. (2003)^[28] describe a common pool ODE network model of calcium oscillations in pancreatic and parotid acinar cells, using experimentally obtained data^[67]. The common pool model was extended into a spatially compartmentalised model, of 50 compartments along the x -axis (assuming uniform concentration along yz) in order to investigate calcium wave propagation initiated in the apical region (Figure 2.6).

The model includes different densities of Markovian chain IPR and RyR channels in the apical and basal regions through control of channel permeability rate constants, and a mitochondrial belt region is included where mitochondria provide a constant extrusion of calcium. The model provided results which concluded that at low concentrations of IP₃, calcium waves that originate from the apical region propagate into the basal region through a diffusive mechanism. Whereas, at higher IP₃ concentrations the calcium wave propagates through an active CICR mechanism.

The Yano et al. model of calcium signalling in the pancreas

Yano et al. (2003)^[77] describe in very brief detail a finite element model of the pancreatic acinar cell. The article does not provide any detail on how the model was constructed, but instead reference a paper that was in press at the time, which does not exist.

One year later the same authors published an article referencing the ODE model described by Sneyd et al., but this model is not finite-element based and is missing features of the Sneyd model such as the RyR channel and inward basal calcium

flux^[78].

The Tsaneva-Atanasova et al. model of calcium oscillations in a triplet of pancreatic acinar cells

Tsaneva-Atanasova et al. (2005)^[79], extended the Sneyd et al. ODE model described in 2003 by coupling a triplet of pancreatic cells via gap-junctions along common cell membrane contacts, in order to investigate intercellular signal communication.

The model uses the finite element technique to solve the diffusion equation for both intracellular calcium and IP₃, on a mesh representative of cell shape. They observed that, when coupled, the cells exhibit a variety of synchronous, phase-locked and asynchronous oscillatory behaviours. The spatial distribution of features in the cell is achieved by enforcing different parameters for model equations in different regions, and so is based upon similar assumptions to Sneyd et al (2003).

3.4 Modelling scope

With knowledge that mitochondrial motility has been observed experimentally, it would be interesting to see if the arrangement of mitochondria in the pancreatic acinar cell ensures that ATP concentration is greater at sites of high metabolism. Sites of high metabolism are characterised by increased calcium cycling, and so a hypothetical mechanism of motility could be designed in order to see if the existence of subpopulations can be attributed to calcium concentration gradients. Neither of these aspects of the mitochondria in pancreatic acinar cells has been found to be investigated through computational modelling efforts, or published previously.

The mitochondrial firewall effect has been modelled computationally in previous studies^[28,77,79]. The mitochondria are represented simply as a flux that removes calcium instead of a buffer with the ability to release it, and suggest that the role of mitochondria is instead more complex than blocking the diffusion of calcium^[28]. Modelling efforts for this cell type would benefit from inclusion of a more complex rep-

resentation of the mitochondria, with additional features such as ATP metabolism.

Pancreatitis is closely linked to the calcium dynamics of the pancreatic acinar cell and the mitochondria. This disease is thought to be initiated through exposure to BA (resulting from blockages of the pancreatic duct) and FAEE (resulting from excessive ethanol consumption). There are no computational studies that attempt to investigate the effect of BA or FAEE on the detailed calcium dynamics of the pancreatic acinar cell. However, recently published research indicates that computational modelling efforts have investigated this disease at the organ level for the lifetime of an organism. The onset of pancreatitis is mediated by trypsin, and the model includes several types of molecule, including calcium^[80]. The ability of a cellular-level system to model altered dynamics in response to exposure to BA or FAEE, could provide rate constants for use in similar organ-level simulations, in order to assess potential treatment avenues.

Tunnelling of calcium in the ER from the base of the acinar cell to other regions of the ER is thought to be a mechanism employed to ensure the ER is not significantly depleted during stimulation. Using a sophisticated modelling technique such as FEM, where the ER is represented as an additional, spatially resolved, compartment should allow observation of these hypothesised concentration gradients. This is a phenomenon observed and commented on experimentally, but not investigated computationally.

Implementation of the above as a computer model will provide support to existing research and may even provide alternate hypotheses on cellular mechanisms. These, and any future improvements to the model, will provide further understanding of the biological processes at work in this cell type, in addition to contributing to the field of cellular computational modelling.

3.5 Summary

This chapter provided an overview of the biology behind cellular calcium and the mitochondria, the pancreatic acinar cell, and the disease state pancreatitis. Under physiological conditions, the pancreatic acinar cell maintains a level of cytosolic calcium concentration much lower than that of intracellular membrane bound stores and extracellular fluid, maintained by ATP dependent pumps. This potential concentration gradient favours diffusion-based calcium entry into the cytosol and enables small calcium oscillations in the apical region of the cell to be used as a signal to control cellular processes, such as exocytosis of granules containing digestive pro-enzymes and promotion of ATP production by the mitochondria. Calcium oscillations may be initiated by intracellular secondary messengers, such as IP₃, which release calcium from the ER by activating the IPR channels, which in turn initiates CICR of the RyR channels. Mitochondria surround the apical region of the cell, acting as both a buffer to contain the majority of apical calcium oscillations and to provide ATP to this site of increased metabolism. In the pancreatic acinar cell, sustained elevation in calcium concentration, coupled with depletion of ATP, increased mitochondrial membrane potential and activation of digestive enzymes, occurs in cases of pancreatitis. Multiple metabolic pathways are activated during this disease state, which hinders the development of specific treatments.

The spatiotemporal nature of calcium signals in this cell type, coupled with distinct arrangement of cellular organelles make it an interesting and complex system for modelling. Computational models of the pancreatic acinar cell exist, but these do not include mitochondrial function much further than as a calcium sink, and certainly do not attempt to model these mitochondria as dynamic entities with regard to movement. These models also do not comment on an ER calcium tunnelling mechanism, use a specific spatial distribution of cellular features such as channels and pumps other than mitochondria, nor attempt to model a disease state such as pancreatitis.

With these points in mind, what follows is detail on the modelling efforts and

path taken in construction of a multiscale model of the pancreatic acinar cell, beginning with implementation of ODE based network models that were later extended using the more sophisticated FEM approach.

Chapter 4

Biological network modelling at the cellular level using ODEs

4.1 Implementation of literature models

4.1.1 The Bondarenko et al. Model of the Cardiac Myocyte

An example of the difficulty in implementing complex literature models

The cardiac myocyte has been a focus of mathematical modelling since the late 1970s, and as such many examples of models may be found in the literature. While this volume of research is a strength of the field, more recent models become highly complex and sensitive to changes in parameters, as techniques in microscopy and electrophysiology improve. The trend seems to be that models published are often a direct extension or modification of other models; for example, updated kinetic rates based upon recent biophysical data, or better characterisation of a particular channel.

The Bondarenko et al.^[24] model of the action potential of mouse ventricular myocytes is based upon biophysical data obtained from voltage-clamp experiments. This model builds upon previous implementations of this cell, and reproduces experimental data for the major ionic currents of myocytes. Markovian models are

used to represent the kinetic properties of activation and inactivation of various channels, and rate constants associated with these may be modified to represent a disease state or genetic mutation. A new Markovian model implementation of LCC kinetics is detailed, and is coupled to a separate cellular sub-compartment to account for the spatial localisation of calcium concentration gradients (Figure 4.1). This compartment provides local control of CICR by sharing the subspace pool with the opposing RyR channel, thus eliminating the need to involve the entire intracellular space as a CICR sensor. The ability of this model to reproduce major ionic currents, while coupling a localised element of calcium signalling, had made the model an attractive candidate for potentially modelling processes occurring at different spatiotemporal scales. This model was therefore chosen as a well explained and fairly recent example of the cardiac cell, and as an introduction to biological network modelling using ODEs.

The model was implemented in Python by coding the approximately 100 parameters and 112 equations that were included in the article. Somewhat unsurprisingly, the model experienced integration errors after this stage of the implementation was thought to be complete. After checking all the equations in the Python implementation against the article it was determined that, apart from an issue involving a typographical error in the article, each had been entered correctly and the fault must lie somewhere else. Since the complexity of the model was such that the problem could not easily be elucidated, the authors were contacted and they kindly supplied the original source code to test against, written in FORTRAN 77. On closer inspection, it was found that some parameters in the source code were calculated on the fly from other unidentified parameters, and the resulting values were not exactly the same as those published.

No details of the unidentified values used to calculate some of the parameters in the original code are included in the article, and so it is likely they were omitted to make the published material less complex. However, these small differences between the source code and the article soon amount to a larger difference in results

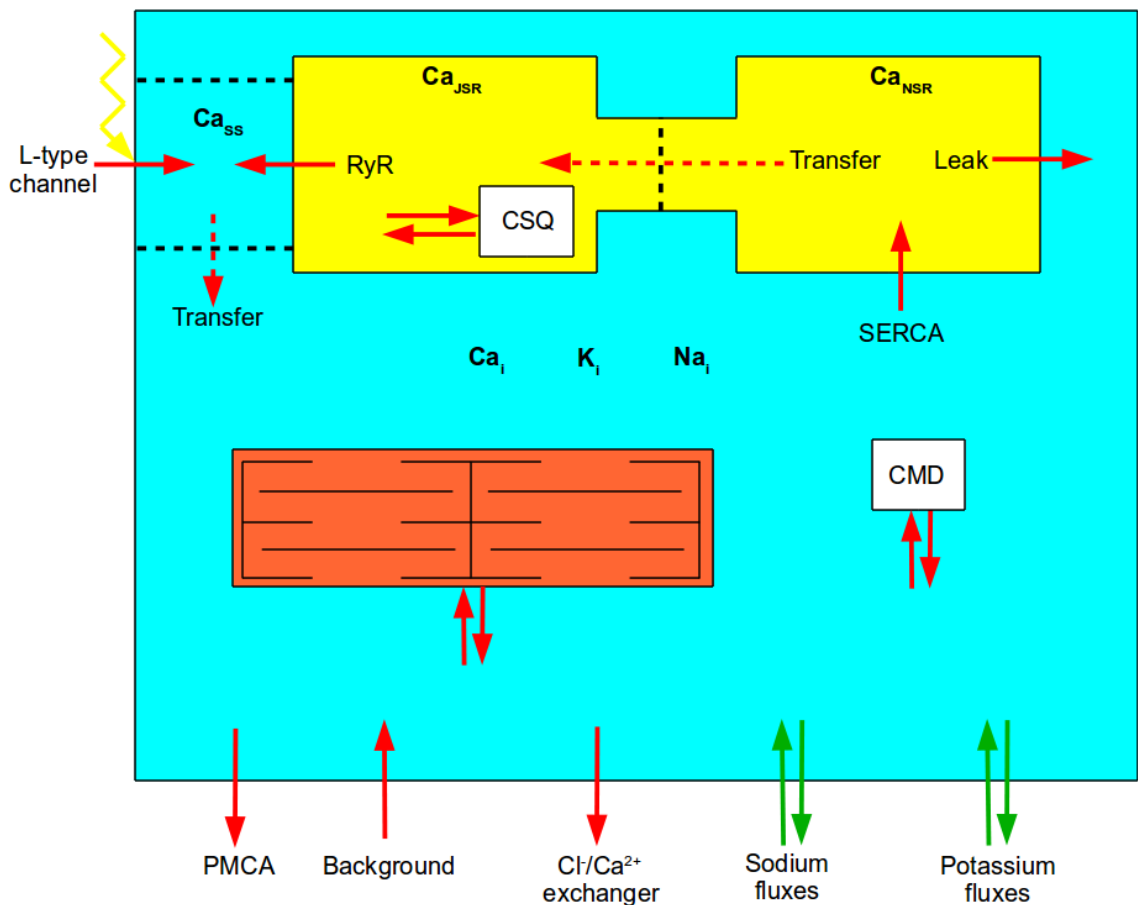


Figure 4.1: Schematic of the fluxes involved in the ODE model of the cardiac cell by Bondarenko et al.^[24]. The yellow area represents the SR, consisting of junctional and network parts (JSR and NSR). The blue area represents the cytosol, consisting of the subspace and intracellular regions (SS and i). The white parts represent calcium buffer proteins calsequestrin and calmodulin (CSQ and CMD). Red represents muscle tissue, specifically the calcium buffer troponin. Red arrows represent calcium fluxes and currents, and green represents other ions. These ions are labelled with the compartment to which they correspond as their subscript (see Section 2.2.3).

when an implementation using the article is attempted. An example of differing values between those in the source code and the article is the parameter $Gkto$, which is calculated using unknown values in the source code as; $0.705/2.08 \times 1.2$, to provide the parameter 0.40673077. There is no parameter in the article named ' $Gkto$ ', however on closer inspection there is a parameter named ' $Gkto, f$ ', equal to 0.4067 mS/ μ F, which means a small difference of approximately 0.00003077 mS/ μ F. Another parameter named $SF1CA$ is included in the original source code, which is calculated as; $4 \times 1.2/(36 \times 6) = 0.02222222$. There is no parameter in the article named ' $SF1CA$ ' but in the source code, this parameter is multiplied by yet another

unknown parameter of 7.78111. This results in a value 0.17291356, which is closest to the parameter $GCaL$ in the article at a value of 0.1729 mS/ μ F, meaning a difference of 0.00001356 mS/ μ F. Similar issues were found with parameters in the source code named $Gkur1$, $Gkur2$, $Gkur3$, Gks and $v2$, of which only $v2$ has a matching name in the article. These small differences in the number of quoted significant figures between published values and those calculated in the source code, although small, accumulate during integration and result in issues while reproducing published data. Although sensitivity to parameters is useful in models that aim to predict behaviour that result from altered kinetics, this raises serious questions on the reliability of parameters in ODE models. How reliable are experimentally obtained parameters? How reliable are those which have been fitted to experimental data? What issues have been unknowingly carried over from earlier models in the field? This also highlights the importance of obtaining original model code to accompany published material; while the values used to calculate these parameters still have unknown dimensions, inconsistencies between the initial Python implementation and published results could not have otherwise been realised, or attempted to resolve.

A script was written to compare all the degrees of freedom between the original source code and the Python implementation. An RK4 method of integration was implemented for the Python version, based upon that used in the source code, so that any errors related to the integration routine were replicated in both. Issues with the Python implementation, with respect to parameters such as those mentioned previously, were found and resolved through a process of elimination. The error between implementations was eventually reduced to less than $1 \times 10^{-10}\%$, and produced comparable plots to the original code.

The model responds to membrane voltage depolarisation (Figure 4.2, top) by releasing calcium from the SR calcium store, into other compartments (Figure 4.2, bottom), which can be viewed schematically in Figure 4.1. Initially, membrane depolarisation activates the LCC, which causes influx of calcium into the subspace

(Ca_{ss}), and is sensed by the RyR channels. The RyR channels are activated via CICR, and increased calcium flows into the subspace from the junctional SR (Ca_{JSR}). The relatively high concentration of calcium in Ca_{ss} compared to Ca_i is due to the difference in relative volume of these compartments. Calcium diffuses from Ca_{ss} into the cytosol (Ca_i), where it is buffered by calmodulin (CMD) and troponin, before it is taken up into the network SR (Ca_{NSR}) by SERCA. Calcium in Ca_{NSR} then diffuses back into Ca_{JSR} , and is partly buffered by calsequestrin (CSQ) ready for the next release event. In addition to these processes, there are also membrane fluxes that add and remove calcium from the cytosolic pool. In addition to calcium, the potassium and sodium concentration in the cell is changed by other pumps and channels, and the balance of ions inside and outside the membrane during stimulation gives rise to change in voltage. The plots on the bottom of Figure 4.2 also show the delay in release and recovery of the junctional SR concentration, which occurs because of the delay between uptake of calcium in Ca_{NSR} by SERCA, and transfer of ions back into Ca_{JSR} .

Owing to the fact that the the Python implementation largely matches the original source code, it could be concluded that both models are error free and dimensionally consistent. To be sure of this however, and assist in future extension or modification of the model, the explicit SI units for each parameter were added using the “SI and simulation units” Python module, created by the University of Southampton Engineering Department (authored by Dr. Thomas Fischbacher, Prof. Hans Fangohr, and Dr. Matteo Franchin). Using this tool, parameters are stored as SI objects that contain dimensional information, and can flag up errors when used incorrectly in a calculation. Initially, the Python implementation flagged dimensional inconsistency errors that resulted from typographical errors, but as these became fixed it was apparent that the majority of equations in the model contain unidentified numbers that do not have units declared in the article (the values 0.0084 and 0.00002 in equation A59^[24], for example). One by one, most of these missing units were calculated, adding a further 100 parameters to the model. The remaining values seem

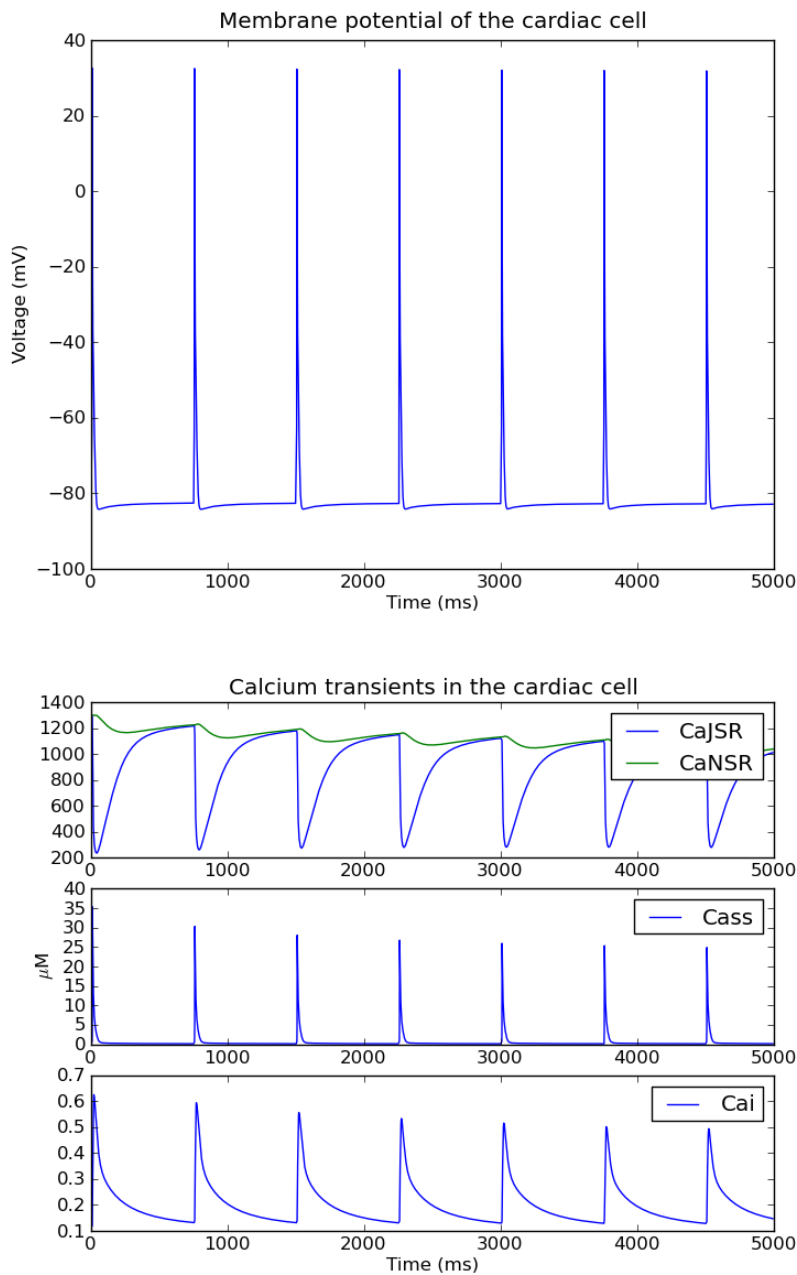


Figure 4.2: Python implementation results of the membrane potential (top) and calcium transients (bottom) for the model of mouse ventricular myocyte by Bondarenko et al.^[24]. The system was stimulated at 80 beats per minute for 5000 ms (resulting in a change of membrane potential, top). A stimulation routine was constructed for the model, that initiates membrane depolarisation at a desired frequency by subtracting a small amount from the membrane potential ODE (V ; cell membrane potential, $CaJSR$; junctional sarcoplasmic reticulum calcium concentration, $CaNSR$; network sarcoplasmic reticulum calcium concentration, Cai ; intracellular calcium concentration, $Cass$; subspace calcium concentration).

to be scaling factors that perhaps convert values between the micro to milli metric prefixes, but this is not clear and many parameters remain unknown. Crucially, one particular ODE in the model that controls the cell membrane potential, (and subse-

quently the majority of ionic fluxes in the model), was found to have inconsistent units that does not result in volts. The ionic channel currents that contribute to the cell membrane potential are shown in Equations 4.1 to 4.4, and should have SI base units of $\text{m}^2\text{kg}/\text{s}^4\text{A}$, (or pA/pF in simulation units), according to model parameters.

The currents that make up the sum of each ionic contribution to the membrane potential in Equations 4.1 to 4.5 demonstrate the complexity and importance of the membrane potential to the cardiac cell model. These currents are converted to fluxes when used to change cytosolic concentrations, and the sums corresponding to each ion are shown in Figure 4.1.

$$I_{sum,Ca} = I_{CaL} + I_{pCa} + I_{NaCa} + I_{Cab} \quad (4.1)$$

$$I_{sum,Na} = I_{Na} + I_{Nab} + I_{NaK} \quad (4.2)$$

$$I_{sum,K} = I_{Ktof} + I_{Ktos} + I_{K1} + I_{Ks} + I_{Kur} + I_{Kss} + I_{Kr} \quad (4.3)$$

$$I_{sum} = I_{sum,Ca} + I_{sum,Na} + I_{sum,K} + I_{ClCa} + I_{stim} \quad (4.4)$$

$$\frac{dV}{dt} = -\frac{I_{sum}}{C_m} \quad (4.5)$$

The currents are named as follows; L-type calcium current (I_{CaL}), calcium pump current (I_{pCa}), sodium-calcium exchange current (I_{NaCa}), calcium background current (I_{Cab}), fast sodium current (I_{Na}), background sodium current (I_{Nab}), sodium-potassium pump current (I_{NaK}), transient outward potassium current (I_{Ktof}), transient outward potassium current (I_{Ktos}), time independent potassium current (I_{K1}), slow delayed rectifier potassium current (I_{Ks}), ultrarapidly rectifying delayed rectifier current (I_{Kur}), noninactivating steady-state potassium current (I_{Kss}), rapid delayed rectifier potassium current (I_{Kr}), and calcium activated chlorine current (I_{ClCa})^[24]. I_{stim} is a stimulus current that is applied during the simulation to initiate membrane potential depolarisation. Each of these currents perform an important part in formation of the action potential, and the inclusion of this amount of detail is desirable when predicting the effect of cardiotoxic drugs on currents. For example, the I_{Kr} cur-

rent contributes to repolarisation of the action potential, and the gene that encodes this channel (human ether-à-go-go) is an important pharmaceutical anti-target^[81]. Therefore, the action potential forms a very important part to the model.

The parameter C_m has SI base units of $s^4 A^2 / m^4 kg$, (or $\mu F / cm^2$ in simulation units), which results in base units for the membrane potential ODE of $m^6 kg^2 / s^8 A^3$ (Equation 4.5), while the expected base units of voltage per unit of time are $m^2 kg / s^4 A$, (or $mV s^{-1}$ in simulation units). This issue could not be resolved even through discussion with the model authors via email.

Although a significant amount of time was invested in implementing this model, and the fact it could reproduce figures found in the original article without treatment with units, it was decided to be too error-prone and further work on this portion of the project ceased. The work carried out up to this point still served a purpose, however; it provided a practical introduction to biological network modelling of ODEs, and provided many more lessons than might have been learned from a model that was more of a success in the project at that point. Notably, it highlighted the need to obtain original source code from any model which a project aims to build upon, in order to check for potential problems, and that not everything may be trusted to be both accurately nor completely included in the literature describing these models.

4.1.2 The Sneyd et al. Model of the Acinar Cell

The Sneyd et al.^[28] model of calcium waves in pancreatic and parotid acinar cells, as previously described in Section 3.3.4, initialises CICR through stimulation of IPR channels by IP₃, which in turn stimulate RyR channels, causing release of calcium from the endoplasmic reticulum (Figure 4.3). By altering parameters relating to the density of these channels, the model predicts the range of IP₃ concentrations required to initiate a local or whole-cell calcium wave. An interesting part to this study was that the ODE model was extended to model diffusion in one dimension along the x -axis as a spatially compartmentalised model, while assuming the con-

centration profile is uniform along yz . The cell is split into 50 compartments along the x -axis linked by diffusive fluxes, that allow the effect of heterogeneous channel densities in the apical and basal regions, separated by a region containing mitochondria, to be modelled.

Using a common pool model of the apical region, it was found that low concentrations of IP3 are enough to initiate small local calcium oscillations, where higher IPR and RyR density are thought to be. The basal region was found to exhibit smaller calcium transients in response to a similar range of IP3 concentrations. When both regions of the cell were spatially compartmentalised as a whole cell model, the model posed that calcium waves follow an active or kinematic mechanism, depending on the stimulus (i.e. propagated through sequential channel activation, or calcium diffusion, respectively). Low concentrations of IP3 result in an oscillatory response local to the apical region, and confined in part to this region by the mitochondrial buffer, while higher concentrations of IP3 allow calcium to break through the mitochondrial buffer and propagate through the basal region via CICR.

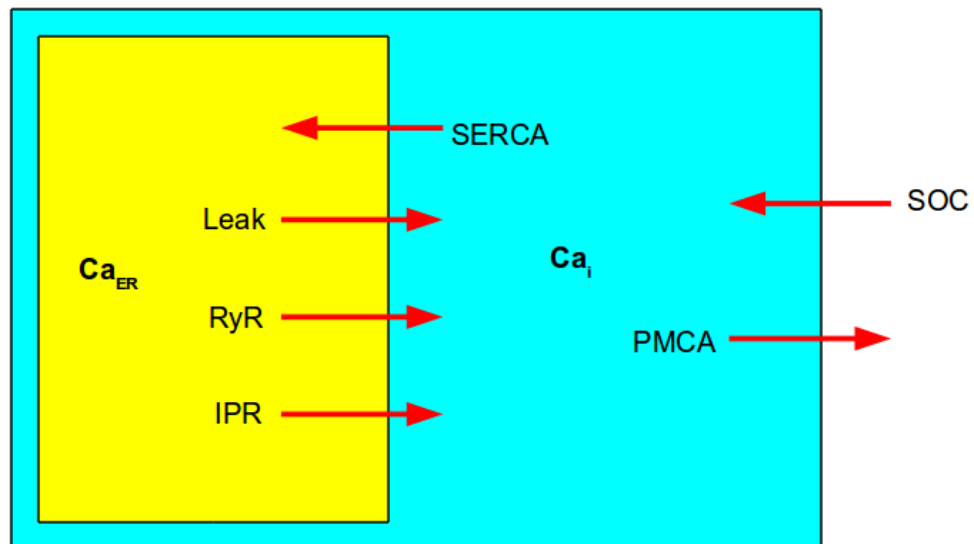


Figure 4.3: Schematic of the fluxes involved in the ODE model of the pancreatic acinar cell by Sneyd et al.^[28]. The biology of this system is discussed in Section 3.3.1.

The equations contained in the article were coded into Python for use with Odeint. However, none of the initial conditions were included in the article, and two parameters for the J_{in} flux did not have units. The authors were contacted, and they kindly

provided a copy of the source code, written in a scripting language for use with the integration software XPPAUT*. Once the model parameters were treated with SI units, it was found that k_{ap} and k_{bp} had typographical errors with respect to the index of their dimension of concentration, which needed to be negative to be compatible with the dimensions of the Markovian RyR model (i.e. $k_{ap}=\mu\text{M}^{-4}\text{s}^{-1}$ and $k_{bp}=\mu\text{M}^{-3}\text{s}^{-1}$, not $k_{ap}=\mu\text{M}^4\text{s}^{-1}$ and $k_{bp}=\mu\text{M}^3\text{s}^{-1}$). The model then ran without integration errors and produced plots similar to those in the article.

This model cannot reproduce all figures in the article quantitatively, since most of the plots correspond to results Sneyd et al. produced using the spatial model, and not the common pool ODE version that has been implemented here. The Python implementation that has been constructed instead reproduces either oscillations that relate to the apical region or the basal region, depending on which parameter set is used. Implementation of the spatially compartmentalised version of this model was deemed too complex, and disregarded in favour of instead extending the model using the FEM method (see Chapter 5).

The Python implementation of the common pool model shows spontaneous oscillations that occur at a frequency that increases as a function of IP3 concentration, and these oscillations occur when the concentration is held fixed. Figure 4.4 shows oscillations in response to a fixed concentration of $3\ \mu\text{M}$ IP3. This figure shows that the RyR open fraction is synchronous with the IPR open fraction, which demonstrates that CICR occurs. Calcium flows into the cytosol from the ER upon IPR and RyR stimulation and, after repeated activation of IPR and RyR channels, the ER reaches a steady state between 40 and $60\ \mu\text{M}$. The reason these oscillations spontaneously occur is due to the complex activation kinetics of the Markovian IPR channel model (a modified version of this channel model is discussed in Section 4.2.2).

A source of confusion in the article by Sneyd et al. was an equation that controls the exponential decay of IP3 concentration. This stimulates the cell in a manner analogous to experiment, where IP3 was photoreleased simultaneously across the

*<http://www.math.pitt.edu/~bard/xpp/xpp.html> (accessed 7/9/12)

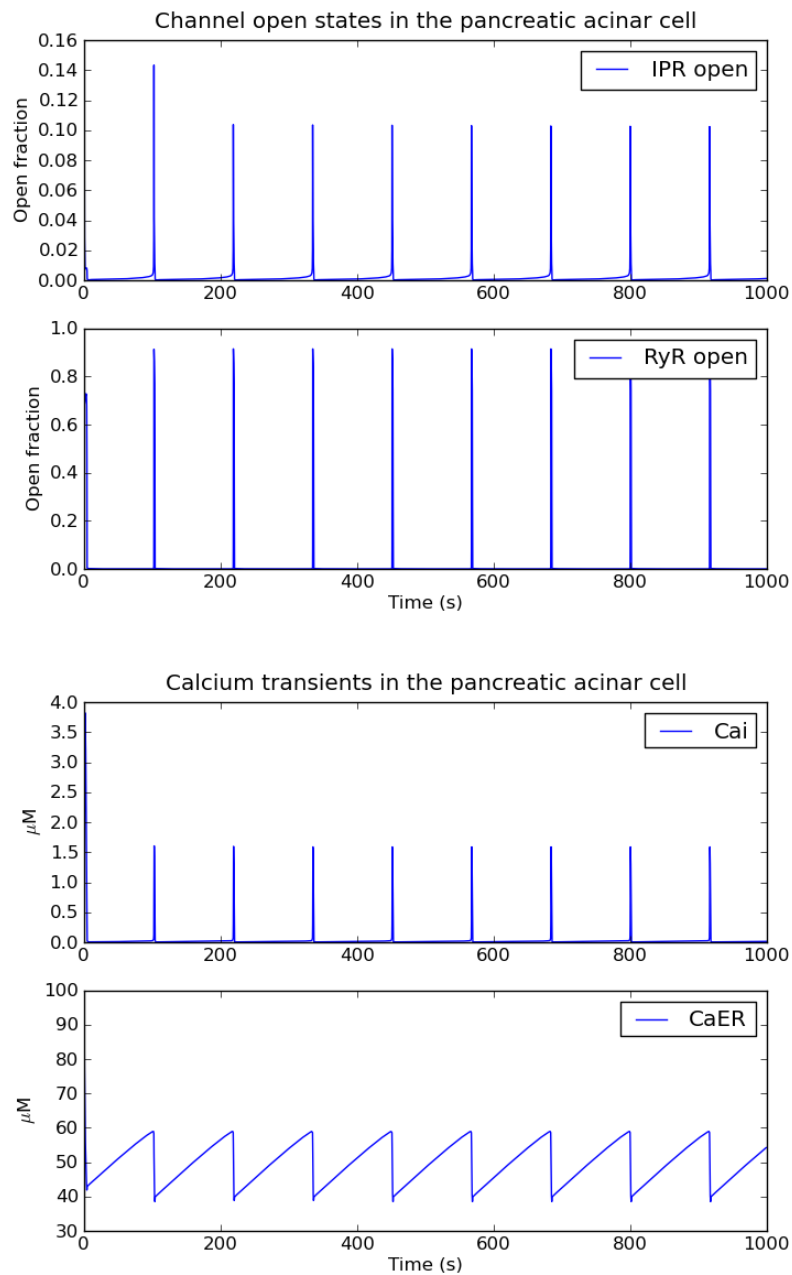


Figure 4.4: Python implementation results of channel states and calcium transients for the common pool model of pancreatic acinar cell by Sneyd et al.^[28]. These plots correspond to the apical region, and the system was stimulated with IP3 at a concentration of $3\mu\text{M}$ for 1000 s (Cai ; intracellular calcium concentration, CaER ; endoplasmic reticulum calcium concentration).

entire cell at a particular concentration that decreased over time, and the results of which were used to parameterise the model. This stimulation protocol was used in simulations by Sneyd et al. for calculation of wave speed in their spatially compartmentalised model. The text states that peak IP3 concentration decreases with a time

constant of $1/0.8$ s, and follows Equation 4.6 (where t is time, $p(t)$ is the concentration of IP3 at time t , and p_0 is the initial concentration of IP3). Later in the article, Sneyd et al. mention that p_0 decays to zero with a time constant of '1.25 s'.

The exponent of Equation 4.6 is required to be dimensionless, whereas the equation that was published has units of s^2 in the exponent. The correct form that should have been published is shown in Equation 4.7, where $-0.8t$ has been replaced by $-(1/0.8)t$. The term $1/0.8$ s results in a time constant of decay equal to $1.25 s^{-1}$. Without the inclusion of dimensionality in these models of the cell, it is easy for errors such as this second typographical error in the article to be overlooked, and cause problems for other modellers.

$$p(t) = p_0 e^{-0.8t} \quad (4.6)$$

$$p(t) = p_0 e^{-(1/0.8s)t} \quad (4.7)$$

Using Equation 4.7 in the Python implementation means that the IPR is activated once during the simulation, rather than multiple times (Figure 4.5 shows this for an initial concentration of $30 \mu\text{M}$ IP3). This results in a single calcium transient that can be used to observe the effect IP3 has on the system and, in the case of models that include spatiotemporal information, the speed of a propagating wave across the cell.

The Sneyd et al. common pool ODE model of the pancreatic acinar cell is less complex than the cardiac cell model by Bondarenko et al. previously detailed. This lowered complexity left more room for changes to the model that may occur through extension as a multiscale model that is unlikely to have been possible with the cardiac cell, even if issues with the membrane potential were resolved. One of the interesting physiological aspects of the pancreatic acinar cell is the involvement of mitochondria, which was represented simply as a negative calcium flux in the model by Sneyd et al. With this in mind, implementation of a published model of the mi-

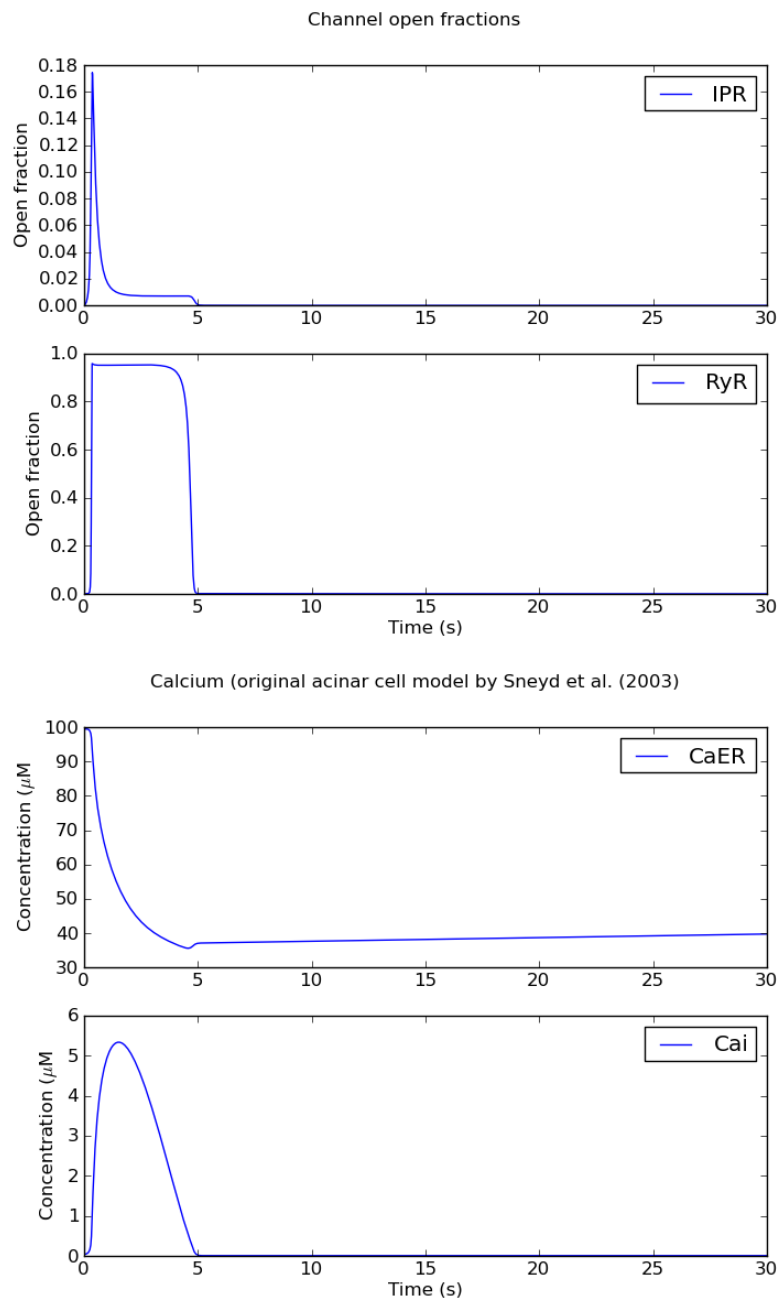


Figure 4.5: Python implementation of the pancreatic acinar cell responding to a decaying concentration of $30 \mu\text{M}$ IP3. The small IPR open state that reacts directly to the concentration of IP3 is translated into a bigger response by the RyR channels. This causes release from the ER, and results in an increase in the intracellular calcium concentration, which returns back to normal as the ER empties, the channels deactivate, and calcium in the cytosol is removed by SERCA and PMCA. Recovery of ER concentration after release takes place over a longer time period than shown in these plots.

tochondria was carried out, with a view to extending the acinar cell model through inclusion of better represented mitochondria.

4.1.3 The Bertram et al. Model of Mitochondria

Detailed models of mitochondrial energy metabolism have been developed in the past, such as the Magnus-Keizer model of mitochondria^[82,83] and the Jafri-Dudycha model of the tricarboxylic acid cycle^[84]. Since publication, these models have been further developed or modified so they may be included in other cell models, for example Cortassa et al.^[85,86] and Nguyen et al.^[87].

An article by Bertram et al. (2006)^[88] described existing models as “extraordinarily complicated”, and continued on to describe a simplified model of the mitochondria that both captures the original behaviour of more complex models, but at the same time is much easier to understand (schematic shown in Figure 4.6). This simplification was achieved by examining the relationship between the degrees of freedom in more complex models, making assumptions (such as ionic concentrations of sodium remaining constant throughout the simulation), and curve-fitting of functions by adjusting parameters (carried out by eye). The article acknowledges that more complex models such as those by Magnus-Keizer and Cortassa et al. have an advantage over the simplified model in that they contain specific biophysical rates for each process. However, the simplified model makes clearer the effect of changes to parameters or mitochondrial input may have, and any re-parameterisation or improvements to the Cortassa et al. or Magnus-Keizer models in the future could be easily used to modify parameters in the simplified model.

The reduction in complexity and the retaining of original behaviour from more complicated models makes the Bertram et al. simplified mitochondria model attractive for use in a multiscale model. This should bring significant richness at reduced computational cost, coupled with increased intuition as to how the mitochondria function. A copy of the original source code, written in a scripting language for XPPAUT, was obtained from Richard Bertram’s faculty website* and converted to work with Odeint in Python. Portions of the source code were not mentioned in the article, such as missing parameters and additional fluxes, however these were

*http://www.math.fsu.edu/~bertram/software/islet/JTB_06.ode (accessed 7/9/12)

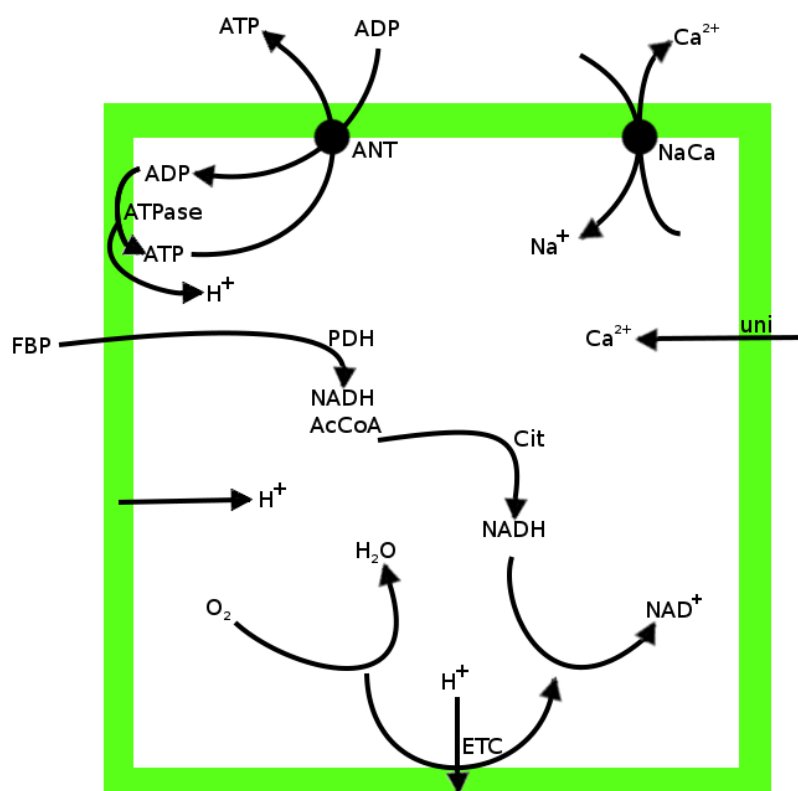


Figure 4.6: Schematic of the mitochondria model by Bertram et al.^[88], showing some of the major interactions that contribute to energy metabolism in the simplified model^[84,88]. The shaded area represents the outer mitochondrial matrix, 'uni' is the mitochondrial calcium uniporter, 'NaCa' is the sodium-calcium exchanger, 'ANT' is the adenine nucleotide translocator, ATPase is where ADP-ATP phosphorylation occurs, utilising the proton gradient. 'Cit' represents the citric acid cycle. Cellular respiration is represented of the O_2 to H_2O flux next to the electron transport chain (ETC) at the bottom of the figure. Fluxes that completely cross the shaded area represent interaction with the cytosol. The processes are described in more detail in Section 3.2.

mostly resolved through careful checking of units to each equation, and the author was helpful when contacted via email with questions.

The resulting Python implementation reproduces figures found in the original article. Figure 4.7 reproduces a figure in the article by Bertram et al., where the intracellular calcium concentration is held fixed at $0.5 \mu\text{M}$ for 30 seconds, for a total of three times over 2.5 minutes. The intracellular calcium concentration is not linked to mitochondrial calcium efflux in this example (this was found to be required in order to reproduce the published figures, and was present in the original source code, but not used in this way later on in the project), and the concentration of fructose 1,6-

biphosphate (FBP, a substrate in the citric acid cycle used for production of NADH) is held fixed at $5 \mu\text{M}$. When the intracellular calcium concentration is raised (Ca_i), the mitochondrial uniporter takes up calcium, increasing the mitochondrial calcium concentration (Ca_m). This initially depolarises the mitochondrial membrane potential (Psim), which results in increased production of NADH in the citric acid cycle (NADH_m), and increases oxygen consumption (J_O). This respiration results in hyperpolarisation of the mitochondrial membrane potential, and results in increased ATP production inside the mitochondria (ATP_m). Mitochondrial ATP is then exchanged for ADP in the cytosol.

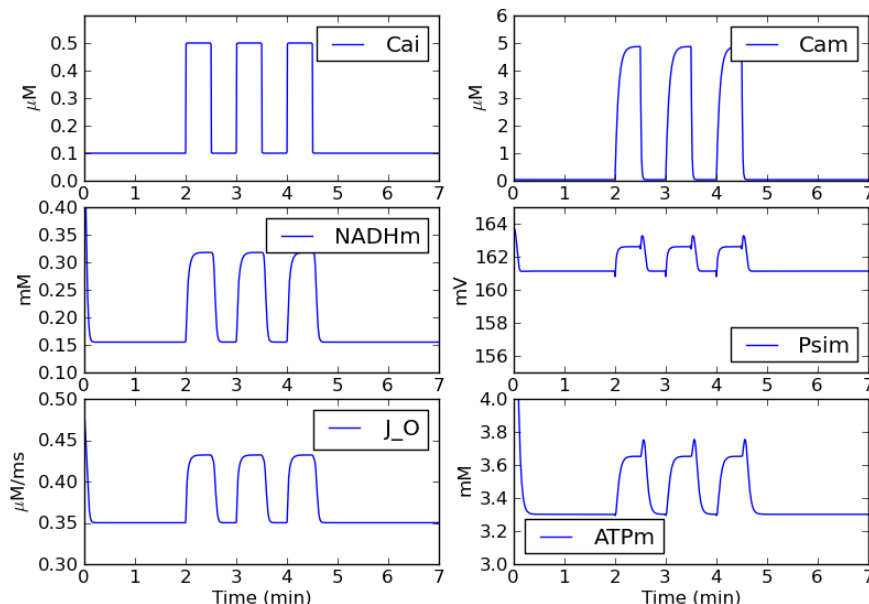


Figure 4.7: Replication of Figure 13 in Bertram et al.^[88]. In response to intracellular calcium elevation, the mitochondria model is stimulated, and produces ATP at an increased rate (Ca_i ; intracellular calcium, Ca_m ; mitochondrial calcium, NADH_m ; mitochondrial NADH, Psim ; mitochondrial membrane potential, J_O ; mitochondrial oxygen consumption, ATP_m ; mitochondrial ATP).

One issue with the physics of this model is that calcium concentration is not conserved, something carried over as a consequence of simplification of the original Magnus-Keizer model. The ODE controlling mitochondrial calcium (Equation 4.8) has a term f_m , which denotes the fraction of unbound mitochondrial calcium, which has a dimensionless value of 0.01 (where $d[\text{Ca}^{2+}]_m$ represents the change in mitochondrial calcium over time, J_{uni} is the mitochondrial uniporter flux, and J_{NaCa}

is the sodium-calcium exchanger). This parameter does not exist on the right hand side of the ODE controlling cytosolic calcium, and so does not result in conservation of calcium in the system. The f_m term appears to have been carried over from the model upon which this simplified version is based. Removal of the f_m term in the mitochondrial calcium ODE ensures that calcium in the system is conserved, but this is a change to the model that has not been parameterised, and results in faster calcium handling rates. In comparison to the cardiac cell model by Bondarenko et al. (which uses specific ODEs for the buffering of calcium and thus keeps track of this quantity), this simplification is a weakness to the simplified model of the mitochondria.

$$\frac{d[\text{Ca}^{2+}]_m}{dt} = f_m(J_{uni} - J_{NaCa}) \quad (4.8)$$

The ODEs controlling NADH_m and ADP_m use a term, γ , which is described as a parameter that converts the contributing fluxes from units of $\mu\text{M}/\text{ms}$ to mM/ms in the model, and is an example of the scaling factors often used in ODE models that can go unnoticed during implementation if they are not declared. Since the implementation in Python handles parameters as SI objects, and therefore has no need to convert between units, the γ terms are removed from the Python equations.

With a working implementation of the simplified mitochondria, the next step was to combine this representation with the model of the pancreatic acinar cell.

4.2 Extension of literature models: the coupled acinar cell and the simplified mitochondria

The pancreatic acinar cell model described by Sneyd et al.^[28] includes a very basic representation of the mitochondria, which continually removes calcium from the system. It is assumed that the mitochondrial calcium pool is never significantly depleted and not of central interest to the study, and thus efflux from the mitochon-

dria is unimportant. In contrast to this assumption, the mitochondrial calcium pool could instead become significantly elevated during exposure of the cell to BA or FAEE, which may lead to opening of MPTP and initiation of the apoptotic chain, as discussed in Sections 3.3 and 3.4.

Diseases in the pancreatic acinar cell such as acute pancreatitis and pancreatic cancer are tightly linked to the dynamics of mitochondria, calcium and ATP^[56,61,64], and so studies on this cell type would benefit from inclusion of a more representative model of the mitochondria. The simplified model by Bertram et al.^[88] could be used in this way, through coupling to the Sneyd et al. acinar cell model via the ODEs controlling intracellular calcium, ADP, and ATP. Calcium is buffered by the mitochondria, causing a dynamic change in ATP production in response to transients, and depletion of ATP is related to ATP-dependent processes in the cell, such as SERCA and PMCA, working to remove calcium from the intracellular compartment during periods of elevated calcium concentration.

In addition to ATP being consumed at a faster rate during calcium elevation in the normal cell, such levels of calcium may be initiated by BA or FAEE molecules at the onset of acute pancreatitis. Sustained elevation of calcium in the cytosol results in accumulation of mitochondrial calcium, and is likely to lead to subsequent formation of MPTP, loss of ATP production and initiation of apoptosis. For these reasons, the pancreatic acinar cell and simplified mitochondria ODE models previously detailed were coupled together, in order to create a novel model of the pancreatic acinar cell that may dynamically change ATP production and also react to conditions likely found in a disease state. Models that already exist of the acinar cell do not include mitochondria detail much further than this organelle being a calcium sink, and there are no examples of altered pump and channel models that react to BA or FAEE.

4.2.1 Coupling of the Acinar cell and the Mitochondria

To couple the pancreatic acinar cell and simplified mitochondria ODEs together, the mitochondria model was made into a Python function that is called from inside the acinar cell function. The mitochondria model is provided with values of the degrees of freedom at the current time, and returns the internal mitochondrial ODE values along with flux values for J_{ANT} , J_{uni} and J_{NaCa} that correspond to the end of current time step. These contributions are used for changing the cytosolic concentration ODEs for ATP, ADP, and calcium, when other acinar cell fluxes have been calculated.

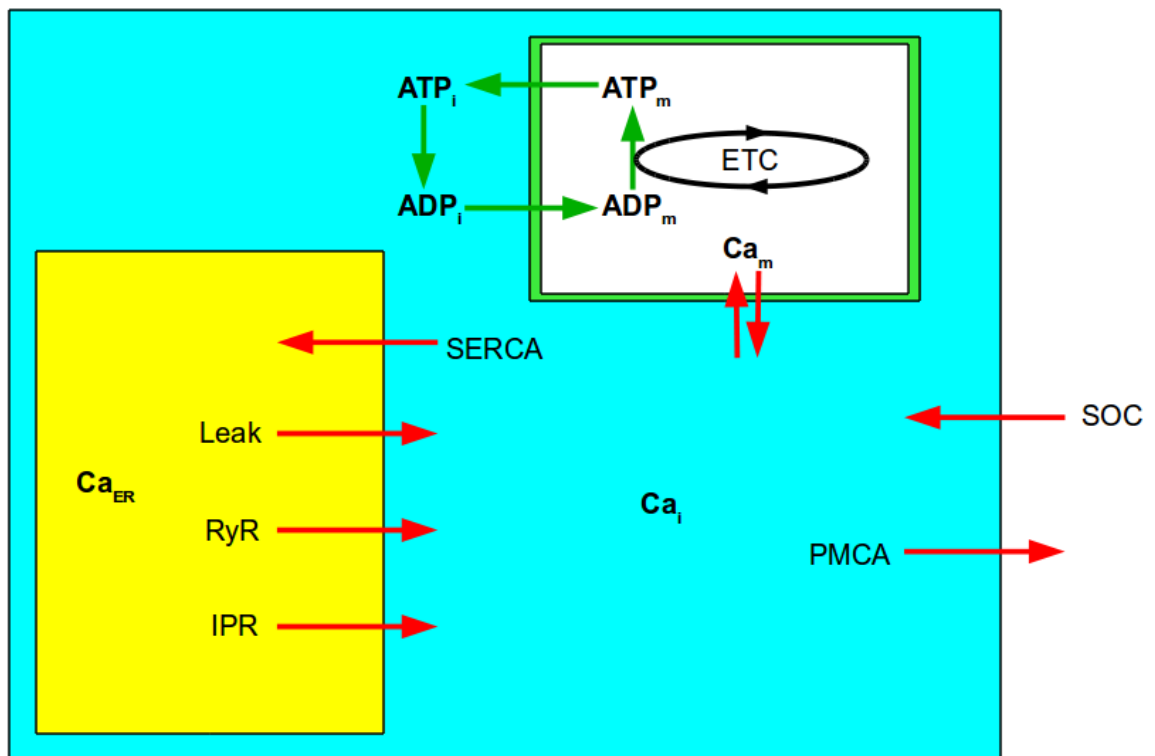


Figure 4.8: Schematic of the fluxes involved in the combined acinar-mitochondria ODE model, achieved by coupling the model of the pancreatic acinar cell by Sneyd et al.^[28] and the simplified model of the mitochondria by Bertram et al.^[88]. The main part of this schematic is the acinar cell from Figure 4.3, but the mitochondria from Figure 4.6 is included as the compartment with the green outline, which shows the main interaction of the mitochondria to the cytosol of the acinar cell. Calcium fluxes are coloured red, while adenine fluxes (involving ATP and ADP) are coloured green. The other processes that occur inside the mitochondria to produce ATP are represented by the black ring where ETC stands for electron transport train.

Both models previously were implemented using SI base unit definitions, so there was no need to manually convert any of the parameters to ensure units be-

tween models were dimensionally consistent. The f_m parameter discussed previously in the simplified mitochondria model was left in the $[Ca^{2+}]_m$ ODE to keep the mitochondria model functioning as intended, but was noted as a source of possible future problems with regard to mass conservation. The metric prefix conversion parameter γ was removed from mitochondrial ODEs controlling NADH and ADPm.

As the literature models provide volume ratios instead of physical parameters for the volume of cytosol, ER and mitochondria, a realistic volume of the cell was calculated for the cytosol in order to define other compartmental volumes. Assuming a spherical cell, and using the length of the pancreatic acinar cell defined by Sneyd et al., the diameter was assumed to be $d=20 \mu\text{m}$. The volume of the cytosol in the pancreatic acinar cell, where radius $r = d/2$, was calculated in Equation 4.9 as $4188.790 \mu\text{m}^3$ ($4.189 \times 10^{-6} \mu\text{L}$).

$$\frac{4}{3}\pi r^3 = 4188.790 \mu\text{m}^3 \quad (4.9)$$

The volume ratio between the ER and cytosol in the acinar cell model by Sneyd et al. is 5.405, which makes the volume of the ER equal to $4188.790/5.405 = 774.984 \mu\text{m}^3$ ($7.750 \times 10^{-7} \mu\text{L}$). The volume ratio between the mitochondria and cytosol in the mitochondria model by Bertram et al. is 0.07, which means a mitochondrial volume equal to $4188.790 \times 0.07 = 293.215 \mu\text{m}^3$ ($2.932 \times 10^{-7} \mu\text{L}$). As both models use scaling factors and not explicit volumes during calculations, these physical volumes do not change model behaviour.

Adjustments: The relationship between homeostatic calcium concentration and the mitochondria

Coupling the models was not as simple as was initially expected. As these models are not explicitly parameterised for each other, the dynamics introduced by coupling them together causes both to behave differently. To begin with, the coupled model produced several integration errors related to the ODEs that control concentration eventually skipping below zero, to become negative. These issues were investigated

by ensuring the models had not been changed during the process of coupling, and that there were no conflicting parameter names. Eventually, it was found that these errors resulted from the homeostatic concentration of calcium for which each model was originally parameterised, and the system being unable to reach a stable steady state.

The parameters in the simplified model of the mitochondria seem to be tightly linked to the original cell for which they were designed, and so do not cope well with the lowered steady state calcium concentration that exists in the acinar cell model. The mitochondrial model was designed for a cell that experiences a homeostatic intracellular calcium concentration of approximately $0.1 \mu\text{M}$ between transients, which is a good estimate for most cell types. However, the pancreatic acinar cell model experiences a homeostatic calcium concentration in the region of $0.015\text{--}0.036 \mu\text{M}$ between transients. This lowered calcium concentration is not enough to sustain a constant mitochondrial calcium concentration, based upon the balance of influx and efflux of calcium by the mitochondria. Over time, the mitochondrial calcium concentration is gradually lost, with the value eventually becoming negative. This resulted in many integration errors in the coupled model, and so the calcium handling of the mitochondria needed to be resolved.

The parameters used by the mitochondrial calcium uniporter flux (J_{uni}) and the mitochondrial sodium-calcium exchanger flux (J_{NaCa}) expect a greater concentration of calcium in the surrounding environment than the acinar cell model provides. It was therefore decided that the rates associated with these mitochondrial fluxes should be reduced in order to account for the reduced calcium offered by the acinar cell (mitochondrial parameters $p21$, $p22$, $p23$ and $p24$ ^[88]). Figure 4.9 shows the same plots as the original model in Figure 4.7, except that the mitochondria are now exposed to a single pulse of calcium instead of three. All other aspects of the mitochondria model remain unchanged. The aim is to arrive at plots similar to Figure 4.9 while the mitochondrial calcium handling parameters are adjusted in order to cope with a lowered calcium concentration in the cytosol.

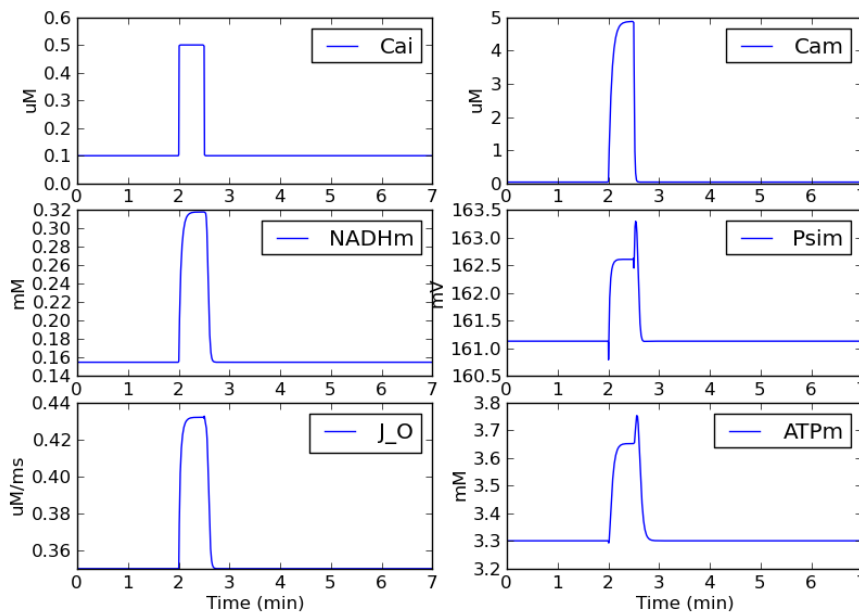


Figure 4.9: Plot showing the behaviour of the simplified mitochondria model under normal conditions designed for this model. Calcium is raised from $0.1 \mu\text{M}$ in the cytosol to a fixed value of $0.5 \mu\text{M}$ for 30 s the same as Figure 4.7 but for a single stimulus rather than three. The 'teeth' shown by Psim and ATPm are elongated in this plot due to axes scaling. The downward 'tooth' of Psim is a result of membrane depolarisation upon initial accumulation of calcium, before membrane hyperpolarisation that results from increased production of NADHm. The final upward tooth results from the loss of mitochondrial calcium occurring at the same time as NADHm production, which reduces thereafter. The hyperpolarisation of Psim at this point results in a transient increase in oxygen consumption (J_{O}), which causes the tooth seen on the ATPm plot.

The plot in Figure 4.10 shows the effect a fixed calcium concentration of $0.03 \mu\text{M}$ has on the mitochondria model, using the original model parameters. An integration error presents itself, which is due to the mitochondrial calcium concentration unable to sustain a stable level; Ca_m decreases until it drops below zero, and this affects other parts of the model.

If the calcium concentration in the cytosol is kept at the same value of $0.03 \mu\text{M}$ and the parameters associated with J_{uni} and J_{NaCa} are changed, the model shows that it can cope with a lower concentration. Reducing the parameters solely associated with J_{uni} by a factor of 10 did not resolve the problem, and instead retained the same integration error that suggests the problem mostly revolves around the J_{NaCa} flux. If J_{NaCa} is instead scaled by factor of 10, this does prevent the integration error, and results in the plots shown in Figure 4.11. Compared to our reference plot,

4.2. EXTENSION OF LITERATURE MODELS: THE COUPLED ACINAR CELL AND THE SIMPLIFIED MITOCHONDRIA

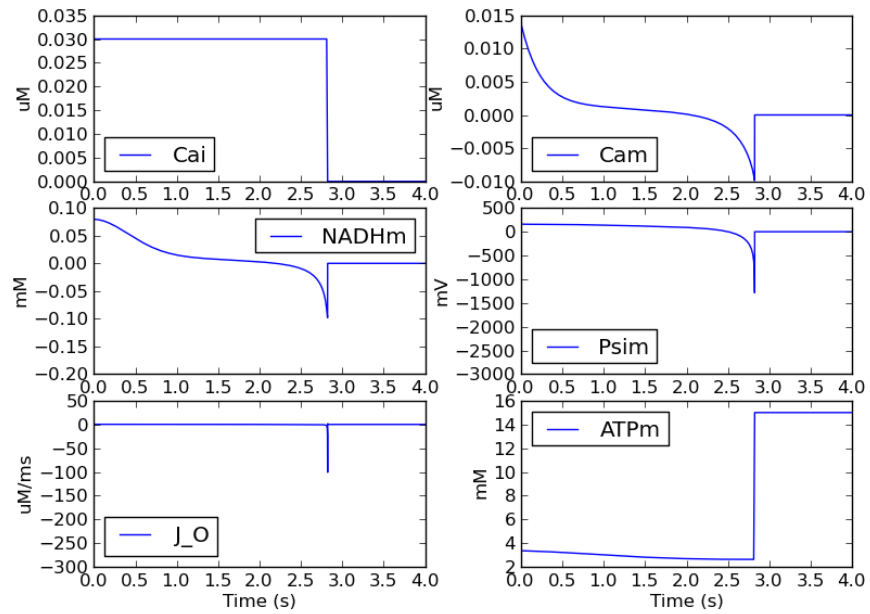


Figure 4.10: Plot showing the effect on the degrees of freedom in the mitochondria model if a homeostatic calcium concentration in the cytosol that is consistent with the acinar cell model is used ($\sim 0.03 \mu\text{M}$ calcium). This resulting behaviour causes integration errors, as well as being physically impossible (negative concentrations), and the values for degrees of freedom in the simulation after this point default to 0.0.

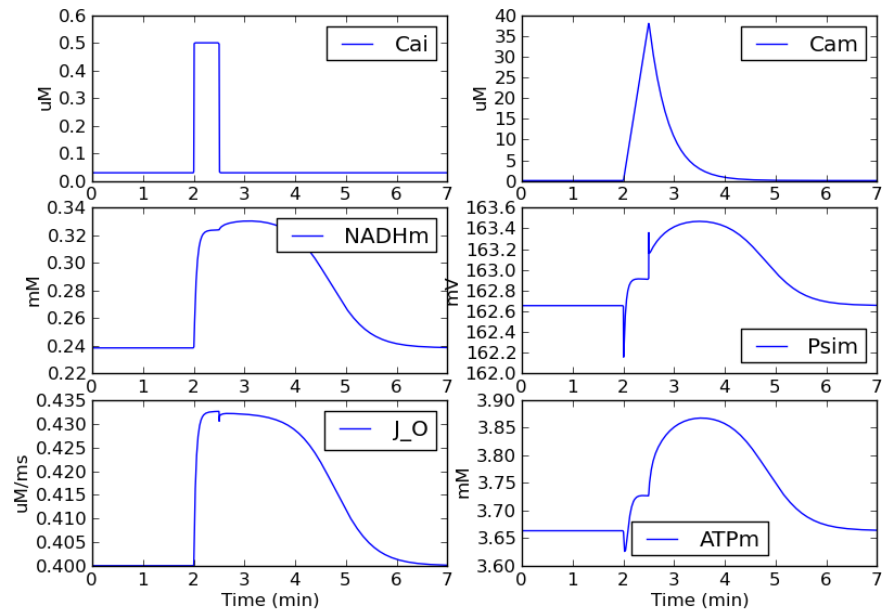


Figure 4.11: Plots showing the effect on the mitochondria model in an environment similar to the acinar cell, if the J_{NaCa} parameters are reduced 10-fold (scaling factor of 0.1). The mitochondria are losing calcium at a slower rate while J_{NaCa} activity is scaled down, hence the altered behaviour and accumulation of mitochondrial calcium.

reducing J_{NaCa} by a factor of 10 causes an increase of Ca_m to around $40 \mu\text{M}$ under conditions in which the original model would reach a maximum of around $6 \mu\text{M}$, and the magnitude of NADH_m , ATP_m and J_{O} (the consumption of O_2 , shown in Figure 4.8) is much smaller. This is due to the rapid accumulation of calcium in the mitochondria resulting from unbalanced mitochondrial influx and efflux.

To maintain the original balance between the mitochondrial calcium fluxes while tackling the problems that present themselves by coupling the two different models, parameters to both J_{uni} and J_{NaCa} should be changed by the same amount. This is shown in Figure 4.12, where parameters to both fluxes are reduced by a factor of 10. Reduced influx and efflux results in the mitochondria having lower Ca_m prior to raising Ca_i , and this results in a lower steady state values for the other degrees of freedom. Upon raising Ca_i , the other degrees of freedom increase to levels approximately the same as the reference (Figure 4.9), although the profile of each is now slightly different and more prolonged.

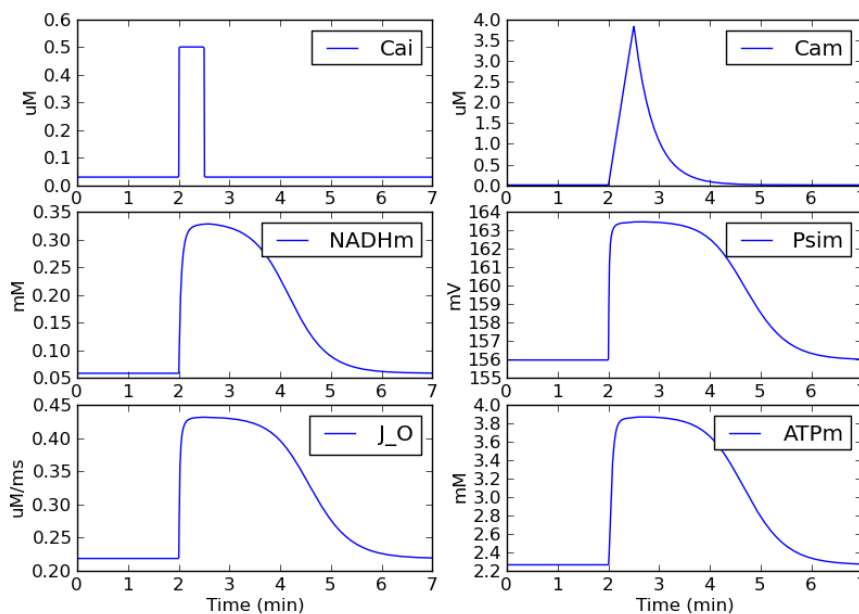


Figure 4.12: Plots showing the effect on the mitochondria model in an environment similar to the acinar cell, if both the J_{uni} and J_{NaCa} parameters are reduced 10-fold (scaling factor of 0.1). The fluxes appear to behave in a similar way to Figure 4.9, however the response of the mitochondria is now spread out over a longer time period, due to the effect of reduced calcium uptake and release.

Based upon the similarity of the figures, reducing the parameters associated with

both J_{uni} and J_{NaCa} by a factor of 10 provides more agreement with the original model. This results in Ca_m being stable over a long simulation period in a similar environment to the acinar cell, and parameters for both fluxes being scaled by the same factor preserves the balance of influx and efflux of calcium.

A somewhat arbitrary factor of 10 is used here to reduce the parameters, and this changes the dynamics of the mitochondria slightly. However, this cost (and indeed weakness) allows the coupled model to work without adjusting each of the mitochondria model parameters. The slightly altered dynamics that have been introduced could also be argued to be irrelevant to a certain extent, when the approximations inherent to the simplified model are considered (i.e. the model parameters were fitted by eye, assume the ATP and ADP ratio inside the mitochondria is roughly equal to that in the cytosol, and that the concentration of sodium in the cytosol is assumed to remain constant).

To get this model even closer to what we expect in the original figure, the factor used to scale the J_{uni} and J_{NaCa} parameters should aim to alter them as little as possible, while still preventing integration errors. If the parameters are changed less, and a scaling factor of 0.65 is used, the resulting plot in Figure 4.13 is produced. Although this shows a mitochondrial calcium concentration approximately twice that of the reference plot, the rate at which calcium is buffered by the mitochondria is much closer to how we expect.

A problem with the above adjustment to J_{uni} and J_{NaCa} parameters using a scaling factor of 0.65 is that if the intracellular calcium concentration is lower than $0.03 \mu\text{M}$ for an extended period of time, integration errors will then surface again and the scaling factor needs adjusting once more. Unfortunately, the acinar cell model cytosolic calcium concentration does fall to around $0.015 \mu\text{M}$ between transients, before the flux equations work toward reaching the homeostatic concentration of $0.03 \mu\text{M}$ again (due to the balancing leak flux from the ER and influx through SOCs). The time it takes to once again reach the steady state homeostatic calcium concentration of $0.03 \mu\text{M}$ from $0.015 \mu\text{M}$ is not fast enough to sustain the mitochondrial calcium

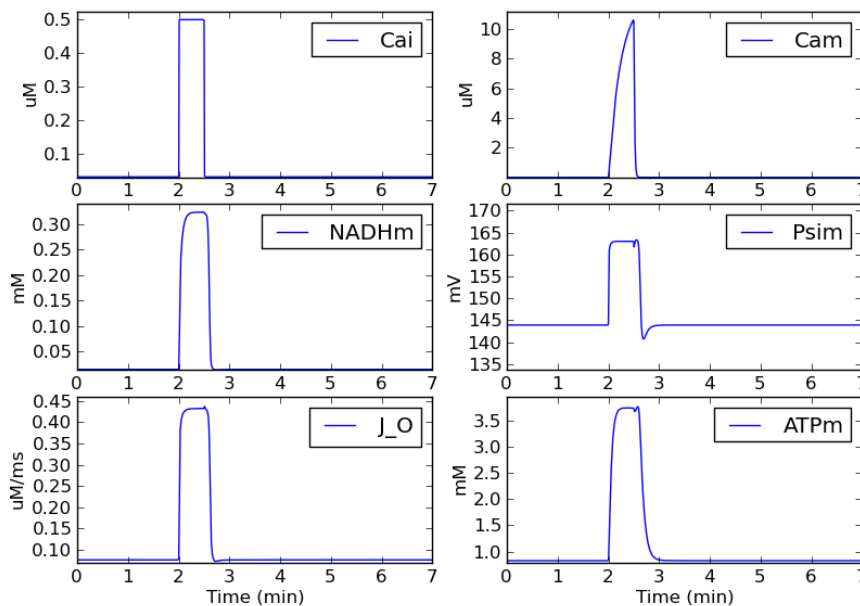


Figure 4.13: Plots showing the effect on the mitochondria model in an environment similar to the acinar cell, if both the J_{uni} and J_{NaCa} parameters are scaled by a factor of 0.65. The mitochondria model is much more responsive to changes in the cellular environment than Figure 4.12, which uses a scaling factor of 0.1.

level, resulting in integration errors. This issue is further enhanced by the fact that introducing the mitochondria model to the acinar cell system reduces the magnitude of calcium transients that were in the original model, due to the buffering effect of the mitochondria itself.

The mitochondrial calcium fluxes require further scaling to ensure they do not interrupt acinar cell calcium dynamics, as this effect should be already encoded into the parameters by Sneyd et al. by fitting to the experimental data. This is also perhaps a failing inherent to common-pool type models of calcium signalling, where all fluxes alter a single pool of concentration in the cytosol. This suggests the coupled acinar-mitochondria model would benefit from simulation with a more sophisticated modelling technique where the cytosol is not treated as having a uniform calcium concentration.

The smaller the factor used to scale the mitochondrial calcium fluxes, the higher the peak calcium concentration in the cytosol during an oscillation, but at the cost of moving further away from the original simplified model of the mitochondria.

Scaling the fluxes further than by a factor of 10 is somewhat justified, however. As the simplified model of the mitochondria is based upon a more complex model of the pancreatic beta cell that contains around 1000 mitochondria^[89], the pancreatic acinar cell contains approximately 25-30^[58]. Therefore, scaling the mitochondrial calcium handling fluxes by orders of magnitude when used in the acinar cell model reflects the cell having fewer mitochondria. A precise scaling factor in addition should depend on the difference in volume of mitochondria between the two cell types.

The dynamic nature of the mitochondria means that actual numbers of this organelle will differ between cells of the same type, due to fusion and fission. However, if we assume the original simplified mitochondria model represents 1000 mitochondria while the acinar cell we wish to use the mitochondria model for contains 30, the model could use a scaling factor of $30/1000 = 0.03$ for the fluxes. Using a scale of 0.03 on the mitochondrial calcium handling fluxes results in the coupled acinar-mitochondria model being stable over a long period of simulation time, reacting to calcium transients in an expected way, and does not affect the peak calcium concentration during an oscillation to the extent that the acinar cell behaves differently to how it was intended (Figure 4.14). On the other hand, the mitochondria now reacts to changes in the surrounding environment a lot more slowly, and so the model now behaves quite differently to the original formulation. The scaling causes altered dynamics in the mitochondria, as the scaling factors have effectively prolonged the mitochondrial response to changes in the cellular environment. This is why the plots shown in this section, after the fluxes are scaled, appear so different.

Although this is not an ideal situation, it was found to be the only way in which to ensure the acinar cell ODE model and the mitochondria ODE model are compatible, without complete reparameterisation of both models, based upon detailed and reliable data of both systems in the pancreatic acinar cell. Reparameterisation of the entire system is beyond the scope and capabilities of this project, so the scaling parameter of 0.03 was used in subsequent modelling efforts for fluxes that involve

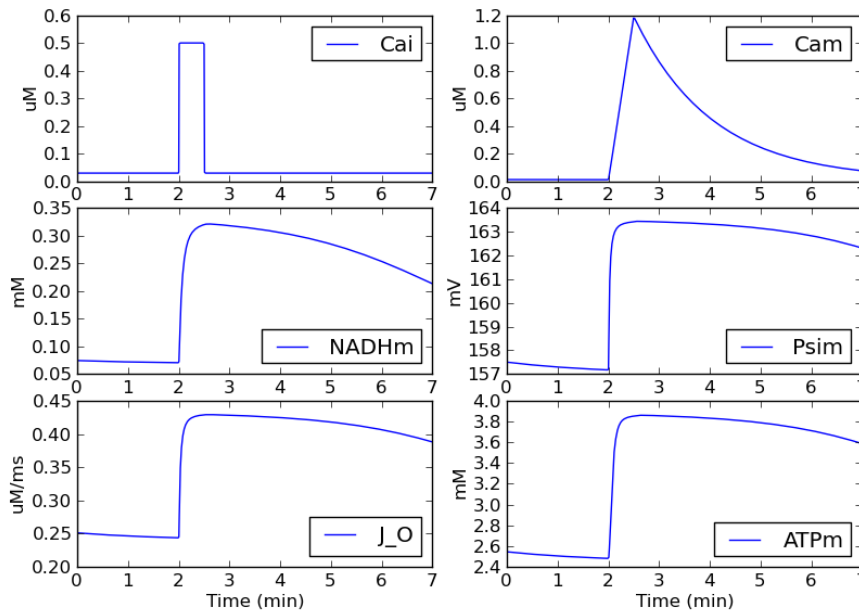


Figure 4.14: Plots showing the effect on the mitochondria model in an environment similar to the acinar cell, if both the J_{uni} and J_{NaCa} parameters are scaled by a factor of 0.03, based upon relative differences between the number of mitochondria in the pancreatic acinar cell that we wish to model, and the pancreatic beta cell on which the mitochondria model is based. This results in even less responsive mitochondria, but is more representative of a cell with lower populations of the organelle.

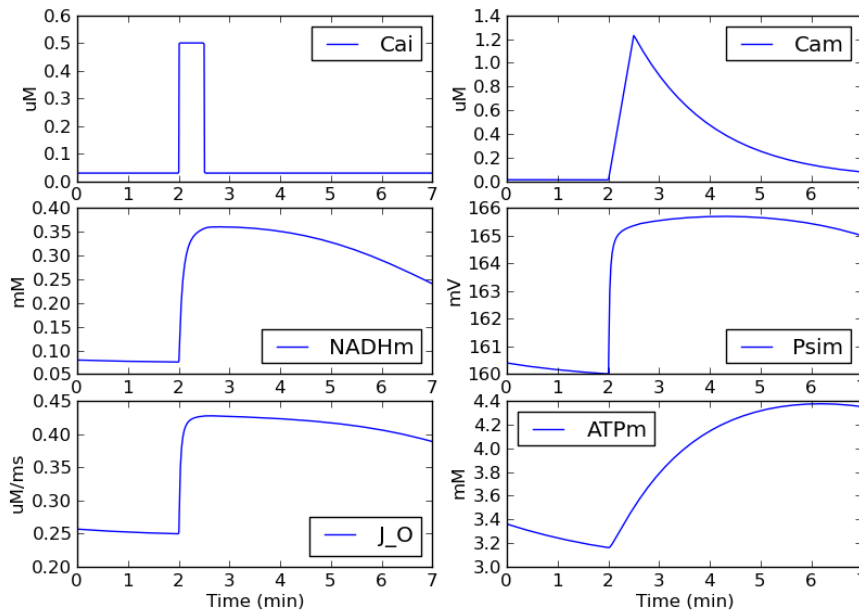


Figure 4.15: In addition to the J_{uni} and J_{NaCa} parameters being scaled by a factor of 0.03, in these plots J_{F1F0} and J_{ANT} have also had their rates scaled by this factor, based upon relative differences between the number of mitochondria in the acinar and beta cells.

crossing the mitochondrial membrane. It should be noted that, if a refined set of parameters for both models were found or calculated, changing anything parameter-related in these models is a trivially simple task, which leaves scope for future improvement. The difficulty lies in finding parameters of compatible dimensions for the relevant equations.

In addition to calcium, the molecules ATP and ADP also cross the mitochondrial membrane and therefore require the same treatment. Scaling the maximal rate parameter for the ATP/ADP exchanger flux, J_{ANT} (parameter $p19$), causes reduction in the activity of the exchanger. The only difference for this flux is that once taken up into the mitochondria, ADP_m is processed into ATP, whereas Ca_m is not changed at all, and so the maximal rate parameter for F1F0-ATPase flux (parameter $p16$) inside the mitochondria, that converts ADP to ATP, also requires scaling. This ensures it does not convert ADP_m to ATP_m faster than J_{ANT} supplies the mitochondria with ADP from the cytosol. The plots in Figure 4.15 show the effect this scaling has on the mitochondria, where it can be clearly seen that the rate at which ATP_m is being produced is reduced.

The points discussed above highlight the impact that combined models can have on each other. The simplified mitochondria model is so heavily fitted to the original models upon which it was based, it may have lost some strengths of the original in the form of flexibility. To perform a complete re-parameterisation of the entire simplified mitochondrial model would require a working implementation of the complex models it was based upon, and solid data for mitochondria in the acinar cell against which to fit. Even then, there is no guarantee that the more complex models would work when used in a different environment, and still perform the same as if the homeostatic concentration were $0.1 \mu\text{M}$.

So, to summarise this point in development of the model, we have a common-pool ODE model of the acinar cell, coupled to a simplified model of mitochondrial metabolism. The mitochondria do not interrupt the dynamics of the acinar cell, but the mitochondria experience changes in the cytosol and react to them by adjusting

ATP production and calcium buffering. Limitations of ODE models of the cell, that lead to an increased number of assumptions about the system, lead to incompatibilities. Due to these incompatibilities, the mitochondrial fluxes needed adjustment, based upon further assumptions. These adjustments mean that dynamics of the mitochondria are now not in keeping with the original formulation, and so results provided by the mitochondria from this model cannot be assumed 'correct'. However, they can give us an idea of the dynamics mitochondria experience during stimulation of the cell, and the model as a whole is still open to future improvement if a set of parameters relevant to the system is found. While keeping this in mind, the next section looks at further extension of the coupled acinar-mitochondria ODE model, through modelling of a hypothetical disease state.

4.2.2 Sensitivity to BA and FAEE

The ODEs associated with RyR and IPR activation were modified to accept another stimulation parameter related to BA and FAEE stimulation, in order to hypothetically model the cell dynamics that occur during onset of pancreatitis. The parameter BA is used to interchangeably represent either BA or FAEE in the model code.

The literature states that BA may induce intracellular calcium oscillations at 50 μM and a peak plateau signal at 500 μM , and only the latter induces acinar cell injury^[90], although it is unclear what concentration of BA may reach the cells^[91]. For detailed behaviour over a specific range of concentrations, the entire channel model would need complete re-parameterisation and data against which to fit, however applicable data on the dynamics of channels and pumps are not available. Instead, the rate constants normally used for activation by IP3 or calcium were empirically scaled, until exposure to 25-50 μM BA (the lower end of concentrations that are thought to cause signalling and cell death^[91]) meant that the channels and pumps in the model exhibit similar behaviour to that discussed in Section 3.3.3.

Modification of RyR

Figure 4.16 shows a schematic of the modified Markovian model for the BA sensitive RyR channel, which is a modified version of Figure 2.3. The concentration of BA is used as a contributing factor to the open state of the channel, in addition to (and used in the same way as) cytosolic calcium, except the rate constants for the same steps were empirically scaled to achieve the desired response of 25-50 μM BA making the RyR transition into an open state for the duration of BA exposure. Returning to the previous equations controlling the RyR, the ODEs for $O1$, $O2$, and $C1$ were modified as in Equations 4.10 to 4.12 (where the parameter $k_{a,BA}^+ = k_a^+ \cdot 0.0001$ and the parameter $k_{b,BA}^+ = k_b^+ \cdot 0.0001$, and the number by which these parameters is scaled is dimensionless). When there is no BA in the system, these changes have no effect on normal RyR function.

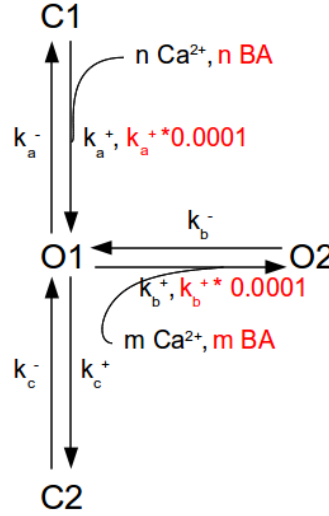


Figure 4.16: Schematic of the Markovian RyR model, modified for sensitivity to BA in addition to calcium. The additional contributions made for the BA sensitive channel are coloured red.

$$\begin{aligned} \frac{dO1}{dt} = & ([\text{Ca}^{2+}]_i^4 k_a^+ + [\text{BA}]^4 k_{a,BA}^+) C1 + k_c^- C2 + k_b^- O2 \\ & - k_a^- O1 - k_c^+ O1 - ([\text{Ca}^{2+}]_i^3 k_b^+ + [\text{BA}]^3 k_{b,BA}^+) O1 \end{aligned} \quad (4.10)$$

$$\frac{dO2}{dt} = ([\text{Ca}^{2+}]_i^3 k_b^+ + [\text{BA}]^3 k_{b,BA}^+) O1 - k_b^- O2 \quad (4.11)$$

$$\frac{dC1}{dt} = k_a^- O1 - ([Ca^{2+}]_i^4 k_a^+ + [BA]^4 k_{a,BA}^+) C1 \quad (4.12)$$

Modification of IPR

The IPR channel model was modified in a similar way, except that in this channel type both the O and A states are used to find the open fraction of the channel, as shown in Figure 4.17 and detailed in Equations 4.14 to 4.18 where red coloured text represents the modification, and $\phi_{2,BA} = \phi_2 \times 50$. The parameters ϕ_x are calculated rate constants that contain the interaction of the channel with cytosolic calcium, such as Equation 4.13 where $k_1 = 0.64 \text{ s}^{-1} \mu\text{M}^{-1}$, $L_1 = 0.12 \mu\text{M}$, $l_2 = 1.7 \text{ s}^{-1}$, and $L_3 = 0.025 \mu\text{M}$, which results in a dimensionless value (see Sneyd et al (2003)^[28] for the remaining IPR model ϕ parameters and original formulation).

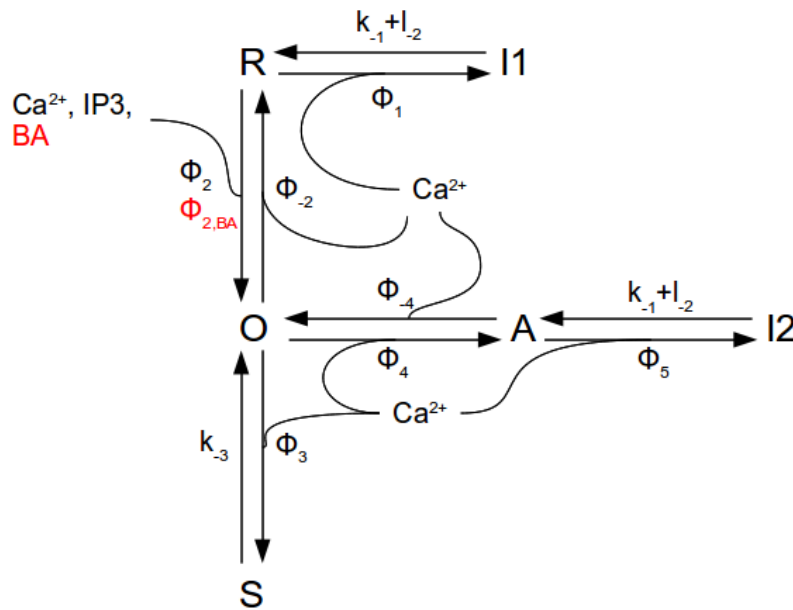


Figure 4.17: Schematic of the Markovian IPR model, modified for sensitivity to BA in addition to calcium and IP3. The parameters labelled ϕ represent calculated rate constants resulting from the concentration of calcium, BA, and IP3 at the current time. The additional contributions made by BA are coloured red.

$$\phi_1 = \frac{k_1(L_1 + l_2)[Ca^{2+}]_i}{L_1 + [Ca^{2+}]_i(1 + L_1/L_3)} \quad (4.13)$$

$$\frac{dR}{dt} = \phi_{-2}O - \phi_2[IP3]R - \phi_{2,BA}[BA]R + (k_{-1} + l_{-2})L_1 - \phi_1R \quad (4.14)$$

$$\frac{dO}{dt} = \phi_2[IP3]R + \phi_{2,BA}[BA]R - (\phi_{-2} + \phi_4 + \phi_3)O + \phi_{-4}A + k_{-3}S \quad (4.15)$$

$$\frac{dA}{dt} = \phi_4O - \phi_{-4}A - \phi_5A + (k_{-1} + l_{-2})L_2 \quad (4.16)$$

$$\frac{dI_1}{dt} = \phi_1R - (k_{-1} + l_{-2})L_1 \quad (4.17)$$

$$\frac{dI_2}{dt} = \phi_5A - (k_{-1} + l_{-2})L_2 \quad (4.18)$$

Modification of SOC, PMCA and SERCA

The SOC channels are thought to activate in response to ER depletion or IP3 concentration. The model by Sneyd et al. models the SOC channels such that flux increases in response to IP3 concentration in the system, which compensates for the calcium lost by PMCA. The SOC flux was modified so that BA also causes an increased SOC flux. This is shown in Equation 4.19, where the SOC flux (J_{SOC}) is equal to a background inward flux ($J_{in,base}$) plus a flux that depends on both the concentration of BA and IP3, multiplied by the rate constant (K_{Jin}).

$$J_{SOC} = J_{in,base} + K_{Jin}([IP3] + [BA]) \quad (4.19)$$

The SERCA and PMCA pumps are thought to be inhibited by BA, and so a Hill function was added to modulate pump activity with an arbitrary half-saturation constant, $K_{m,BA}$, of 25 μM . This means a 50% inhibition of pump activity for BA concentrations at 25 μM , and further inhibition when concentrations are higher than this. Equation 4.20 shows the term used to scale pump activity by a number between 1 and 0, where higher concentrations of BA result in a smaller number, and thus decreased pump activity.

$$\text{Pump modulation} = 1 - \frac{[BA]^2}{(K_{m,BA}^2 + [BA]^2)} \quad (4.20)$$

The combined effect of these modifications to the model in the presence of BA is that calcium and IP3 sensitive channels are activated, ATP dependent pumps are inhibited, and Ca_i increases in the cell. Results to the ODE portion of this project for

a system exposed to 25 μM BA are presented and discussed in Chapter 6, and later used as a comparison to similar results generated in the multiscale FEM implementation of this cell.

Steady state cytosolic ATP concentration

One of the species included in the model that is of interest is cytosolic ATP. After coupling the acinar cell and the mitochondria models together, with the adjustments detailed previously, the combined dynamics of the system result in a steady state ATP concentration of approximately 0.039 mM, which is lower than the concentration that has been observed in the pancreatic acinar cell at 1 mM^[75]. To achieve cytosolic ATP concentrations in the coupled acinar-mitochondria model that are comparable to physiological values would require re-parameterisation of the mitochondria model based upon detailed physiological data of mitochondria in the pancreatic acinar cell, as previously stated.

When generating results using this ODE implementation, the coupled model was allowed to reach a steady state for 1000 s, where all degrees of freedom remained constant, before initiation of stimulus.

4.3 Summary

While it is an appreciably difficult task to include every last detail and justification to a model, it should be common practice to comment source code in an informative way, especially when dealing with units. The negative effect of lacking published detail was learned in a difficult and time-consuming way with regard to the cardiac cell model, and what was more distressing is that certain issues with the model could not be resolved even when in contact with the authors. Easily accessible online resources, such as the source code and raw data, provides something against which to test an implementation, and a huge helping hand to anyone attempting to recreate a model. As mentioned previously, while obtaining models is possible

using databases such as CellML there is no guarantee the model is correct. Model curation that has been performed by the original model authors is the best way to ensure a correctly implemented model.

When extending models, a certain degree of re-parameterisation is required, but this should ensure that the model behaves closely to the original, while at the same time enabling the model to run. It is unlikely that different models which are coupled together will work as desired, as they are may be too complex or too highly parameterised for their original purpose.

Models of the cell often combine parameters that are not only from different species, but different cells altogether This is an issue that can be overlooked when combining models, or modifying parameters in any way. Later on, this can lead to problems such as that discussed, with the mitochondria and the cytosolic calcium concentration of the acinar cell. These issues are often difficult to predict and, as was certainly the case in this project, take a long time to narrow down due to the combined complexity of processes in the model.

This experience during the study suggests that cellular ODE models can be overly or under complex with regard to the system upon which they are based, and that the articles they come from often contain multiple typographic errors, or are incomplete. The degree to which these models are parameterised is ultimately the determining factor to their predictive capabilities; when fitted closely to a single set of experimental data or another model, these models may mimic the data. When the environment changes, these models can easily become unstable and require the inclusion of additional assumptions to ensure compatibility, which detracts confidence of their predictive capabilities.

This chapter was intended as an overview of the problems that were experienced and justification of the steps that were taken to overcome them. By the end of this chapter, we have seen two separately implemented ODE models combined as one to create a more complex system. The pancreatic acinar cell is frequently described as 'polarised', and clearly does not operate in a single pool as described by this ODE

version. This is the motivation behind the Sneyd et al. implementation of a spatially compartmentalised model. Sneyd et al. used this more complex spatially compartmentalised model to hypothesise that the mitochondrial belt is typically ineffective at restricting calcium oscillations to the apical region, as the spatial heterogeneity of calcium waves is a direct result of channel distribution. Because of this, the article mentioned that inclusion of both mitochondrial calcium influx and efflux (instead of just influx) will lessen the effect even more so, dismissing the need for more complex mitochondrial calcium handling. The article also suggested that the mitochondrial belt region has a more complex role than acting as a 'firewall' to calcium oscillations which, judging from the literature, is most likely to be an increased supply of ATP to the metabolically active apical region. Based on these assumptions, the ODE model of the pancreatic acinar cell coupled with the simplified model of the mitochondria would benefit from further extension into multiple dimensions. Separation of the degrees of freedom in the ODE model, and treatment with FEM is the focus of the next chapter.

Chapter 5

Biological Finite Element Modelling

5.1 Finite element modelling of the pancreatic acinar cell in two dimensions

5.1.1 Considerations

Translating the somewhat single dimensional ODE model discussed in the previous chapter into a PDE model of multiple dimensions is necessary to observe the spatio-temporal behaviour of the cell. This requires consideration of several factors, and the next section will examine these and justify the choices made.

Geometry

The shape of a pancreatic acinar cell schematically resembles the quarter of a circle, where the cell apex is the would-be centre and the base is the circumference. The apical region extends from the apex to a position inside the quartered circle area, and the remaining space is considered the basal region, as we saw in Figure 3.2.

One strength of FEM is the ability to solve domains with complex shapes, and FEniCS has several shapes built-in such as a cube, rectangle, box, circle and sphere. While any of these shapes could in theory be used in this model, the decision was made to use the two dimensional rectangle function as a somewhat rough approxi-

mation of shape, where one corner represents the apex. Using a simple geometry in this first implementation of the model keeps the potential issues to a minimum.

Owing to the fact that we are extending the acinar cell model by Sneyd et al., cell size was inferred from their description of the spatially compartmentalised model. The distance between apex and base is $20 \mu\text{m}$ in length, so in order for the apex of the cell in the top-right corner of the rectangle to be approximately $20 \mu\text{m}$ away from the base in the bottom-left corner, the length of sides to the rectangle were set to $20 \mu\text{m} / \sqrt{2} = 14.14 \mu\text{m}$, and rounded to $14 \mu\text{m}$ for simplicity. The apical region of the model by Sneyd et al. occupies one-fifth of the distance from the apex to the base of the cell, and based upon this the apical region was set to extend to the coordinate $x,y = 11.2, 11.2 \mu\text{m}$, with this region being represented as a square (Figure 5.1).

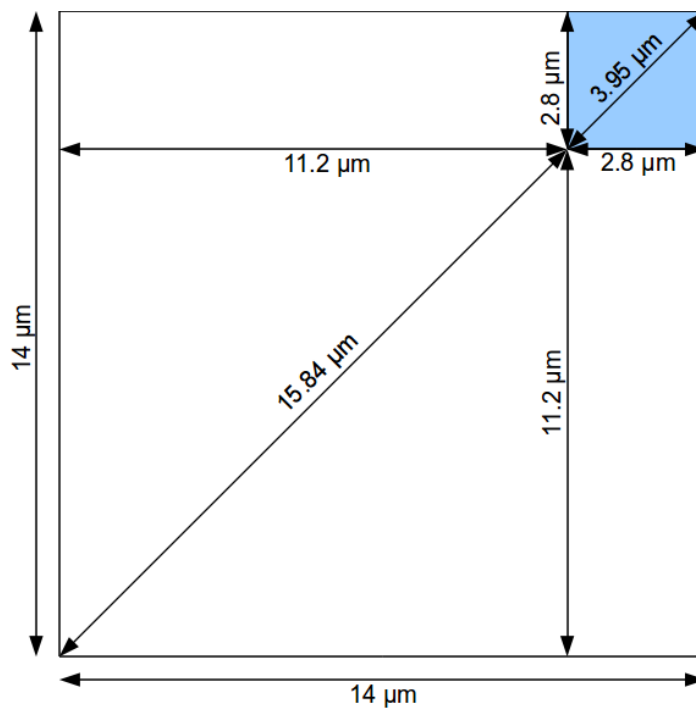


Figure 5.1: Schematic of the geometry used in the FEM model of the pancreatic acinar cell. The blue shaded area represents the apical region, while the remaining area is the basal region. The total length corner to corner is $19.79 \mu\text{m}$.

Compartmental volumes were found in the same manner as the combined ODE model detailed previously, using relative volume ratios. The mesh over the simulation domain contains cells of different sizes, as set by the DOLFIN mesh algorithm, to fit the area. The sum of the area occupied by these mesh cells is equal to the

total 2D area of the cell. To find the theoretical volume of each mesh cell per compartment, the volume of the compartment in question (in μm^3) is divided by the 2D area of the mesh (in μm^2), and this value is multiplied by a Python array containing each individual mesh cell area (in m^2). This changes the area in each index of the array that corresponds to a mesh cell to a volume, and is used to calculate the exact amount by which to change concentration at a point on the domain, effectively representing the 2D domain in three dimensions.

The concentration of each species, in each compartment in the model is represented as a 'layer'. This results in separate domains for Ca_i , Ca_{ER} , ATP and ADP for which the diffusion equation needs to be solved at each step (Figure 5.2). The ER is described as being a continuous structure throughout the basal region of the acinar cell, with rod-like extensions projecting into the apical region. As a simplification in this model, the ER was assumed to share the same 2D area as the cytosol such that it is entirely continuous, but the volume it represents is different.

Each layer of concentration is linked by fluxes from the pumps, channels, and mitochondria that have been described in previous ODE model sections. However, whereas the ODE models use fluxes that contribute to the change in species in a common pool, and thus assume a 'well mixed' environment, this multiscale FEM model separates these contributions in space. Each pump, channel, and mitochondria in this model is distributed heterogeneously around the cytosol and ER based upon interpretation of the literature.

Distribution of channels, pumps and mitochondria

The spatial arrangement of channels, pumps and mitochondria is of importance in the acinar cell. In the coupled ODE model all intracellular fluxes occurred in a common pool. Using FEM allows us to individually place these features anywhere over the spatial domain.

The channels, pumps, and mitochondria in this model shall be collectively termed 'agents' here. Agents of each type have identical initial values for the degrees of free-

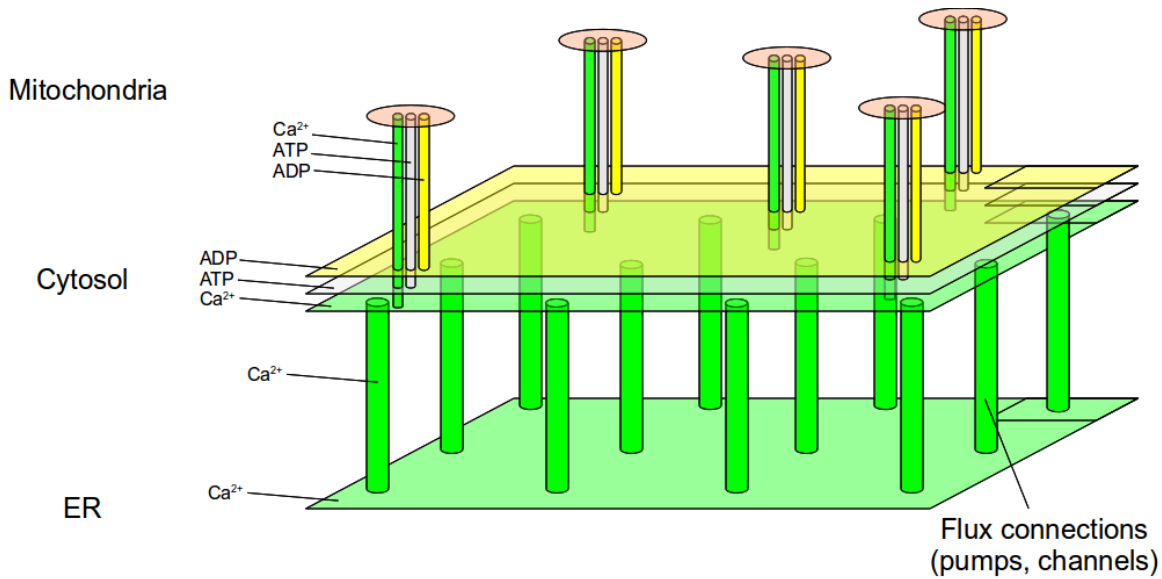


Figure 5.2: Schematic of the 'layers' explanation in the text, where each species is represented as a different layer (Ca^{2+} , ADP, ATP), grouped by compartment (Mitochondria, cytosol, ER), and linked via fluxes. Connections are made between each layer by fluxes at coordinates in a compartment that correspond to agent position. After changes to species concentration have been made by fluxes at the end of the current time step, the diffusion equation is solved for each layer. The mitochondrial agents are represented solely by ODEs, and only interact with the layers by sampling and changing the local concentration in the cytosol during integration. Thus, the layers that are solved by FEM at each time step total four; cytosolic ATP, cytosolic ADP, cytosolic calcium and ER calcium.

dom they contain at the beginning of a simulation, and these degrees of freedom are allowed to change, independently between agents, over time. This is possible for each agent due to the spatial distribution of features in the cell and the diffusion of cellular species around the simulation domain. A different local environment is experienced by each agent.

The spatial polarisation of cellular features in the pancreatic acinar cell required functions in the model to provide controlled agent distribution around the cell. The distribution of RyR, IPR, and SERCA is specified by providing details on the ER geometry (specifically, the length of sides of the rectangle and the apical region extent) along with the density of the agent type in the basal and apical regions ($\text{agents}/\mu\text{m}^2$). Using this information, an array of data is returned containing the coordinates to each agent, and the mesh cell index each agent corresponds to, for the entire ER surface area.

Distribution parameters

Physiological values for the density of RyR, IPR, and SERCA can theoretically be used in the model, but the use of densities approaching realistic values increases the intractability of the solution, would require more refined parameterisation of the agents based upon accurate single channel data, and require a FEM mesh of increased density. The ER membrane of a mast cell, for example, is estimated to contain approximately 14,000 IPR channels and 1.6 million SERCA pumps^[37]. To reduce this problem to one that can be solved, a low density value of *agents*/ μm^2 was used, where each individual agent located on the ER membrane represents a theoretical cluster of channels or pumps. The relative density of each agent type in the cell was estimated and refined, based upon interpretation from the literature and behaviour of the model.

The RyR channels are often referred to as being abundant on the ER in the basal region and mostly absent in the apical region, and IPR channels are referred to as being abundant in the apical region, and more diffuse in the basal region.^[66,69] The interpretation of this was that RyRs exist in a higher density in the basal region compared to the apical region, and vice versa for the IPRs, to allow coordinated release of calcium in the apical region by the IPRs and communication to the rest of the cell by RyRs^[69] (Figure 5.3). Two isoforms of SERCA are found in the pancreatic acinar cell on the ER membrane, where SERCA2a are found almost exclusively in the apical region with a close localisation to IPRs, and SERCA2b are found mainly in the basal region^[66]. The ODE model by Sneyd et al. assumed that SERCA was distributed homogeneously, and that only a single representation of the pump was used, and for these reasons a homogeneous distribution was also chosen in this implementation (Figure 5.4, top). The constant ER leak flux represents a passive channel on the ER membrane, and is used in the ODE model to balance the uptake by SERCA. Due to the association with SERCA, the leak channel fluxes were chosen to be localised to the same positions. .

The PMCA pumps were assumed to extrude calcium only on the apical mem-

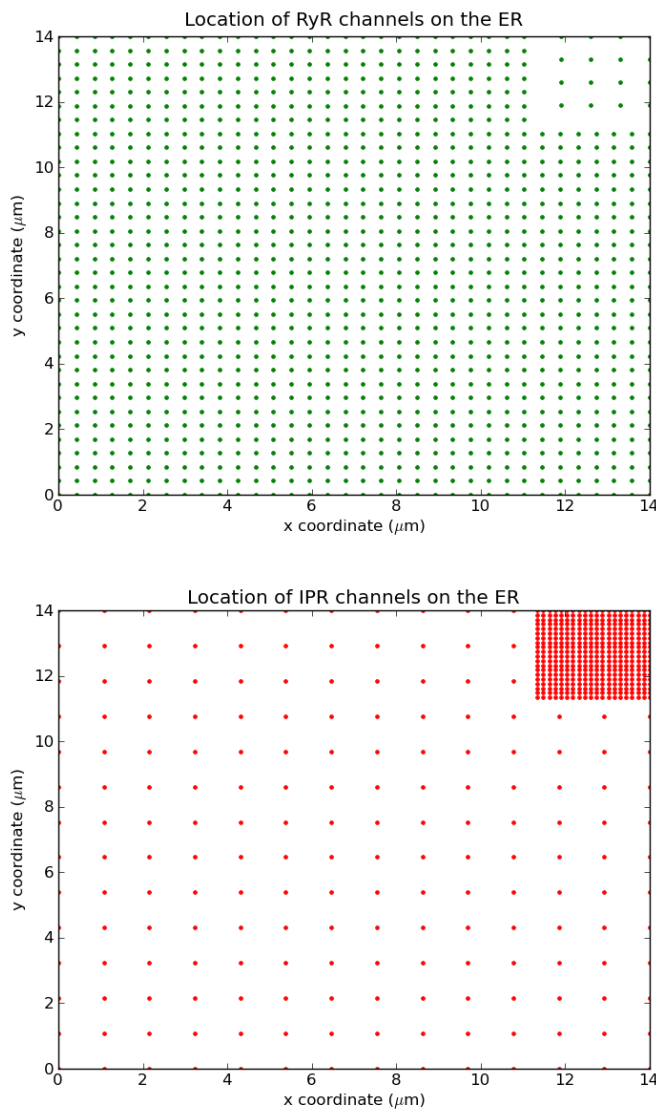


Figure 5.3: Plots showing the distribution of the RyR (top) and IPR channel (bottom) agents over an area that represents the ER and cytosol. Different densities of agents per μm^2 were used to represent the apical and basal regions.

brane^[66], and SOC provide influx over a portion of the basal membrane close to blood capillaries^[65] (chosen to be between the coordinates $xy=0,0 \mu\text{m}$ and $xy=7,7 \mu\text{m}$ along the cell boundary on the model). The distribution of PMCA and SOC was achieved by providing data on cell geometry (the length of sides of the rectangle and the apical region extent), and a density expressed as $agents/\mu\text{m}$ as the cell is two-dimensional, and these agents are placed around the edge of the cell (Figure 5.4, bottom). The contribution of PMCA and SOC in the ODE model by Sneyd et al. was controlled by the parameter δ , used as a scaling factor, and in the FEM model

5.1. FINITE ELEMENT MODELLING OF THE PANCREATIC ACINAR CELL IN TWO DIMENSIONS

this was empirically reduced from a value of 0.1 (as found in the ODE model) to 1×10^{-15} , until a resting cytosolic calcium concentration of approximately $0.03 \mu\text{M}$ was achieved. This was necessary due to the dominating effect these fluxes had on cellular dynamics; too much calcium was removed by even a single PMCA agent, and too much was added by SOC. Sneyd et al. stated that changing this scaling factor enables control of the trans-membrane fluxes relative to the trans-ER fluxes, without changing the homeostatic concentration of calcium^[28].

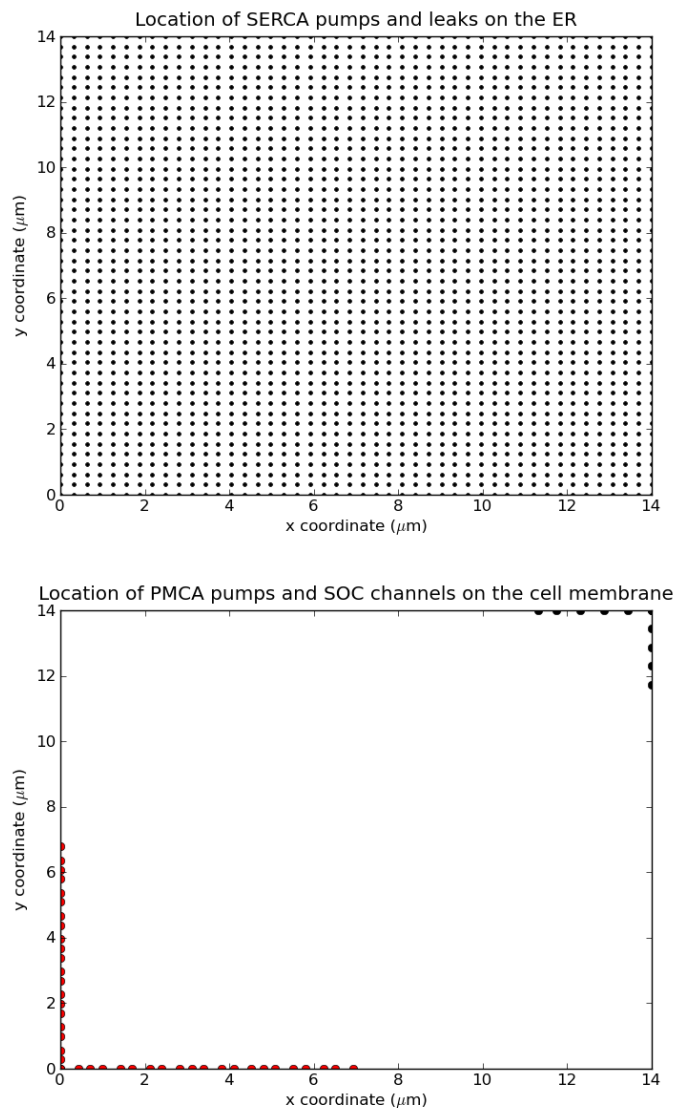


Figure 5.4: Plots showing the distribution of the SERCA (top) and PMCA (bottom) pumps, and SOC channel (bottom) agents over an area that represents the ER and cytosol. SERCA is distributed homogeneously throughout the cell, while the PMCA are only located on the apical membrane (top right corner) and SOC only on the basal membrane (bottom left corner). The ER leak flux is associated with the SERCA pumps and as such is located at the same positions as the SERCA agents.

A total of 30 mitochondrial agents were included in the model, as was assumed in the ODE acinar-mitochondria model and previously described in Section 4.2.1. One third of this population was chosen to form the mitochondrial firewall around the apical boundary (10 agents). The 20 remaining mitochondrial agents were then assumed to be evenly distributed around the cell membrane, excluding the apical region (Figure 5.5). As different cells of the same type are likely to have differing numbers of mitochondria in them due to fissure and fusion, each mitochondrial agent could also be perhaps considered a cluster of mitochondria, similar to the channels and pumps.

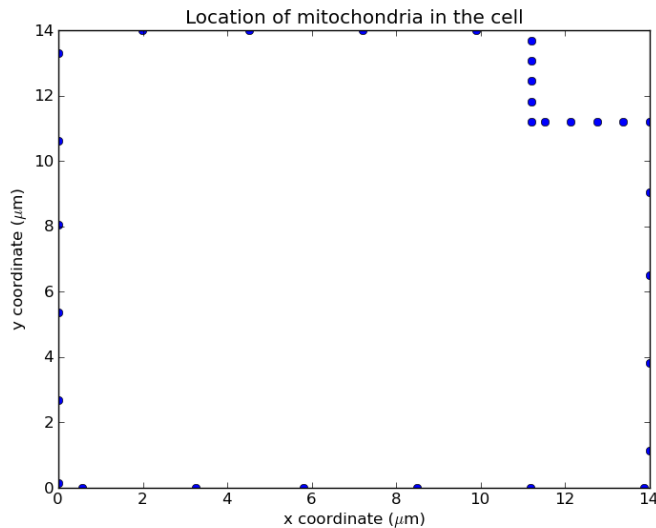


Figure 5.5: Plots showing the distribution of the mitochondrial agents over an area that represents the ER and cytosol. One third of the population of 30 agents was used to form the apical boundary, while the remaining agents were distributed homogeneously on the cell boundary.

The parameters for channel densities that were eventually found for this FEM implementation are different to that inferred from the relative rate constants for the apical and basal regions used by Sneyd et al. in the spatially compartmentalised model. The relative rate constants used by Sneyd et al. were obtained by fitting to experimental data, to account for the complex underlying dynamics. The article explains that the experimental data to which the model was fitted encompasses a mixture of both type-II and type-III IPR channels in the pancreatic acinar cell, and these types exhibit different responses to IP₃. The lack of a Markovian model of the

type-III IPR in the model by Sneyd et al. meant that the type-II IPR model was used instead, and rate constants were adjusted until they reproduced experimental data. The article also explains that the Markovian Keizer-Levine RyR channel model used in the study was originally intended for use in the cardiac cell, and that while the isoform found in the acinar cell is the same, the behaviour exhibited by this channel in a different cell type may potentially be different.

The FEM model by Tsaneva-Atanasova et al. (2005)^[79], which builds on the model by Sneyd et al. (2003)^[28], does not make clear how the channels are represented in space, but models the heterogeneity in the same way as the spatially compartmentalised model using rate constants. Moving away from modelling channel density as rate constants that are different depending on the region, the method chosen for use in this study was to use the same rate constant for each agent of a channel type, and control the distribution explicitly, as previously discussed. This way relative channel densities can be inferred from the literature, instead of fitting to experimental data, and a spatial distribution may be specified. For example, the IPR channels in the basal region are assumed to have the same maximal flux rate as those in the apical region, but the actual number of IPRs/ μm^2 is different for each region. This same assumption was also used for the RyRs. This means that the response of channels to stimulation is now entirely dependent on the spatial distribution.

The ratio of maximal flux rates used by Sneyd et al. for IPRs and RyRs in the apical and basal regions were initially used as the basis for controlling the spatial distribution of channels. These rate constants Sneyd et al. found through fitting to experimental data suggest that there are approximately 7 times more IPRs in the apical region than RyRs (0.71 s^{-1} : 0.098 s^{-1}), and approximately 8 times more IPRs than RyRs in the basal region (0.32 s^{-1} : 0.04 s^{-1}). For both channels, the parameters suggest that there are approximately twice as many channels in the apical region than the basal region. Owing to the spatial separation of these channels, and other components such as SOC, PMCA, the mitochondria, with the 2D cell geometry, these ratios were found to require adjustment in order to allow emergent behaviour to arise.

This resulted in the final set of distribution parameters arrived at being somewhat different to what might have been expected from the original article by Sneyd et al. The agent density parameters that were used to distribute these agents in this study are detailed in Table 5.1. These agent density parameters resulted in behaviour that was more comparable to the original study by Sneyd et al.

Agent type	Apical	Basal
IPR	$60 \mu\text{m}^{-2}$	$1 \mu\text{m}^{-2}$
RyR	$4.5 \mu\text{m}^{-2}$	$6 \mu\text{m}^{-2}$
SERCA	$11 \mu\text{m}^{-2}$	$11 \mu\text{m}^{-2}$
PMCA	$2 \mu\text{m}^{-1}$	
SOC		$3 \mu\text{m}^{-1}$

Table 5.1: Agent densities used in simulations for distribution of IPR, RyR and SERCA on the ER surface, and PMCA and SOC on the cell membrane, in the acinar cell FEM model.

Mitochondrial agent movement

In addition to the ability to enforce the spatial distribution of cellular components, and model the diffusion of species using FEM, mobile mitochondrial agents were included. The notion of mitochondrial motility was mentioned in Section 3.2.1, where the mitochondria perform bursts of directed movement for approximately 6% of their time^[49], and motility is temporarily arrested when the cytosolic concentration of calcium is elevated^[57]. The motivation of this study was spontaneous formation of the mitochondrial firewall in the apical region of the acinar cell, where it is thought mitochondria provide enhanced local calcium buffering and ATP supply. The signal used by the cell for recruitment of mitochondria to specific locations in the cell is unknown, but for the purpose of this study it was assumed to be related to the concentration gradient of calcium (the theory being that higher calcium concentration in a region of the cell is a sign of increased energy demand).

The complex cytoskeletal structure of the acinar cell, consisting of actin filaments and microtubules that the mitochondria use to pull themselves along during directed movement, is not modelled. Instead, it was assumed that the mitochondria may move in any direction they wish, and the direction they move is controlled

by the direction of the calcium concentration gradient local to each mitochondrial agent. The speed with which the mitochondria move up the calcium concentration gradient was set to 290 nm s^{-1} ^[49], and moderated by a Hill equation that reduces the speed of movement as the threshold for complete arrest is approached at $2 \text{ }\mu\text{M}$ (Equation 5.1). A half-saturation constant (K_m) of $0.4 \text{ }\mu\text{M}$ was used based upon Figure 2B in Yi et al. (2004)^[57], as the concentration at which approximately 50% of mitochondrial movement is inhibited.

$$\text{Speed} = \left(1 - \frac{[\text{Ca}^{2+}]_i^2}{K_m^2 + [\text{Ca}^{2+}]_i^2} \right) \times 290 \text{ nm s}^{-1} \quad (5.1)$$

No implementation of the frequency and period of mitochondrial movement was attempted, due to the short length of simulation time which this model is going to be run (30 s). Instead, in simulations where mitochondrial motility is enabled, the mitochondria is allowed to move freely for the entire simulation.

Computational efficiency

With the potential for thousands of agents in the form of channels, pumps, and mitochondria that require integration, and multiple solutions to the diffusion equation to be solved at each step, the model required construction with multiple processing in mind.

A finer mesh results in a more accurate solution of the diffusion equation, at the cost of computation time, and this is multiplied by the number of species for which it is solved. The number of nodes along the x and y boundaries of the rectangular mesh was set to 100, such that there were 100×100 mesh nodes. This provided sufficient detail to observe local calcium peaks, while keeping the speed of computation down. FEniCS/DOLFIN allows a single simulation domain to be spread over multiple processors during solution to speed up the calculation, but this is more suited to using a much more complex and finer mesh and was not enabled during these simulations.

Each agent representing PMCA, SERCA, leak flux and SOC is relatively fast to

calculate, since these are essentially represented by a flux equation. The mitochondria, RyRs and IPRs on the other hand require integration over the time period, as they are controlled by multiple ODEs. If there are thousands of agents in total to integrate, the problem benefits from multiprocessing. An array was constructed to hold all data associated with each agent, which stores location details along with values for the degrees of freedom information at the current time step (Figure 5.6). The array is passed into a function which sets up multiple Odeint jobs, which are then executed in parallel using the maximum number of CPU cores available. The amount of time for which the agents are integrated depends on the size of the main time step controlling the solution of the diffusion equation. The time step chosen for solution of the agent ODEs is smaller than the time step for the diffusion equations, and these were found through manual adjustment until integration errors did not occur. A time step of 0.1 ms was required for the RyR and IPR channel agents, and a time step of 0.001 ms was required for the mitochondrial agents. Section 5.1.4 contains further details on the order in which the model is solved.

```
agents = [[x, y, index, DOF1, ..., DOFn],
          [x, y, index, DOF1, ..., DOFn],
          .
          .
          .
          [x, y, index, DOF1, ..., DOFn]]
```

Figure 5.6: Format of the array used to store agent information. The coordinates and closest mesh cell index are always stored at the beginning of the array slice, and the degrees of freedom follow.

In order to find the best time step for solution of the diffusion equation, a range of time steps were used to solve the decay of a Gaussian distribution of physiological calcium concentration (peaking at $2.5 \mu\text{M}$ in the centre), similar to Figure 2.11. The concentration at the centre of this distribution in a cell was monitored and plotted against time, for a range of time steps in Figure 5.7. Using the same diffusion constant as Sneyd et al. of $10 \mu\text{m}^2\text{s}^{-1}$, it was judged that a time step of 2 ms is suitable to sample a localised calcium concentration transient, without losing detail due

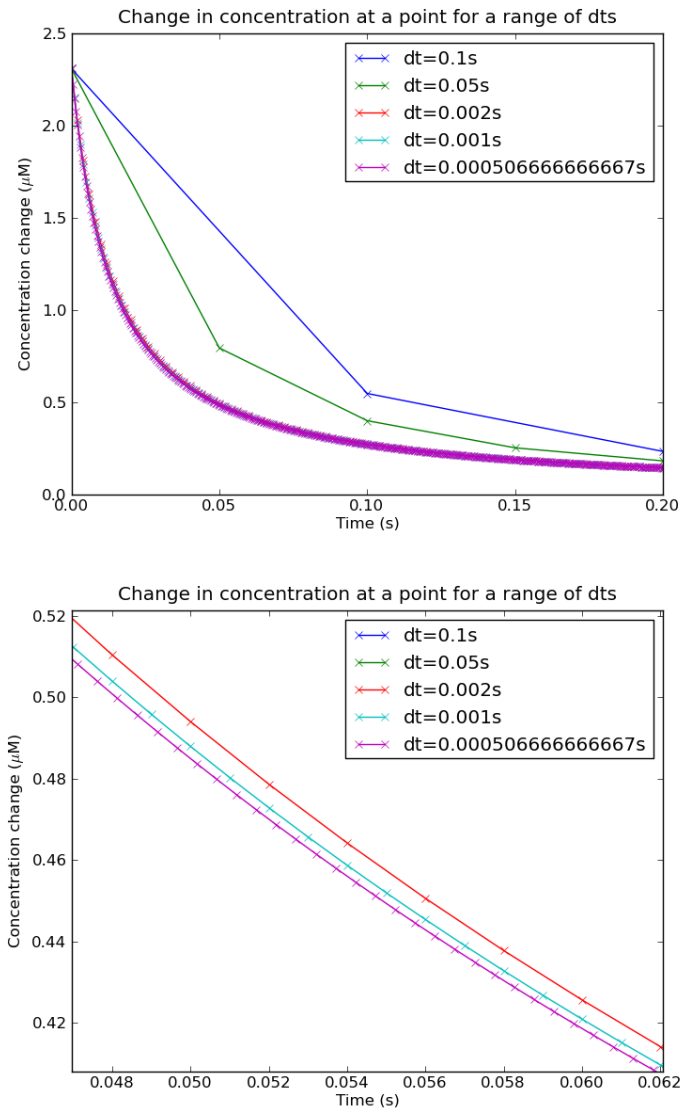


Figure 5.7: A range of time steps used to track the decay of calcium concentration from the centre of an initial Gaussian distribution. The smaller the time step, the more accurately the diffusion equation is solved over the mesh. The top plot shows a range of time steps that were considered; those which are large (0.1 s and 0.05 s) give a more approximate distribution of concentration over time. The bottom plot is a close-up of the three smallest time steps. Decreasing time step size results in a more defined and detailed curve. From these test simulations, a time step of 2 ms was judged to be sufficiently large without losing too much detail in the change of concentration.

to diffusion during the time step. Time steps larger than this lose detail in the expected curve of concentration decay for this particular diffusion constant, as can be seen by comparing the time step of 0.1 and 0.05 s with the other step sizes in Figure 5.7. An additional time step was added to the test in the form of the size of time step needed to sample the fastest simulation event occurring with the ODEs: channel

opening. The IPR and RyR channel models were stimulated with their respective agonists in order to measure what was the fastest channel opening event, and what time step would be required to sample this event three times between the closed and open state. Sampling the channel opening event three times was considered to be a balance between detail and time step size. The RyR channel was found to have the fastest transition and, in order to sample this three times, the time step needs to be approximately 0.0005 s. However, the rate in which calcium concentration increases, and subsequently activates the RyR, in the final FEM model is much slower than the instantaneous change that was used in this test. Therefore, the smallest time step was disregarded in the model in favour of using 2 ms.

While developing the model a problem with the efficiency of FEniCS/DOLFIN (version 1.0.0) itself was discovered, and brought to the attention of the FEniCS/-DOLFIN developer community. A modified and minimal FEniCS/DOLFIN tutorial script was provided and explained in the developer forum*, in the hope that a bug could be found and fixed. Figure 5.8 shows the result of this script, and that with each solution per time step during a simulation, the time taken to solve the problem increases indefinitely (although the increase shown in the figure is small, this is only a small and simple test case). This is a significant problem for a model that requires stepping over time, and was only found later in the project. Unfortunately the issue that was raised seems to either have been ignored by the developers, or there is no solution.

It was discovered that the initial computation time per step could be recovered if the simulation was halted and then restarted from that point. The model code was restructured so that a simulation could be stopped manually when the calculation time per step seemed too long, and then restarted from the last checkpoint. On a positive note, this workaround evolved to allow simulations that start from a set of user-provided initial conditions. The ability of the model to use a set of initial conditions, generated from previous simulations, is vital for consistency between

*<https://answers.launchpad.net/dolfin/+question/197950> (accessed 15/9/12)

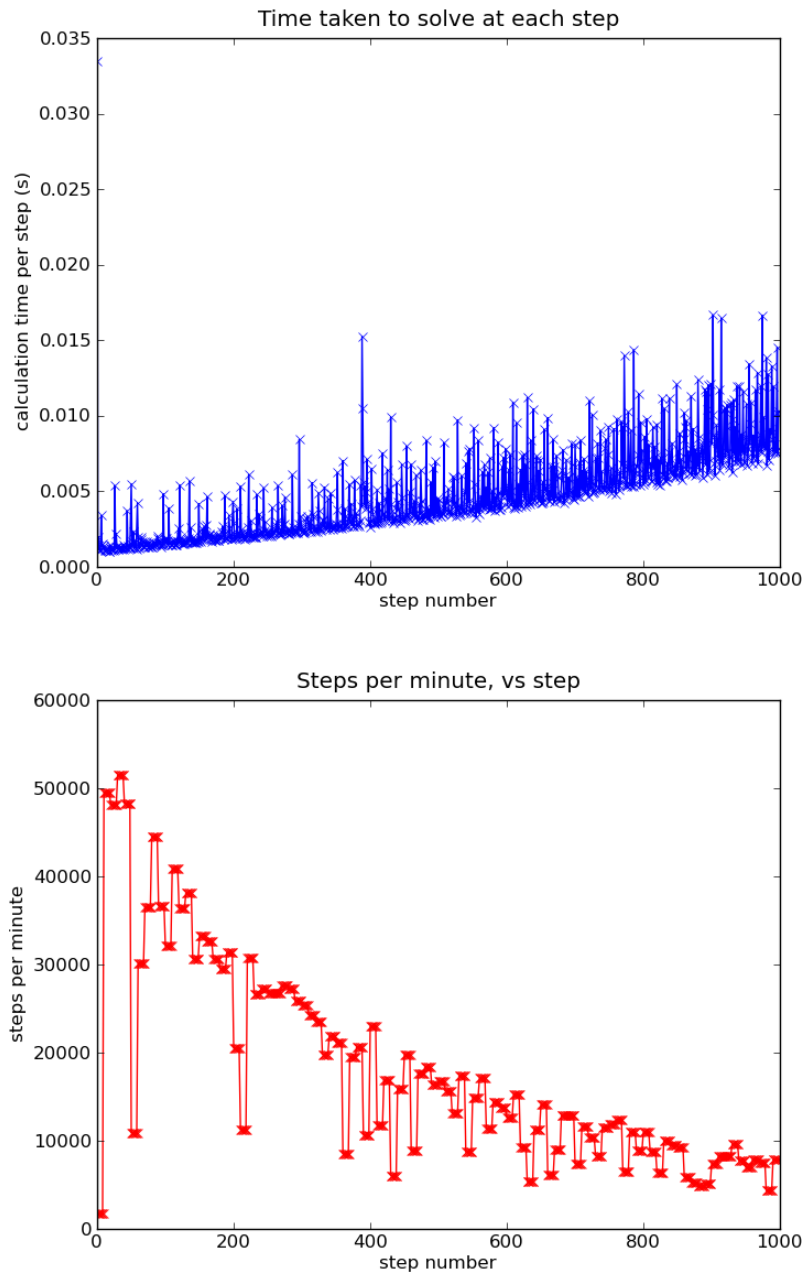


Figure 5.8: The slowdown discovered in FEniCS/DOLFIN that accumulates over repeated solution of the diffusion equation. This plot corresponds to a very small test system, and so is solved more quickly than the acinar cell model, but the issue is still there.

simulation runs. This ensures that each simulation can begin from a single, stable, configuration and does not require spending time waiting for the steady state before stimulation and collecting results. However, while this workaround allows simulations to finish in a more satisfactory time, each simulation requires constant observation of performance to decide if a restart is necessary. Figure 5.9 shows the acinar cell model performance over time when stimulated with $20 \mu\text{M}$ IP3 for 30

s, using a 100×100 rectangular mesh. The simulation was restarted twice to regain the initial speed of computation, and each of these restarts added a gain of approximately 15 steps per minute to the simulation; approximately doubling the rate in which the simulation progressed.

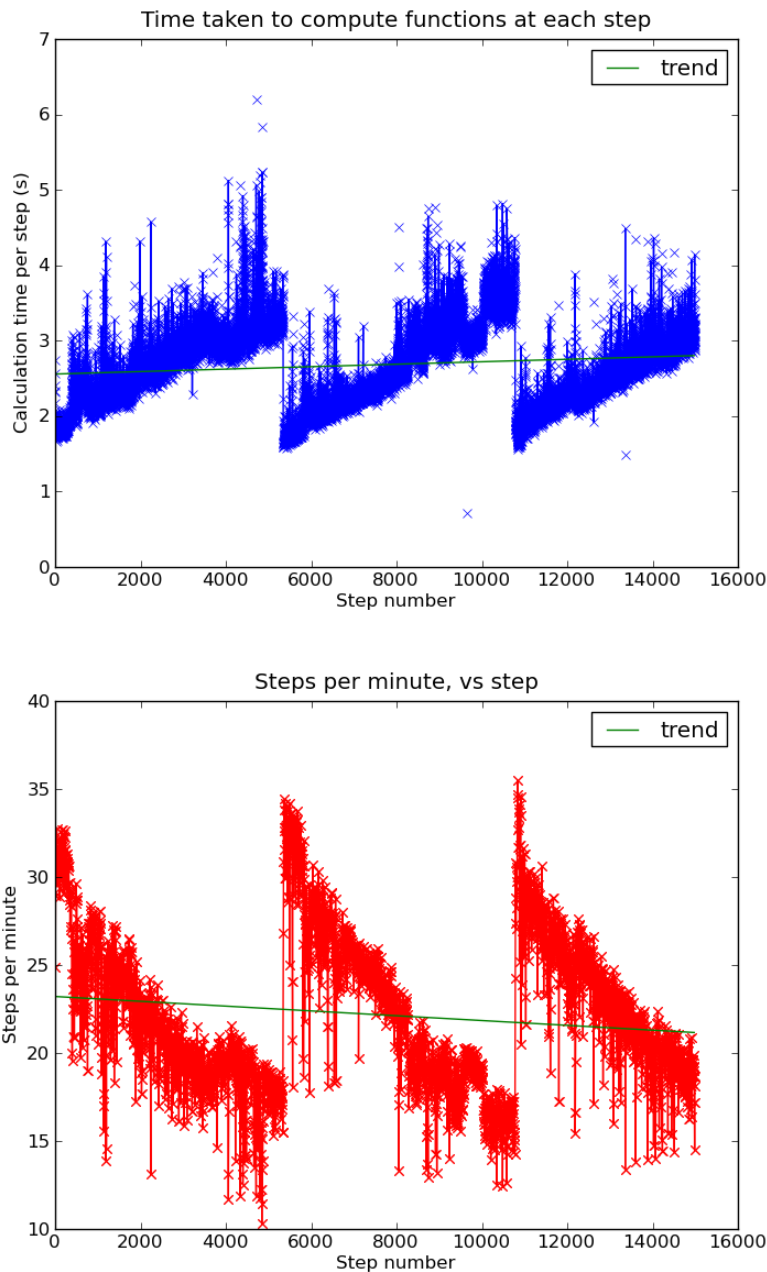


Figure 5.9: The slowdown discovered in FEniCS shown in a simulation of the acinar cell FEM model that was stimulated with $20 \mu\text{M}$ IP3 for 30 s. The time per step increases the longer a simulation runs, but the speed is regained if the simulation is restarted. The trend line was used as a visual aid to the rate in which the simulation is progressing, such that the need to restart can be assessed.

Owing to the complexity of the FEM implementation of the acinar cell and the problems with computation speed, the model cannot currently be run for simulation time of the scale of minutes without constant monitoring of performance. This makes it difficult to investigate processes that occur over the time scale of minutes, in contrast to the ODE implementation. An important part to creating this implementation is stability over time. The parameters that were found and used for generating results provide simulations that are stable over the time scale of approximately 1-2 minutes. This is the approximate total time for which each result has been simulated, including the prior steady state simulation (detailed in Section 5.1.5). In the short term the model looks stable, but perhaps 5-10 minutes of simulation time later, the model may not be. Owing to the computation time required for solution of the model, this time scale is not easily accessible and therefore stability issues are not necessarily found.

In order to investigate parameter stability, simulations were carried out using a longer FEM time step. At one stage of development, for example, a main time step of 10 ms was used instead of 2 ms, so that a new set of parameters could be quickly tested. The results from this 10 ms time step simulation showed a wave of calcium propagating from one side of the cell to the other, upon stimulation by IP3. This interesting result gave the impression that the balance of channels in the apical and basal regions was 'just right', and a number of simulations were set up using the smaller, more time consuming, 2 ms time step, so that more detail could be extracted. Upon analysing the results, not one of the simulations reproduced the plots that resulted from the 10 ms time step exploratory simulation. These differing results arise from a combination of two factors related to the chosen time step. Firstly, species diffuse further around the domain during larger time steps, which results in a more approximate distribution of matter. This means that a quantity of calcium added to the cytosol at a particular coordinate, at time t , is lower at $t + dt$ when $dt = 10$ ms than if $dt = 2$ ms. Agents that then sample a local concentration at each step are exposed to different concentrations over time, between simulations with

different time steps. Secondly, the method used to calculate the amount of calcium through a channel (after integration of the channel ODEs) involves multiplying the open fraction at the current time step by a concentration difference, with the maximal channel flux rate and the main time step. This means that the greater the main time step, the greater the change in calcium will be, and the same goes for other pumps and channels in the model.

Therefore, the model behaves differently depending on the chosen time step, and this increases the difficulty in finding and refining a set of parameters. While a time step of 2 ms could indeed be too long, this was selected for generating results in the study due to the relationship between the diffusion constant ($D = 10 \mu\text{m}^2 \text{s}^{-1}$), and the range of physiological calcium concentrations that are expected. The combination of these factors, together with consideration of computational speed and detail, resulted in the choice of 2 ms as the diffusion time step.

Example system

Once agents have been placed at a position in the cell, they may interact with the dynamics of the system over time. The diffusion of species over the domain is modelled at one time step, and the equations that control channel states at another (further detailed in Section 5.1.4). Contribution of a quantity of a species at a position on the domain results in an increased concentration, and the gradients of concentration in space point toward this position as matter diffuses away. Removal of species at a position results in the opposite effect.

The following is an example of a single SERCA pump and a single IPR channel, changing the concentration of calcium in the cytosol over time (Figure 5.10). The overall spatio-temporal change in concentration for the ER and the cytosol is extremely small, due to the the fact there is only a single instance of each agent. However, it can be clearly seen that activation of the IPR channel by IP3 causes a change in the system.

Throughout this example the SERCA pump is working continuously to remove

5.1. FINITE ELEMENT MODELLING OF THE PANCREATIC ACINAR CELL IN TWO DIMENSIONS

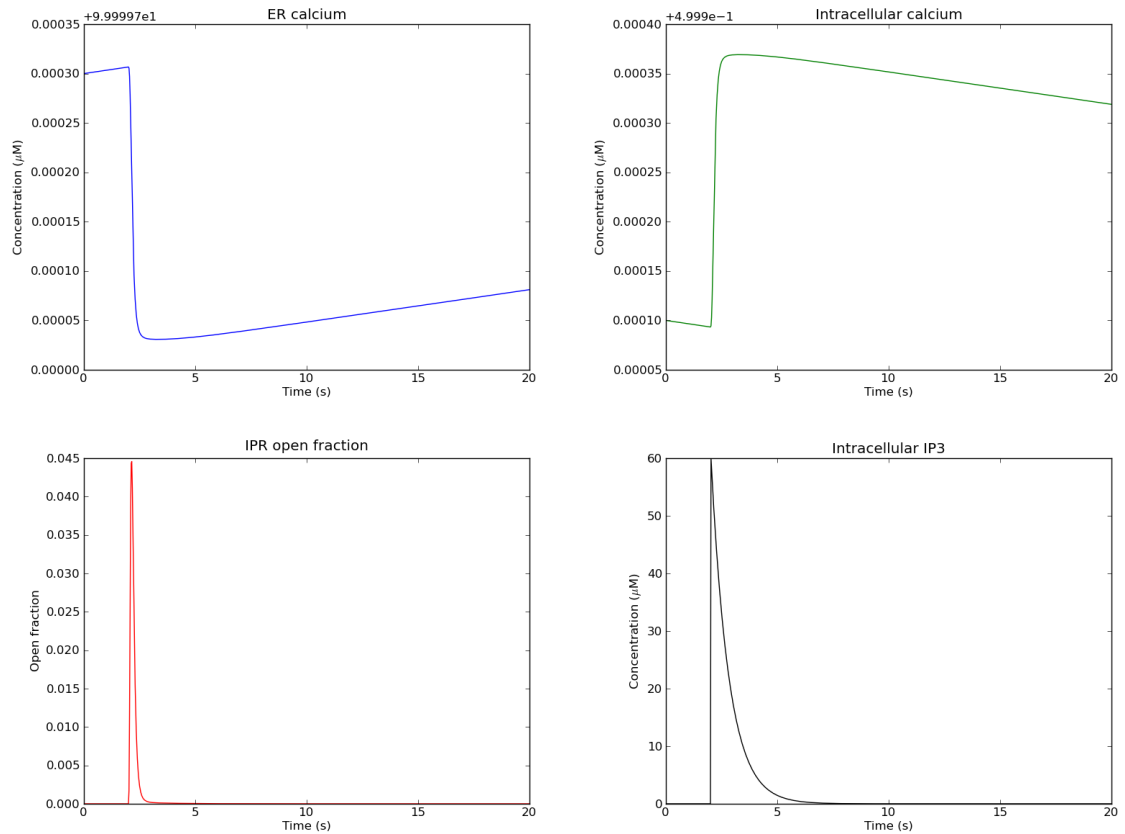


Figure 5.10: Plots showing the change in total calcium concentration in the ER (top left), and intracellular (top right) layers. This is due to transition of the IPR channel into a temporary open state (bottom left), upon exposure to IP3 (bottom right). The numbers at the top of the y axis in the top two plots are displayed by the plotter when the line shows little change at large values. Therefore numbers on the y axis for ER calcium are equal to $y+9.99997e^1 \mu\text{M}$, and the maximal loss of ER calcium is approximately $0.000275 \mu\text{M}$. Intracellular calcium shows a maximal gain of approximately $0.000275 \mu\text{M}$, because the same compartmental volumes were used for both ER and cytosol in this example.

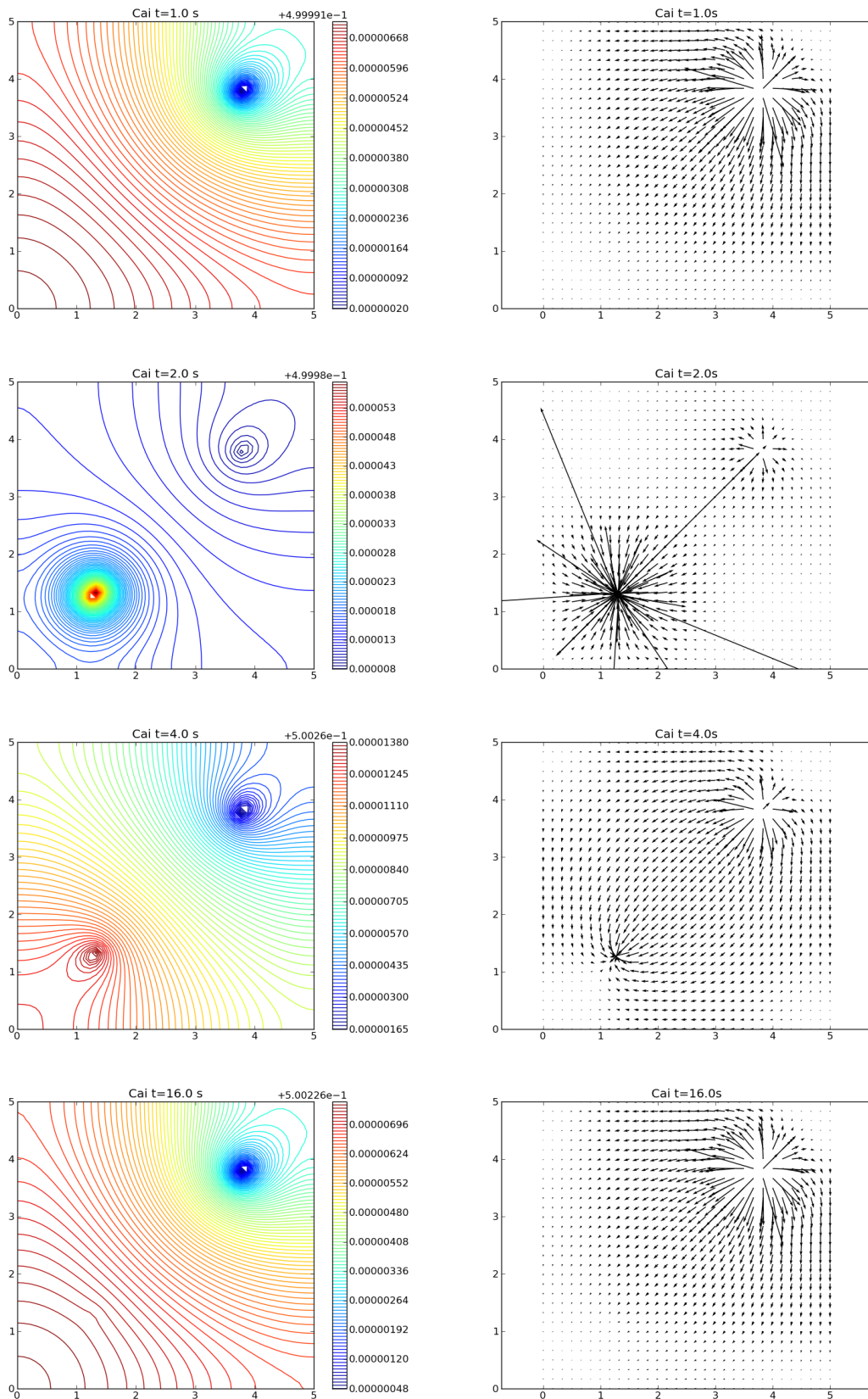


Figure 5.11: A series of contour plots (left, units of μM) and concentration gradient plots (right, where longer arrows represent a steeper gradient), that show the spatial diffusion of calcium in the cytosol over time, related to Figure 5.10. The IPR channel (bottom left of each plot) transitions into a temporary open state, which releases calcium into the cytosol, while SERCA (top right of each plot) remained continuously active throughout the simulation.

calcium from the cytosol, yet the IPR channel only adds calcium to the cytosol in response to raised IP3 concentration. Figure 5.11 shows a more visual representation of the changes seen in Figure 5.10. Before the IP3 concentration is raised at $t=0$ s, the calcium concentration is lower in the area close to SERCA (top right), and the calcium concentration gradient is shown to point away from this location as SERCA removes matter. Upon increase of IP3 concentration at $t=2$ s, an influx of calcium occurs at the location of the activated IPR channel (bottom left), for a short period of time. The calcium concentration in the ER decreases and the calcium concentration in the cytosol increases, due to the calcium flux occurring between the two compartments (ER layer not shown). As the IPR channel deactivates, the SERCA pump continues to remove calcium from the cytosol and the ER begins to recover the lost concentration ($t=4-16$ s).

Moving on to a more complex example of agent interaction with the diffusion of calcium, Figure 5.12 shows the result of a simulation using a density of RyR channel agents of $40 \mu\text{m}^{-2}$, and a density of SERCA pumps of $80 \mu\text{m}^{-2}$, distributed evenly over the ER, and releasing calcium into the cytosol. The RyRs were activated at one end of the cell by raising the concentration to initiate CICR, which propagates across the cell over time, (Figure 5.13). Although CICR does actively propagate over RyRs across the cell, they do not close because of continual stimulation by calcium flowing out of the ER. If the density of SERCA is increased only slightly to $81 \mu\text{m}^{-2}$, the pumps have a deactivating effect on the RyRs by reducing the amount of calcium the RyRs are exposed to. The degree to which each RyR channel is activated with slightly more SERCA is much lower, as shown in Figure 5.14, which highlights the sensitivity of parameters in such a model.

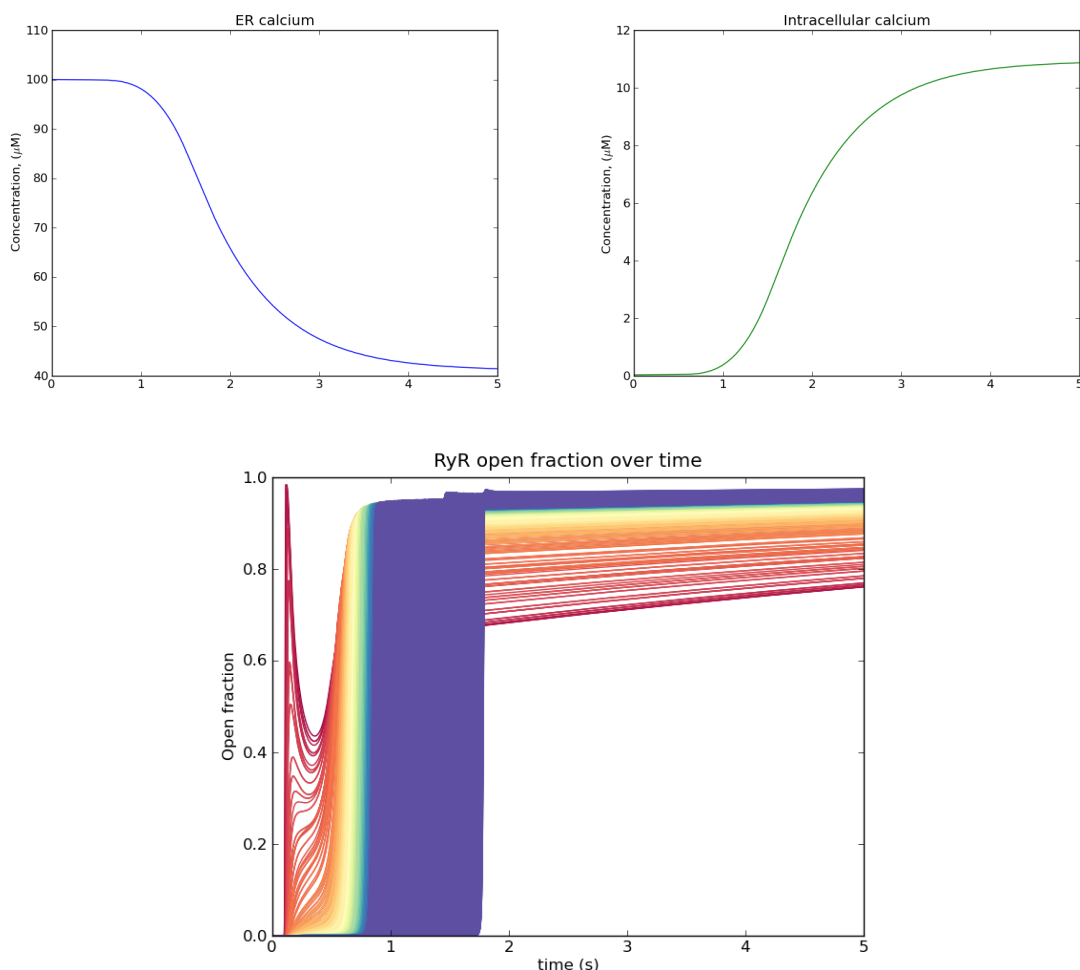


Figure 5.12: The total change in ER (top left) and intracellular calcium (top right) for a CICR example, where a density of $40 \mu\text{m}^{-2}$ RyR and $80 \mu\text{m}^{-2}$ SERCA were spread out uniformly across the ER membrane of the cell. The RyR channels were stimulated at a single point in the corner of the cell by raising the calcium concentration temporarily. CICR propagated across the cell, activating the RyRs (bottom plot). The RyR channels in this example did not deactivate after opening, due to continued stimulation from subsequently activated channels. Each line represents a RyR agent open fraction, and is coloured differently to provide more contrast. Red coloured lines represent agents toward the bottom-left region of the cell in Figure 5.11, and blue coloured lines represent agents in the top-right of the cell.

5.1. FINITE ELEMENT MODELLING OF THE PANCREATIC ACINAR CELL IN TWO DIMENSIONS

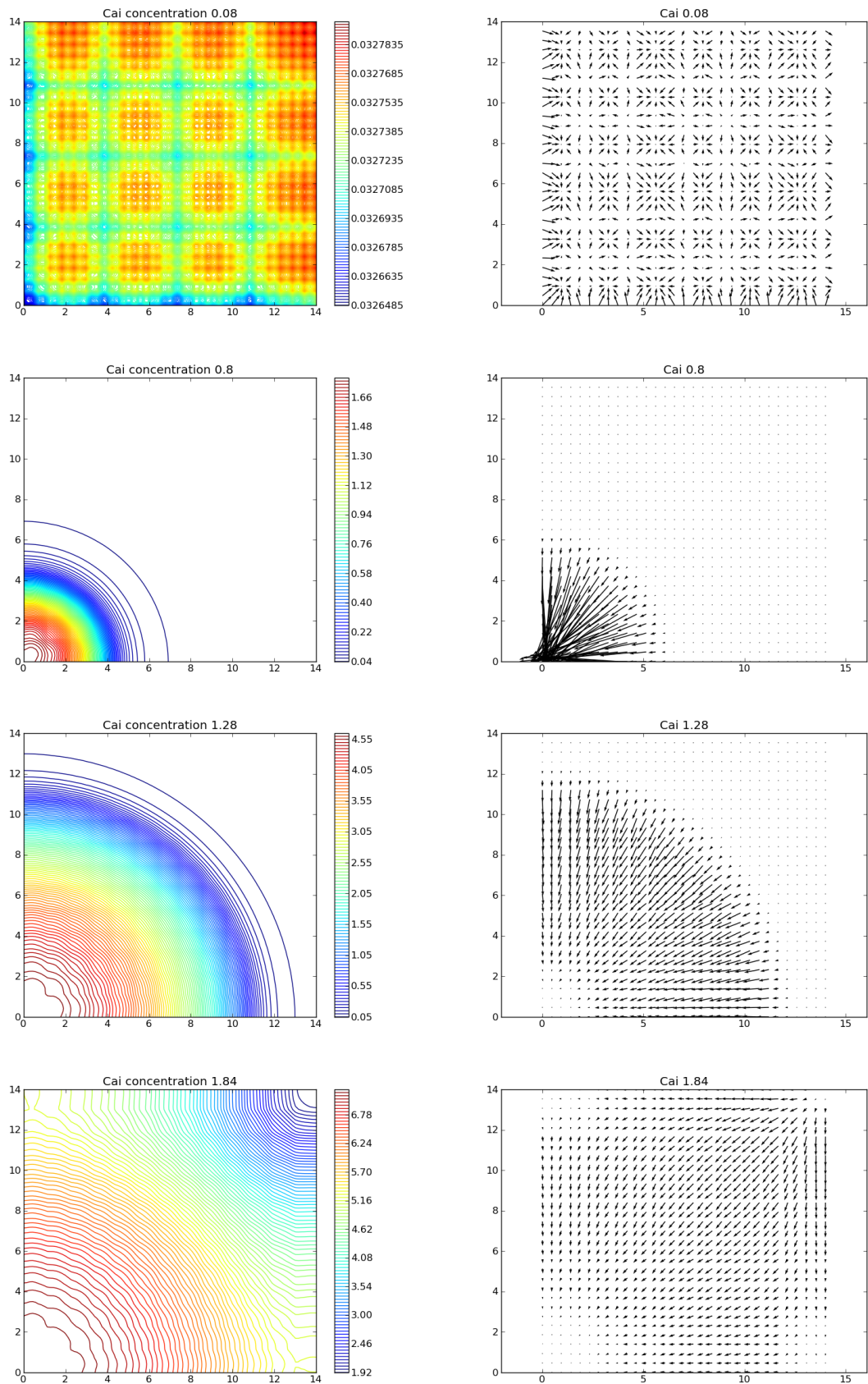


Figure 5.13: A series of contour plots (left, units of μM) and concentration gradient plots (right, where longer arrows represent a steeper gradient), that show the spatial diffusion of calcium in the cytosol over time, related to Figure 5.12. CICR is initiated at the bottom left of the cell, and quickly propagates across the surface of the ER in the cytosol.

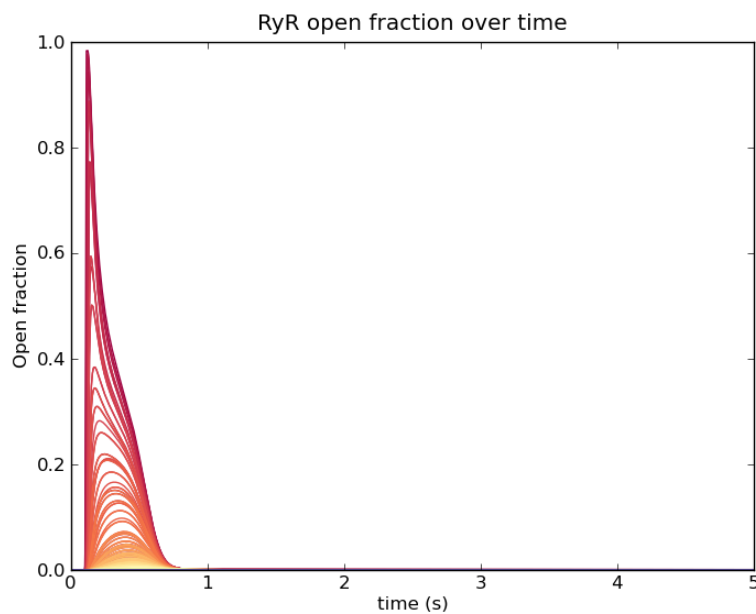


Figure 5.14: A plot shown for comparison to that at the bottom of Figure 5.12. In this example, a slightly increased $81 \mu\text{m}^{-2}$ SERCA density was used, instead of $80 \mu\text{m}^{-2}$, which has resulted in deactivation of the RyRs before CICR can occur. This demonstrates the sensitivity of parameters in this model type.

Background testing

Background tests for the script were developed to assure that any changes to the model still provide the expected behaviour to the physics of the system. These tests can be invoked at any time using the Pytest environment*, and ensured conservation of concentration through the methods used to change the finite element solution, time step tests, and agent movement tests. Mass conservation in the model is a requirement of correct implementation. Test scripts are included on the supplementary disk.

Fixed IP3 oscillations

The concentration of IP3 in cells may appear constant or fluctuate over time^[92]. Spontaneous oscillations resulting from fixed IP3 concentration^[28,79,92] did not appear to occur in this FEM implementation of the acinar cell, in contrast to the ODE version by Sneyd et al. The reason for this is unknown, but either this involves a time step issue, or repeated oscillations may occur in unexplored time space beyond the time scale of the FEM model, due to the different interactions between calcium concentration and IPR channel activity experienced in the FEM model compared to the ODE version.

5.1.2 Preliminary code development

Preliminary code was developed by Marijan Beg of the Southampton University Engineering Department. Parts of Marijan's code that demonstrated assembling FEniCS components and solving the diffusion equation over a 2D domain were modified through conversion into Python functions. This enabled initialisation and solution of multiple 'layers', the use of expressions for an initial concentration distribution, and altered variable names to ensure similarity to the FEniCS tutorial while error tracking.

*<http://www.pytest.org> (accessed 7/9/12)

This contributed code also demonstrated the use of ODE controlled agents using the RK4 integration routine interacting with concentration at a position on the 2D domain. This was used for guiding the channel, pump and mitochondrial agent implementations in the final model. Agent information and variables were modified for storage in a single large array, but looped over in a similar way to the preliminary code, while calculating fluxes for SERCA, PMCA, SOC and the ER leak. For RyR, IPR, and mitochondrial agent integration over time, the final code instead uses the Odeint integration routine, together with multiprocessing, to ensure the code runs as quickly as possible.

The preliminary code also demonstrated how concentration gradients are extracted during a simulation, such that they can be later used to control mitochondrial movement in a specific direction. This was later modified to ensure that mitochondrial agents move at a consistent speed regardless of the magnitude of the gradient, and that this speed decreases to zero as the calcium concentration increases to the threshold, as detailed in Section 5.1.1. Where possible, the model code has been commented to show contributions from others.

5.1.3 Error and numerical stability

Before generating results using the parameters of agent distribution, the FEM implementation of the pancreatic acinar cell was checked for numerical stability. With extracellular fluxes disabled (SOC and PMCA) the number of moles of calcium is conserved between the ER, cytosol, and mitochondria (Table 5.2). The extracellular source is not tracked since the concentration of this source is assumed to be inexhaustible, so when extracellular fluxes are enabled this causes the total moles of calcium to change. The number of moles of ATP and ADP is also conserved with respect to both the mitochondrial and cytosolic concentrations (Table 5.3).

Individual compartments that contain the diffusive species of the model do not experience conservation, due to the movement of molecules between these compartments over time (with the exception of ATP and ADP, which exchanges between

mitochondria and cytosol via J_{ANT} at a 1:1 ratio), so conservation in the system as a whole needs to be considered. The molar concentration of a 'layer' is calculated using the `assemble` function in DOLFIN, and converted to moles using the total volume of that layer. The number of moles of a species inside the mitochondria is found by multiplying the molar concentration inside each mitochondrion by the total mitochondrial volume. Using calcium as an example, the number of moles of calcium in the ER, plus the number of moles of calcium in the cytosol and the mitochondria, are summed to obtain a total in the cell.

Table 5.2 shows the change in moles of calcium per compartment, output by the model during a 10 s simulation with a 2 ms time step. The simulation started from a non-steady state, with disabled extracellular fluxes and no IP3 stimulation, and demonstrates the transfer of calcium between compartments without changing the total number of moles in the system. Similarly, Table 5.3 shows the compartmental change of moles of adenines in the system, expressed as ADP and ATP, that also individually change and keep a constant total.

Compartment	$\mu\text{mol at 0 s}$	$\mu\text{mol at 10 s}$
Cytosolic calcium	0.1521	0.1557
ER calcium	77.3884	77.4469
Mitochondrial calcium	0.3171	0.2550
Total	77.8576	77.8576

Table 5.2: Table showing the total and compartmental change in moles of calcium over the time course of 10 s.

Compartment	$\mu\text{mol at 0 s}$	$\mu\text{mol at 10 s}$
Cytosolic ATP	4188.7900	4190.8627
Cytosolic ADP	6283.1850	6281.1123
Mitochondrial ATP	733.0383	777.9718
Mitochondrial ADP	3665.1912	3620.2577
Total	14870.2045	14870.2045

Table 5.3: Table showing the total and compartmental change in moles of ATP and ADP over the time course of 10 s.

The same data produced for a simulation where the system was stimulated with 6 μM IP3 is shown in tables 5.4 and 5.5, and this also exhibits mass conservation.

Any change to the mass conservation of species in the system is either due to the inclusion of extracellular fluxes, or machine precision.

Compartment	$\mu\text{mol at 0 s}$	$\mu\text{mol at 10 s}$
Cytosolic calcium	0.1521	0.1693
ER calcium	77.3884	77.0225
Mitochondrial calcium	0.3171	0.6658
Total	77.8576	77.8576

Table 5.4: Table showing the total and compartmental change in moles of calcium over the time course of 10 s, when stimulated with 6 μM IP3.

Compartment	$\mu\text{mol at 0 s}$	$\mu\text{mol at 10 s}$
Cytosolic ATP	4188.7900	4190.8948
Cytosolic ADP	6283.1850	6281.0802
Mitochondrial ATP	733.0383	784.3097
Mitochondrial ADP	3665.1912	3613.9198
Total	14870.2045	14870.2045

Table 5.5: Table showing the total and compartmental change in moles of ATP and ADP over the time course of 10 s, when stimulated with 6 μM IP3.

5.1.4 Simulation method

What follows is a short description of the actions carried out by the model during a simulation. The simulation code consists of several Python scripts as tools for performing different tasks, totalling approximately 6,000 lines. At any time, the methodology behind these calculations can be tested to ensure the system is working correctly using `pytest`^{*}. The version control system Mercurial[†] was used to incrementally track code development throughout construction. All model code is included on the supplementary disk under 'Code/FEM/'.

1. A simulation begins when 'simulation.py' is executed by Python within the script directory. Simulation data is saved in the 'simdata' subdirectory.

^{*}<http://pytest.org/> (accessed 21/9/12)

[†]<http://mercurial.selenic.com/> (accessed 23/9/12)

2. Simulation parameters that have been set up in 'simconf' are imported for use in the main simulation.
 - The simulation will either use the defined initial parameters in 'simconf', a set of initial conditions taken from the final state of another simulation, or restart a simulation from a stored checkpoint.
 - If the simulation begins from the set of initial conditions taken from the 'simconf' file, a uniform distribution of species concentration is applied to the 'layers'. Similarly, the values for degrees of freedom for each agent are identical, as defined in 'simconf'. Alternatively, an expression to describe the distribution of matter in each layer may be used instead.
 - If the simulation begins using conditions from the end of a previous simulation or checkpoint, the distribution of species concentration from these files is applied to the 'layers'. Similarly, the values for degrees of freedom of each agent are extracted from the files.
3. The main loop is entered, and the simulation begins. The function of this main loop is for solving the diffusion equation for each 'layer'. A 2 ms time step is used.
 - The concentration of IP3 and BA at the current point in time are calculated. These are either fixed or decaying values, that begin at time t .
 - Information about the state of the system at the current time step is calculated, and printed to the screen. This includes total species concentration per layer, the average state of agent degrees of freedom, and information about the conservation of mass.
 - ATP across the entire cytosolic layer is hydrolysed to ADP at each of the mesh nodes, represented as a flux with a background rate ($J_{hyd,bas}$, 0.00005 ms^{-1}) and a rate dependent on the local concentration of cytosolic calcium (k_{hyd} , $0.00005 \text{ } \mu\text{M ms}^{-1}$), obtained from the model by Bertram et

al.^[88]:

$$J_{hyd} = (k_{hyd} * [Ca^{2+}]_i + J_{hyd,bas}) * [ATP] \quad (5.2)$$

The concentration of species at mesh nodes is altered according to the detail in Section 2.4.2. In this instance, the concentration of ATP is decreased at a point in space, while the concentration of ADP is increased.

4. Before solution of the diffusion equation, the cellular agents are integrated using a smaller time step than the main loop. A time step of 0.1 ms is used for channel agents, and 0.001 is used for mitochondrial agents. This means that each agent is integrated, using these smaller time steps, for a period of time equal to the main time step (2 ms).

- The IPR and RyR agents, together with data on their local environment, are passed into a function that sets up jobs to take advantage of multiple CPU cores, and each set of agent ODEs are solved using the Odeint integration routine.
 - When the IPR and RyR agents have been solved, the open fraction of each agent at the current time step is extracted, and used to change the concentration of ER and cytosolic calcium accordingly (for detail, see Section 2.2.3). The concentration by which the ER and cytosol layers change depends on the volume ratio, expressed in terms of the FEM mesh cells, and the concentration gradient between them.
- The mitochondrial agents are solved using a similar method to the IPR and RyR channels. The difference is that the mitochondria change their local mesh cell concentration of calcium, ATP and ADP, throughout the integration, stored as an internal degree of freedom.
 - If mitochondrial motility has been enabled in 'simconf', the movement of each mitochondrion is calculated, based upon the local calcium gradient and concentration.

- After the mitochondrial agent ODEs have been solved, their local calcium, ATP and ADP concentrations are simply copied from the mitochondrial degrees of freedom, and directly applied to the corresponding mesh cell.
 - The PMCA, SERCA, leak flux, and SOC are not treated to multiprocessing, as these are not modelled using a collection of ODEs, and are therefore quicker solve. Instead, these agents are looped over and change concentrations in the model based upon fluxes, similar to how the RyR and IPR fluxes change concentration when the open state is found. The SERCA and PMCA are represented by Hill equations (Section 2.2.3), while the leak and SOC fluxes are modelled similarly to Equation 5.2.
5. After changes have been made to the layers by agents, the results are saved to file, at intervals defined in 'simconf'. This includes the current distribution of concentration for each simulation domain, channel open states, and mitochondrial degrees of freedom.
- At another short interval, restart files are saved to allow continuation of simulations if they are stopped.
6. The diffusion equations associated with each diffusing species in each layer of the system is then solved by FEniCS/DOLFIN.
- To judge if a simulation requires restarting due to the FEniCS/DOLFIN performance issues, data on the time taken to calculate the current step is output to screen, such that an informed decision can be made.
7. Finally, time is incremented, and the main loop repeats.

5.1.5 Steady State

The system was left to reach a steady state for 60 seconds prior to gathering results, and the final values for all degrees of freedom in the model were used as initial

conditions. All degrees of freedom remained at either an approximately constant value, or the changes were less than 1% over a period of 20 s.

Although the mitochondrial ATP and ADP concentrations reached a steady state in the model, the cytosolic ATP and ADP concentrations did not reach a steady state within this time, even with initial conditions that were similar to the steady state observed in the ODE model. This is most likely due to complex interactions between diffusion and the ATP hydrolysis flux that was not understood. The initial ATP and ADP concentrations were set to 1 mM^[75] and 1.5 mM respectively, and the final concentration and distribution of ATP and ADP in the system after all other degrees of freedom in the model reached an approximate steady state was used (approximately 1.003 mM ATP and 1.497 mM ADP).

Owing to the lack of a steady state for cytosolic ATP and ADP, the dynamics of these molecules was not examined in detail during this investigation. Instead, the relative distribution of ATP and ADP concentration is considered, which results from the mitochondrial distribution. More detailed study of the pancreatic acinar cell ATP and ADP dynamics requires modelling efforts that consider more detailed representation of ATP supply and demand by cellular machinery.

The steady state initial conditions used for generating the results in this thesis are included in the supplementary disk under 'FEM/simdata/'.

5.2 Summary

This chapter has described the process of constructing the FEM implementation of the pancreatic acinar cell. While the thinking behind parts of the model have been explained as concisely as possible here along with a pseudo code summary, the actual model code consists of 6,000 lines. The majority of this is commented for reference, and included on the supplementary disk.

With the ODE and multiscale FEM models of the pancreatic acinar cell implemented, the next chapters shall explore and discuss the results that show the in-

creased complexity and detail a multiscale model can provide in contrast to ODE models on a single scale.

Chapter 6

Results and Discussion I: ODE model of the coupled acinar cell and the mitochondria

The pancreatic acinar cell ODE model was allowed to reach a steady state, as described in Section 4.2.2. The following simulations show results sampled from $t = 1000$ s onward, as this was the end of the steady-state period. The duration of each simulation after this point may continue for minutes due to the low computational cost of solving the ODEs contained in the model, but the plots are cropped to display the appropriate amount of information.

As previously mentioned, the adjustments made to the mitochondrial contributions in this implementation mean that the mitochondria do not play a major role in shaping the calcium dynamics. Therefore, simulations where the mitochondria are disabled are not included.

6.1 The effects of stimulation by IP₃ on the coupled ODE model

6.1.1 Single pulse on unstimulated steady-state system

After allowing the combined acinar-mitochondria model to reach a steady state for 1000 seconds, the cell was exposed to IP₃ at a concentration of 30 μM , which decayed with a constant of 1.25 s^{-1} (Figure 6.1). Immediately, the IPR channels open, causing influx of calcium into the cytosol from the ER. This small amount triggers the RyR channels to open via CICR, resulting in a greater influx of calcium into the cytosol, and this then contributes to IPR deactivation. The cytosolic calcium concentration increases from approximately 0.036 μM to a peak of 2.25 μM before quickly returning to the homeostatic level as the SERCA and PMCA remove calcium to the ER and extracellular source. Initially, the cytosolic calcium concentration falls to a value lower than before stimulation before increasing to the homeostatic level because of a combined effect of refilling the ER, and removal of calcium from the cell by PMCA. The cytosol homeostatic concentration eventually returns as the ER leak flux balances with the SERCA influx, together with influx from the SOC into the cytosol.

The mitochondria buffer cytosolic calcium (Ca_i), which increases Ca_m to a concentration of approximately 0.69 μM from a starting concentration of approximately 0.03 μM , before slowly decaying, and this is a consequence of the lowered calcium flux rates we introduced earlier. An increase in mitochondrial calcium results in an increased production of NADH (not shown) and hyperpolarisation of the mitochondrial membrane (Psim). Hyperpolarisation of Psim increases production of mitochondrial ATP (ATP_m) from mitochondrial ADP, and this is transported to the cytosol to replenish the ATP that has been consumed by intracellular processes. The initial consumption of cytosolic ATP can be seen in the combined ADP and ATP plot, which is eventually overcome by mitochondrial ATP production, before production slows and the ATP concentration begins to return again to a steady state.

6.1. THE EFFECTS OF STIMULATION BY IP3 ON THE COUPLED ODE MODEL

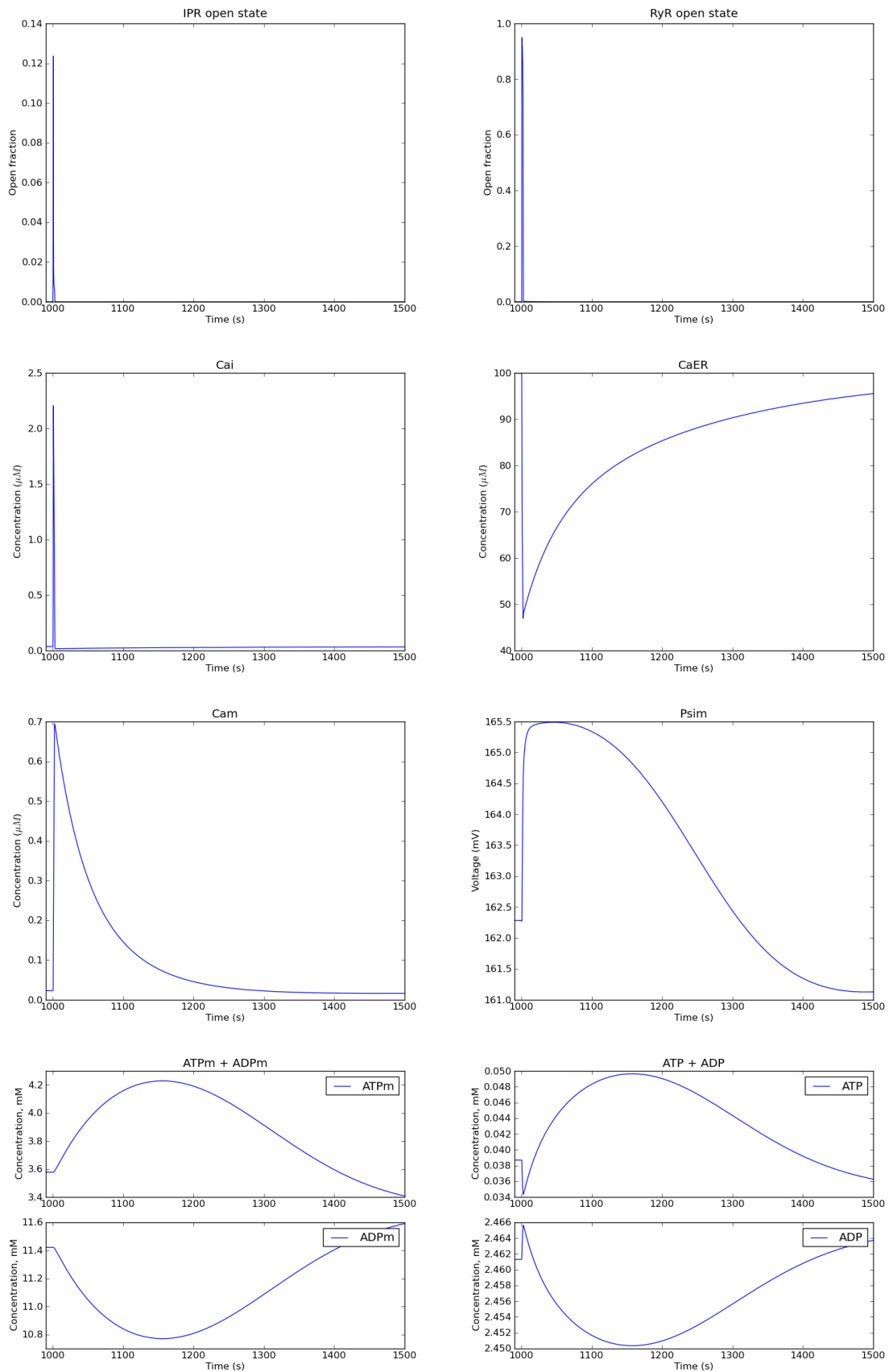


Figure 6.1: Collection of plots showing the effect on several degrees of freedom that occur when the combined model is left to reach a steady state for 1000 seconds, before exposure to an concentration $30 \mu\text{M}$ IP3 with a 1.25 s^{-1} second decay constant.

The stimulation protocol used here to model IP3 concentration decay over time is representative of experimental methods where IP3 is initially bound to molecules, and subsequently released by flash photolysis to produce a single oscillation. Under normal conditions the pancreatic acinar cell produces oscillations that result from a variety of signalling events. Regularly occurring oscillations can be simulated by the Markovian IPR channel model, as a consequence of the complex channel kinetics, by holding the concentration of IP3 at a fixed value throughout the simulation.

6.1.2 Constant concentration of IP3 in the cell

The system was exposed to IP3 at a lower, but fixed, concentration of $3 \mu\text{M}$, and the resulting oscillations were allowed to reach a steady state for 1000 seconds before producing the plots in Figure 6.2. The IPR channel is temporarily opened through IP3 stimulation, releasing calcium from the ER into the cytosolic pool. Elevation of calcium in the cytosol results in CICR of the RyR channels, and further increases in cytosolic calcium. Before the system can return to homeostatic levels, as was possible before with using the decaying IP3 concentration, the IPR channel kinetics result in another calcium transient approximately 75 s later. The ER cannot refill within this time, and as a result the concentration of this compartment oscillates between 60 and $40 \mu\text{M}$ during stimulation.

When the concentration of IP3 was raised at $t = 1000$ s before reducing over time, as shown previously, the cytosol experienced a calcium transient of approximately $2.25 \mu\text{M}$, due to the ER calcium concentration being close to $100 \mu\text{M}$. The lowered ER calcium concentration of $60 \mu\text{M}$ at the time of IPR activation during the steady state oscillations when IP3 is held fixed results in lower cytosolic calcium transients of approximately $1.2 \mu\text{M}$. Exposure to higher levels of fixed IP3 concentration cause oscillations of increased frequency, and as a result the ER has less time between transients to recover released calcium. Lowered ER calcium concentration at the time of IPR and RyR activation results in lowered cytosolic calcium transients due to Fick's laws, as the concentration gradient between the ER and cytosol is lowered.

The smaller cytosolic calcium transients due to fixed IP3 concentrations in Figure 6.2 result in smaller and more rapid mitochondrial calcium oscillations. These small calcium concentration transients cause a small and rapid change in the mitochondrial membrane potential, which drives the ATP production. The change in ATP consumption and production when IP3 is held fixed is smaller than the previous example where IP3 was only raised once, and this is due to the cytosolic ATP hydrolysis flux, which converts more ATP to ADP when the calcium concentration is higher.

After observing behaviour of the model under physiological stimulatory conditions^[70], it is possible to compare behaviour of the model in a hypothetically diseased state. The coupled acinar cell and mitochondria ODE model behaviour is next exposed to BA, as an example of the processes that occur during the onset of acute pancreatitis.

6.2 Onset of acute pancreatitis induced by BA or FAEE-like molecules

At the onset of acute pancreatitis, a chain of events is initiated that results in activation of the digestive enzymes inside ZGs by trypsin, which cause autodigestion of the cell and apoptosis. The specific cause of trypsin activation is unknown, but involves stimulation of RyR, IPR, and SOC by BA or FAEE molecules over the time course of 15-20 minutes. Gallstones that form in the gall bladder and move into the pancreas can cause reflux of BA that reaches the acinar cells, and moderate to heavy ethanol consumption can result in the production of FAEE^[61]. Stimulation of RyR, IPR and SOC is coupled with inhibition of PMCA and SERCA, which results in sustained cytosolic calcium concentration and is accompanied by almost complete emptying of the ER^[64,73]. Sustained calcium elevation in the cytosol results in mitochondrial accumulation and the formation of MPTP that hinders ATP production and initiates the apoptotic chain^[76]. Both BA and FAEE are referred to as 'BA'

CHAPTER 6. RESULTS AND DISCUSSION I: ODE MODEL OF THE COUPLED ACINAR CELL AND THE MITOCHONDRIA

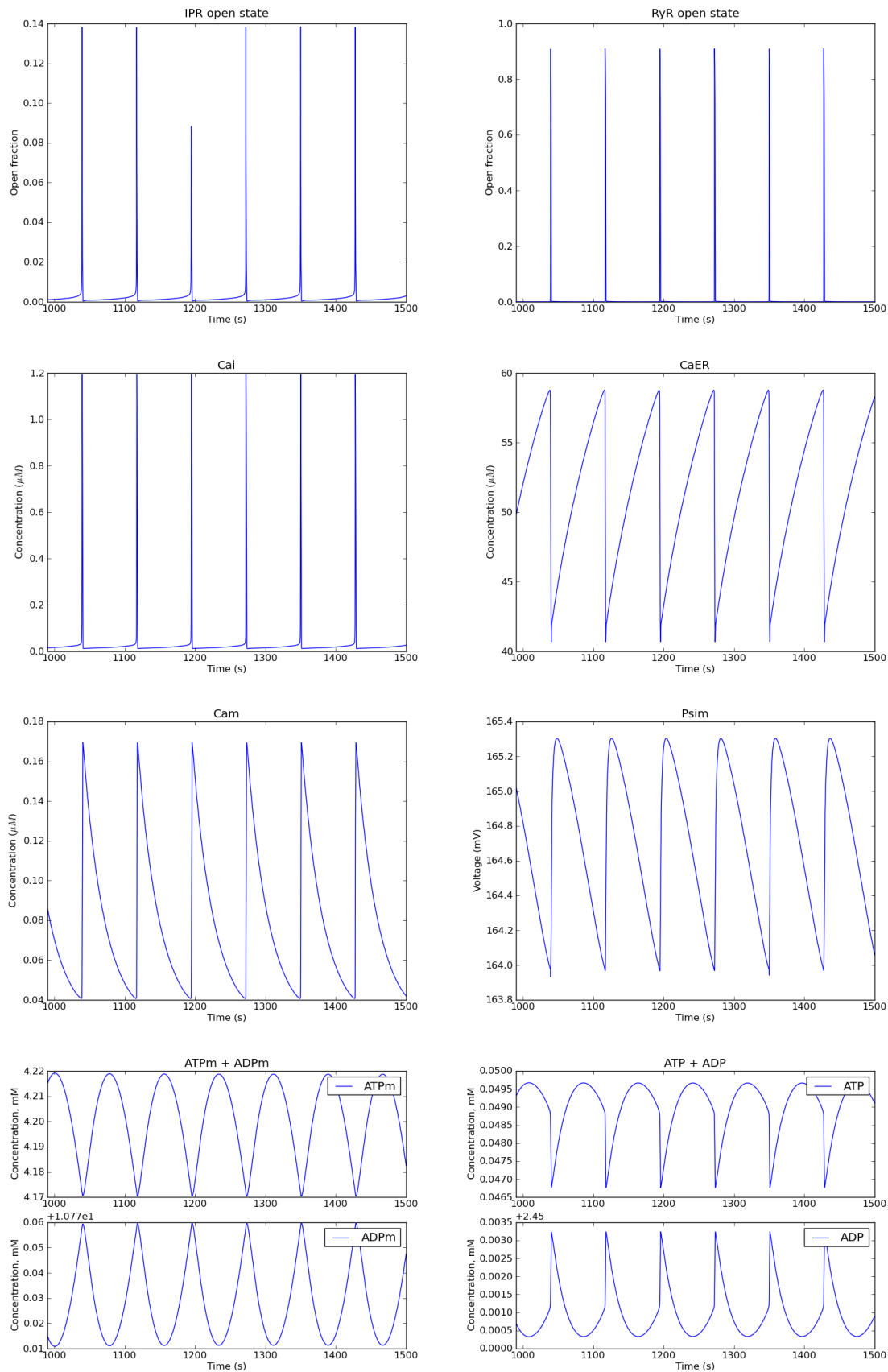


Figure 6.2: Collection of plots showing the effect on several degrees of freedom that occur when the combined model is exposed to a constant $3 \mu\text{M}$ IP3.

in the following results, as the same mechanism was assumed to be true for both molecules.

The plots in Figure 6.3 show the model exposed to a rising concentration of BA up to 25 μM between 900 and 1000 s, and held at 25 μM for the remaining simulation time. The simulation time prior to 900 s was to allow attainment of a steady state. The effects of BA on the system is that the RyRs remain at a semi-open state, similar to the IPR (although the open fraction for IPR is smaller). The multiple spikes between $t = 900\text{-}1000$ s present in the RyR and IPR open state plots are caused by the Markovian model adjustments detailed in Sections 4.2.2 and 4.2.2, which has disrupted the channel kinetics. This unintended feature of the channel kinetics, coupled with the common pool formulation of this model, means that such rapid spikes have an immediate effect on the cytosol and ER as the concentration of BA increases. However, these spikes settle once BA is held constant.

This results in ER calcium depletion that eventually reaches a steady state with the calcium concentration of the rest of the cell. This is due to the nature of the diffusive fluxes through the open channels, soon after exposure to BA. The SOC is also stimulated by BA to cause an influx of calcium into the cytosol, combined with influx from the ER. As PMCA and SERCA are inhibited, the ER cannot refill and the cytosol cannot lose calcium to the extracellular space. A rising intracellular calcium concentration results, that is buffered by the mitochondria. The mitochondrial calcium concentration continually increases, but this appears to have little effect on the mitochondrial membrane potential, and the concentration of ATP is shown to slowly increase over time. The concentration of ATP in the cytosol is not greatly different to the model during normal operation through IP₃ stimulus, which was not expected. The cytosolic calcium concentration experienced during BA activation rises to approximately 0.1 μM . Without inclusion of a model for ATP consumption by PMCA and SERCA in this implementation, the effect of this elevated calcium concentration on ATP supply and demand cannot be commented on directly. A concentration of 0.1 μM is within the range that SERCA and PMCA are exposed

to in other cell type models as the homeostatic level, such as in the cardiac cell^[24]. Therefore SERCA and PMCA should theoretically be supplied with enough ATP to cope with 0.1 μM calcium in the cytosol by default. Therefore, the model suggests that another mechanism contributing to ATP depletion must be the dominating factor. From what can be observed in the results from this implementation, is that the mitochondria must ultimately fail due to calcium accumulation.

Exposure of the cell to BA inhibits the SERCA and PMCA pumps, and stimulates IPR, RyR, and SOC channels. This results in a gradually increasing intracellular concentration of calcium that is buffered by the mitochondria. As the mitochondrial calcium concentration increases due to interaction with cytosolic calcium dynamics resulting from BA exposure, the mitochondria gradually increase their internal calcium concentration over time. Although this does not seem to have an effect on the mitochondrial membrane potential, which was expected to reduce ATP production, the accumulation of mitochondrial calcium is still of interest. The observation that mitochondria in pancreatic acinar cells in cases of acute pancreatitis have a depolarised membrane potential is possibly due to opening of MPTP, which is caused by high levels of calcium inside the mitochondria. The mitochondrial membrane is usually highly regulated, but upon formation and opening of MPTP, this membrane permeability increases, and depolarises the mitochondria^[44]. As the mitochondrial calcium concentration in this model continually increases during BA exposure, it could be assumed that this would ultimately lead to formation of MPTP, and other characteristics found in cells with acute pancreatitis that include reduction in the rate of ATP production, as a consequence.

Therefore, the main cause of ATP reduction in pancreatitis is likely not elevated calcium levels that result in increased ATP consumption, but the inability of the cell to produce ATP from ADP due to a compromised mitochondrial membrane potential^[75]. The mitochondria model used in this combined model cannot show MPTP formation, nor does it show mitochondrial membrane changes consistent with experimental observation as a result, but it does show increased calcium concentration

6.2. ONSET OF ACUTE PANCREATITIS INDUCED BY BA OR FAE-LIKE MOLECULES

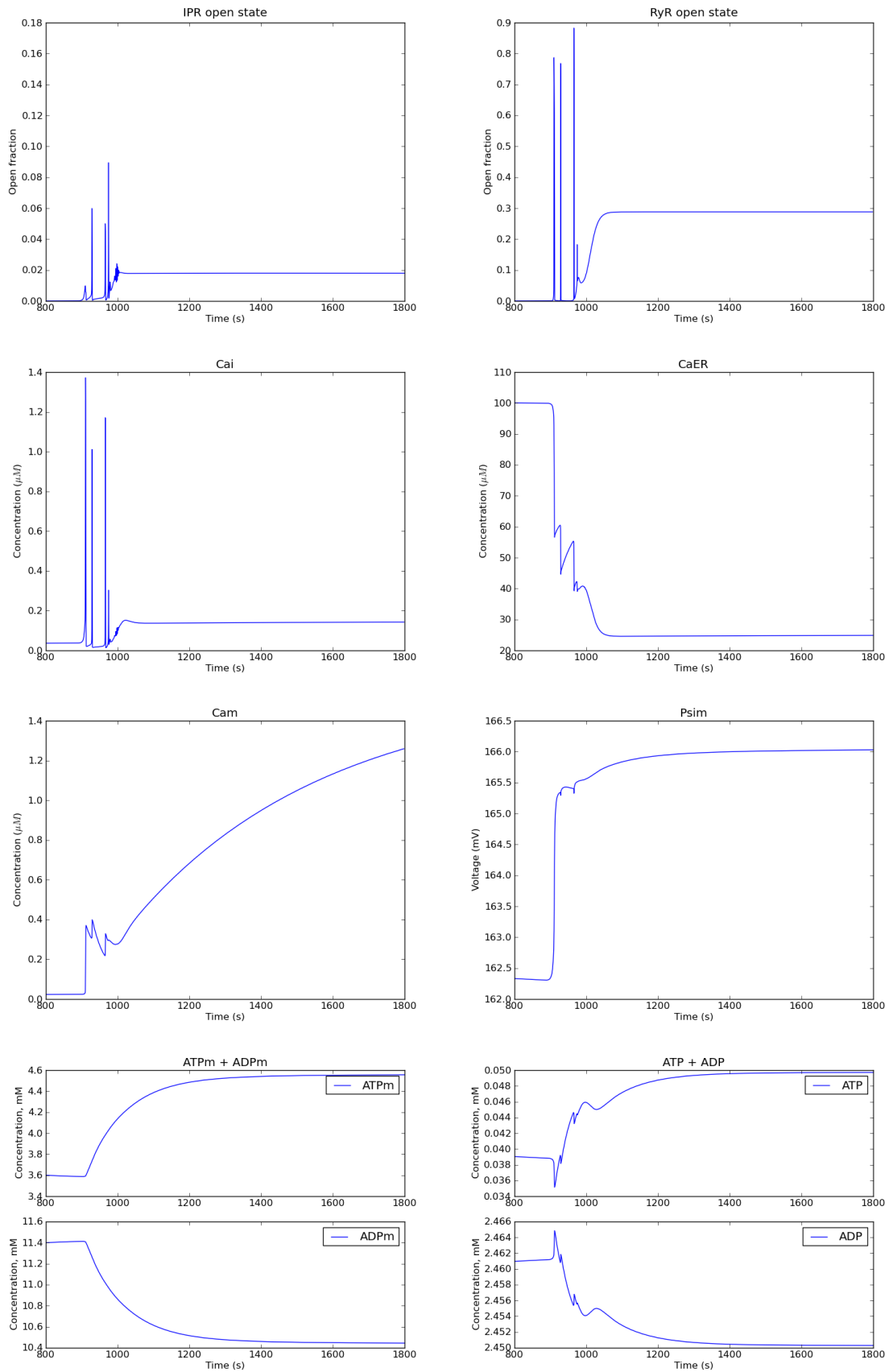


Figure 6.3: Collection of plots showing the effect on several degrees of freedom that occur when the combined model is exposed to a concentration of BA increasing from 0-25 μM BA between 900-1000 s. After 1000 s, BA is held constant. BA modulation of SERCA and PMCA is included, along with modified RyR and IPR models, and SOC, that are activated by BA.

during BA exposure. The constant accumulation of mitochondrial calcium would result in formation of MPTP, and this is likely to contribute to pancreatitis^[43,44,75]. In addition, opening of MPTP releases further calcium from the mitochondria into the cytosol, contributing to the toxic effect of increased calcium concentration. However, this conclusion can only be arrived at if the adjustments made to mitochondrial dynamics detailed previously are assumed correct.

6.3 Summary

This chapter analysed the trends shown by the ODE model when the pancreatic acinar cell coupled to a more detailed representation of the mitochondria than the original representation by Sneyd et al., is stimulated by either a temporary or fixed concentration of IP₃, or exposed to BA.

The results for stimulation by IP₃ show expected interaction between the acinar cell and the mitochondria for the most part. The results for exposure to BA were not entirely as expected however, and suggest that the main contribution to ATP depletion and calcium increase in the acinar cell is due to formation of MPTP after mitochondrial calcium accumulation, rather than increased ATP consumption by SERCA and PMCA.

These simulations use the common pool approach to modelling the pancreatic acinar cell. As a result, it is likely there is a lot of detail encoded into the plots previously shown that can be extracted from the equations, if the model is treated as multidimensional. Sneyd et al. already performed these kind of simulations through construction of the spatially compartmentalised model, and even a FEM implementation of a triplet of coupled acinar cells^[28,79]. However, each spatially resolved compartment into which the cell was divided is treated as a common pool, and still controlled purely by rate equations, rather than a true spatial representation of channels, pumps and mitochondria. Additionally, the mitochondria in these examples were very basic and only consisted of a calcium flux equation. Next, we

shall examine results obtained through extension of the coupled acinar cell and mitochondria ODE model into a multiscale model with spatial resolution.

Chapter 7

Results and Discussion II: FEM model of the coupled acinar cell and the mitochondria

The pancreatic acinar cell FEM model was allowed to reach a steady state, as detailed in Section 5.1.5. The final values to each degree of freedom in the model after this steady state were used as initial conditions to all of the following FEM simulations (excluding those where the mitochondrial distribution was changed, for which a new steady state had to be found).

Each set of results ran for 30 seconds of simulation time, as this was sufficient to observe the change in calcium dynamics in response to stimulation by IP₃, and allows the major cellular processes to return to homeostatic levels. The mitochondrial degrees of freedom are observed to change in response to their surroundings during this time, and the majority of these agents return to an approximate steady state at the end of the simulation. The duration of 30 s provides a balance between obtaining sufficient information to form conclusions, and the time it takes to complete simulations; a 30 second simulation with 10 μ M IP₃ takes approximately 14.5 hours of computation time using a quad-core 2.4 GHz processor (with code restart for performance gain with DOLFIN). Simulations were carried out for a range of initial

IP3 concentrations that decayed with a time constant of 1.25 s^{-1} , unless otherwise stated.

The apical region was considered to occupy one fifth of the distance between the base and apex of the cell, in the top-right of the rectangular compartment, with the remaining area forming the basal region (as detailed in Section 5.1.1). The points of interest when tracking concentration over time were chosen to be the centre of the apical region ($xy=12.57 \mu\text{m}$, where xy represents the coordinate for both x and y in Figure 5.1), and the centre of the basal region ($xy=5.71 \mu\text{m}$). This is similar to Sneyd et al. (2003)^[28], who stated the point of interest in the apical region to be at ' $x=2 \mu\text{m}$ ', which corresponds to middle of the apical region in their model (where the very apex of their model as $x=0 \mu\text{m}$). However, the measurement for the basal region used in this study is different to Sneyd et al., who state that the basal region was measured at $x=15 \mu\text{m}$. This means that measured calcium waves travel approximately 64% of the defined basal region in their model, but this was judged to be too close to the SOC channels in this FEM implementation, which interfere with the measurement of wave propagation.

Figures 7.4 and 7.9 in the following section show results generated from the spatially compartmentalised model by Sneyd et al., for comparison, and this data was approximated from the published figures. Experimental results determined by Giannucci et al. (2002)^[70] are included in Figure 7.5, also for comparison, and were also obtained from published values.

7.1 The 'natural' model cell

The following simulations of the multiscale FEM pancreatic acinar cell model are considered 'natural'. In other words, these results use the model in a state where all pumps, channels and mitochondria are enabled, while mitochondrial motility is disabled*. The model cell was exposed to a range of initial concentrations of IP3,

*For visual assistance to the observations described in the text, please see the videos contained in the 'Natural cell' subdirectory of the supplementary disk.

which decayed over time to provide comparison to data generated by Sneyd et al. and Giovannucci et al., as well as the data generated by the previously detailed ODE implementation.

7.1.1 Apical and basal calcium responses to stimulation by IP3

Peak time and concentration

The plot at the top of Figure 7.1 shows the concentration and location at which calcium reaches a peak across 50 sampled points, from the very base to the very apex of the pancreatic acinar cell, for an initial IP3 concentration of 3 μM . This concentration of IP3 was raised uniformly throughout the cell, as a single value, and the concentration decayed following Equation 4.7 in Section 4.1.2. The measured peak calcium concentrations in the apical region reach an approximate maximum of 0.85 μM , before declining rapidly as the mitochondrial firewall at $xy=11.2 \mu\text{m}$ is neared. Moving through the basal region, away from the mitochondrial firewall, the decline in peak calcium concentration is less dramatic. The times at which these peaks occur is shown in the plot at the bottom of Figure 7.1, and shows that points sampled in the apical region all reach a peak calcium concentration at approximately the same time, despite the range of concentrations observed in the plot above. Between the mitochondrial firewall at $xy=11.2 \mu\text{m}$, and the greatest time to peak in the basal region at $xy=4 \mu\text{m}$, there is an approximate 1 s delay in the time to peak. Further away from the apical region than $xy=4 \mu\text{m}$, the time to peak tails off, as samples are recorded nearer to SOC along the basal cell boundary. This suggests that the influx of calcium by SOC, at low concentrations of IP3, are the main cause of peak calcium concentration in this part of the basal region. Additionally, this suggests that there is very little calcium wave propagation mediated by CICR of RyR channels, hence the low peak concentration in the basal region compared to the apical region, and that the mechanism of this wave is mainly diffusion based. This is most likely due to the mitochondria confining the majority of calcium released to the apical region, such that RyR activation in the basal region is minimal. The involvement of the

mitochondria and RyR channels is discussed later.

The diffusion coefficient for calcium in this model ($D = 10 \mu\text{m}^2\text{s}^{-1}$) can be used to determine if the time difference to peak concentration is roughly equal to that expected by diffusion alone. The distance between the mitochondrial firewall at $xy=11.2 \mu\text{m}$ and the location of maximum time to peak in the basal region at $xy=4 \mu\text{m}$, is $7.2 \mu\text{m}$. This means that calcium needs approximately 2.6 s to travel this distance, based on Equation 7.1. Returning to the plot at the bottom of Figure 7.1, the time delay between a peak at $xy=11.2 \mu\text{m}$ and one at $xy=4 \mu\text{m}$ is faster, at approximately 1 s, which supports mechanisms other than diffusion contributing to these dynamics.

$$\frac{x^2}{2D} \approx t \quad (7.1)$$

Stimulating the same system with a higher concentration of IP3 results in a similar profile of calcium peaks throughout the cell, where each is larger in magnitude. The plots in Figure 7.2 show that the highest peak concentration observed in the apical region is approximately $1.5 \mu\text{M}$, when stimulated with $30 \mu\text{M}$ IP3, and that the time taken to reach this peak is slightly shorter than when stimulated with $3 \mu\text{M}$ IP3. The higher IP3 concentration of $30 \mu\text{M}$ also results in a slightly altered time to peak profile in the basal region, where the delay continues with distance from the apical region, all the way to the base of the cell at $xy=0 \mu\text{m}$ instead of halting at around $4.5 \mu\text{m}$. The time taken to reach peak calcium concentration between the mitochondrial firewall and the base of the cell is approximately 2 s, whereas if this peak resulted from a purely diffusion based mechanism, calcium would require 6.3 s to reach the base of the cell after passing the mitochondrial firewall.

While these two examples of IP3 stimulus suggest a relatively fast travelling wave of calcium moving across the cell, the increase in concentration in the basal region is small in comparison to the apical region. This does not support the expectation and theory that apical calcium release events breach the mitochondrial firewall at higher IP3 concentrations, resulting in sequential activation of RyRs via

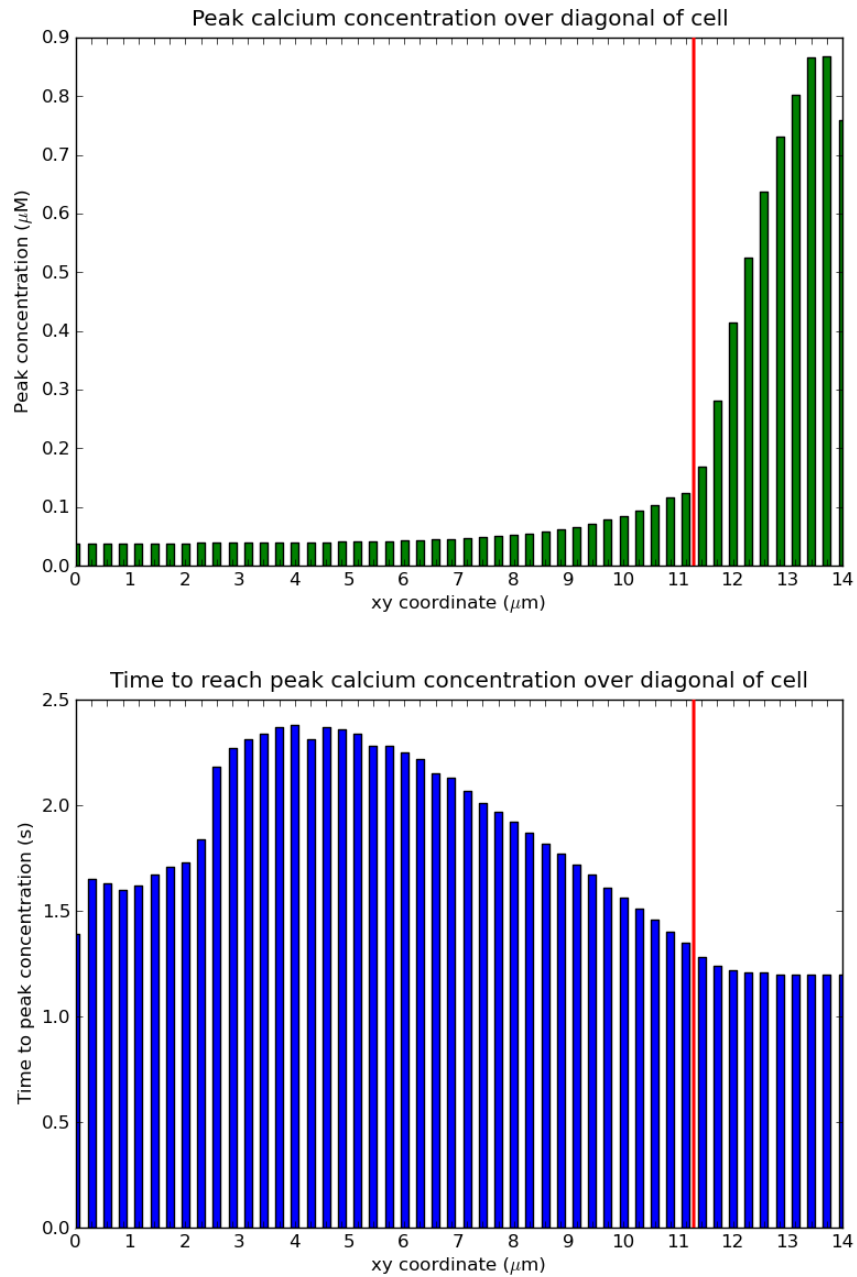


Figure 7.1: Plots showing calcium peak data in response to $3 \mu\text{M}$ IP3. The values on the x-axis correspond to the coordinates for x and y between the very base (0.0,0.0) and apex (14.0,14.0) of the 2D cell representation. The apical boundary, represented by the red line, is at $xy=11.2 \mu\text{m}$, and also corresponds to the location of the mitochondrial firewall. At $xy=11.2 \mu\text{m}$, it can be seen that the peak concentration declines in the apical region as it is neared (top), while the time to peak (bottom) remains constant in the apical region. This suggests that the mitochondria are buffering the majority of apical calcium. The time to peak is shorter at the very base of the cell, than nearer the centre and this likely indicates a peak is reached more due to the local SOC channels than from diffusion from the apical region moving across the cell.

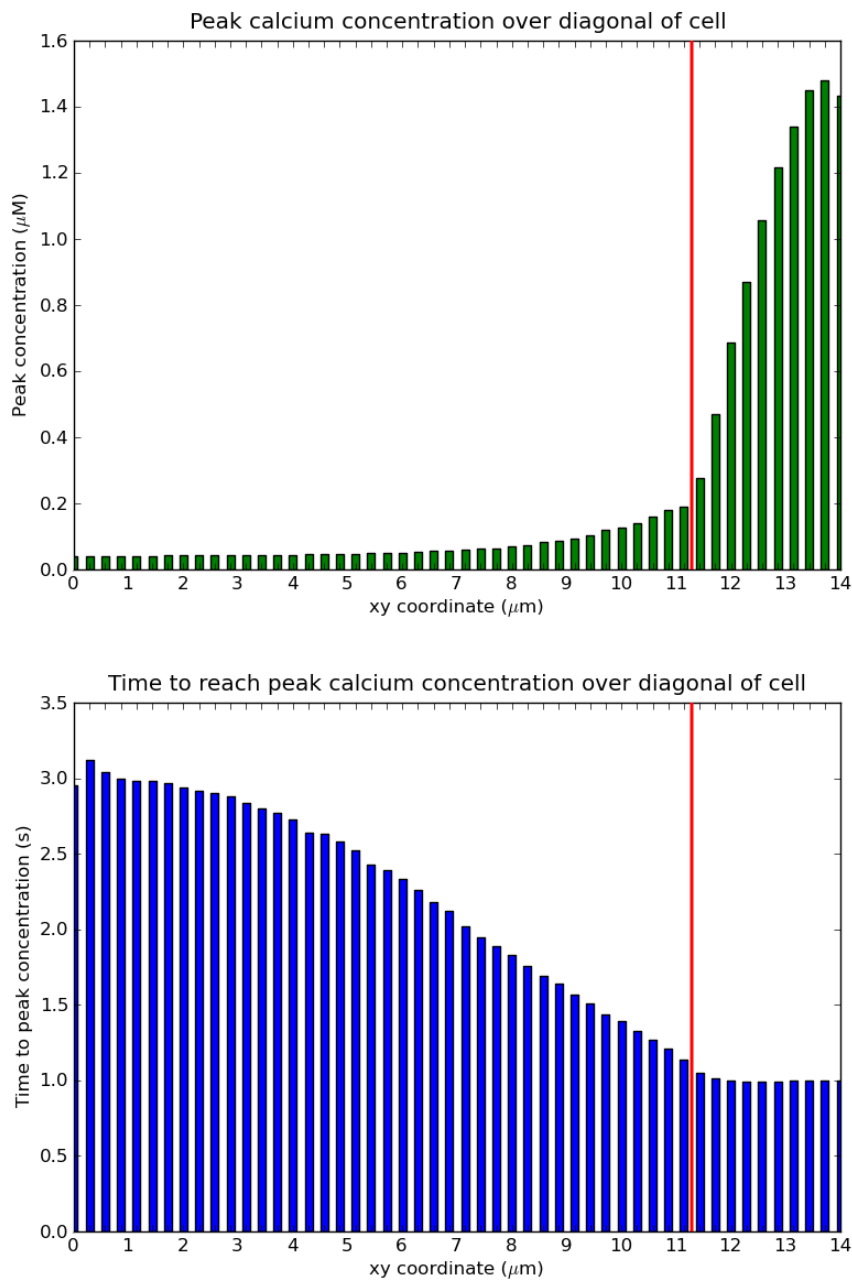


Figure 7.2: Plots showing calcium peak data in response to $30 \mu\text{M}$ IP3. The values on the x-axis correspond to the coordinates for x and y between the base $(0.0,0.0)$ and apex $(14.0,14.0)$ of the cell. The apical boundary, represented by the red line, is at $xy=11.2$.

CICR. Therefore, the most likely mechanism of this travelling wave is IPR activation of the lower channel density of the basal region, coupled with local SOC calcium influx.

The plot at the top of Figure 7.3 shows the apical and basal peak calcium concentration responses for the model when exposed to a range of initial IP3 concentrations. At $1 \mu\text{M}$ IP3 there is little concentration difference between the apical and

basal regions, however, upon increase of IP3 up to 10 μM , the apical region maximum calcium concentration increases rapidly. Between 10 and 100 μM IP3, the increase in apical peak calcium concentration is smaller than shown for IP3 concentrations lower than 10 μM . The time taken to reach a peak calcium concentration in the cytosol at each concentration of IP3 is shown at the bottom of Figure 7.3. It can be seen that the time taken to reach a peak in the apical and basal regions increases rapidly between 1 and 1.5 μM IP3, suggesting a trend that higher concentrations of IP3 stimulate more channels. However, this is not the case and the trend reverses at IP3 concentrations higher than 1.5 μM (if only temporarily for the basal region). After 10 μM IP3, the change is gradual as IP3 is increased further.

The reason behind these small trends exhibited by the model at low IP3 concentrations is not clear, but is possibly due to the particular spatial arrangement of cellular features used in this model. To summarise these observations:

- The peak concentration in the apical region is typically higher than the basal region when the entire cell is stimulated by IP3.
- Apical and basal region peak calcium concentrations become increasingly different as IP3 increases.
- This divergence is less for IP3 concentrations lower than 10 μM .
- The time to peak concentration is lower in the apical region than the basal region.
- The apical time to peak calcium concentration increases while the basal time to peak decreases, as increased concentrations of IP3 are used to stimulate the cell. This is most likely due to the higher density of IPR channels that react to IP3 in the apical region. The density of IPR channels in the basal region is lower, and not large enough to sufficiently stimulate local RyR channels. There is also likely to be an additional effect imparted by the localisation of SOC in the base of the cell.

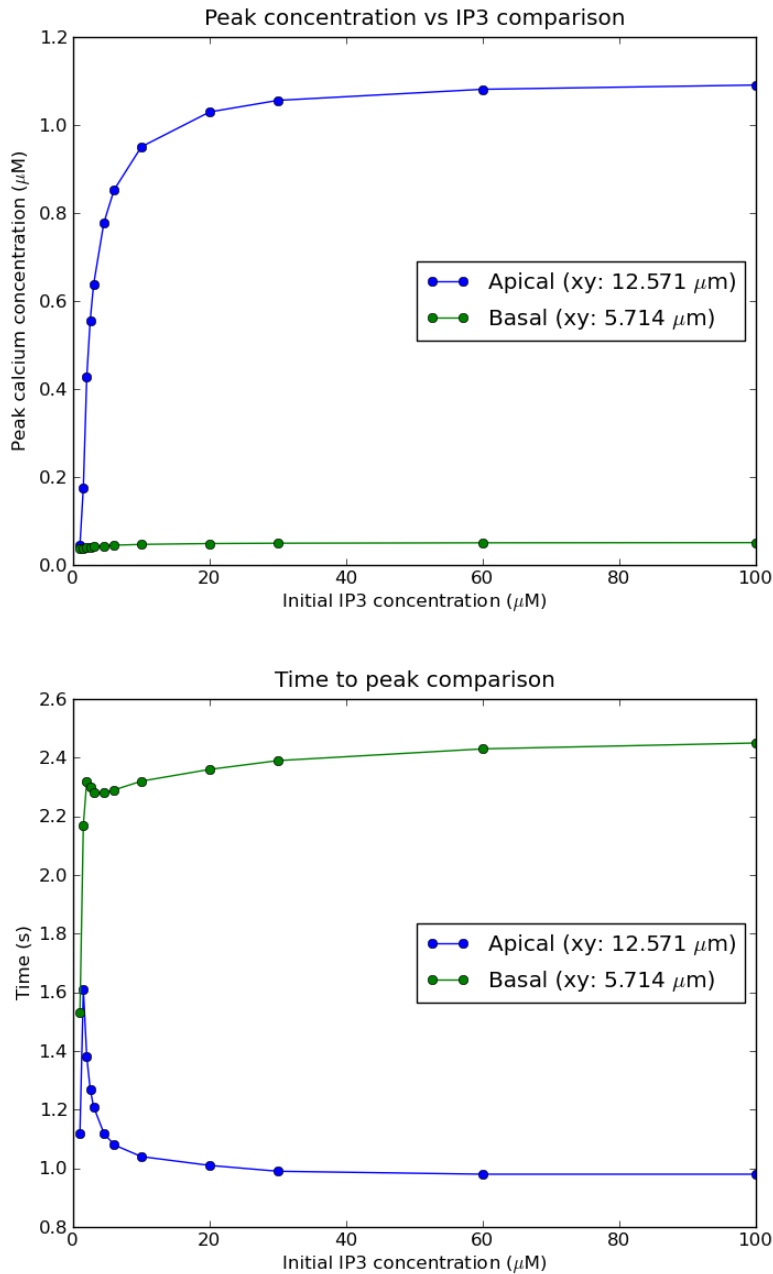
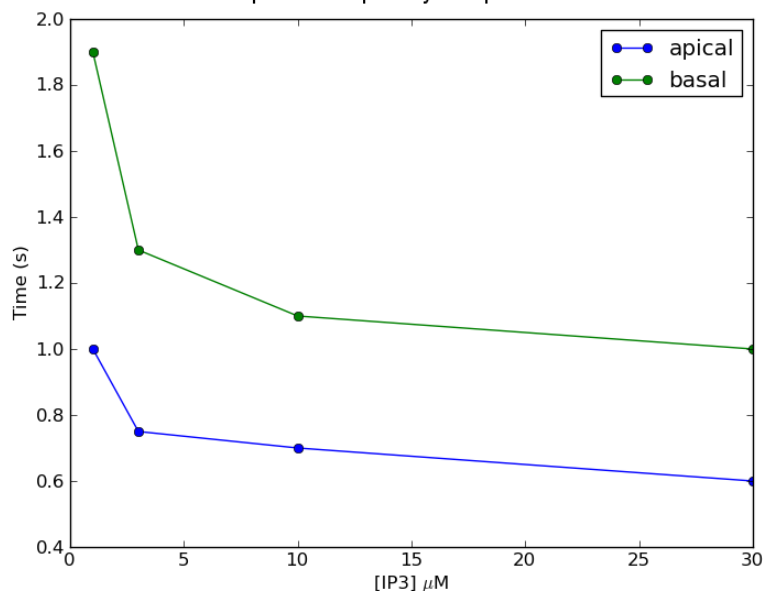


Figure 7.3: Top: Plot showing the corresponding peak calcium concentrations. Bottom: Plot showing the time taken to reach a peak calcium concentration at a position in apical and basal regions of the cell, after exposure to IP3 over the entire cell at a range of concentrations. The range of IP3 concentrations simulated was 1, 1.5, 2, 2.5, 3, 4.5, 6, 10, 20, 30, 60 and 100 μM .

Comparison of the plots produced by this implementation at the bottom of Figure 7.3, and the data produced in the model by Sneyd et al. in Figure 7.4, shows that the models do not agree with regard to the trend of the basal response, although the greater time to peak is in agreement. The trend Sneyd et al. observed both experimentally and in their spatially compartmentalised model is that the time taken to reach peak calcium concentration in the apical and basal regions of the cell decreases with increasing IP3 concentration, and was attributed to the IPR model kinetics. In their spatially compartmentalised model they state that the results indicate apical responses at lower IP3 concentrations are propagated across the basal region through a combination of CICR and diffusion. At higher IP3 concentrations, the apical and basal regions both react quickly to globally raised IP3, and this is faster than diffusion of calcium from the apical region that would activate the basal RyRs. This results in the basal and apical regions acting as independent oscillators during IP3 stimulation.

The absence of this apparent behaviour in the basal region of the FEM model with increasing IP3 suggests that the density of IPR channels could be too diffuse in this implementation to sufficiently stimulate the basal RyRs at higher concentrations of IP3. Although the model results and experimental data published by Sneyd et al. for time to peak calcium does not correlate with this FEM implementation, the methodology and representation of the cell in these two models is very different. However, while there was insufficient data in the article by Sneyd et al. for comparison of peak calcium concentration data, there does appear to be a correlation between the apical concentration peaks produced by the FEM model at the top of Figure 7.3, and the experimental data obtained from Giovannucci et al. in Figure 7.5, where apical peak concentration data was recorded for a range of IP3. This data obtained by Giovannucci et al. also cannot be compared to Sneyd et al. However, Sneyd et al. parameterised their model using data obtained from Giovannucci et al., which suggests that the correlation which can be seen between the plot at the top of Figure 7.3 and Figure 7.5 shows that the model is behaving similarly to how

Sneyd et al. (2002) apical and basal times to peak calcium concentration vs IP3
Data estimated from published spatially compartmentalised model results



Sneyd et al. (2002) apical and basal times to peak calcium concentration vs IP3
Data estimated from published experimental results

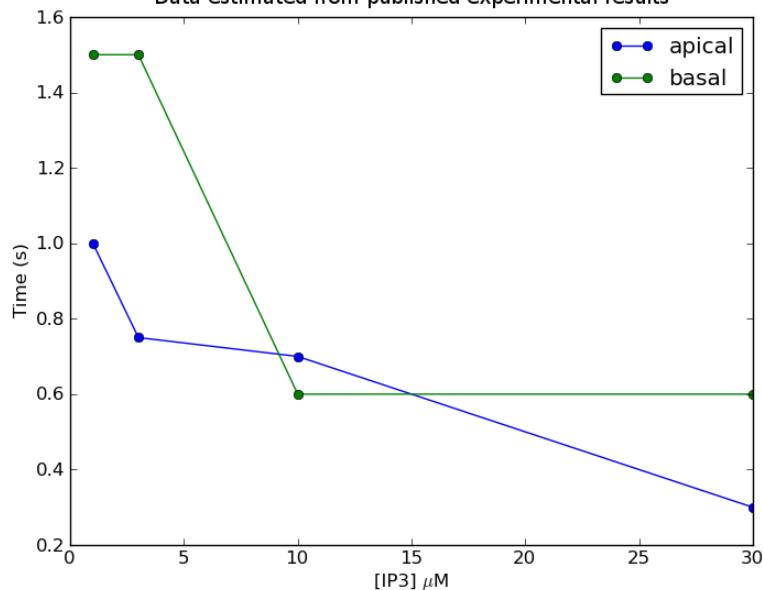


Figure 7.4: Top: Plot showing the approximate time to peak calcium concentration data in the spatially compartmentalised model by Sneyd et al., (estimated data from Sneyd et al. (2002) Figure 4), over a range of IP3 concentrations. Bottom: Plot showing the experimental data used by Sneyd et al. (2002) for parameter fitting (estimated data from Sneyd et al. (2002) Figure 4), over a range of IP3 concentrations^[28].

it should be. While peak concentration magnitudes differ between the multiscale FEM model and experimental data in Figure 7.5, this hints at potential for the FEM model to reproduce experimental results more closely, with better parameterisation of agent density. The most likely requirement is a higher density of channels and pumps in the multiscale model to achieve the greater calcium concentration peaks observed experimentally by Giovannucci et al..

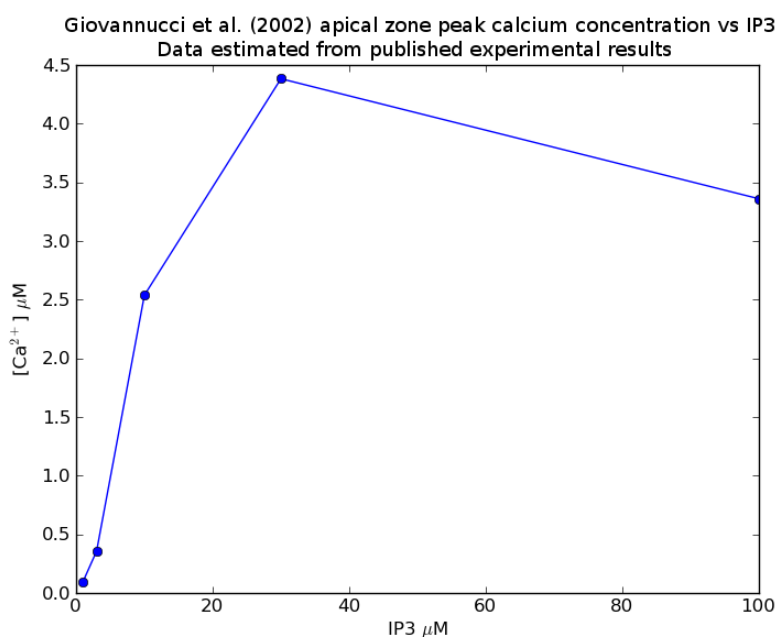


Figure 7.5: Plot showing the apical peak calcium concentration data, obtained from Giovannucci et al. (2002), for a range of IP3 concentrations^[70].

Channel activation and calcium wave speed

The activation of RyRs via CICR in the pancreatic acinar cell has been previously mentioned as a mechanism of wave propagation. So far in these simulations of the 'natural' cell, there has been little CICR and propagation of the wave appears to have been mostly due to diffusion from the apical region. Figure 7.6 shows the average openness of RyR channels in the basal region in response to the magnitude of apical calcium concentration peak, and also in response to IP3 concentration (i.e. mediated by IPR channels).

The strongest relationship is between the peak RyR open fraction and peak apical

calcium concentration (Figure 7.6, top), which suggests that increased apical calcium concentration is the key to initiating a global wave of calcium propagating across the cell via CICR. This is behaviour that was expected of the model. However, the plot at the bottom of Figure 7.6 suggests that such an increase in apical calcium concentration requires a far higher concentration of IP₃ than used experimentally by Sneyd et al., and Giovannucci et al., and was not observed in these results. This hints that the IPR channels are not likely to be activated further than the response they already show, and that the model requires further parameter adjustment before it can better replicate experimental observations. The reason that the model cannot currently elicit a large enough response to IP₃ is likely due to the IPR density being too low. This channel density could be easily increased, but without adjusting all of the other distribution parameters at the same time the result is likely to be model instability.

As there is a lack of significant RyR channel activation across the cell, the mechanism of wave propagation must mainly consist of activated IPR channels in the basal region at the lowered channel density. A complex interaction between IPR, SOC, and a small population of RyRs closest to the apical region, coupled with diffusion, must be the cause the delayed basal calcium concentration peak.

The speed of the diffusing wave is decoupled in Figure 7.7 where we return to the cell being stimulated by 3 and 30 μM IP₃, but instead data is measured at specific coordinates in the apical and basal regions over time. As can be seen in both plots, the apical region reaches a peak calcium concentration that is greater and earlier than the basal region, due to the higher apical IPR channel density. The speed of the travelling wave for the cell stimulated with 3 μM IP₃ is faster than that for 30 μM IP₃. This can be attributed, in part, to IPR activation being lower in response to the 3 μM IP₃ simulation than 30 μM , and therefore it takes less time to reach a peak calcium concentration. When greater IP₃ concentrations stimulate the cell, this causes an increased IPR and SOC response that results in more calcium diffusion around the cell, and activates slightly more RyR channels, which contributes to the

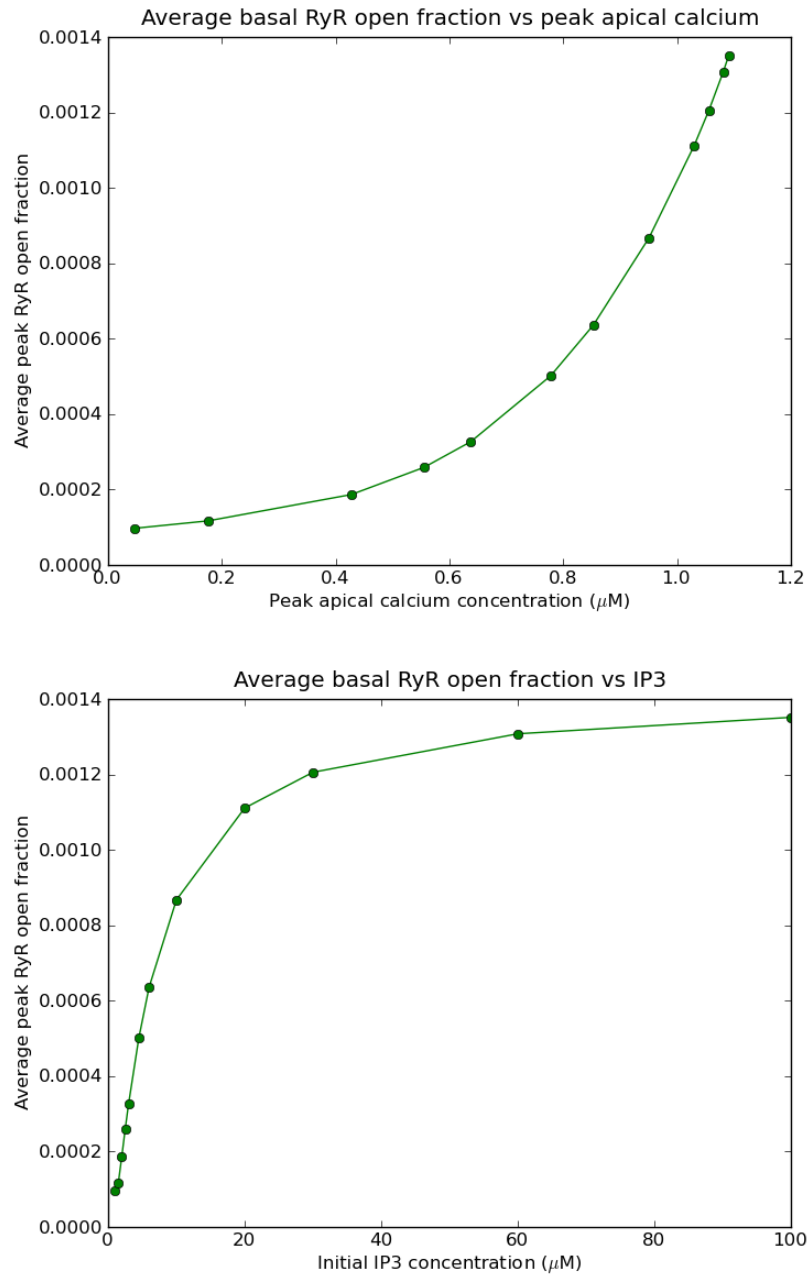


Figure 7.6: Top: Plot showing the average basal RyR channel open fraction in response to a range of peak calcium concentrations measured in the apical region. Bottom: Plot showing the average basal RyR channel open fraction response to IP3 concentration.

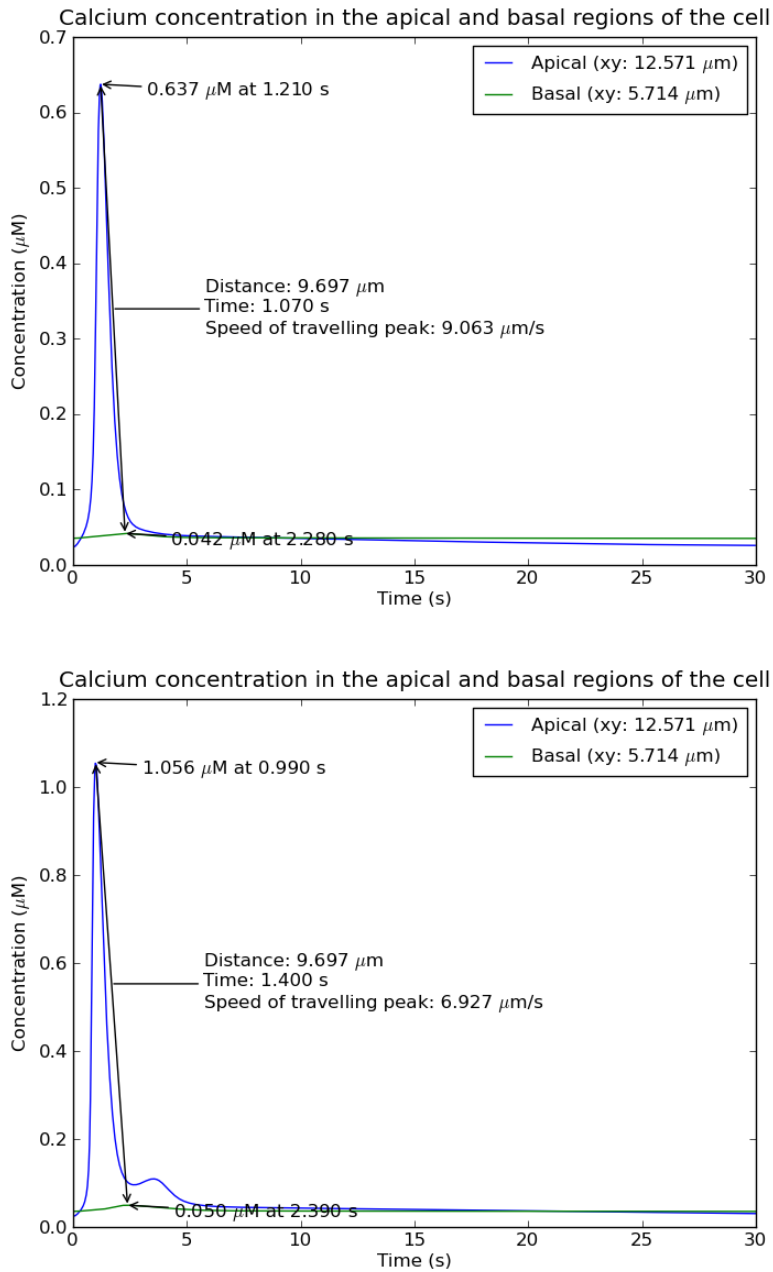


Figure 7.7: Plots to compare the different peak concentrations and rise times, and corresponding wave speeds, in response to two different concentrations of IP3. Top; 3 μM IP3, bottom; 30 μM IP3.

amount of time taken to reach peak calcium concentration.

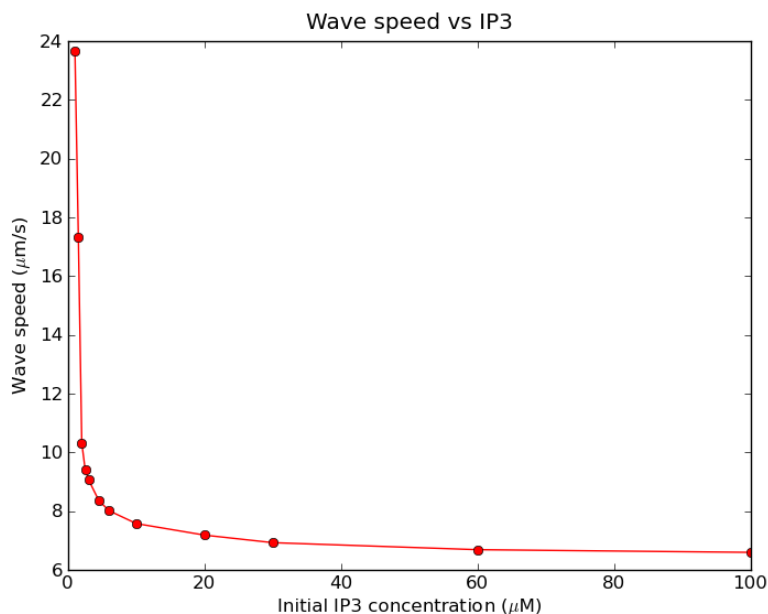


Figure 7.8: Plot showing the speed of the calcium concentration wave in the 'natural' cell, calculated using the difference in time taken to reach a peak in the apical and basal regions (i.e. found in the same way as Figure 7.7). The significant drop off observed at the lower range of IP3 concentrations is largely due to the SOC channels at the base of the cell coupled with basal IPRs mimicking a wave. There is very little effect attributed to CICR in this model while the mitochondria are buffering apical calcium.

The calculated wave speeds found for each initial IP3 concentration in these simulations is shown in Figure 7.8. Wave speed in the model decreases as IP3 concentration increases, but does not change by much past 10 μM IP3. This is likely due to the mitochondrial firewall effect, which has diminished the ability of apical IPRs and RyRs to initiate further CICR (the cellular response to disabled mitochondria is shown in Section 7.2). Basal IPR activation is not sufficient to activate basal RyRs alone, again suggesting that an increased basal IPR density is required to reproduce experimental observations more closely, such as in the data published by Sneyd et al. in Figure 7.9. The results by Sneyd et al. show that wave speed increases with increasing IP3 stimulus, and was attributed to the 'apparent wave' hypothesis, where the apical and basal regions oscillate independently of one another rather than via CICR, at high concentrations of IP3.

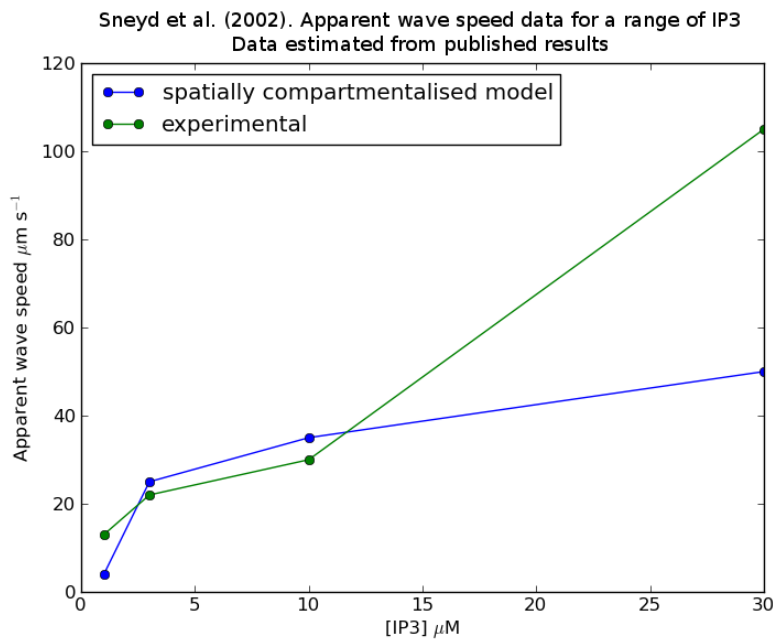


Figure 7.9: Plot showing the apparent wave speeds observed both experimentally and computationally, obtained from Sneyd et al. (2002), for a range of IP3 concentrations (approximate).

7.1.2 Apical and basal mitochondrial responses to stimulation by IP3

Mitochondrial subpopulations in the pancreatic acinar cell are thought to provide a more dedicated ATP supply to regions of higher metabolism, respond to calcium signals for initiation of the apoptotic chain, and shield areas of the cell from harmful calcium elevations. So far in these simulations of the 'natural' cell, we have seen significant reduction of apical calcium concentration peaks close to the mitochondrial firewall (Figures 7.1 and 7.2), and this is in contrast to the results reported by Sneyd et al. who represented the mitochondria as a constant negative calcium flux, and commented that adjusting the rate constant associated with this flux had little effect on results.

The peak internal calcium concentration of the mitochondria, and the effect on the mitochondrial membrane potential in response to IP3 is shown in Figure 7.10. Mitochondria nearer the apical region are exposed to a greater range of calcium concentration magnitudes in response to a relatively narrow range of IP3 concentration

(Figure 7.10, top), which suggests that apical mitochondria experience enhanced communication with cellular processes in this region in comparison to basal mitochondria. The effect on apical mitochondria that buffer this calcium is a resulting change in the mitochondrial membrane potential (Figure 7.10, bottom). The higher channel density of the apical region results in an increased local calcium concentration for the mitochondria, which is taken up by the mitochondrial uniporter flux (J_{uni}), to increase the mitochondrial membrane potential for driving ATP production. This ATP diffuses to the immediate area to provide an enhanced local supply. As elevated calcium concentrations local to the mitochondria diminish, the mitochondria lose calcium via the mitochondrial sodium-calcium exchanger flux (J_{NaCa}).

The apical region of the pancreatic acinar cell is higher in metabolic activity, and so requires a more readily available supply of ATP to power the PMCA and SERCA pumps that ensure calcium homeostasis in-between calcium oscillations, as well as for functions involving the ZGs. Data from the FEM model supports the hypothesis that the reasons for recruitment of mitochondria to the apical boundary are twofold; the mitochondria shield the basal region from the majority of apical calcium transients, and the mitochondria increase ATP production in response to elevated calcium concentrations during signalling events in the apical region. Therefore, production of ATP is not only higher in the apical region due to the high density of mitochondria (Figure 7.11), but also due to the local environment that causes change in the mitochondrial membrane potential. Section 7.2 investigates the effect that removal of this mitochondrial firewall has on cellular dynamics.

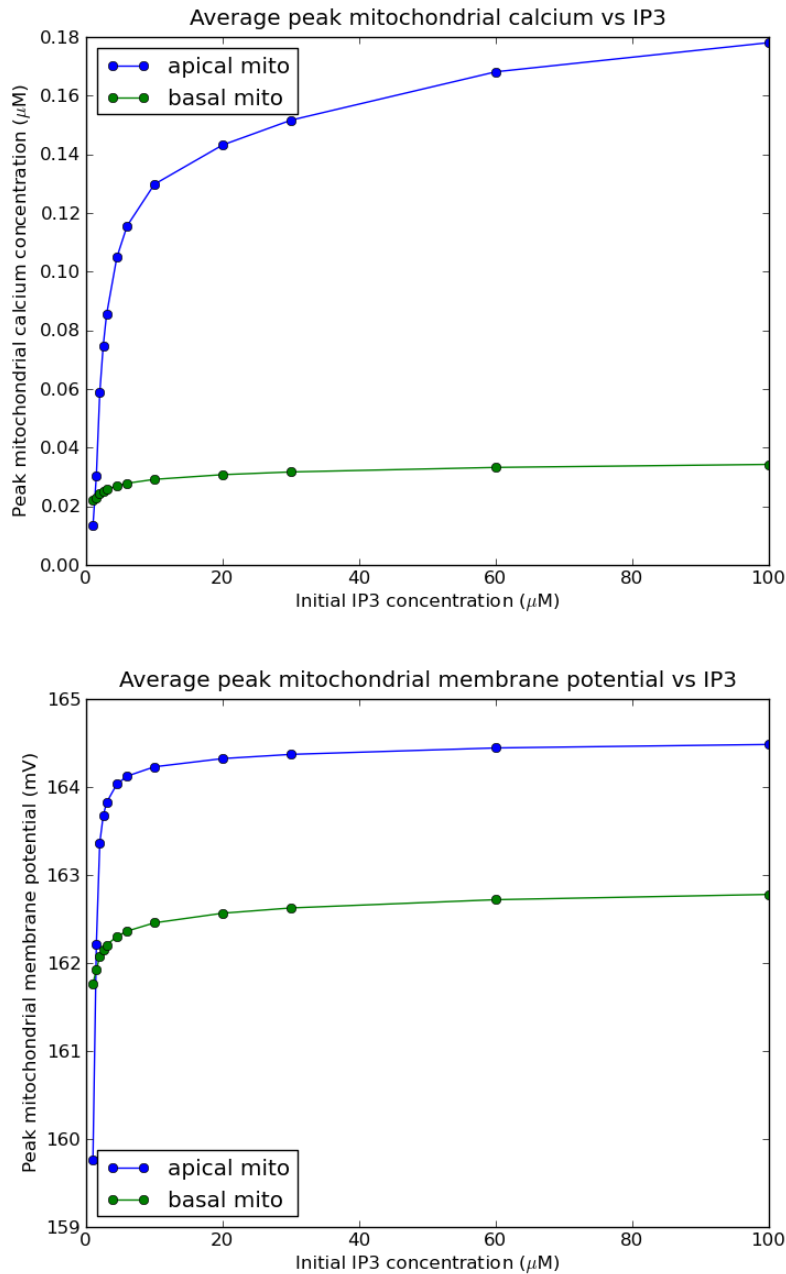


Figure 7.10: Top: Plot showing the average peak mitochondrial calcium concentration for mitochondria in the basal and apical regions, in response to cell stimulation by IP3. Bottom: Plot showing the average peak mitochondrial membrane potential for mitochondria in the basal and apical regions.

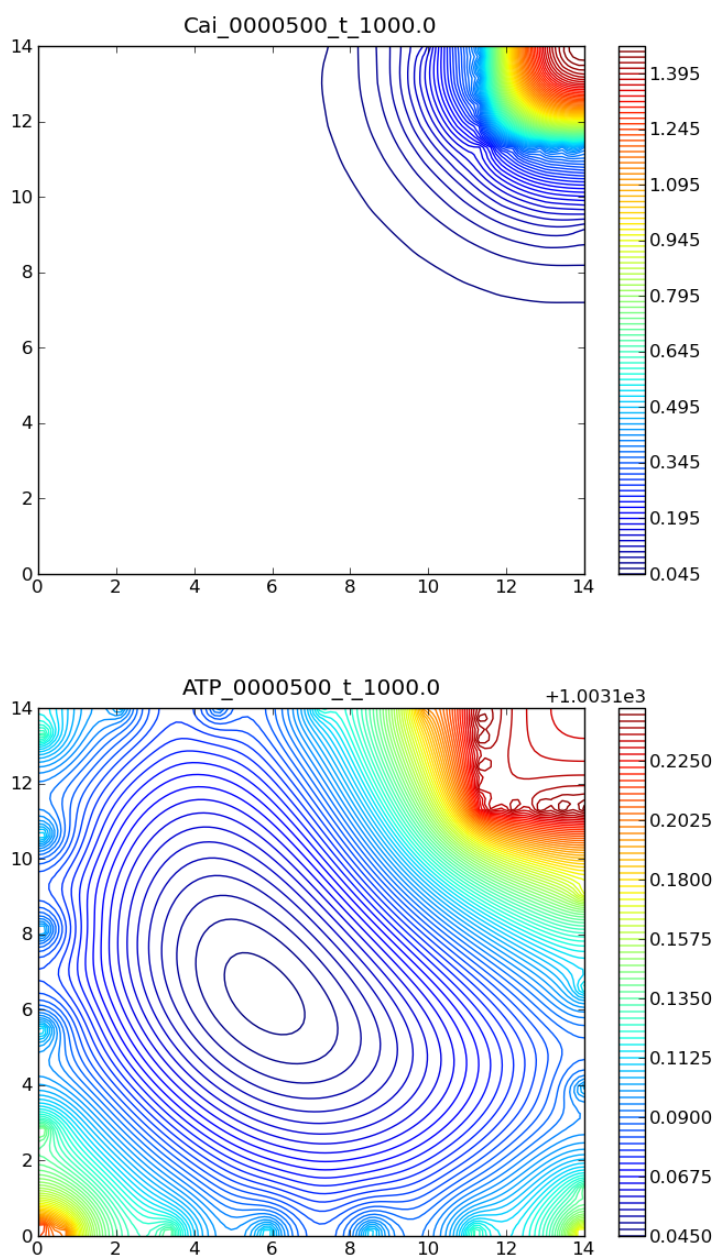


Figure 7.11: Top: Contour plot showing the distribution of Cai in the cytosol near the time of apical peak concentration (step=500, $t=1000$ ms) in a cell stimulated by $30 \mu\text{M}$ IP3 . Bottom: Contour plot showing the distribution of ATP in the cytosol at (step=500, $t=1000$ ms). In both plots, the effect of the mitochondria on the local environment can be clearly seen. Units of vertical information bars are μM .

7.1.3 ER concentration changes

The ER is thought of as a continuous calcium pool that allows repetitive and short calcium transients in the apical region of the pancreatic acinar cell, and does so without major reduction of internal concentration^[71]. Experimental evidence supports the hypothesis of an ER calcium tunnel, where calcium released by the ER in the apical region is replenished by SERCA uptake from local SOCs at the base of the cell^[66,71,72]. This allows transportation of calcium to the apical portion of the ER without elevation of the cytosolic calcium concentration.

Figure 7.12 shows the change in ER calcium over time, and the maximum concentration depletion of the ER over the diagonal of the cell when stimulated by 30 μM IP3. While this is essentially the opposite of peak concentrations reached in the cytosol when stimulated by 30 μM IP3 (Figure 7.2), the ER in this model exhibits behaviour where the internal ER concentration gradient caused by calcium release in the apical region and calcium uptake in the basal region shown is similar to that hypothesised by experimentalists where refilling occurs at the base of the cell^[71,72]. In addition, the plot at the top of Figure 7.12 shows that the ER does not experience a major change in calcium concentration during the calcium transient. The ER loses approximately 10% of concentration at points sampled in the apical region when stimulated, before recovering, which is consistent with the experimental observation that there is no major reduction in ER calcium during stimulation^[71]. This is not reproduced in the model by Sneyd et al., where approximately 60% of calcium in the ER is lost with the common pool formulation during stimulation.

A time evolution of the ER calcium concentration gradient change is shown in Figure 7.13 for the cell stimulated by 30 μM IP3. At $t=0$ ms, the gradient initially points toward the base of the ER, where the SOC channels flow into the corresponding region of the cytosol. At $t=2000$ ms, the influx of calcium from the SOC channels at the base is shown to be taken up by the SERCA pumps in this region, while the concentration gradient in the rest of the ER continues to remain pointed toward the basal region. Calcium in the apical portion of the ER is being removed due to chan-

nel activation, which keeps this gradient. By $t=9300$ ms, the IPR and RyR channels near the apical region have deactivated, and calcium that was released in the apical region of the cytosol is taken up more readily than it is released by the ER, causing the ER concentration gradient to point toward the apex in a wave of gradient change that continues to move until $t=16000$ ms. During this time, the PMCA at the apex of the cytosol is removing calcium to the extracellular source and, as this results in less calcium for uptake by SERCA into the ER, the concentration gradient in the ER points away from the apex. After $t=16000$ ms, the recovery of homeostatic calcium in the cytosol by SERCA and PMCA results in the ER concentration gradient pointing toward the base of the cell, toward the region of SOC channel location. This is due to the SOC being the dominant source of cytosolic calcium influx at this time, and so the ER concentration gradient begins to reset back to pointing toward the base of the cell. After 40000 ms the ER calcium concentration gradient has returned to the initial configuration.

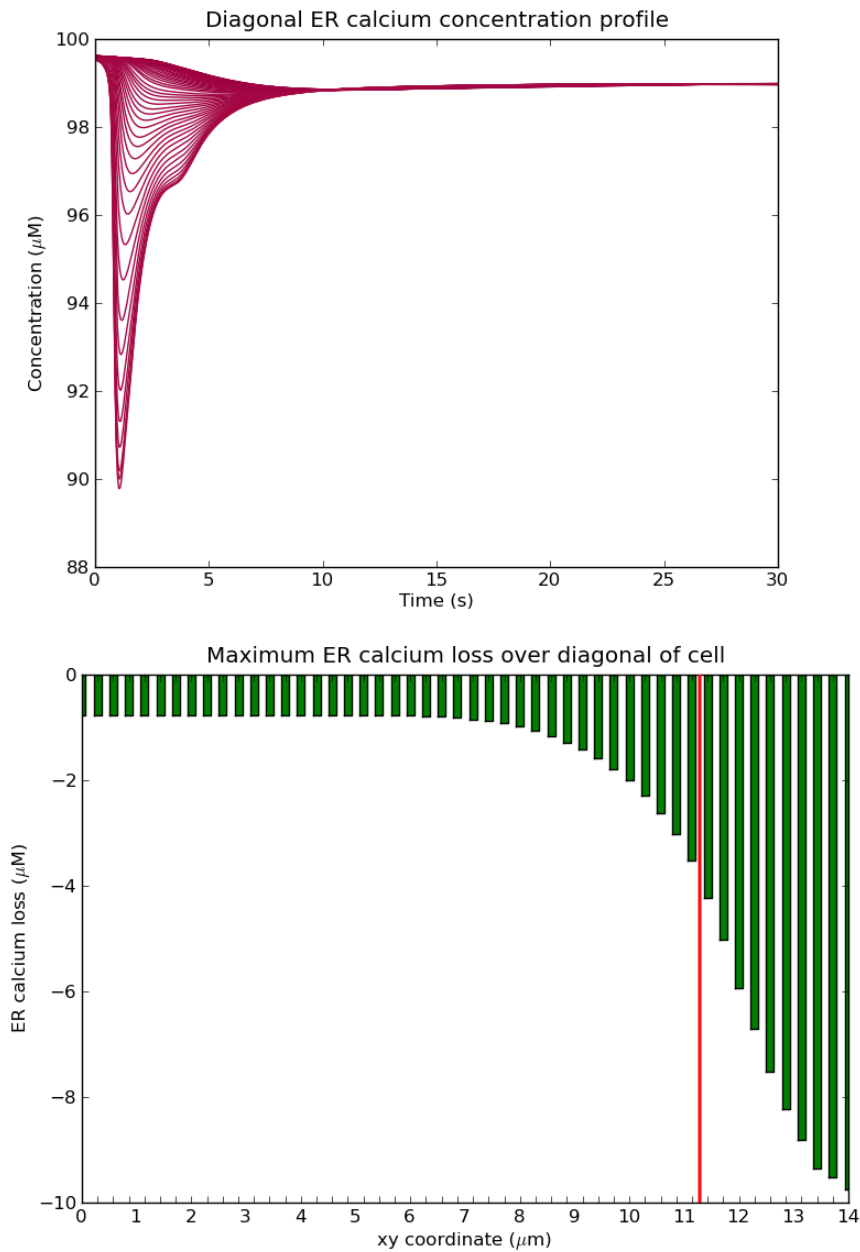


Figure 7.12: Top: Plot showing the change in calcium concentration in the ER compartment for 50 locations across the centre of the cell vs time, from the base to the apex, upon stimulation by 30 μM IP3. Bottom: The same plot as top, but showing the maximum amount of calcium lost by the ER before refilling, against xy coordinates of each sample. The red line at $xy= 11.2 \mu\text{m}$ represents the apical boundary and location of the mitochondrial firewall.

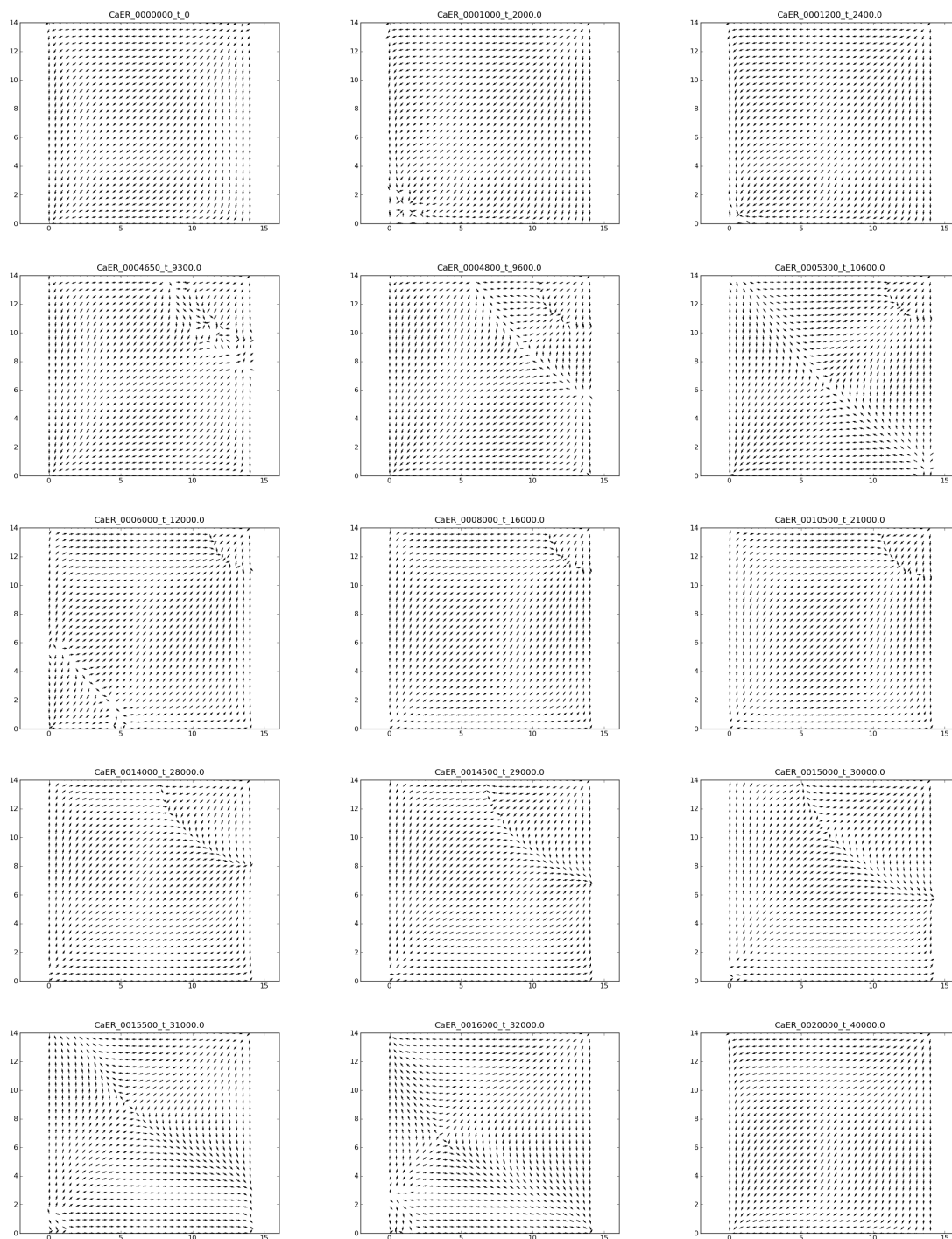


Figure 7.13: Time evolution of a normalised quiver plot for calcium concentration gradient in the ER during stimulation by $30 \mu\text{M}$ IP₃. Please see the video included on the supplementary disk as a visual aid ('Videos/Natural cell/30 uM IP₃/CaER quiver normalised.avi').

7.1.4 Comparison to the ODE implementation

As this FEM implementation was based upon the coupled acinar-mitochondria ODE model, it is of interest to look at data that is directly comparable. Previously, results from the FEM model have shown that the maximum concentration change at a specific location in space is up to approximately $1.5 \mu\text{M}$ in the cytosol and $10 \mu\text{M}$ in the ER, when stimulated with $30 \mu\text{M}$ IP3. In addition to this spatial detail of concentration change, the FEM model allows us to see the bigger picture of calcium dynamics in the form of total concentration change in each layer, which encodes the complex interactions of all processes in the model contributing to concentration change as a single degree of freedom. These total changes to concentration are shown in Figure 7.14, again for the cell stimulated by $30 \mu\text{M}$ IP3. In contrast to the previously quoted values of concentration at specific regions of the cell, these plots show that the peaks as a whole in these compartments are significantly smaller; an approximate peak of $0.05 \mu\text{M}$ calcium in the cytosol and an approximate $0.85 \mu\text{M}$ peak loss in the ER. The maximum loss of calcium from the ER does not match the maximum peak of the cytosol, due to the difference in volume of these two layers.

The calcium concentration changes that result in the corresponding ODE implementation of the coupled acinar-mitochondria model (described in Section 4.2) for the ER and intracellular compartment are shown in Figure 7.15. The ODE model shows that total compartmental changes to concentration in the ER and cytosol are greater than in the FEM model. The total concentration change experienced by the ER in the FEM implementation is very small (Figure 7.14, top) in comparison to the ODE implementation (Figure 7.15, top), however the FEM model is more consistent with the experimental observation that the ER concentration does not experience a major reduction in concentration during a transient, as previously mentioned. The cytosolic calcium concentration in the FEM model (Figure 7.14, bottom) does not experience a total increase of the same magnitude as the ODE version (Figure 7.15, bottom), although plots such as that in Figure 7.7 show localised transients that are almost as large.

Figure 7.16 shows the same stimulus, but using the original implementation of the Sneyd et al. acinar cell model (i.e. without the mitochondria). In this plot it can be seen that the calcium peak in the cytosol is double that of Figure 7.15, which indicates the degree to which the mitochondria are buffering calcium in the version where the mitochondria is coupled in.

Figure 7.17 shows the difference in calcium buffered by the mitochondria in the coupled ODE model and the FEM multiscale model. The mitochondria in the ODE model is controlled by a single set of ODE values, while each mitochondrial agent in the FEM model is separate to enable spatial distribution. As can be seen, the ODE acinar cell model mitochondria experiences a higher internal calcium concentration than each of the FEM model mitochondria. This is due to the increased amount of calcium that flows into the cytosol of the common pool model over a longer time period, compared to the spatially resolved FEM model. However, the calcium that flows into the cytosol in the FEM model is shared between each agent in space, and the agents buffer more calcium in total in the FEM model than the ODE. The spatial distribution of mitochondria can be inferred from the plot at the bottom of Figure 7.17. The highest mitochondrial calcium concentrations shown in the bottom plot correspond to the apical mitochondria, who are providing the mitochondrial fire-wall. Mitochondria in the basal region near to SOCs buffer calcium, but this is less than is buffered by the apical mitochondria. Those mitochondria whose concentration does not change so much are agents that are positioned on the cell membrane away from the apical region and the SOCs. Owing to the common pool methodology and the increased cytosolic calcium of the ODE model (Figure 7.17, top), the mitochondria take longer to return to steady state. The FEM implementation is shorter, owing to the fact that the calcium concentration in the cytosol is smaller, and calcium released by the mitochondria diffuses away.

The reason for the differences previously described is due to the more sophisticated physical representation of the FEM model, which the common pool ODE implementation lacks. The common pool ODE model has no other way to express

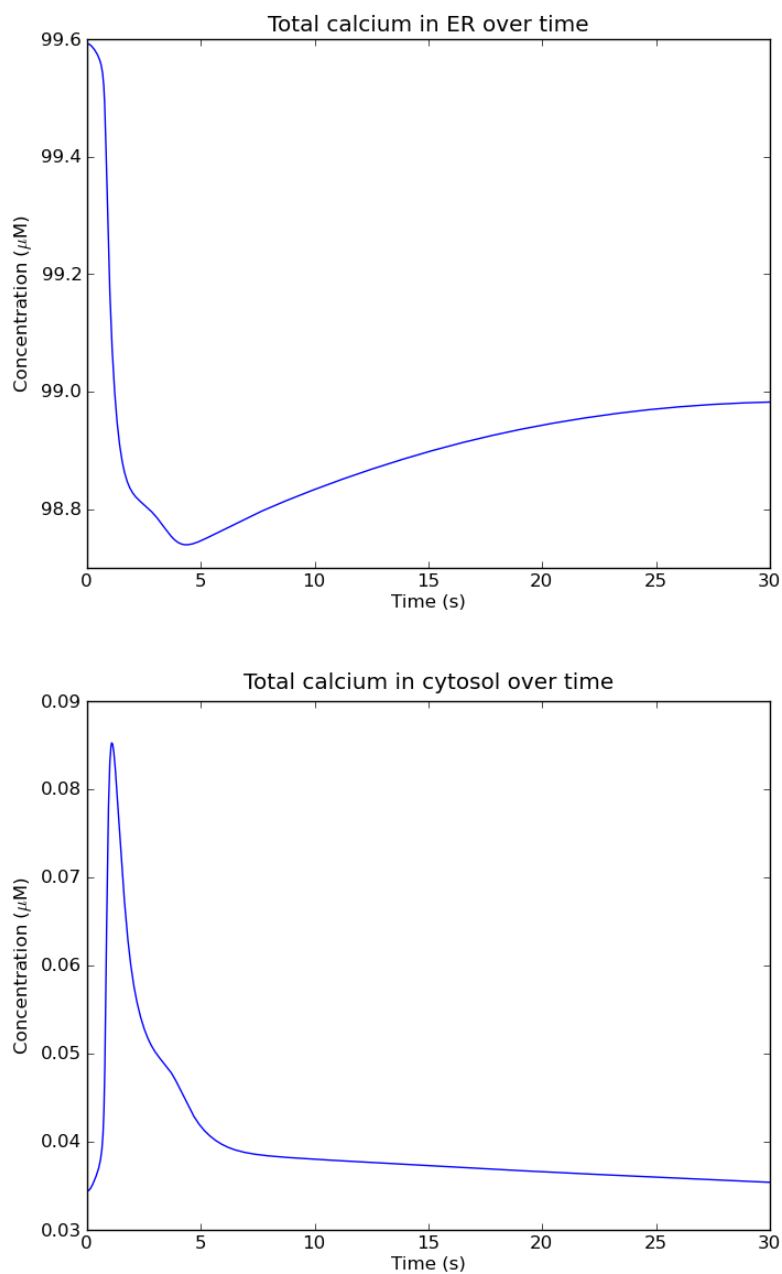


Figure 7.14: Plots showing the total change in calcium in the coupled acinar and mitochondria FEM model when stimulated with $30 \mu\text{M}$ IP3 for 30 s at a decay constant of 1.25 s^{-1} .

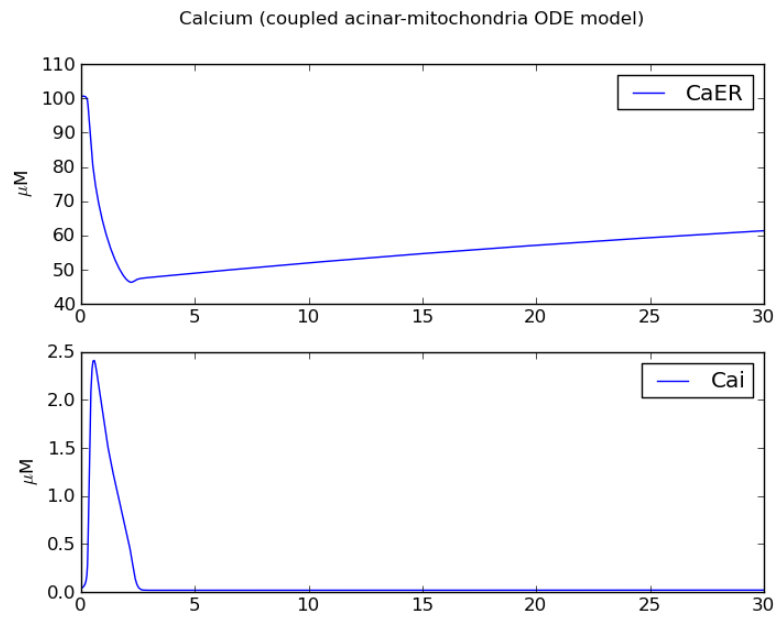


Figure 7.15: Plots showing the change in calcium in the coupled acinar-mitochondria ODE model detailed in Section 4.2. The cell was allowed to reach a steady state for 60 s prior to stimulation with $30 \mu\text{M}$ IP3 for 30 s at a decay constant of 1.25 s^{-1} .

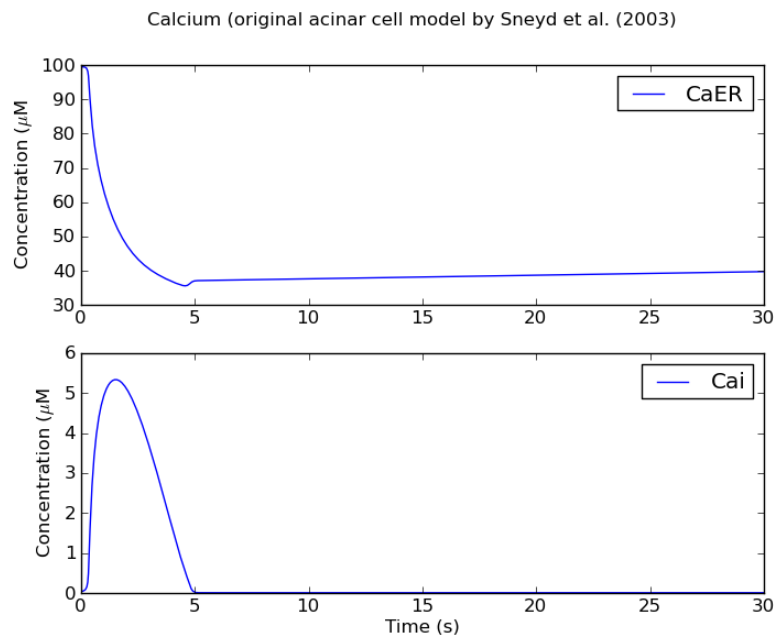


Figure 7.16: Plots showing the total change in calcium in the implementation of the Sneyd et al. (2002) ODE model detailed in Section 4.1.2. The cell was allowed to reach a steady state for 60 s prior to stimulation with $30 \mu\text{M}$ IP3 for 30 s at a decay constant of 1.25 s^{-1} .

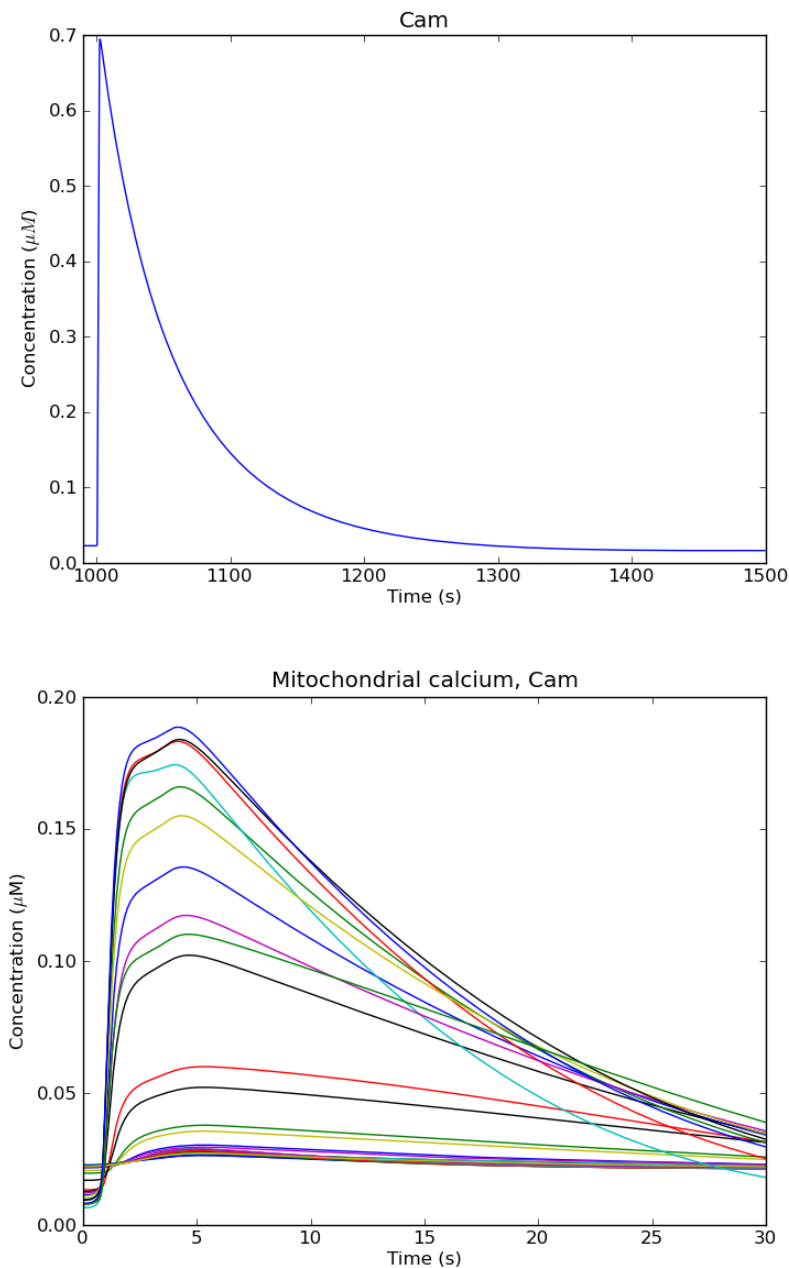


Figure 7.17: Plots showing the total change in calcium the coupled acinar-mitochondria ODE model (top) and each mitochondrial agent in the FEM multiscale model (each coloured differently bottom). The FEM cell was allowed to reach a steady state for 60 s prior to stimulation with 30 μM IP3 for 30 s at a decay constant of 1.25 s^{-1} . The ODE model was allowed to reach a steady state for 1000 s. The ODE model exposes the mitochondria to the same, greatly elevated, common pool of calcium, while the FEM multiscale model exposes each mitochondrial agent to a localised calcium concentration. This results in a much higher mitochondrial calcium concentration for those in the ODE model than the FEM, although when summed, the mitochondria in the FEM model (bottom) are collectively buffering more calcium than the ODE model (top).

the peak calcium concentration changes than to assume a 'well-mixed' cytosol without localised transients, while the more detailed FEM technique may consider the heterogeneous distribution of calcium in the cell. Although this could perhaps suggest that far greater IPR and RyR channel densities are required in the FEM model to achieve identical total peak concentrations to the cytosol in the ODE model, the FEM implementation does, however, produce peak calcium concentrations localised to parts of the cell that are within the physiological range suggested by the common pool ODE model version, and exhibits behaviour observed experimentally.

We have so far examined the behaviour of the 'natural' cell, where all agents were allowed to interact in the environment considered normal for the model. Next, we shall examine the effect removal of the mitochondrial firewall has on the rest of the model, particularly where wave propagation between the apical and basal regions is concerned.

7.2 Removal of the mitochondrial firewall

Simulations of the 'natural' cell have so far suggested that mitochondria contribute a great deal to the buffering of calcium transients that occur in the apical region. Calcium transients appear to be confined to this area, while the rest of the cell is shielded from major elevations in concentration, as hypothesised by experimentalists^[11,58,59,63]. Simulations with IP3 concentrations greater than 10 μM in the previous section have shown the mitochondrial firewall to be very effective at restricting apical transients. In contrast to these findings, the study by Sneyd et al. regarded the mitochondria as ineffective at confining these transients over the same range of IP3 stimulus. In addition, Sneyd et al. claimed that the rate constant used to represent mitochondrial calcium uptake could be varied between 0-200 s^{-1} without any significant changes to the results.

Moving from simulations where the cell model environment is considered 'natural', these next simulations show the behaviour of the model when the mitochondrial contribution to cell dynamics is disabled, and the cell is not shielded from apical calcium transients*.

7.2.1 Apical and basal calcium responses to stimulation by IP3

Peak time and concentration

Figure 7.18 shows the calcium responses in the model after stimulation with 3 μM IP3 while the mitochondria are disabled. In comparison to the 'natural' cell stimulated with 3 μM IP3 (Figure 7.1), the change in peak concentration measured across the cell without mitochondria appears to be more gradual, and the magnitude of each peak is greater. This suggests RyR activation, but could simply be due to the lack of mitochondrial calcium buffering. The profile of the time taken to reach peak calcium concentration between the apical and basal regions is also similar to the previous results, where the delay in time to peak increases with distance from the

*For visual assistance to the observations described in the text, please see the videos contained in the 'Mitochondrial firewall removal' subdirectory of the supplementary disk.

apical region. In this example, the time taken to travel from apical boundary to the base of the cell is approximately 3 seconds, which is longer than both the 3 and 30 μM IP3 stimulus in the previous simulations, at 1 and 2 s, but this is still shorter than that expected by a purely diffusion based mechanism of 6.3 s. This suggests there is again some emergent behaviour arising from the complex dynamics of agent interaction. However, the curve of peak calcium concentrations originating from the apical region at the top of Figure 7.1 is smooth, which is indicative of a diffusion-based mechanism.

Upon stimulation of the system with 30 μM IP3, the peak concentration and time profile is quite different than the previous example with 3 μM IP3, and this is shown in Figure 7.19. The peak calcium concentration measured in the apical region is higher with 30 μM than with 3 μM IP3, due to the increased density of channels in this region, and the magnitude of peaks begin to drop as the apical boundary at $xy = 11.2 \mu\text{m}$ is neared, as seen in the 'natural' cell simulations. However, at approximately $xy = 9.71 \mu\text{m}$, the peak calcium concentration begins to increase with distance from the apical region (Figure 7.19, top). The plot at the bottom of Figure 7.19 shows that the time to peak calcium concentration between the apex of the cell and $xy = 9.71 \mu\text{m}$ behaves largely the same as we have observed previously; the apical region reaches peak concentration first, and then the time to peak increases linearly toward the basal region. However, at $xy=9.71 \mu\text{m}$, where peak concentration begins to increase in Figure 7.19 (top), there is a sudden increase in the time to reach a peak that is approximately constant over the remaining basal region. The time taken to reach a peak concentration between the apical boundary and the base of the cell in this instance appears to be consistent with the time for a purely diffusion based mechanism (i.e. approximately 6 s). Though it appears there is a different mechanism at work here at higher concentrations of IP3 that has not been observed in the previous simulations when the mitochondrial agents were enabled.

The response of the model cell with disabled mitochondria to a range of IP3 concentrations is shown in Figure 7.20. The time to peak calcium concentration in

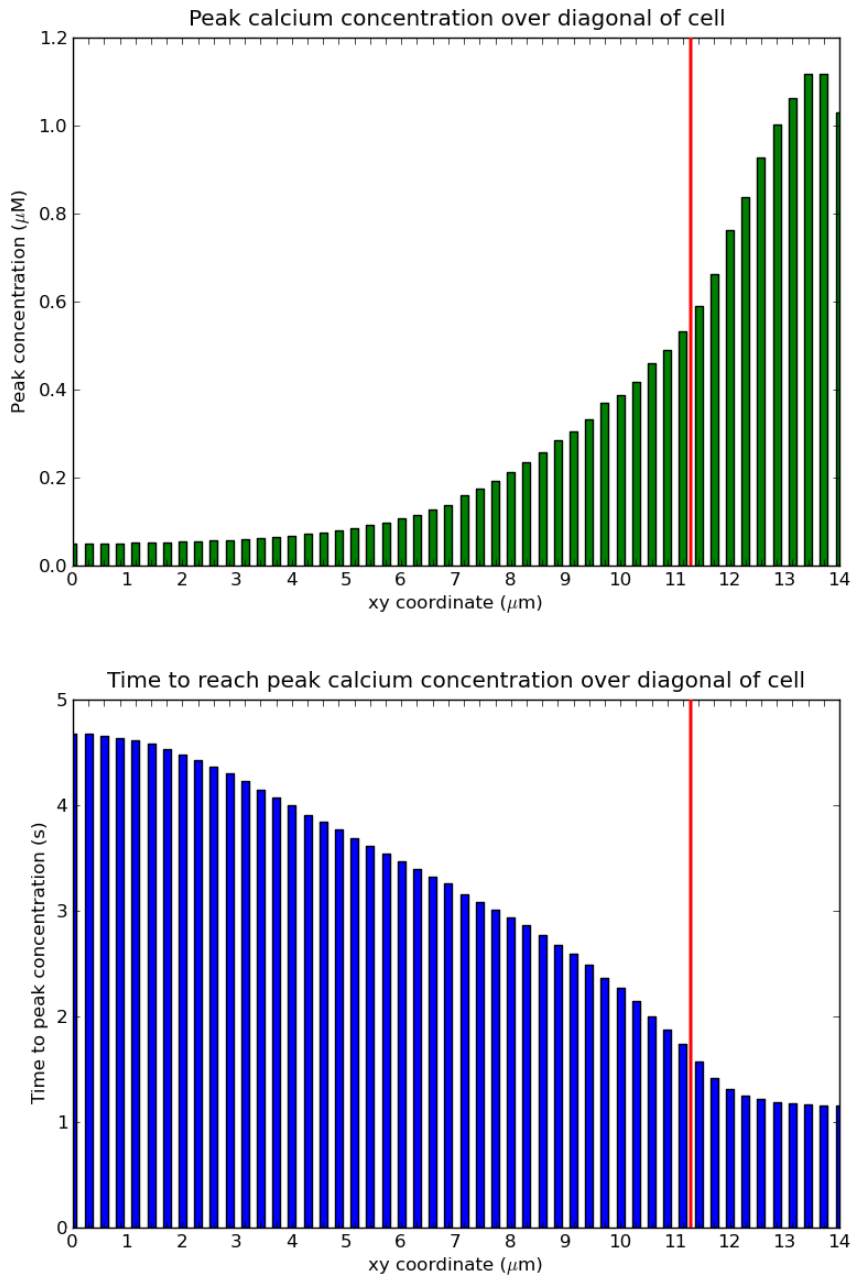


Figure 7.18: Top: Plot showing calcium peak data in response to 3 μM IP3. The values on the x-axis correspond to the coordinates for x and y between the base (0,0) and apex (14,14) of the cell. The apical boundary is at $xy=11.2$.

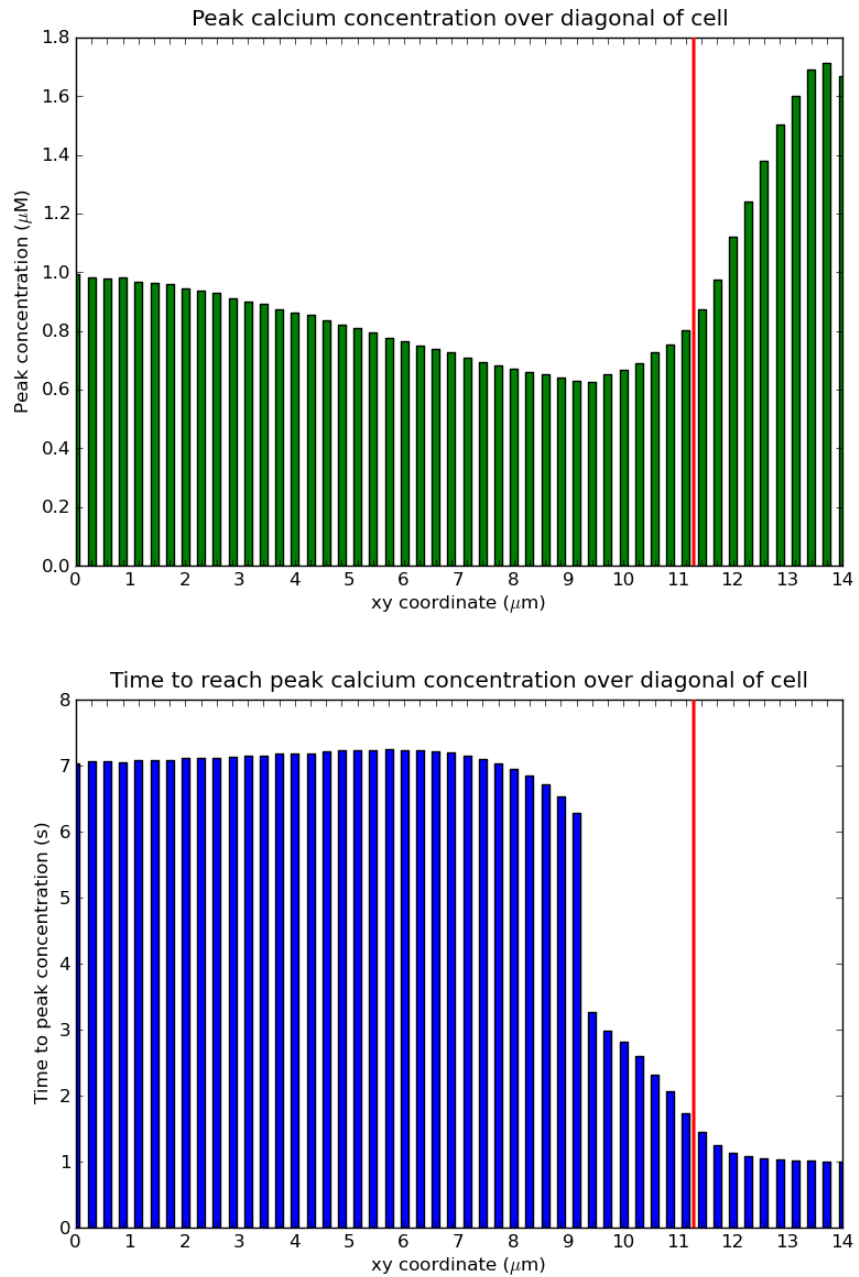


Figure 7.19: Top: Plot showing calcium peak data in response to $30 \mu\text{M}$ IP₃. The values on the x-axis correspond to the coordinates for x and y between the base (0,0) and apex (14,14) of the cell. The apical boundary is at $xy=11.2$. The increasing calcium peak concentration, that increases with distance from the apical region (top) is indicative that a CICR mechanism is occurring, rather than simple a diffusion based mechanism that was indicated in Figure 7.18. The time to peak data on the bottom plot shows that the apical region reaches a peak calcium concentration at approximately 1 s, while the basal region reaches a peak at 7 s, and shows that across this part of the cell, the peaks are reached at approximately the same time.

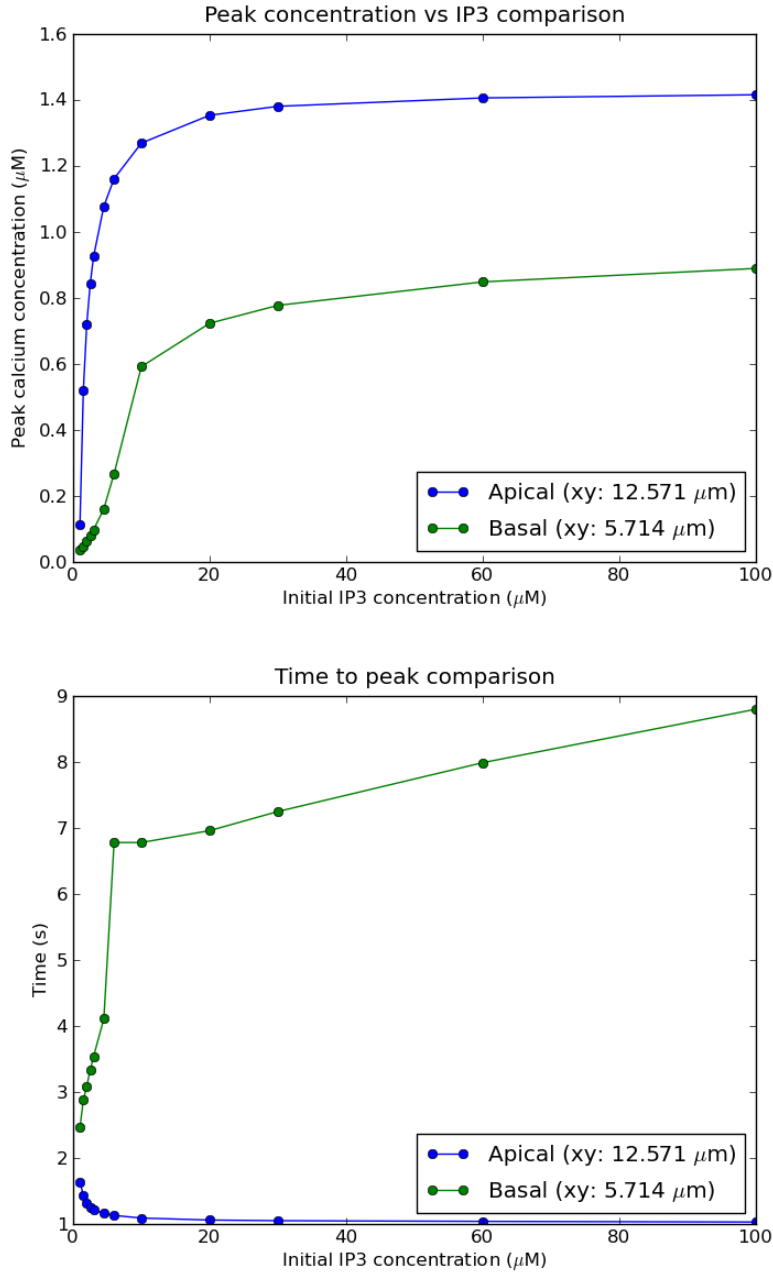


Figure 7.20: Top: Plot showing the time taken to reach a peak calcium concentration in a position in apical and basal regions of the cell, after exposure to IP3 over the entire cell at a range of concentrations. Bottom: Plot showing the corresponding peak calcium concentrations. The sudden change in time to peak calcium concentration between 4 and 6 μM IP3 is most likely due to a complex interaction of the cellular agents that was not previously observed when the mitochondria were enabled.

the apical region decreases as IP3 concentration increases, whereas the basal region experiences an increase in peak calcium concentration (Figure 7.20, bottom). This suggests that increasing IP3 concentrations result in channel activity that was not previously observed in the 'natural' cell (Figure 7.3, top). The plot at the top of Figure 7.20 also supports this, showing that increased IP3 concentration results in greater peak calcium concentrations in the basal region than observed when the mitochondrial firewall is intact. To achieve this response, it is most likely that increased channel activation is occurring, and this shall be examined next.

Wave speed and channel activation

Removal of mitochondrial firewall is thought to enable propagation of a global calcium wave through the cell, via CICR of RyR channels. Since the apical region initiates this propagated wave due to the high density of IPR channels, the relationship between IP3 concentration, the peak calcium concentration of the apical region, and the relationship with basal RyR channel activity is once again of interest. The top plot of Figure 7.21 shows the response of basal RyRs to peak calcium concentration in the apical region. The peak apical calcium concentration appears to elicit the largest response by basal RyRs from approximately 1 μM onwards, where the average basal open fraction increases from just under 0.1 to just over 0.5. Compared to the response of basal RyRs in the 'natural' cell model, where the maximum average basal RyR open fraction was approximately 0.0014 (Figure 7.6, top), this demonstrates how effective the mitochondria in this model are at shielding the cell from apical calcium transients, and that mitochondrial inhibition results in CICR, as observed experimentally^[67]. The plot at the bottom of Figure 7.21 shows the relationship between the average basal RyR open fraction and IP3 concentration. This shows a similar trend to that seen for the 'natural' cell in Figure 7.6 (bottom), except that the extent to which RyRs are activated without the presence of the mitochondrial firewall is much greater.

The effect on wave speed of this increased RyR response in the basal region is

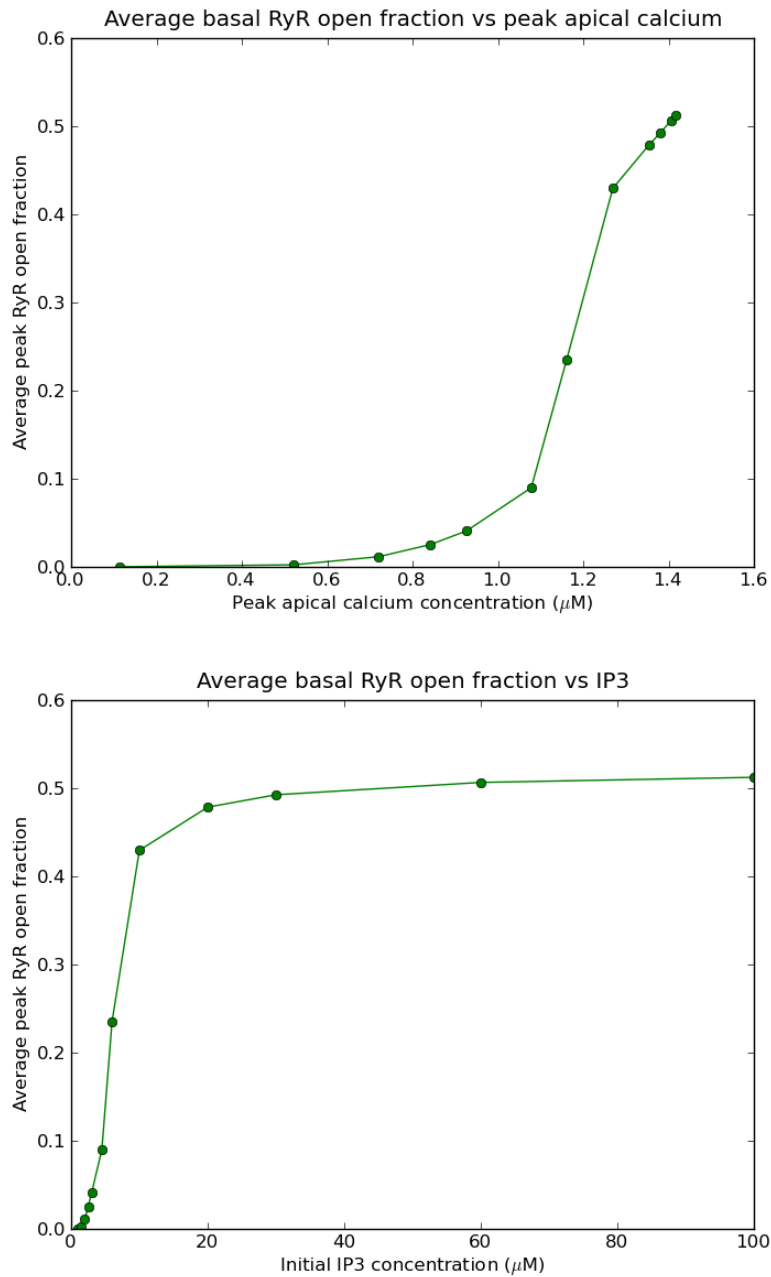


Figure 7.21: Top: Plot showing the average basal RyR channel open fraction in response to a range of peak calcium concentrations measured in the apical region. Bottom: Plot showing the average basal RyR channel open fraction response to IP3 concentration.

shown in Figure 7.22 for simulations using 3 and 30 μM IP3. Both plots show that the speed of the travelling wave peak is slower than for the example of the 'natural' cell in Figure 7.7 (due to the dynamics of SOC and IPR resulting in a degree of cellular 'noise'), and that the higher concentration of 30 μM IP3 again results in the slowest wave speed of the two plots. The time taken for the apical region to return to a normal calcium concentration after stimulation with 3 μM is less than

when stimulated with $30 \mu\text{M}$, and this is likely due to an increased basal calcium concentration diffusing back into the apical region.

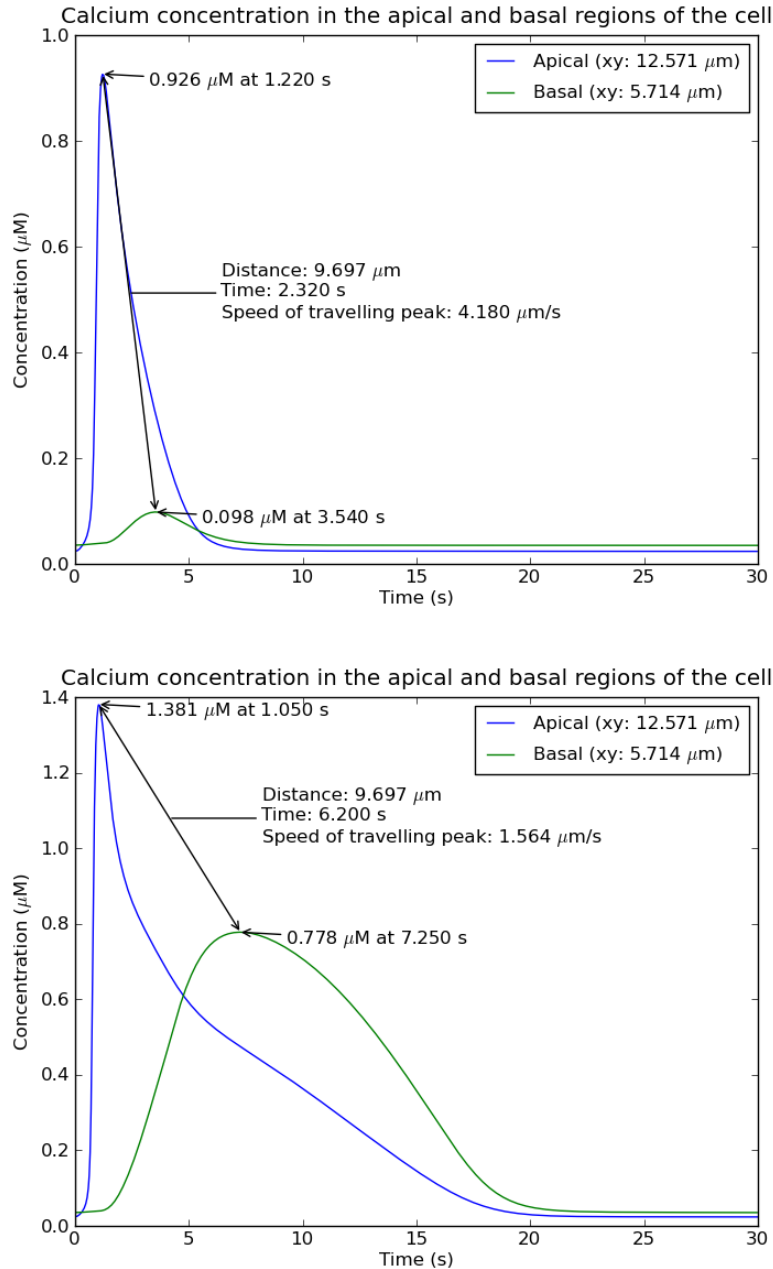


Figure 7.22: Plots to compare the different peak concentrations and rise times, and corresponding wave speeds, in response to two different concentrations of IP3. Top; $3 \mu\text{M}$ IP3, bottom; $30 \mu\text{M}$ IP3.

The wave speeds achieved over a range of IP3 concentrations is shown in Figure 7.23. The speed reduces quickly as the IP3 concentration is increased to $6 \mu\text{M}$, and declines more gradually thereafter. These speeds of wave peak propagation are all slower than observed when the mitochondrial firewall was enabled, which

suggests that calcium wave propagation mediated by CICR of RyR channels can be expected to reach speeds of approximately $1.5\text{-}2 \mu\text{m s}^{-1}$ for IP3 concentrations over $6 \mu\text{M}$, which is slower than observed by Sneyd et al. in their spatially compartmentalised model. The model by Sneyd et al. was in agreement with experimental data by Straub et al (2000)^[67], where the spatially compartmentalised model predicted that CICR propagation results in a wave speed of approximately $15\text{-}20 \mu\text{m s}^{-1}$. To achieve these speeds of wave propagation, it is likely that increased channel agent densities are required so the model can react quicker to stimulation.

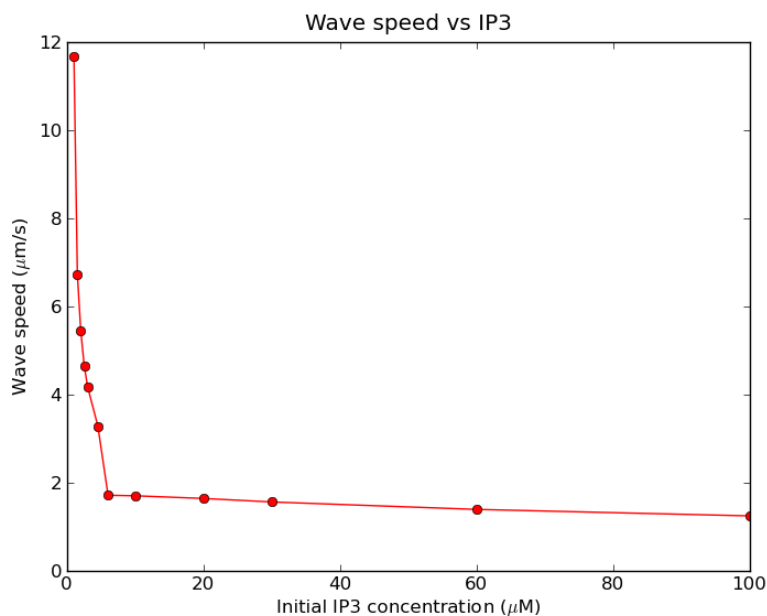


Figure 7.23: Plot showing the speed of the calcium concentration wave, calculated using the difference in time taken to reach a peak in the apical and basal regions (i.e. found in the same way as Figure 7.22).

Figure 7.24 shows the sequential activation of RyR channels when the cell was stimulated with $30 \mu\text{M}$ IP3. The initial peak open fractions at the beginning of the simulation result from RyRs in the apical region, which also reach a higher open fraction than other RyR channels in the cell over the same duration. As the apical RyRs deactivate, having already released calcium from the ER, RyRs in the basal region closest to the apical region increase their open fraction, and so on, as CICR propagates across the cell. The delay between each RyR is due to the speed of diffusion of calcium between each RyR agent.

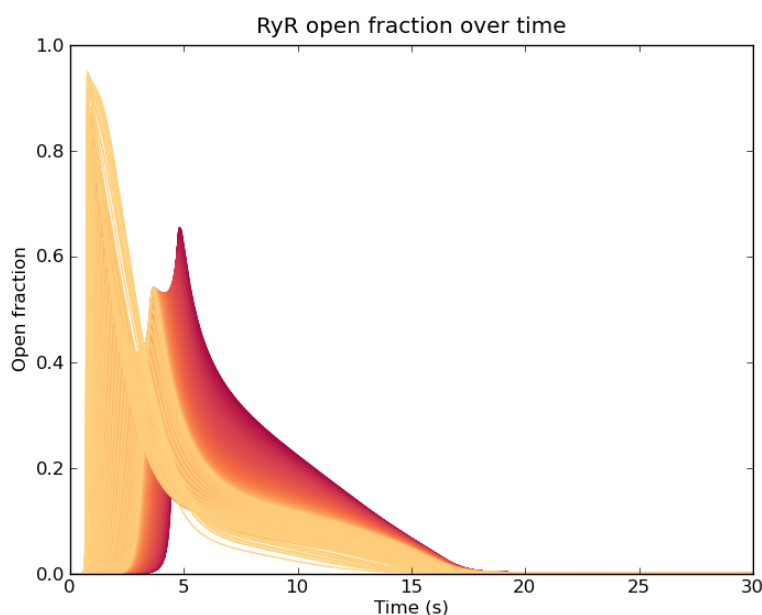


Figure 7.24: Plot showing the open fraction of all RyR channels in the model cell with disabled mitochondria and stimulation by $30 \mu\text{M}$ IP3. The difference in colour is used to provide contrast between the plots of the many RyR channel agents. Light orange indicates RyRs closer to the apex of the cell, while darker red indicates RyRs closer to the base of the cell. The first group of peaks that are also the largest are the RyRs contained in the apical region. As these initial agents begin to deactivate, RyRs further away are activated by the calcium diffusing from the apical region, propagating the wave over the cell via CICR.

7.2.2 ER concentration changes

The altered dynamics of calcium in the cytosol, due to the disabled mitochondrial firewall, also result in altered ER dynamics. Figure 7.25 shows the concentration profile of 50 samples across the diagonal of the cell in response to $30 \mu\text{M}$ IP3. This is very different to $30 \mu\text{M}$ IP3 stimulation in the 'natural' model cell examined previously in Figure 7.12.

Initially, the apical portion of the ER containing the majority of IPR and RyR channels releases calcium, as shown in the plot at the top of Figure 7.25. After 3-4 s of simulation time, RyRs in the basal region start to be activated via CICR initiated in the apical region, which causes the concentration over the entire ER to drop as more RyRs open. Shortly after this, the ER recovers. The plot at the bottom of Figure 7.25 shows the maximal ER calcium concentration loss, and is essentially a mirrored profile of Figure 7.19. The amount of calcium lost by the ER as distance from the

apical region increases is likely due to additional activation of RyRs, as a larger area of the ER surface containing the RyRs becomes activated by the travelling wave. The internal ER calcium concentration gradient shows a similar process of recovery to stimulus in the 'natural' model cell,

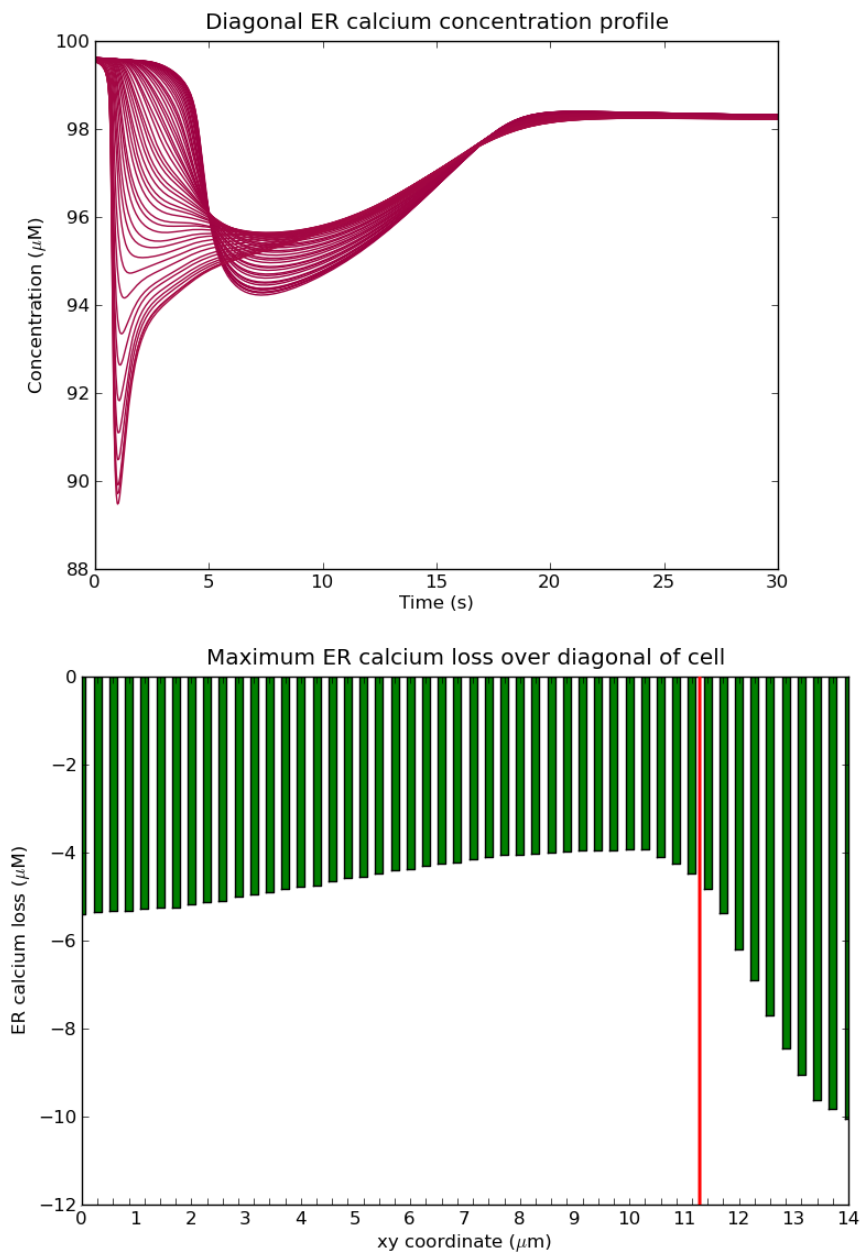


Figure 7.25: Top: Plot showing the change in calcium concentration in the ER compartment for 50 locations across the centre of the cell vs time, from the base to the apex, upon stimulation by 30 μM IP3. Bottom: The same plot as top, but showing the maximum amount of calcium lost by the ER before refilling, against xy coordinates of each sample.

7.3 The model cell and mitochondrial motility

Previously, mitochondria in the cell have been fixed to a pre-defined location that was based upon interpretation of mitochondrial distribution in the literature. Thirty mitochondrial agents were distributed around the cell, by allocating one third to the mitochondrial firewall and the remaining two thirds to the cell membrane. It would be interesting to see if the mitochondrial agents, given simple rules for movement, cluster or accumulate at different parts of the cell and perhaps automatically form a mitochondrial firewall.

Mitochondria have been observed to undergo bursts of directed movement along microtubule and actin filament tracks approximately 6% of the time, at a speed of 290 nm s^{-1} ^[49]. Mitochondrial distribution is thought to involve local calcium transients, where concentrations raised between 1-2 μM cause arrest of motility that is recovered upon returning calcium to normal homeostatic levels^[57].

The speed of mitochondrial movement, coupled with moving only 6% of the time mean that leaving the model to run under these conditions until the mitochondria redistribute themselves is going to require an extremely long simulation time, and computer time as a result. Instead, the process was accelerated by allowing the agents to move freely around the cell for a period of 30 s, which is equivalent to allowing the mitochondria 6% movement time for 500 s. In order to provide calcium movement during the 30 s of simulation time, which the mitochondria require to find a preferential distribution, 20 μM IP3 was held constant during the redistribution simulations. Although calcium oscillations do not occur in the FEM model implementation when IP3 is held fixed, this does cause a small open fraction of IPR channels after the initial transient, causing influx of calcium into the cytosol from the ER, as well as from the SOCs, that result in calcium gradients and microdomains. Mitochondrial motility, as a function of local calcium concentration, was reduced using a Hill equation formulation with a half-saturation constant of 0.4 μM , as described in Section 5.1.1. The path mitochondrial agents take is dictated solely by the calcium concentration gradient in the cytosol local to each agent. This path is

also assumed to be unhindered by intracellular structures such as the positioning of microtubules, and navigation around other organelles such as the ER and other mitochondria. The combination of all these factors mean the mitochondrial agents will stay at a position in the cytosol if either the calcium concentration causes arrested movement, or if there is no greater concentration gradient than at the current position of the agent.

The desired outcome from these simulations is observation of any mitochondrial agents clustering at particular regions that have been recognised experimentally. This may then support evidence that the calcium signal serves as a mechanism of mitochondrial distribution, as well as provide a distribution of mitochondria that can be used in the model for further simulations and allow observation of altered dynamics. The three initial mitochondrial starting positions were; random, boundary (distributed evenly around the cell boundary), and inferred (the distribution that was inferred from literature, and used in previous simulations).

The path that mitochondrial agents took from random starting positions is shown in Figure 7.26, where the starting position is coloured green, the location at which the mitochondria ended up after 30 s is coloured red, and the path taken is coloured blue. The majority of mitochondria that began the simulation near the middle of the cell make their way toward the apical region, where the highest density of IPR channels stimulated by fixed IP₃ are located. Those mitochondria near to the basal membrane, and a few near the centre of the cell, find their own localised gradients, and remain in these positions for the remaining simulation time. The mitochondria that end up in the centre of the cell may be regarded as non-specific, and those that end up near the cell membrane may be regarded as sub-plaslemmal, as named by Park et al. (2001)^[59]. The cluster of mitochondria in the apical region could be considered the perigranular mitochondria, however these mitochondrial agents do not form a periphery around the apical boundary. If this model of the pancreatic acinar cell included ZGs in the apical region that the mitochondrial agents could not occupy the same space as, it is likely they would automatically form a firewall

arrangement. Alternatively, if several apical oscillations occurred during redistribution, the mitochondrial agents may have naturally clustered at positions where oscillations result in arrested movement the majority of the time. A stimulation protocol where the concentration of IP3 is raised and allowed to decay several times over the course of a simulation would be possible to implement in this multiscale FEM model. However, the length of time to perform the simulation, the frequency in which to stimulate the cell, and the concentration of IP3 uses would need consideration. While this is an interesting future direction of mitochondrial redistribution, for the purposes of this current study, it could be assumed that the arrangement of mitochondrial agents in the apical region of Figure 7.26 would form such a boundary.

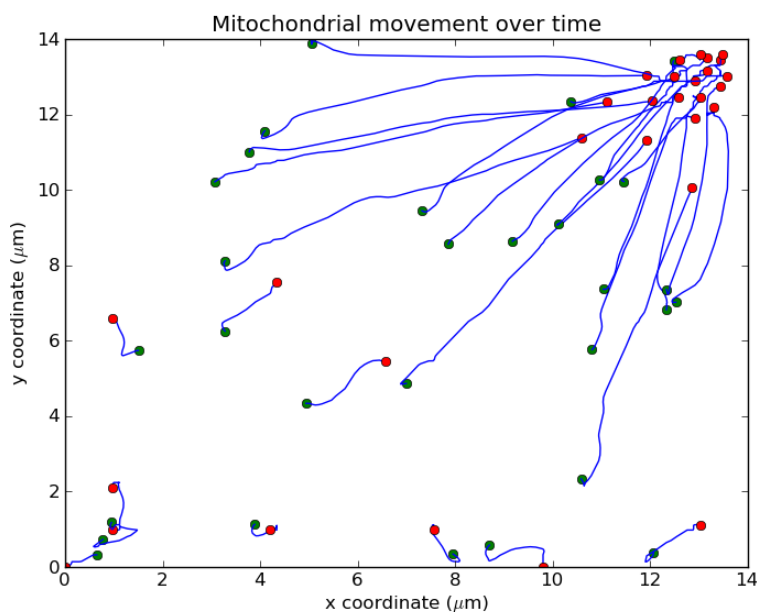


Figure 7.26: Automated redistribution of mitochondria from random positions. The starting positions are coloured green, the location at which the mitochondria ended up after 30 s is coloured red, and the path taken is coloured blue.

The path taken by mitochondria that start from an initial distribution around the cell boundary is shown in Figure 7.27. Similar to the example where random starting positions were used in Figure 7.26, the mitochondrial agents closest to the apical region move toward this region of higher IPR density while other mitochondria in the basal part of the cell find their own microdomains over time.

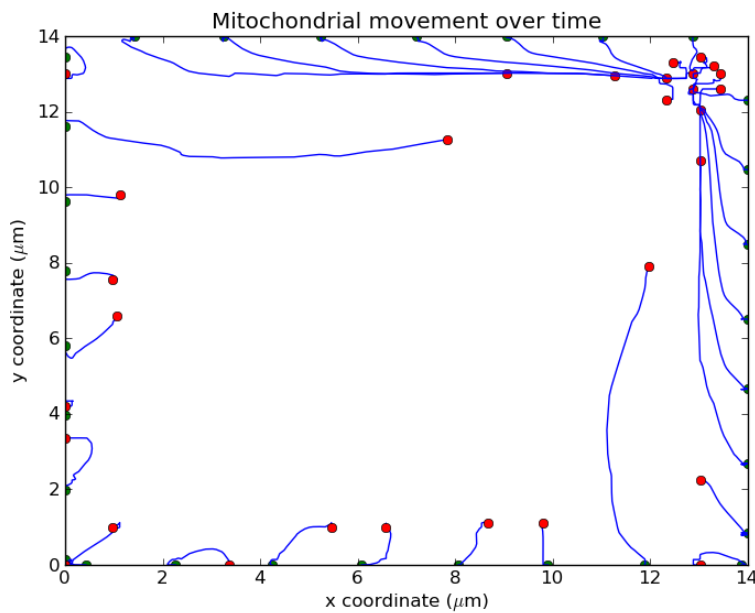


Figure 7.27: Automated redistribution of mitochondria from the cell boundary. The starting positions are coloured green, the location at which the mitochondria ended up after 30 s is coloured red, and the path taken is coloured blue.

The final example of mitochondrial redistribution uses starting positions inferred from the literature, which were used to produce results found in the ‘natural’ cell simulations detailed earlier. Owing to the large number of mitochondria that already form the mitochondrial firewall, a much larger number of mitochondrial agents end up inside the apical region, than seen in the previous examples.

All three examples show two or more of the mitochondrial sub-populations observed experimentally, excluding the perinuclear sub-population due to the lack of a represented nucleus. Each example has emerged from combination of a few simple rules of mitochondrial agent movement, related to the calcium dynamics of the cell (albeit during an accelerated simulation with respect to mitochondrial motility). To test the effect mitochondrial redistribution has on cellular calcium dynamics, a set of redistributed mitochondria shall be used to generate results similar to the ‘natural’ cell simulations detailed earlier.

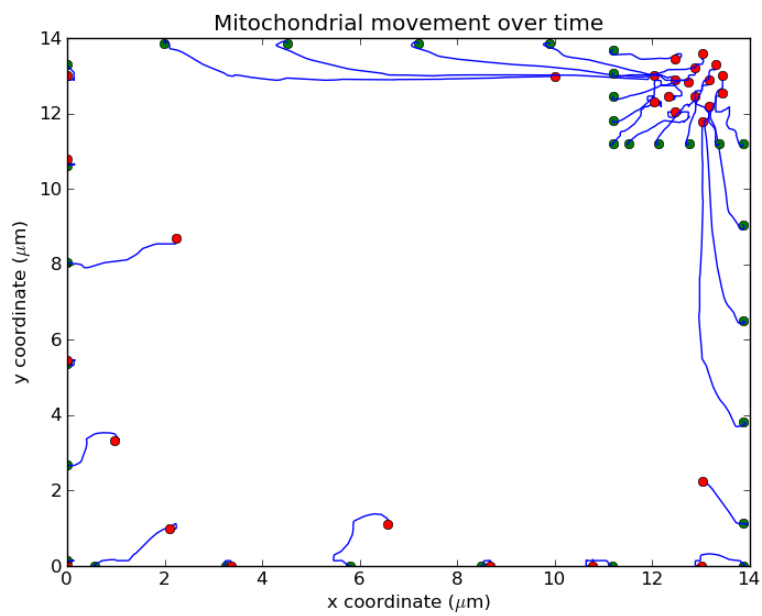


Figure 7.28: Automated redistribution of mitochondria from inferred locations. The starting positions are coloured green, the location at which the mitochondria ended up after 30 s is coloured red, and the path taken is coloured blue.

7.4 Simulations carried out with redistributed mitochondria

The previously described mitochondrial motility simulations began from random, cell boundary, and inferred starting positions in the cytosol, and were allowed to move freely around a perturbed cellular environment that was stimulated by a fixed concentration of $20 \mu\text{M}$ IP3 for 30 seconds. The final distribution of mitochondria in all three simulations show clustering in the apical region, near the cell boundary, and in the centre of the cell. The following results show the effect of this mitochondrial redistribution on the calcium dynamics of the cell, in comparison to the inferred distribution that was used in other simulations*.

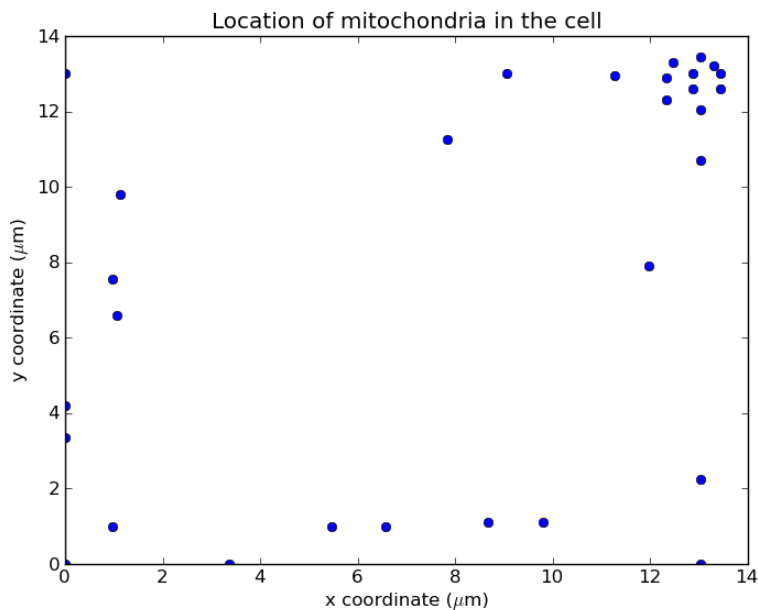


Figure 7.29: Final positions of the redistributed mitochondria that began at the cell boundary. Using this configuration of mitochondrial distribution, stimulation for a range of IP3 concentrations was performed, to observe the effect of mitochondrial distribution on model behaviour.

The results generated by mitochondrial redistribution that started from cell boundary simulations were chosen for use in the following simulations. Uniform starting positions at the cell boundary are easily reproducible for future comparison (unlike

*For visual assistance to the observations described in the text, please see the videos contained in the 'Mitochondrial redistribution' subdirectory of the supplementary disk.

the random starting positions), and are not biased to a particular region of the cell (unlike the inferred starting positions). Additionally, the distribution of mitochondria that resulted from starting positions on the cell boundary shows clustering in the perigranular and sub-plaslemmal regions, and some non-specific positions (Figure 7.29).

7.4.1 Apical and basal calcium responses to stimulation by IP3

Peak time and concentration

In the 'natural' cell simulations, the mitochondria were clearly positioned at the apical boundary and confined calcium oscillations to this high density IPR region, at all IP3 concentrations. In addition, mitochondria were also located uniformly around the cell membrane. A high peak calcium concentration was observed in the apical region with the mitochondrial firewall configuration, but this was well buffered by the mitochondria before it could significantly activate the RyR channels in the basal region.

Figure 7.30 shows the effect of using a set of redistributed mitochondria in the pancreatic acinar cell model, when stimulated with 3 μM IP3. Compared to the equivalent 'natural' cell simulation results in Figure 7.1 where a peak apical calcium concentration of approximately 0.85 μM was observed, Figure 7.30 (top) shows that the new mitochondrial distribution has significantly reduced this peak response. The maximum peak calcium concentration now observed after stimulation by 3 μM IP3 is just under 0.05 μM , and the location of this peak is at $xy=11.71-12.0 \mu\text{m}$; just outside the main cluster of apical mitochondria in Figure 7.29.

The plot at the bottom of Figure 7.30 shows two positions that were sampled (at $xy=0.0 \mu\text{m}$ and $xy=0.86 \mu\text{m}$), where the time to peak calcium concentration is far longer than other samples. With reference to Figure 7.29, $xy=0.0 \mu\text{m}$ and $xy=0.86 \mu\text{m}$ each show a nearby mitochondrial agent that may have resulted in dynamics that simply delayed the time to peak. The remaining times to peak calcium concentration that were sampled show that the apical region reaches a maximal concentration

before the rest of the cell, and that this time to peak increases similarly to the plot at the bottom of Figure 7.1. This suggests that a similar mechanism of wave movement is occurring in Figure 7.30.

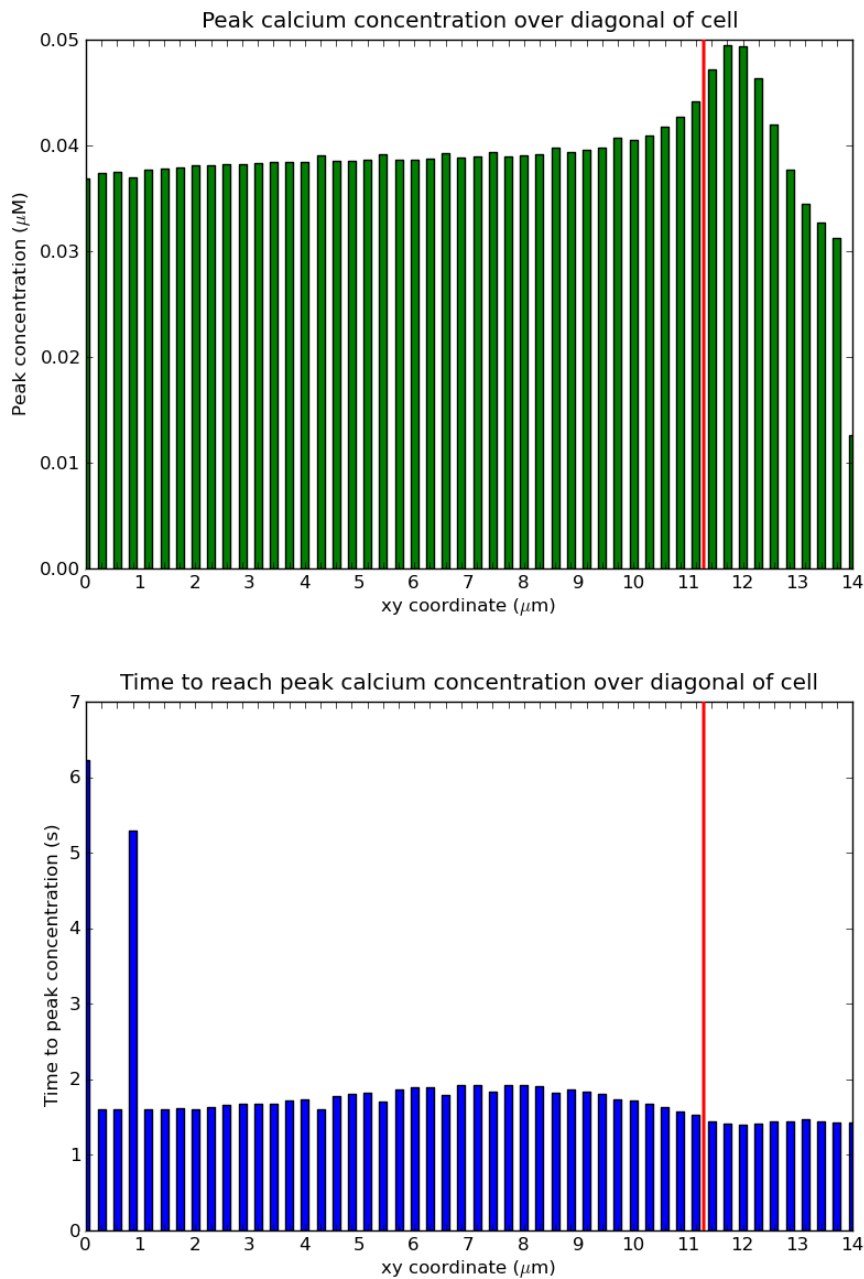


Figure 7.30: Plots showing calcium peak data in response to 3 μM IP3. The values on the x-axis correspond to the coordinates for x and y between the base (0.0,0.0) and apex (14.0,14.0) of the cell. The apical boundary is at $xy=11.2$.

Figure 7.31 shows the same system of redistributed mitochondria that is exposed to 30 μM IP3. The plot at the top of Figure 7.31 shows that the apical region is experiencing a much larger peak calcium concentration than when exposed to 3 μM ,

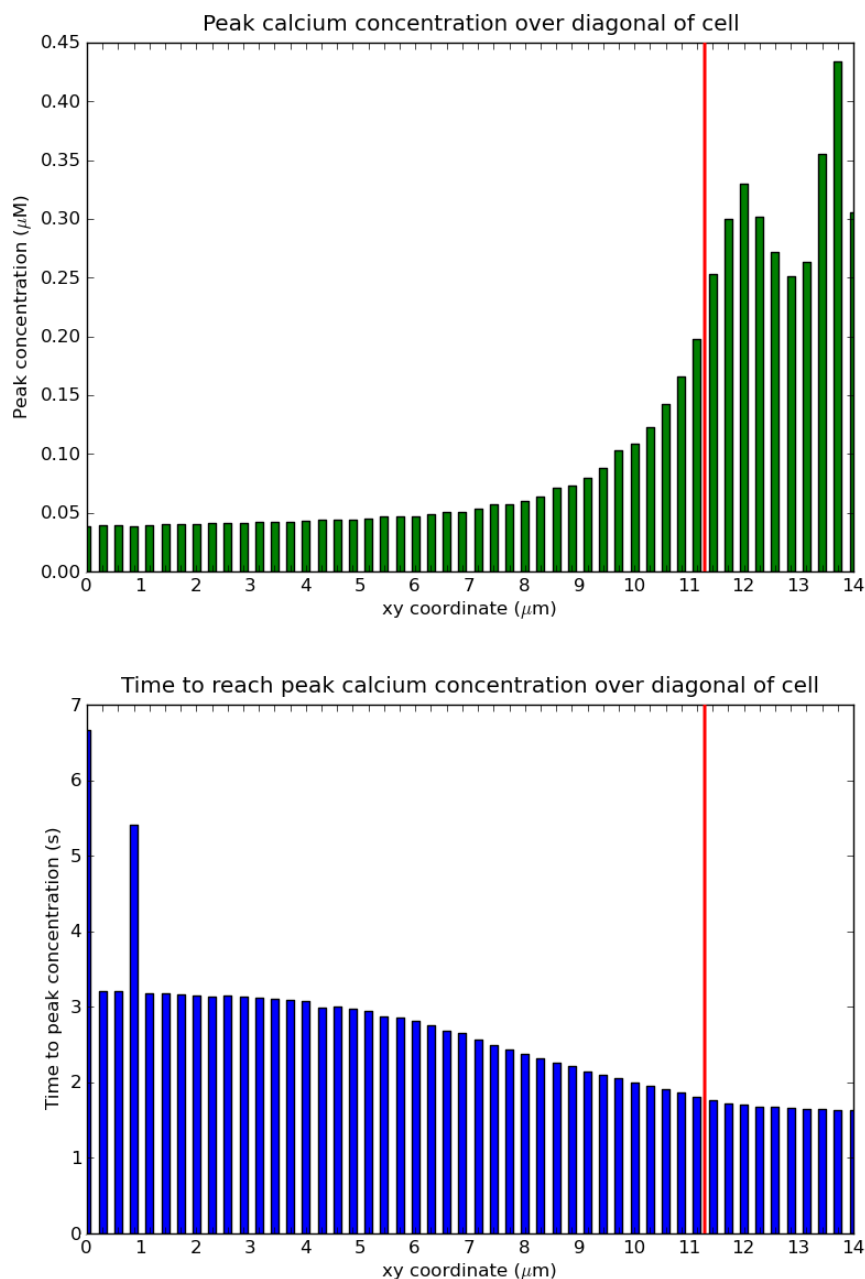


Figure 7.31: Plots showing calcium peak data in response to $30 \mu\text{M}$ IP3. The values on the x-axis correspond to the coordinates for x and y between the base (0.0,0.0) and apex (14.0,14.0) of the cell. The apical boundary is at $xy=11.2$.

although this is still significantly lower than the response observed in the 'natural' cell simulation with $30 \mu\text{M}$ IP3 in Figure 7.2. The main body of the mitochondrial cluster in the apical region is around $xy=13 \mu\text{m}$ in Figure 7.29, and the effect this clustering has is shown at the top of Figure 7.31 as a collection of lower peak data than the trend of increasing peak concentrations moving toward the apical region suggests there should be. The plot at the bottom of Figure 7.31, (ignoring the irreg-

ularities resulting from mitochondria near positions $xy=0.0 \mu\text{m}$ and $xy=0.86 \mu\text{m}$), shows that the time to peak across the cell is very similar in profile to the bottom of Figure 7.2, indicating that mechanisms of calcium dynamics throughout the basal region remain largely the same as the inferred distribution of mitochondria.

Figure 7.32 compares the apical and basal responses at the regions of interest, over a range of IP3 concentrations. The plot at the top of Figure 7.32 shows that the difference between apical and basal peak calcium concentrations over the range of IP3 is much smaller than that shown in the simulations where the mitochondrial distribution was inferred from the literature in Figure 7.3. This suggests that the combined buffering effect of the clustered mitochondria is absorbing the majority of calcium released by the apical IPR channels, before this initiates CICR of the apical RyRs. This results in a reduced apical calcium concentration compared to the 'natural' cell simulations, however the apical region does still experience larger calcium transients than the basal region.

The plot at the bottom of Figure 7.32 shows that the time to peak in the apical region is slower than when the inferred mitochondrial positions are used in the 'natural' cell, remaining at just over 1.6 s for the majority of IP3 concentrations compared to just under 1 s with the inferred distribution. The basal time to peak increases with IP3 concentration, between 2.8 and 2.9 s for IP3 concentrations over $10 \mu\text{M}$, which is shorter than observed for the inferred distribution in Figure 7.3 between 2.3 and 2.45 s over the same range of IP3 concentrations. Although small, it is not clear why there should be a difference, but this could be due to decreased RyR activation in this instance compared to the results shown in the 'natural' cell.

Channel activation and calcium wave speed

As previously mentioned, the time to peak concentration in response to IP3 stimulation in the 'natural' cell with a mitochondrial firewall is shorter than when the redistributed mitochondria form a cluster in the apical region. Additionally, the peak calcium concentrations observed in the apical region is much lower due to the

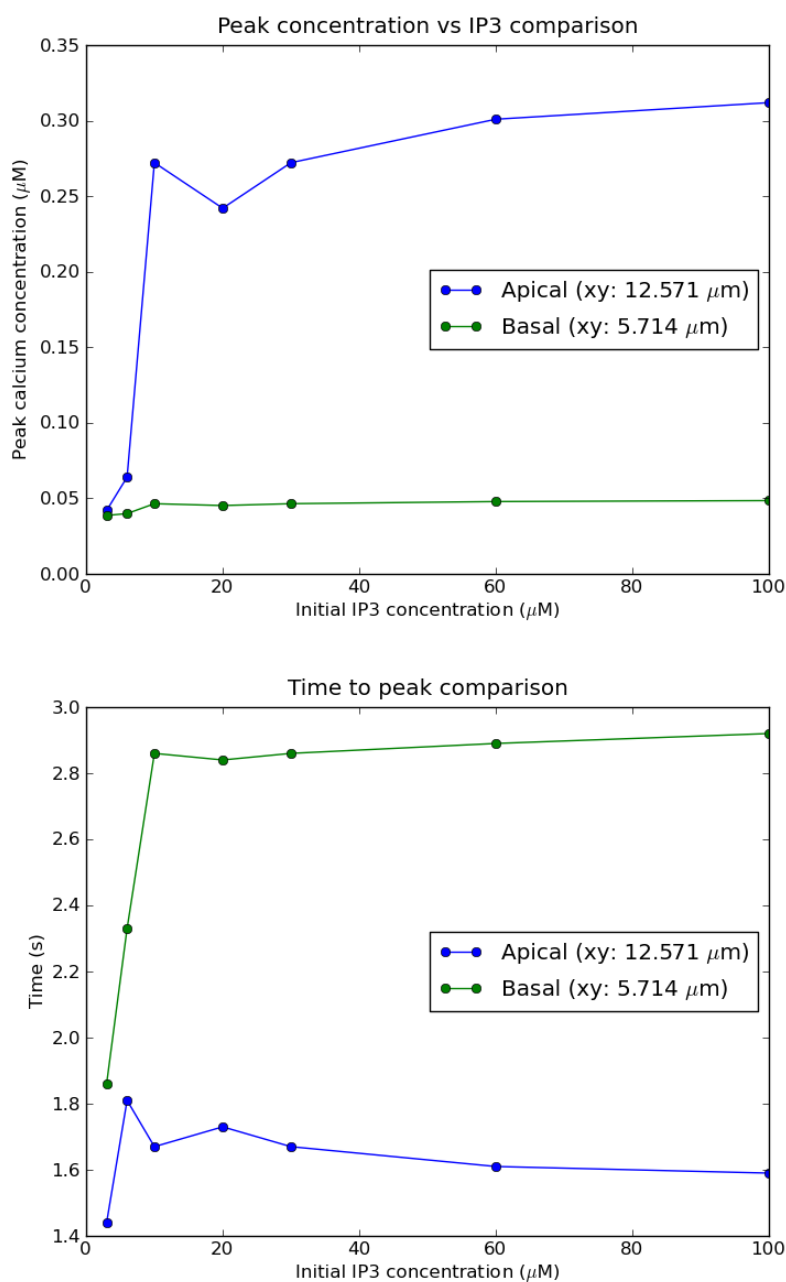


Figure 7.32: Top: Plot showing the corresponding peak calcium concentrations. Bottom: Plot showing the time taken to reach a peak calcium concentration at a position in apical and basal regions of the cell, after exposure to IP3 over the entire cell at a range of concentrations. The range of IP3 concentrations simulated was 3, 6, 10, 20, 30, 60 and 100 μM .

clustered configuration of apical mitochondria. Although the degree to which CICR was observed in the 'natural' cell simulations was minimal, perhaps this longer time to peak concentration in the basal region is due to further reduced CICR.

Figure 7.33 shows the average RyR peak response observed in response to peak apical calcium concentration and the relationship between average peak RyR re-

sponse with IP3. In comparison to the same plots for the 'natural' cell in Figure 7.6, the plots in Figure 7.33 show that the trend of RyR response to both peak apical calcium concentration and IP3 concentration is very similar, except the maximal RyR response is slightly reduced.

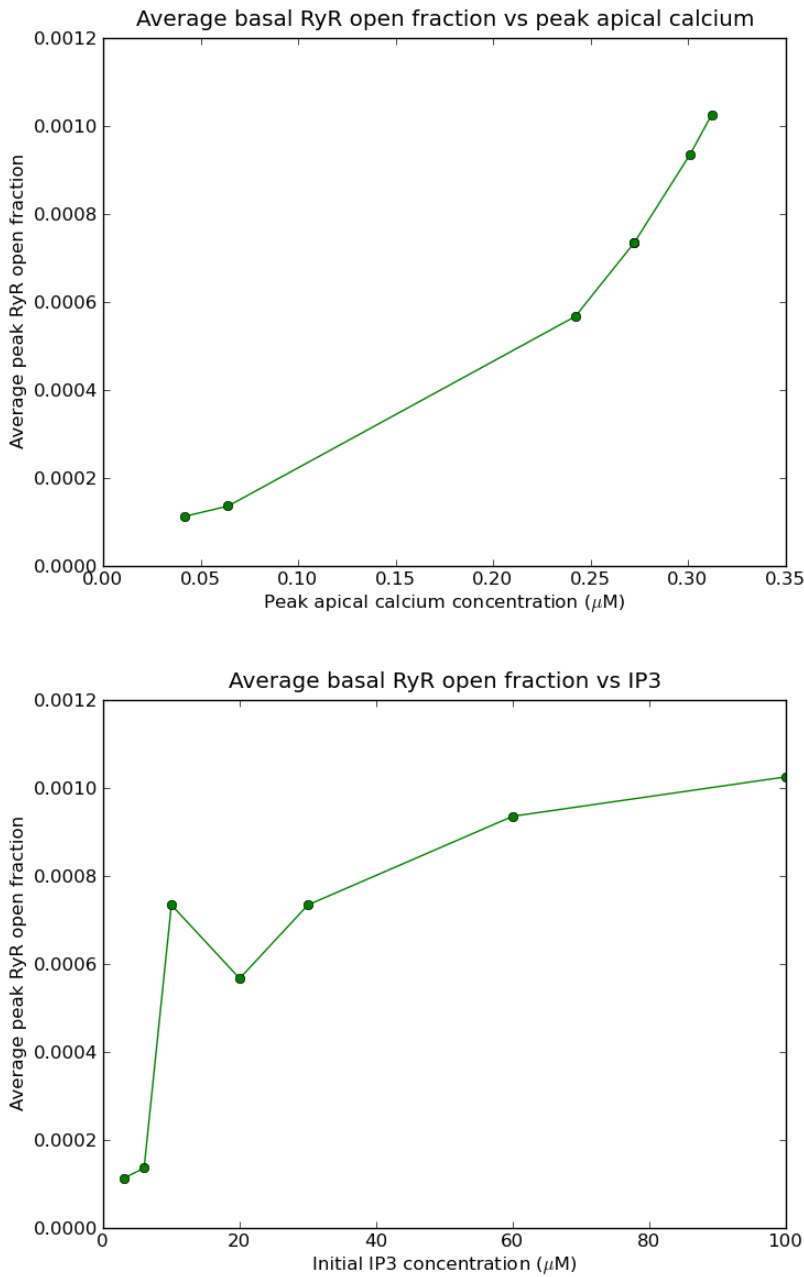


Figure 7.33: Top: Plot showing the average basal RyR channel open fraction in response to a range of peak calcium concentrations measured in the apical region. Bottom: Plot showing the average basal RyR channel open fraction response to IP3 concentration.

Reduced RyR activation in the basal region is unlikely to be the reason for increased basal time to peak calcium concentration. The trend in wave speed shown

7.4. SIMULATIONS CARRIED OUT WITH REDISTRIBUTED MITOCHONDRIA

previously in Figure 7.8, and the trend shown in Figure 7.34, both show that an increase in IP3 concentration results in a similar reduction in wave speed. In addition to this, we know that increased IP3 results in an increased RyR response, due to the increase in apical peak response shown in Figure 7.33. Therefore the increased time to peak observed when mitochondria are clustered in the apical region is due to dynamics that are more complex and hidden, related to mitochondrial distribution.

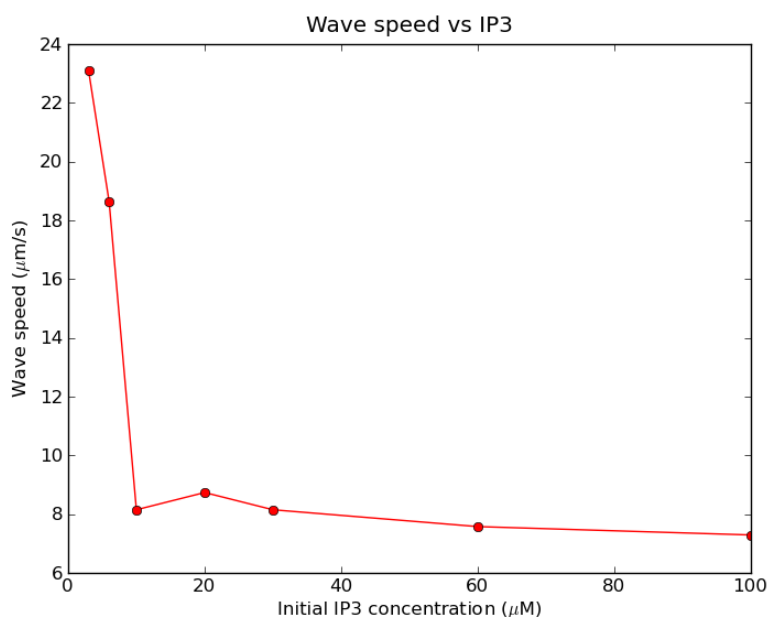


Figure 7.34: Plot showing the speed of the calcium concentration wave, calculated using the difference in time taken to reach a peak in the apical and basal regions.

7.4.2 Apical and basal mitochondrial responses to stimulation by IP3

The response of the mitochondria to stimulation of the cell by IP3 is shown in Figure 7.35. Apical mitochondria buffer more calcium than the basal mitochondria, but they increase to a maximal $0.12 \mu\text{M}$ at $100 \mu\text{M}$ IP3, in comparison to the 'natural' cell simulations where maximal mitochondrial calcium was recorded as just under $0.18 \mu\text{M}$ (Figure 7.10, top). Although the clustered mitochondria are reducing the maximal apical peak calcium concentration to a greater degree, they are buffering less calcium than the mitochondrial firewall, which suggests it is not how much calcium the mitochondria buffer in the apical region that controls the global calcium response, but at what time this occurs. If the mitochondria buffer calcium before it stimulates the apical RyRs, this means that the apical response is further reduced. A lowered apical peak calcium concentration means that less mitochondrial calcium is accumulated during cell stimulation, in addition to less calcium diffusing into the cytosol.

Reduced calcium being released into to the apical region is supported by Figure 7.36, during stimulation with $30 \mu\text{M}$ IP3. The amount of calcium lost from the ER is lower than shown for the inferred mitochondrial distribution in Figure 7.12, where just under $8 \mu\text{M}$ was lost, in comparison to just under $10 \mu\text{M}$. Interestingly, in both of the bottom plots of Figures 7.36 and 7.12, the maximal concentration lost by the ER is closest to the very apex of the apical region, despite the different mitochondrial distribution. This is most likely due to closely positioned PMCA pumps, which result in a lowered calcium concentration closer to the apex that reduce the degree to which calcium deactivates the IPR channels. This allows those closest to the PMCA pumps to activate more fully than the rest of the cell, and is likely to be true for IPR channels in the basal region nearest to SERCA.

It is unclear how representative the mitochondria in this particular model are, due to the steps taken to ensure compatibility between the mitochondria model and the environment of the acinar cell. However, the results generated by stimu-

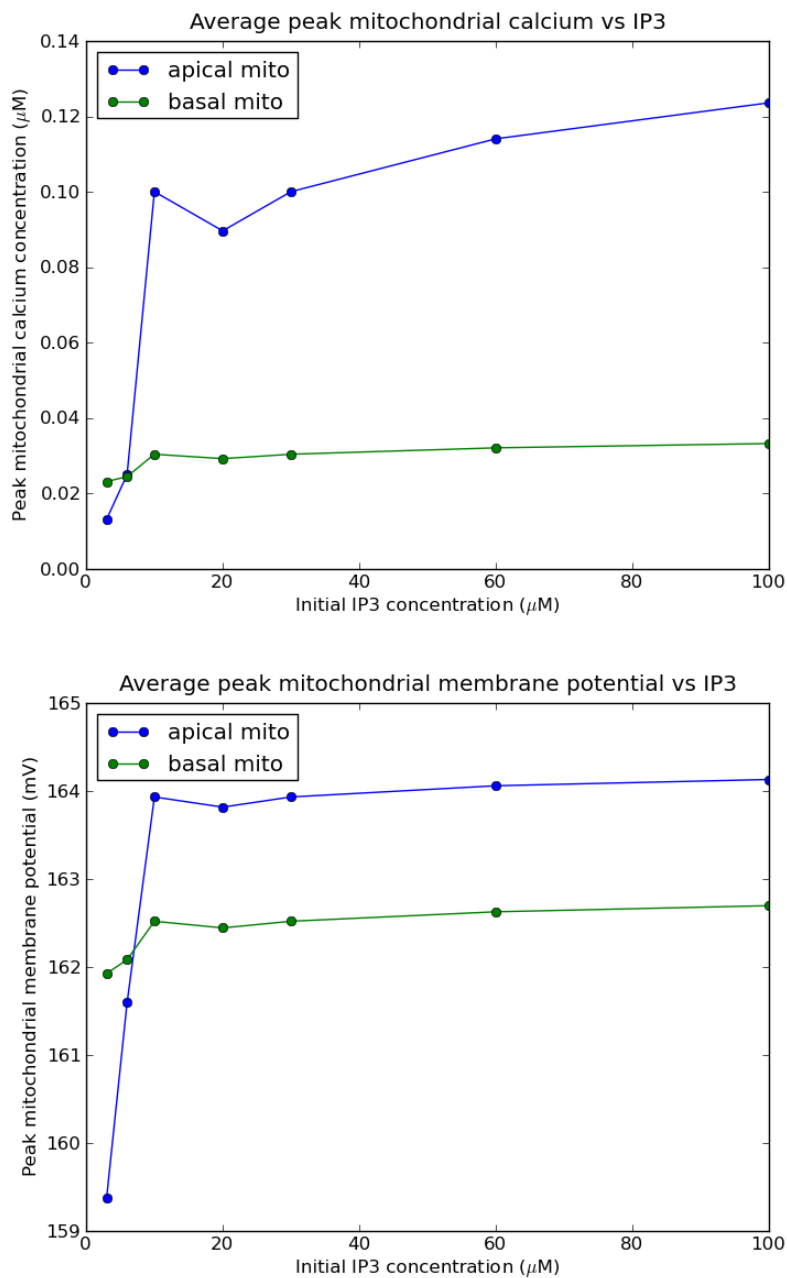


Figure 7.35: Top: Plot showing the average peak mitochondrial calcium concentration for mitochondria in the basal and apical regions, in response to cell stimulation by IP3. Bottom: Plot showing the average peak mitochondrial membrane potential for mitochondria in the basal and apical regions.

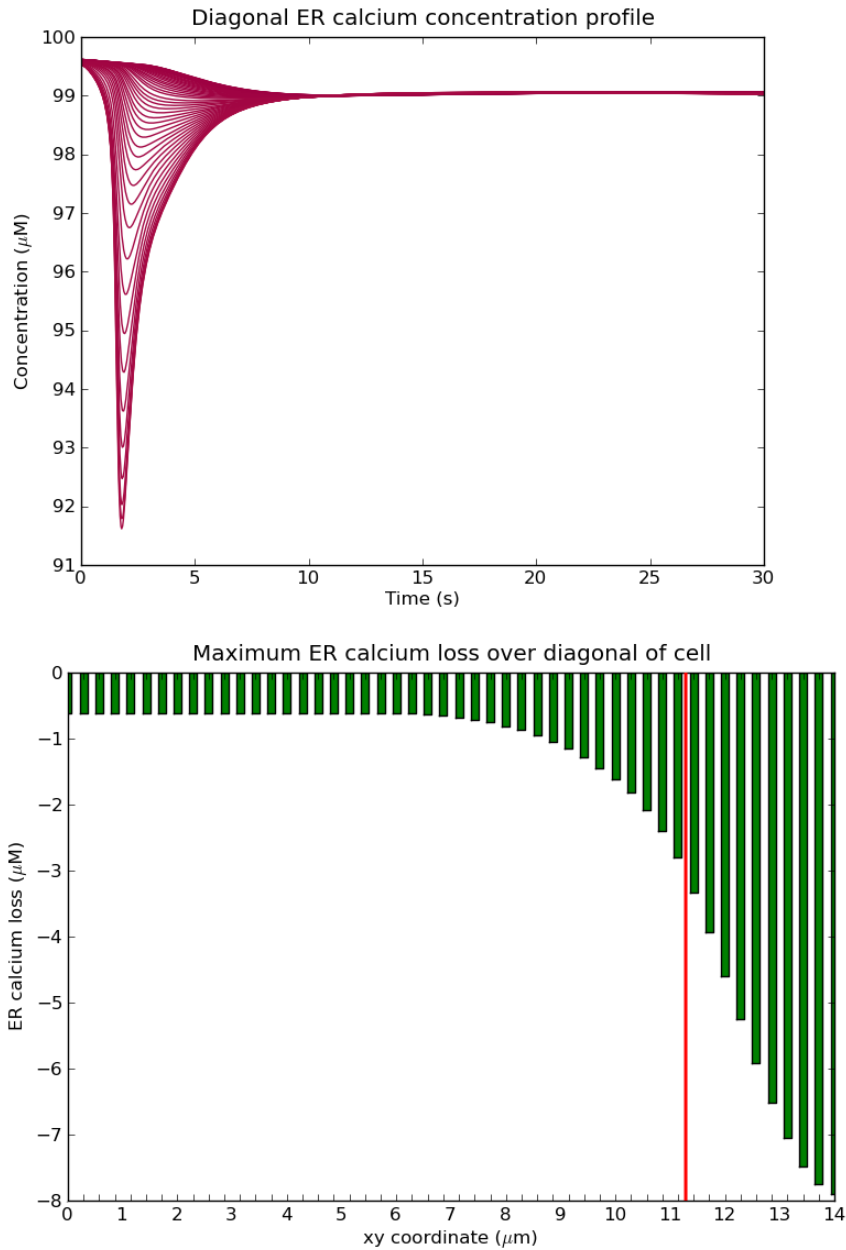


Figure 7.36: Top: Plot showing the change in calcium concentration in the ER compartment for 50 locations across the centre of the cell vs time, from the base to the apex, upon stimulation by 30 μM IP3. Bottom: The same plot as top, but showing the maximum amount of calcium lost by the ER before refilling, against xy coordinates of each sample.

7.4. SIMULATIONS CARRIED OUT WITH REDISTRIBUTED MITOCHONDRIA

lating the cell with redistributed mitochondria show that altered dynamics in the system do arise, and that clustering of the mitochondria provides an effective calcium buffer. The adjustments made to the mitochondrial ODE model, detailed in Section 4.2, have effectively slowed the calcium handling of this organelle, yet in the FEM model it appears that the mitochondria are still very much in control of local calcium dynamics. It is likely that these reduced calcium handling rates are in fact causing the mitochondria to 'hold on' to this calcium for a longer duration when the cell is stimulated, than was intended by the original mitochondria model formulation. As previously discussed in Section 4.2, either the current mitochondrial model requires parameterisation based upon applicable experimental data, or a more flexible model of the mitochondria that can cope with the steady-state calcium concentration in the pancreatic acinar cell is required.

After simulating the cellular response to the stimulus that model equations were originally intended for, the next section examines the effect of exposing the model to BA or FAEE-like molecules, using the modifications that were detailed in Section 4.2.2.

7.5 Onset of acute pancreatitis induced by BA or FAEE-like molecules

The effect of BA and FAEE molecules on the agents included in this implementation may hypothetically recreate the cellular dynamics that occur at the onset of acute pancreatitis, when the cell is first exposed to BA. The processes of autodigestion and apoptosis are not included in the FEM implementation, and so a time course of 15-20 minutes is not necessary. Instead, the following results look at the processes that occur in the first 30 s after the entire cell is exposed to BA or FAEE-like molecules, and the resulting trends assumed to continue. Both BA and FAEE are referred to as 'BA' in the following results, as the same mechanism was assumed to be true for both molecules. The RyR, IPR, and SOC are activated by BA, and the PMCA and SERCA are inhibited by BA^[61,64,74], whereas the mitochondrial agents are left to interact with the calcium dynamics that occur due to the effect BA has on the other agents, as described in Section 4.2.2. Returning to the original distribution of mitochondria in the cytosol, the cell was exposed to BA at a fixed concentration to represent BA entering the system from a constant source, and the concentration was raised over the entire cell at once*.

7.5.1 ER response to BA exposure

An observation commented on experimentally is that the ER is almost completely emptied in cases of pancreatitis, and this is due to stimulation of RyR and IPR coupled with inhibition of SERCA refilling^[61]. Figure 7.37 shows the total ER calcium concentration in response to 25 μM BA over time. Although it is unclear what concentrations of BA are likely to reach the acinar cells, 25 μM BA represents the lower end of concentrations of BA that are thought to induce a response in the cell^[91]. In previous results where the model was stimulated by 30 μM IP3, (either with or without the mitochondrial firewall), the ER was found to lose a maximum of 10%

*For visual assistance to the observations described in the text, please see the videos contained in the 'BA exposure' subdirectory of the supplementary disk.

concentration at individual positions in the cell before recovering and the total ER concentration experienced even less reduction. This reduction in ER calcium seems to be consistent with experimental observation that the ER does not experience a major loss of calcium under normal conditions^[71]. However, the total loss of ER calcium in Figure 7.37 is approximately 43% after just 30 s, and the effect of BA on RyR, IPR, and SERCA means that this loss is not recovered. A steady state between the ER and cytosol will ultimately be reached after 15-20 minutes of continual BA exposure, and the concentration in the ER at this point will be further reduced, similar to the loss found in the ODE implementation, which is consistent with the experimental observation.

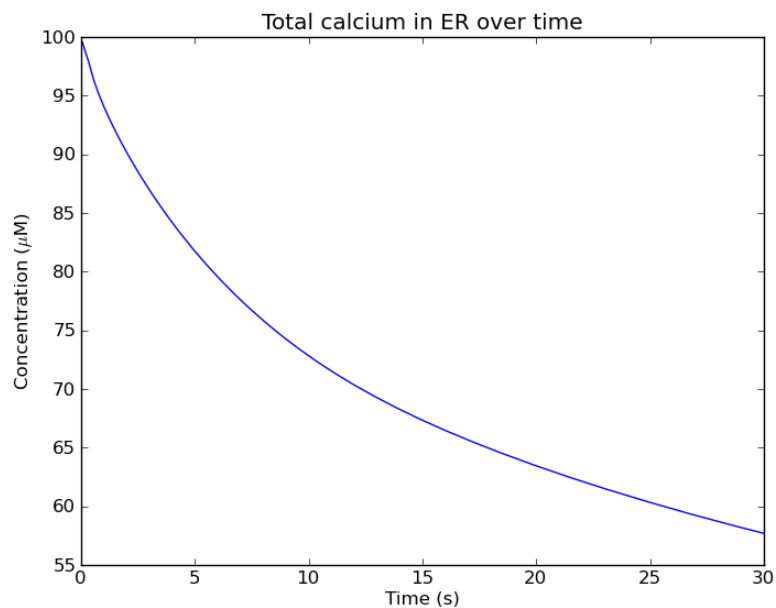


Figure 7.37: Plot showing the effect of stimulation by 25 μM BA on the total ER calcium concentration of the FEM model. A total loss of approximately 43% of ER calcium occurs after just 30 s, and this is consistent with the experimental observation of almost complete emptying of the ER calcium in cases of pancreatitis^[61], whereas experimental observation of cells under normal conditions has shown that there is no major loss of ER calcium^[71].

7.5.2 Cytosol response to BA exposure

Figure 7.38 shows the peak calcium concentration and time to peak data across the diagonal of the cytosol. If the location of mitochondria at the apical boundary ($xy = 11.2 \mu\text{m}$) is considered as well as at the cell boundary ($xy = 0 \mu\text{m}$), the profile

of peak calcium concentrations suggest that the majority of calcium that enters the system in these regions as a result of BA exposure is buffered by the mitochondria (Figure 7.38, top). Channel activation is expected to be uniform across the entire cell in these simulations, however the time taken to reach peak calcium concentration on the plot at the bottom of Figure 7.38 shows that the apical region reaches a peak concentration before the rest of the cell, and this is most likely due to the increased IPR channel density, coupled with PMCA reducing the time to peak. In contrast to the apical region, the basal region takes around 2.5-3 s longer to reach peak calcium concentration, and this is most likely due to different channel densities, coupled with SOC.

Overall, the time it takes to reach a maximal cytosolic calcium concentration is shown to be just over 3.5 s, however the simulation length that produced these results was 30 s (Figure 7.38, bottom). During this time the ER has continually emptied, yet there has not been a continual increase in cytosolic calcium concentration; instead, the cytosol is in fact shown to decrease in calcium concentration after reaching a maximum at approximately 3 s (Figure 7.39). The cytosolic calcium concentration falls to approximately $0.37 \mu\text{M}$ after 30 s, where it appears to be slowly working toward an elevated steady state. While only 50% of the PMCA pumps are inhibited by $25 \mu\text{M}$ BA in this model, due to the $25 \mu\text{M}$ half saturation constant for BA that was applied, these pumps are not solely responsible for the reduction of cytosolic calcium. Instead, the mitochondria are accumulating this calcium over time.

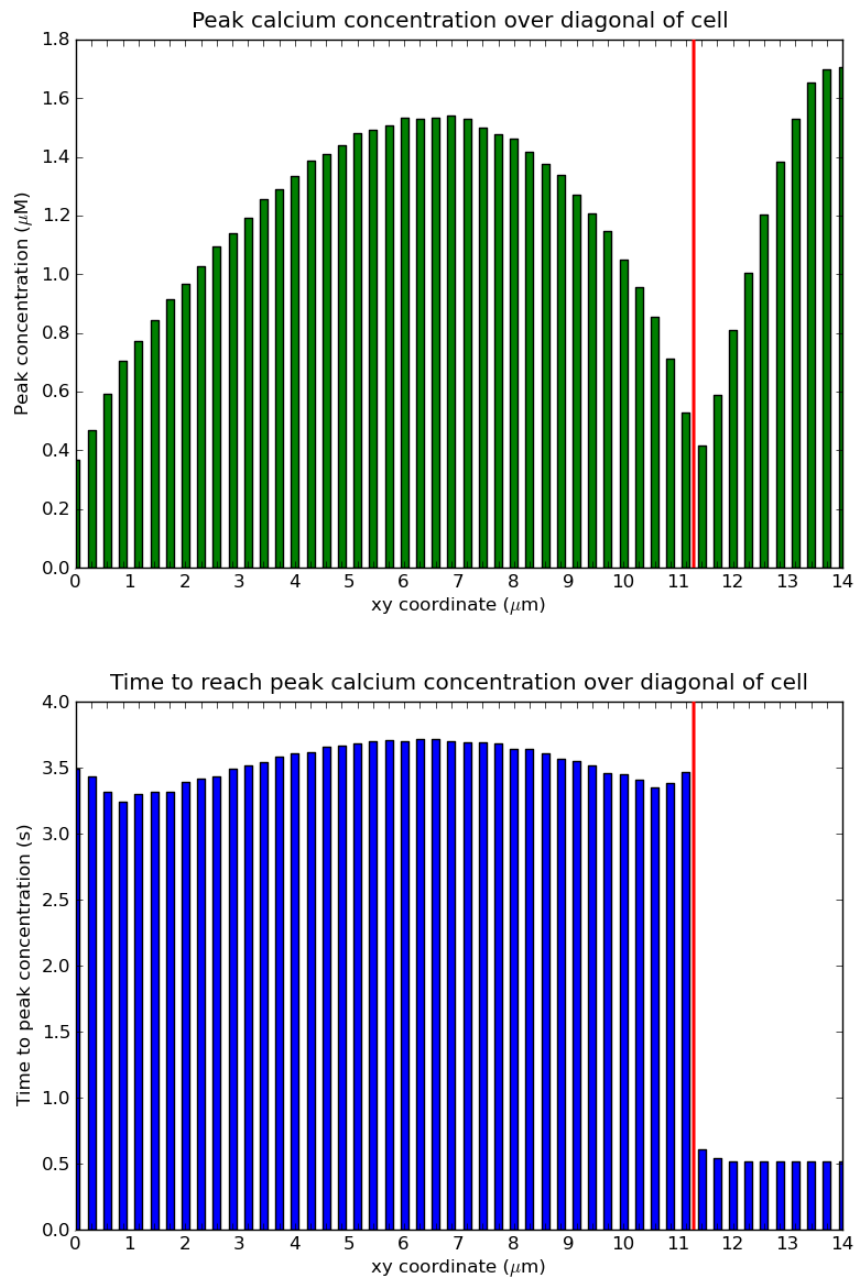


Figure 7.38: Top: Plot showing calcium peak data in response to 25 μM IP3. The values on the x-axis correspond to the coordinates for x and y between the base (0,0) and apex (14,14) of the cell. The apical boundary is at $xy=11.2$. The mitochondria appear to buffer the majority of calcium released during exposure to BA at the apical boundary and nearer to the cell boundary (top). The difference in channel densities between the apical and basal regions is responsible for difference in time to peak calcium concentrations shown in the bottom plot. The basal region contains a higher density of RyR channels than the apical region, and the combined release of these channels over a large area results in a longer time to peak.

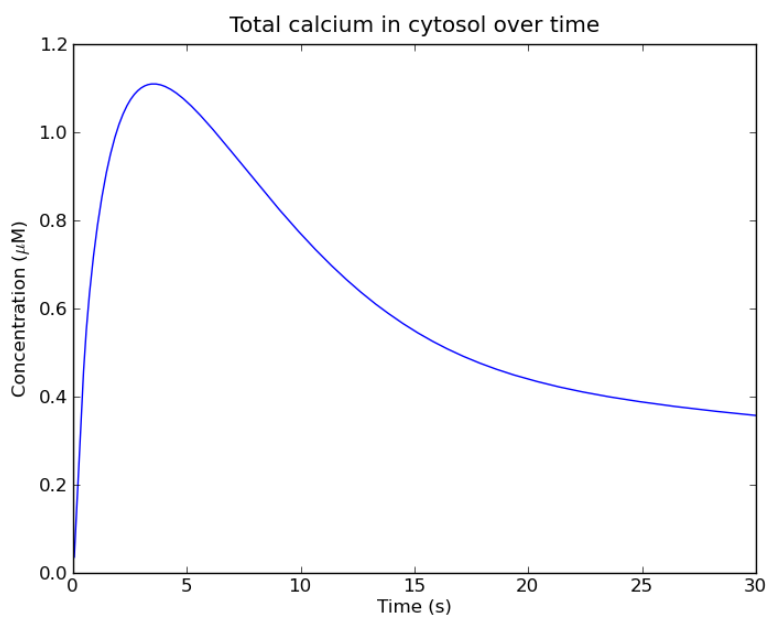


Figure 7.39: Plot showing the total calcium concentration change in the cytosol over time, when the cell is exposed to 25 μM BA.

7.5.3 The mitochondrial response to BA-induced calcium dynamics

The plot in Figure 7.40 shows the change in mitochondrial calcium over time for each agent in the model, when stimulated with 25 μM BA. During the 30 s simulation, the mitochondria have accumulated the majority of calcium released from the ER into the cytosol, which has increased the mitochondrial calcium concentration from between 0.007 and 0.025 μM , to concentrations between 1.4 and 5.3 μM , after 30 s of BA stimulation. Mitochondria located around the cell membrane nearer to the SOC channels accumulate the most calcium during BA exposure, due to continued influx from the extracellular source.

Exposure of the cell to a higher concentration of 50 μM BA shows that the mitochondria accumulate more calcium than at 25 μM BA (Figure 7.41). This is due to the combined effect of almost 100% inhibition of SERCA and PMCA in the model and increased ER calcium loss, together with further increase in SOC flux into the cytosol.

7.5.4 Usefulness as a model of acute pancreatitis onset

The mitochondria in these simulations appear to buffer the majority of calcium that cause elevated concentrations in the cytosol. This is a safety mechanism of the mitochondria under normal conditions, which is thought to protect parts of the cell from increased calcium concentrations that may be harmful. The FEM implementation does not include representation of the apoptotic chain or activation of digestive enzymes that may simulate the entire mechanism of pancreatitis. However, sustained elevation of cytosolic calcium is shown here to accumulate inside the mitochondria, and this is consistent with the literature for cells that are in such a diseased state^[74].

An aspect of the model which is of interest to the treatment of acute pancreatitis is ATP depletion in the acinar cell. Diseased cells exhibit reduced ATP concentration, due to increased consumption by ATP-dependent pumps, and reduced

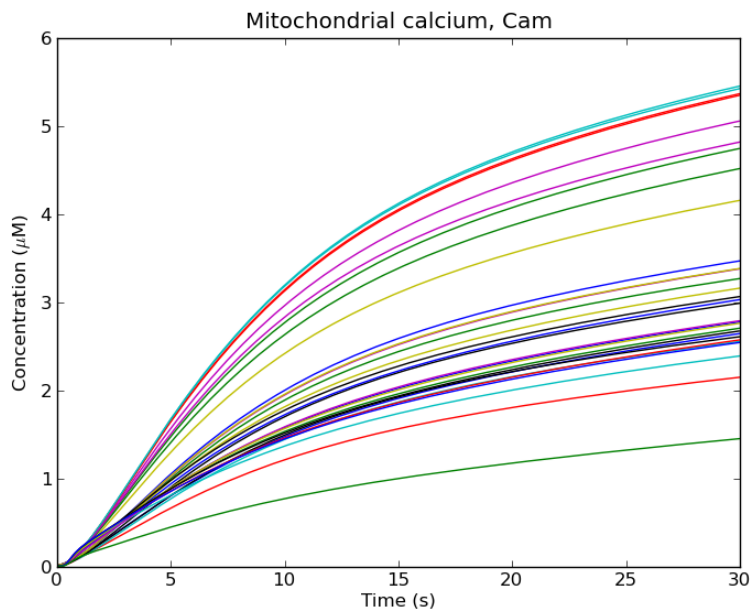


Figure 7.40: Plot showing the effect of $25 \mu\text{M}$ BA on mitochondrial calcium in the cell. The mitochondria have buffered much of the influx of calcium into the cytosol, and only decrease in rate as the ER empties and reaches a steady state with the cytosol. Each mitochondrion is coloured differently to allow each to stand out. The range of concentrations and grouping is a consequence of spatial localisation. Mitochondrial agents closer to channel agents accumulate calcium faster than those that are not.

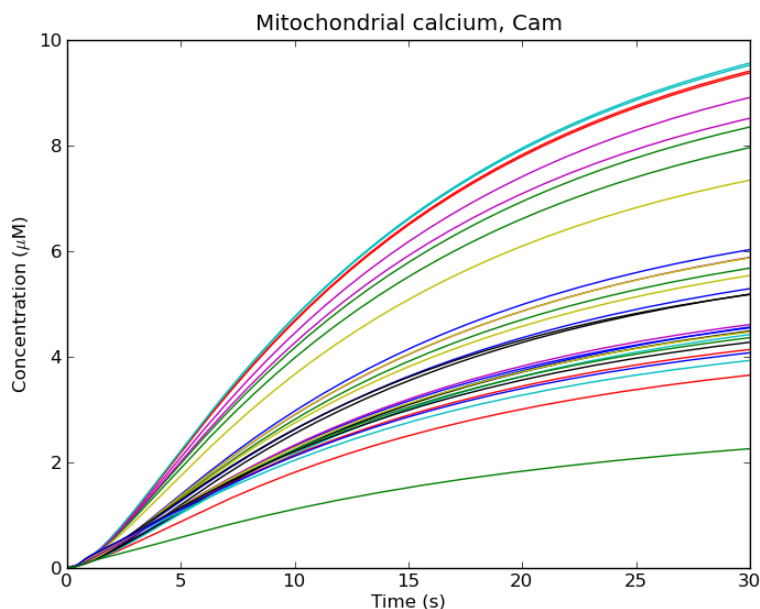


Figure 7.41: Plot showing the effect of $50 \mu\text{M}$ BA on mitochondrial calcium in the cell. The mitochondria have buffered much of the influx of calcium into the cytosol, and only decrease in rate as the ER empties and reaches a steady state with the cytosol. Each mitochondrion is coloured differently to allow each to stand out. The range of concentrations and grouping is a consequence of spatial localisation. Mitochondrial agents closer to channel agents accumulate calcium faster than those that are not.

production of ATP by compromised mitochondria, which suggests a route to treatment and reduction of cytosolic calcium through delivery of encapsulated ATP to the cell^[61]. This implementation of the pancreatic acinar cell does include ATP, and has the ability to include simplistic ATP consumption by SERCA and PMCA, as well as ATP-supply pump rate modulation. However, a set of parameters for ATP consumption and supply could not be found that adequately balance all of the above without destroying the expected 'natural' model behaviour. Therefore, the ATP mediated effects of calcium dynamics were not used when generating results for the investigation. With a better representation of ATP supply and consumption, the model may enable further understanding into this aspect of pancreatitis.

7.6 Summary

This section has analysed the results produced by the FEM implementation that was based upon the ODE model of the coupled acinar cell and the mitochondria. The components included in the coupled acinar cell and mitochondria model were extracted and distributed, such that a spatial representation of SERCA, IPR, RyR, SOC, and mitochondria was achieved. These were linked by the physical diffusion of calcium in the cytosol and ER, and both ATP and ADP in the cytosol. The aim of simulating these components using a spatial representation was to allow emergent behaviour to arise from the detail encoded in the simplistic ODE model.

The models by Sneyd et al. represent channels in the apical and basal regions of the cell as identical, but with different rate constants that depend on their location. In addition to this, all model components contributed to the same local space, and this was also the case for the ODE implementation of the coupled mitochondria-acinar ODE model that was previously analysed. In this multiscale FEM implementation, channels are used that have identical rate constants but exist at different densities, depending on the region of the cell. Additionally, particular regions of the cell include channels and pumps that others do not, resulting in the polarised

distribution of features characteristic of this cell type.

These results do not reproduce global oscillations that originate from the apical region in response to the physiological range of IP₃ concentrations used experimentally, nor does it allow detailed analysis of ATP consumption and supply. However, the results from these simulations show that behaviour has been successfully decoupled such that localised oscillations may be confined to the apical region, and propagate throughout the basal region upon removal of the mitochondrial firewall. The detail included in these results allows observation of local calcium microdomains that occur in the cytosol during stimulation due to distribution of agents, demonstration of ER calcium tunnelling, propagation of the calcium wave via CICR of RyRs, and the privileged communication of calcium signals between the ER and a subpopulation of the mitochondria. The model also demonstrates a possible mechanism to the formation of mitochondrial subpopulations near the apical boundary and the cell membrane, resulting from distribution of cytosolic calcium. Additionally, the hypothesised calcium dynamics that occur during the onset of acute pancreatitis are demonstrated that result from exposure to BA or FAEE-like molecules. The majority of these details previously mentioned have not been found to be modelled or commented on in previous computational models of the cell.

Chapter 8

Conclusions

8.1 Lessons learned from multiscale modelling

The complex characteristics exhibited by calcium dynamics in the cell make this ion important for understanding cellular processes and research into disease. Therefore, aims for this study began simply; research into biological systems and diseases that involve calcium.

Well remembered at the beginning of this research is the number of results retrieved for the search term 'calcium signalling in the cell' in a popular journal database. Tens of thousands of these hits revealed the true breadth of this field of biology, hinted at in textbooks. A path that led to the cardiac cell was initially followed, due to the importance of calcium dynamics in producing a healthy heartbeat. The implementation of published ODE models of the cardiac cell provided a feel for the relationship between fluxes, compartments, channels, and rate equations. From here, a number of conclusions about these models were derived.

The first conclusion involved understanding that these models are very sensitive to minor changes, which can cause integration errors that are frustratingly difficult to understand and resolve. The more complex a model becomes the more difficult it is to resolve these issues, due to the extent in which degrees of freedom interact with one another.

The second conclusion involved recognising that dimensional consistency is key

to producing a working implementation. With missing parameter dimensions, or dimensional inconsistencies in model equations, such complex models can lose the confidence of a modeller trying to reproduce published results. Unfortunately, the more complex a system becomes, the easier it is to make mistakes in published material. The best way found for reproduction of results was to directly contact the model authors for the original source code, rather than use a model repository such as CellML. However, models obtained from online repositories such as this increase in reliability after curation by experts.

At this point in the project, the lessons learned about cardiac cell dynamics were that these models are extremely complex, and prone to errors as a result. It is difficult to tell how much detail emerges from the contributing features of models so complex, and how much simply exists because it was parameterised to make it exist in the first place. Additionally, the existing research into this cell type is extensive, and while a multiscale model could be constructed of this system, it is unlikely to enable investigation of hypotheses that have not already been extensively modelled. The mitochondria had previously been identified as an interesting target for multiscale modelling, and this ultimately led to interest in the pancreatic acinar cell, where the particular arrangement of mitochondrial subpopulations proved intriguing, together with events that occur at different timescales. Very few models of the pancreatic acinar cell were found to have been published, and those that have appeared to be relatively simple in structure. In addition to this, the published models did not specifically investigate some of the biological observations that made this cell type of interest to the project.

The third conclusion involved understanding the issues that can arise when extending these types of mathematical model. Coupling two models together can upset the complex and sensitive dynamics of both, and increase the likelihood of integration errors. However, understanding how the two models behave independently of each other provides some advantage when faced with these issues. The importance of model parameterisation was also reinforced through this process of

coupling models together. Individually, the model of the mitochondria was found to be highly parameterised to the system upon which it was based, and the acinar cell model was tightly fitted to experimental data. When combined, the mitochondria model could not cope with the lowered homeostatic concentration of calcium in the acinar cell model, and the acinar cell model could not cope with the altered dynamics introduced by the mitochondria model. This highlighted a lack of flexibility in cellular models. These issues were resolved through the use of scaling parameters that adjust the interaction between mitochondria and the surrounding environment. While this was justified to an extent, it is not an ideal solution to the problem, and a full reparameterisation is really called for. Despite the seeming complexity of these models, they are still highly parameterised in order to achieve the desired result, and make many assumptions. Again, the extent to which a model exhibits emergent behaviour is unclear, and it seems like the cellular level modeller is only likely to observe behaviour that has been programmed in. By working with incomplete information about a system, this is perhaps necessary, but this also results in models that are in many ways non-transferable or extendible into other models.

The fourth conclusion was more of a lesson in construction, and involved gaining experience in the extension of a somewhat singular dimension ODE model into, with a little imagination, a model with multiple dimensions in the form of the FEM model. To represent the system in a better physics-based environment, this required application of different programming techniques than used for construction of the ODE models. The experience gained previously in the project with respect to error tracking in ODE models proved invaluable, as this portion of the project did not come without problems. Time step issues, parameter searching, extraction of relevant information, and computational efficiency all needed consideration. Further than this, interpretation of the results produced by such a multiscale model was found to require all experience gained from previous modelling efforts of these systems.

8.1.1 Concluding remarks on model results

This example of a multiscale model incorporates events that occur on a time scale for diffusion of species, channel state transition, mitochondrial metabolism, and mitochondrial motility. The combined effect of all these components contributes to a much broader representation of the cell, on a larger time scale. The microscopic spatial propagation of a calcium wave can be observed, and the effect of this wave on a much lower, molecular, level can also be seen, where diffusing calcium may activate RyR channels. Calcium that diffuses toward a single mitochondrion imparts an effect on the production of ATP that may not be observed in a mitochondrion at another location that this elevated calcium did not reach.

All this information is missing from simulations that consider events on a single spatio-temporal scale, as shown by the ODE implementation. Everything is assumed to occur in the same compartment, and occur instantaneously across the entire cell. While ODE models have the advantage of being simple, of relatively low computational cost to solve, and easy to test hypotheses, the detail offered by diffusional PDE models such as FEM is very attractive to the modeller who wishes to investigate cellular dynamics. However, the detail available to the modeller is restricted by the computational cost that results from using a more sophisticated modelling technique, the capability of the underlying model, and the availability of relevant parameters. Computational cost increases as more scales are incorporated into the model, so it is important to consider what is important, and what assumptions are required to allow conclusions to be made.

The models that have been implemented in this study include the common pool ODE model representation of the pancreatic acinar cell by Sneyd et al., and a simplified model of the mitochondria by Bertram et al., for use in place of the basic representation of mitochondria in the acinar cell ODE model by Sneyd et al. Both of these original models make assumptions about the cellular environment, which enabled them to be simple representations of a complex problem to begin with. The common pool acinar cell ODE model by Sneyd et al. only models processes that

include calcium, assumes that all of these processes occur in the same pool of concentration, and that the mitochondria simply absorb calcium and do not release it back into the cell. The mitochondria ODE model by Bertram et al. reduces the complexity of more detailed models of mitochondrial metabolism by assuming that several steps of the citric acid cycle can be reduced to a single rate-limiting step, and that ionic concentrations of sodium in the cytosol are constant, in addition to others. The ability to make assumptions such as these is a strength of mathematical modelling at higher scales, however these can also make the extension of such models a challenging task. Sometimes these are too heavily parameterised with the assumptions they make, that any attempt to change the model without destroying the underlying dynamics can be difficult. Other models of calcium dynamics in the cell may be more sophisticated than the model by Sneyd et al. used in this study, however these may also make assumptions. Models of the cardiac cell for example, are extensively studied and increasingly complex^[93,94]. However, while they may model the detailed diffusion around complex geometry, they may also assume that the physiological process of contraction, whereby the cell changes shape, does impart an additional effect on cell dynamics.

Results from the coupled acinar and mitochondria ODE model of the cell helped gain understanding of the complexity that could be disentangled by the FEM implementation. The effect of IP₃ on the mitochondria, mediated by all of the cellular processes that occur in the system, was observed quickly, and the ODE implementation allowed adjustments to be made to channel dynamics and the mitochondria to be tested for stability. When implementing the FEM model some of this stability was lost, because some parameters were not directly transferable. Upon finding a set of parameters that reproduced the majority of expected results, based upon information found in scientific literature, the resulting information could be processed with the predictions offered by the ODE version in mind.

The FEM implementation showed that the apical region reaches a peak calcium concentration before the rest of the cell due to the increased density of channels, as

shown by experimentalists. These regions of different channel density were previously modelled through altered rate constants, whereas the direction taken in this study was to represent the regions in a more physical manner. Also observed was how the ER allows a constant supply of calcium to the apical region, in-between IP₃ mediated stimulus. This is made possible by tunnelling calcium from SOC at the base of the cell to the apical portion of the ER, as hypothesised by experimentalists. Mitochondria in the apical region of the cell were found to act as a considerable firewall to apical calcium transients, and blocked the majority of calcium that was released in this area. This was consistent with experimental observations to an extent, but the model could not reproduce the expected transients generated by higher IP₃ concentrations that break through the firewall. Removal of the mitochondria did however result in a propagated calcium wave, that extends throughout the rest of the cell, as observed by experimentalists. The adjustments made to the mitochondria model to enable it to be compatible with the conditions offered by the acinar cell meant that the calcium handling was too slow. This reinforced the idea that either reparameterisation, or a more transferable model of the mitochondria is required.

Mitochondrial motility was included, to test the hypothesis that mitochondria are recruited to regions of the cell that have increased metabolic activity. Metabolic activity was inferred from the literature as regions of increased calcium concentration, so simple rules were put in place for the mitochondria to move around the cytosol on a path dictated by the local calcium gradient. This was coupled together with the notion that calcium concentrations nearing 1-2 μM result in temporary arrest of mitochondrial motility. The results of mitochondrial motility simulations from a selection of different starting positions showed that mitochondria clustered in the apical region, remained near the cell boundary, and in some cases remained in the centre of the cell. These subpopulations have been described in the literature as perigranular, sub-plaslemmal, and non-specific. While the true mechanism behind mitochondrial distribution in cells is not yet clear, these results provide some insight into the effect that the local environment may have on the mitochondria in

the pancreatic acinar cell.

A hypothetical disease state representing the onset of pancreatitis was also modelled. Sensitivity of the cell to BA or FAEE-like molecules was achieved through modification of the Markovian RyR and IPR models through addition of these molecules to rate equations that contribute to channel open state, modification of SERCA and PMCA pumps to be inhibited by the molecules, and increased influx through SOC during exposure. The combined effect of these modifications was then observed for the cell and the mitochondria. The ODE implementation provided the expected results of exposure to BA, which included ER calcium depletion, and cytosolic calcium elevation; both observed experimentally in cells that have developed acute pancreatitis due to BA or FAEE exposure. These observations were replicated in the FEM model. Owing to issues with modelling ATP supply and demand, the hypothesis that increased ATP consumption by the ATP-dependent SERCA and PMCA pumps caused ATP depletion in the cell could not be directly modelled. However, it was shown that accumulation of calcium occurred in the mitochondria and this is observed experimentally. Continued mitochondrial calcium accumulation can over time result in the formation of MPTP, which disrupts the mitochondrial membrane potential, as well as other mitochondrial processes. This was put forward as the main mechanism of ATP depletion in the cell, along with depletion due to ATP-dependent processes.

8.1.2 Future extension and improvement to the multiscale model of the pancreatic acinar cell

Parameterisation and construction

To find a collection of parameters in the model that exhibit all of the phenomena observed experimentally in the pancreatic acinar cell is a mammoth task, given the assumptions in the current model. The parameters used in both ODE and FEM implementations were taken from simple models, where parameters were fitted in

order to reproduce experimental data. Therefore, placing them in a differently constructed model environment does not guarantee similar results. Although the multiscale model distributed the agents based upon what was inferred from the literature, and behaviour that appeared 'correct', the model cannot be taken as 'correct' because of the assumptions that have been made. However, this does not mean that with a better set of parameters and computational resources the model cannot provide a result that reproduces experimental data more fully.

To consider parameters as 'better', or 'realistic', they should be obtained from studies of the same cell type that is modelled. A diffusion constant measured for calcium in water is different to that measured in the cytosol of a cell, and this may vary cell to cell. This is due to the difference in content of proteins that may interfere with diffusion (such as buffers), and the complex geometry found in each cell type. Sneyd et al. used a diffusion constant of $10 \mu\text{m}^2 \text{s}^{-1}$ for calcium in their models, but this is quite different to the same parameter for the cytosol in another cell model by Means et al (2006)^[37], where a diffusion constant of $223 \mu\text{m}^2 \text{s}^{-1}$ was used. The diffusion constant used by Sneyd et al. together with the other parameters in the model provided them with results that were comparable to experiment, and for this reason it was used as the diffusion constant in this multiscale model. However, this same parameter was also used here for calcium diffusion in the ER, and both ATP and ADP in the cytosol. The use of a single diffusion constant for each species removed potential issues arising from the need for different sized time steps, or finding a single time step that provided an adequate trade off between detail and computational speed between the layers in which the diffusion equation is solved. But this also contributed to the problem of parameterisation. For example, the ER is thought to diffuse 3-6 times slower than the cytoplasm, which may affect the time for recovery of concentration in the apical portion of the ER^[95].

As stated before, increasingly complex models become difficult to make changes to without disrupting the dynamics that already exist. Parameter optimisation of the ODE type models could perhaps use some kind of custom and automated param-

eter optimisation routine designed for fitting to experimental data. More complex types of model that include spatiotemporal dynamics would be much more difficult to optimise in this way. The complex relationship between all parameters in the model, combined with additional factors such as spatial localisation and behaviour such as wave speed, would be very computationally expensive, and would likely require a lot more experimental data. Therefore, improvement of the multiscale FEM model would, in part, depend on further development of the ODE version. However, this is only possible for the parameters that are directly transferable, such as those involving the ODEs for the mitochondria and channel dynamics. Parameters that involve the distribution of agents, agent density, or diffusion require adjustments to be made directly to the FEM model, which takes more time to solve and are more difficult to interpret.

Research that follows on from this study would involve complete reparameterisation of the mitochondrial agents with reference to mitochondrial data obtained from the pancreatic acinar cell, or the use of a completely different model altogether. This would ensure that the interaction between mitochondrial adenines and calcium with cytosolic concentrations is better represented. A better representation of IPR, RyR, and SERCA distribution over the ER membrane, would benefit the model as being more realistic, however this could increase computational cost.

One of the disadvantages to modelling using FEM in comparison to ODE models is the increased amount of computing power required, and the efficiency of the code. The multiscale model in this study suffered from a combination of these problems, which meant that incredibly detailed simulations involving much smaller time steps and higher agent densities simply were not possible. In addition, the University of Southampton supercomputer Iridis II was not configured to run the software required by Python for this simulation at the time, and FEniCS suffered from performance issues that further increased computation time. This meant that while the model was constructed with the a view to utilising the supercomputing facilities, the final results had to be generated using desktop PCs. Each running job needed con-

tinuous observation, such that a job could be restarted if the performance dropped. Future modelling efforts that enable the multiscale model to run using more powerful computing resources brings the possibility of increased realism to parameters and removal of some of the assumptions made.

Cellular geometry

Currently, the pancreatic acinar cell is being represented by the FEniCS 2D rectangle function, which was only used as an approximation of shape. FEM allows the solution of PDEs over virtually any geometry that can be designed, and therefore future models should involve a better representation of the 2D acinar cell shape, which may exhibit more realistic calcium dynamics. Further species could be included through the addition of more 'layers', as could additional organelles, such as the nucleus and golgi.

Extension of the 2D representation into 3D would impart an additional effect on the calcium dynamics of the system. For example, if the same number of apical mitochondria are used to create a mitochondrial firewall, each agent would be more spread out in 3D space than represented in 2D. This could mean that oscillations in the apical region can in fact break through the mitochondrial firewall at a low range of IP₃ concentration, compared to the results shown in this study.

Taking model extension to 3D further, a realistic geometry of the pancreatic acinar cell could be obtained by tomography, and this could even include the location of the mitochondria, the complex geometry of the ER, and the location of ZGs. The calcium handling of each organelle could be modelled, along with other cellular processes, and the diffusion of calcium around more complex geometry would provide further insight into the calcium signalling dynamics of the acinar cell.

Pancreatitis

Future research into the mechanisms of pancreatitis may require the inclusion of additional cellular organelles and processes in this model, such as mathematical

models of mitochondrial apoptosis^[96], the inclusion of ZGs with premature activation of their digestive contents, and organ level scales that glean information from this cellular representation^[80]. Better representation of ATP supply and demand in the model cell will benefit research involving encapsulated ATP therapy for pancreatitis^[61].

Collaboration

Collaboration with experimental biologists who specialise in the pancreatic acinar cell is probably one of the most important parts of future modelling efforts. Working with those who have first-hand experience of this area of biology can provide further insight into results produced by the model, customised experimental data, and knowledge of sensible parameters. In almost all published models researched during the project, the authors seemed to be a mix of mathematicians or computer scientists, and biologists who specialise in the particular field of the cell type. This interaction between areas of expertise would be very beneficial for such a complex system.

Final words

To conclude, this study involved construction of a multiscale model of the pancreatic acinar cell, based upon a more simple representation of the system. Where possible, the assumptions made by the model have been justified. Many of the assumptions that had to be made are a result of the complexities that arise from combining models of dynamic and sensitive systems. These complexities highlight the difficulty in constructing multiscale models at the cellular level.

Results were produced that indicate processes occurring at multiple scales of time and space, which include the activation of channels, the movement of mitochondria, the propagation of calcium waves, ER calcium tunnelling, the onset of acute pancreatitis, and calcium transients localised to portions of the cell. The majority of these results, and the approach taken to generate them, are unique in the

field of computational models of the pancreatic acinar cell.

Glossary

ACh Acetylcholine.

AChE Acetylcholinesterase.

AChR Acetylcholine receptor.

ADP Adenosine diphosphate.

agonist A molecule or that stimulates a reaction.

Apoptosis Programmed cell death.

AT Atomistic model

ATP Adenosine triphosphate.

BA Bile acid.

Brownian dynamics A molecular simulation method that describes the motion of molecules.

CaRU Calcium release unit; theoretical coupling of RyR and LCC channels into a single functional unit.

CellML Cell markup language.

CG Coarse-grained model.

CICR Calcium induced calcium release; a phenomena in excitable cells that allows communication of signals through a self-propagating calcium wave.

CMD Calmodulin.

COR Cellular open resource.

CSQ Calsequestrin.

Cytosol The intracellular compartment of the cell that contains other organelles.

DNA Deoxyribonucleic acid.

ER Endoplasmic reticulum, a cellular organelle that among other purposes acts as a calcium store.

F1F0-ATPase An enzyme that synthesises ATP using the mitochondrial proton gradient.

FAD Flavin adenine dinucleotide, where FADH is the reduced version of FAD⁺.

FAEE Fatty acid ethyl ester.

FBP Fructose 1,6-bisphosphate.

FEM Finite element method.

FEniCS/DOLFIN Collection of Python tools that enable automated solution of differential equations by finite element methods.

Golgi A cellular organelle that stores and packages proteins for transportation to other parts of the cell.

IP3 Inositol triphosphate.

IPR Inositol trisphosphate receptor.

JSR Junctional sarcoplasmic reticulum.

LCC L-type calcium channel; a voltage gated channel that results in calcium influx to the cell.

M Molar; the number of moles of a substance per cubic metre.

Mitochondria A cellular organelle responsible for providing the majority of ATP as a source of energy.

MM Molecular mechanics.

Mole A unit describing the amount of a substance.

Motility Movement.

MPTP Mitochondrial permeability transition pore.

NAD Nicotinamide adenine dinucleotide, where NADH is the reduced version of NAD⁺.

NMJ Neuromuscular junction.

NSR Network sarcoplasmic reticulum.

ODE Ordinary differential equation.

Parotid cell A cell found in salivary glands, used in production of saliva.

PDE Partial differential equation.

PKC Protein kinase C.

PMCA Plasma membrane ATPase.

QM Quantum mechanics.

RK4 Runge Kutta fourth order integrator.

RyR Ryanodine receptor; a calcium channel sensitive to the molecule ryanodine, and is involved with calcium induced calcium release (CICR).

SERCA Sarco-endoplasmic reticulum ATPase.

SI The international system of units.

SOC Store-operated channel.

SPiM Stochastic Pi Machine.

SR Sarcoplasmic reticulum.

Tomography The building up of a three dimensional image from two dimensional slices.

ZG Zymogen granule.

Bibliography

- [1] Mulholland, A. J. Computational enzymology: modelling the mechanisms of biological catalysts. *Biochemical Society transactions* **36**, 22–6 (2008).
- [2] Southern, J., Pitt-Francis, J., Whiteley, J., Stokeley, D., Kobashi, H., Nobes, R., Kadooka, Y. & Gavaghan, D. Multi-scale computational modelling in biology and physiology. *Progress in biophysics and molecular biology* **96**, 60–89 (2008).
- [3] Qu, Z., Garfinkel, A., Weiss, J. N. & Nivala, M. Multi-scale modeling in biology: how to bridge the gaps between scales? *Progress in biophysics and molecular biology* **107**, 21–31 (2011).
- [4] Stein, M., Gabdouliline, R. R. & Wade, R. C. Bridging from molecular simulation to biochemical networks. *Current opinion in structural biology* **17**, 166–72 (2007).
- [5] Gabdouliline, R. R., Kummer, U., Olsen, L. F. & Wade, R. C. Concerted simulations reveal how peroxidase compound III formation results in cellular oscillations. *Biophysical journal* **85**, 1421–8 (2003).
- [6] Bondarenko, V. E. & Rasmusson, R. L. Action Potential Propagation in Inhomogeneous 2D Mouse Ventricular Tissue Model. *World Academy of Science, Engineering and Technology* **54**, 269–275 (2009).
- [7] Orsi, M., Sanderson, W. E. & Essex, J. W. Permeability of small molecules through a lipid bilayer: a multiscale simulation study. *The journal of physical chemistry. B* **113**, 12019–29 (2009).

- [8] Karr, J. R., Sanghvi, J. C., Macklin, D. N., Gutschow, M. V., Jacobs, J. M., Bolival, B., Assad-Garcia, N., Glass, J. I. & Covert, M. W. A Whole-Cell Computational Model Predicts Phenotype from Genotype. *Cell* **150**, 389–401 (2012).
- [9] Clancy, C. E. Na⁺ Channel Mutation That Causes Both Brugada and Long-QT Syndrome Phenotypes: A Simulation Study of Mechanism. *Circulation* **105**, 1208–1213 (2002).
- [10] Berridge, M. J. Calcium microdomains: organization and function. *Cell calcium* **40**, 405–12 (2006).
- [11] Walsh, C., Barrow, S., Voronina, S., Chvanov, M., Petersen, O. H. & Tepikin, A. Modulation of calcium signalling by mitochondria. *Biochimica et biophysica acta* **1787**, 1374–82 (2009).
- [12] Bers, D. M. Cardiac excitation-contraction coupling. *Nature* **415**, 198–205 (2002).
- [13] Garny, A., Nickerson, D. P., Cooper, J., Weber dos Santos, R., Miller, A. K., McKeever, S., Nielsen, P. M. F. & Hunter, P. J. CellML and associated tools and techniques. *Philosophical transactions. Series A, Mathematical, physical, and engineering sciences* **366**, 3017–43 (2008).
- [14] Leach, A. R. *Molecular Modelling: Principles and Applications* (Pearson Prentice Hall, 2001), 2nd edn.
- [15] Keizer, J. & Levine, L. Ryanodine receptor adaptation and Ca²⁺-induced Ca²⁺ release-dependent Ca²⁺ oscillations. *Biophysical journal* **71**, 3477–87 (1996).
- [16] Stern, M. D. Theory of excitation-contraction coupling in cardiac muscle. *Biophysical journal* **63**, 497–517 (1992).
- [17] Soeller, C. & Cannell, M. B. Analysing cardiac excitation-contraction coupling with mathematical models of local control. *Progress in biophysics and molecular biology* **85**, 141–62 (2004).

- [18] Winslow, R. L., Cortassa, S., O'Rourke, B., Hashambhoy, Y. L., Rice, J. J. & Greenstein, J. L. Integrative modeling of the cardiac ventricular myocyte. *Wiley interdisciplinary reviews. Systems biology and medicine* **3**, 392–413 (2011).
- [19] Winslow, R. L., Tanskanen, A., Chen, M. & Greenstein, J. L. Multiscale modeling of calcium signaling in the cardiac dyad. *Annals of the New York Academy of Sciences* **1080**, 362–375 (2006).
- [20] Hilgemann, D. W. & Noble, D. Excitation-Contraction Coupling and Extracellular Calcium Transients in Rabbit Atrium: Reconstruction of Basic Cellular Mechanisms. *Proceedings of the Royal Society B: Biological Sciences* **230**, 163–205 (1987).
- [21] Luo, C. H. & Rudy, Y. A dynamic model of the cardiac ventricular action potential. I. Simulations of ionic currents and concentration changes. *Circulation research* **74**, 1071–96 (1994).
- [22] Soeller, C. & Cannell, M. B. Numerical simulation of local calcium movements during L-type calcium channel gating in the cardiac diad. *Biophysical journal* **73**, 97–111 (1997).
- [23] Yu, Z., Holst, M. J., Hayashi, T., Bajaj, C. L., Ellisman, M. H., McCammon, J. A. & Hoshijima, M. Three-dimensional geometric modeling of membrane-bound organelles in ventricular myocytes: bridging the gap between microscopic imaging and mathematical simulation. *Journal of structural biology* **164**, 304–313 (2008).
- [24] Bondarenko, V. E., Sziget, G. P., Bett, G. C. L., Kim, S.-J. & Rasmusson, R. L. Computer model of action potential of mouse ventricular myocytes. *American journal of physiology. Heart and circulatory physiology* **287**, H1378–403 (2004).
- [25] Noble, D., Varghese, A., Kohl, P. & Noble, P. Improved guinea-pig ventricular cell model incorporating a diadic space, IKr and IKs, and length- and tension-dependent processes. *The Canadian journal of cardiology* **14**, 123–34 (1998).

- [26] Bondarenko, V. E., Bett, G. C. L. & Rasmusson, R. L. A model of graded calcium release and L-type Ca^{2+} channel inactivation in cardiac muscle. *American journal of physiology. Heart and circulatory physiology* **286**, H1154–69 (2004).
- [27] Greenstein, J. L. & Winslow, R. L. An integrative model of the cardiac ventricular myocyte incorporating local control of Ca^{2+} release. *Biophysical journal* **83**, 2918–45 (2002).
- [28] Sneyd, J., Tsaneva-Atanasova, K., Bruce, J. I. E., Straub, S. V., Giovannucci, D. R. & Yule, D. I. A model of calcium waves in pancreatic and parotid acinar cells. *Biophysical journal* **85**, 1392–405 (2003).
- [29] Wagenknecht, T., Hsieh, C.-E., Rath, B. K., Fleischer, S. & Marko, M. Electron tomography of frozen-hydrated isolated triad junctions. *Biophysical journal* **83**, 2491–2501 (2002).
- [30] Perkins, G., Renken, C., Martone, M. E., Young, S. J., Ellisman, M. & Frey, T. Electron tomography of neuronal mitochondria: three-dimensional structure and organization of cristae and membrane contacts. *Journal of structural biology* **119**, 260–272 (1997).
- [31] Frey, T. G., Renken, C. W. & Perkins, G. a. Insight into mitochondrial structure and function from electron tomography. *Biochimica et biophysica acta* **1555**, 196–203 (2002).
- [32] Sachse, F. B., Savio-Galimberti, E., Goldhaber, J. I. & Bridge, J. H. B. Towards computational modeling of excitation-contraction coupling in cardiac myocytes: reconstruction of structures and proteins from confocal imaging. *Pacific Symposium on Biocomputing. Pacific Symposium on Biocomputing* **339**, 328–39 (2009).
- [33] Boncompagni, S., Rossi, A. E., Micaroni, M., Beznoussenko, G. V., Polishchuk, R. S., Dirksen, R. T. & Protasi, F. Mitochondria are linked to calcium stores in

- striated muscle by developmentally regulated tethering structures. *Molecular biology of the cell* **20**, 1058–67 (2009).
- [34] Smart, J. L. & McCammon, J. A. Analysis of synaptic transmission in the neuromuscular junction using a continuum finite element model. *Biophysical journal* **75**, 1679–88 (1998).
- [35] Tai, K., Bond, S. D., MacMillan, H. R., Baker, N. A., Holst, M. J. & McCammon, J. A. Finite element simulations of acetylcholine diffusion in neuromuscular junctions. *Biophysical journal* **84**, 2234–2241 (2003).
- [36] Cheng, Y., Suen, J. K., Radić, Z., Bond, S. D., Holst, M. J. & McCammon, J. A. Continuum simulations of acetylcholine diffusion with reaction-determined boundaries in neuromuscular junction models. *Biophysical chemistry* **127**, 129–39 (2007).
- [37] Means, S., Smith, A. J., Shepherd, J., Shadid, J., Fowler, J., Wojcikiewicz, R. J. H., Mazel, T., Smith, G. D. & Wilson, B. S. Reaction diffusion modeling of calcium dynamics with realistic ER geometry. *Biophysical journal* **91**, 537–557 (2006).
- [38] Goel, P., Sneyd, J. & Friedman, A. Homogenization of the cell cytoplasm: the calcium bidomain equations. *Multiscale Modeling and Simulation* **5**, 1045–1062 (2006).
- [39] Shorten, P. R. & Sneyd, J. A mathematical analysis of obstructed diffusion within skeletal muscle. *Biophysical journal* **96**, 4764–78 (2009).
- [40] Alnæs, M. S., Kirby, R. C. & Wells, G. N. *Automated Solution of Differential Equations by the Finite Element Method*, vol. 84 of *Lecture Notes in Computational Science and Engineering* (Springer Berlin Heidelberg, Berlin, Heidelberg, 2012).
- [41] Alberts, B., Bray, D., Lewis, J., Raff, M., Roberts, K. & Watson, J. *Molecular Biology of the Cell* (Garland Publishing Inc., 1994), 3rd edn.

- [42] Splawski, I., Timothy, K. W., Decher, N., Kumar, P., Sachse, F. B., Beggs, A. H., Sanguinetti, M. C. & Keating, M. T. Severe arrhythmia disorder caused by cardiac L-type calcium channel mutations. *Proceedings of the National Academy of Sciences of the United States of America* **102**, 8089–96 (2005).
- [43] Szalai, G., Krishnamurthy, R. & Hajnóczky, G. Apoptosis driven by IP(3)-linked mitochondrial calcium signals. *The EMBO journal* **18**, 6349–61 (1999).
- [44] Halestrap, A. P., Clarke, S. J. & Javadov, S. A. Mitochondrial permeability transition pore opening during myocardial reperfusion—a target for cardioprotection. *Cardiovascular research* **61**, 372–85 (2004).
- [45] Duchen, M. R., Verkhatsky, A. & Muallem, S. Mitochondria and calcium in health and disease. *Cell calcium* **44**, 1–5 (2008).
- [46] Wallace, D. C. Mitochondrial diseases in man and mouse. *Science* **283**, 1482–8 (1999).
- [47] Murphy, M. P. & Smith, R. A. Drug delivery to mitochondria: the key to mitochondrial medicine. *Advanced drug delivery reviews* **41**, 235–50 (2000).
- [48] Kuznetsov, A. V., Hermann, M., Saks, V., Hengster, P. & Margreiter, R. The cell-type specificity of mitochondrial dynamics. *The international journal of biochemistry and cell biology* **41**, 1928–39 (2009).
- [49] Saunter, C. D., Perng, M. D., Love, G. D. & Quinlan, R. A. Stochastically determined directed movement explains the dominant small-scale mitochondrial movements within non-neuronal tissue culture cells. *FEBS letters* **583**, 1267–73 (2009).
- [50] Salmeen, I., Zacmanidis, P., Jesion, G. & Feldkamp, L. a. Motion of mitochondria in cultured cells quantified by analysis of digitized images. *Biophysical journal* **48**, 681–686 (1985).

- [51] Russo, G. J., Louie, K., Wellington, A., Macleod, G. T., Hu, F., Panchumarthi, S. & Zinsmaier, K. E. Drosophila Miro is required for both anterograde and retrograde axonal mitochondrial transport. *The Journal of neuroscience : the official journal of the Society for Neuroscience* **29**, 5443–55 (2009).
- [52] Reis, K., Fransson, A. & Aspenström, P. The Miro GTPases: at the heart of the mitochondrial transport machinery. *FEBS letters* **583**, 1391–8 (2009).
- [53] Oancea, E. & Meyer, T. Protein kinase C as a molecular machine for decoding calcium and diacylglycerol signals. *Cell* **95**, 307–18 (1998).
- [54] Jeyaraju, D. V., Cisbani, G. & Pellegrini, L. Calcium regulation of mitochondria motility and morphology. *Biochimica et biophysica acta* **1787**, 1363–73 (2009).
- [55] Miller, K. E. & Sheetz, M. P. Axonal mitochondrial transport and potential are correlated. *Journal of cell science* **117**, 2791–2804 (2004).
- [56] Singh, L., Bakshi, D. K., Majumdar, S., Arora, S. K., Vasishta, R. K. & Wig, J. D. Mitochondrial dysfunction and apoptosis of acinar cells in chronic pancreatitis. *Journal of gastroenterology* **43**, 473–83 (2008).
- [57] Yi, M., Weaver, D. & Hajnóczky, G. Control of mitochondrial motility and distribution by the calcium signal: a homeostatic circuit. *The Journal of cell biology* **167**, 661–72 (2004).
- [58] Johnson, P. R., Dolman, N. J., Pope, M., Vaillant, C., Petersen, O. H., Tepikin, A. V. & Erdemli, G. Non-uniform distribution of mitochondria in pancreatic acinar cells. *Cell and tissue research* **313**, 37–45 (2003).
- [59] Park, M. K., Ashby, M. C., Erdemli, G., Petersen, O. H. & Tepikin, a. V. Perinuclear, perigranular and sub-plasmalemmal mitochondria have distinct functions in the regulation of cellular calcium transport. *The EMBO journal* **20**, 1863–74 (2001).

- [60] Hom, J. & Sheu, S.-S. Morphological dynamics of mitochondria - a special emphasis on cardiac muscle cells. *Journal of molecular and cellular cardiology* **46**, 811–20 (2009).
- [61] Hegyi, P., Pandol, S., Venglovecz, V. & Rakonczay, Z. The acinar-ductal tango in the pathogenesis of acute pancreatitis. *Gut* **60**, 544–52 (2011).
- [62] National Health Service Information Centre for Health and Social Care. Statistics on Alcohol : England, 2011. Tech. rep. (2011).
- [63] Tinel, H., Cancela, J. M., Mogami, H., Gerasimenko, J. V., Gerasimenko, O. V., Tepikin, a. V. & Petersen, O. H. Active mitochondria surrounding the pancreatic acinar granule region prevent spreading of inositol trisphosphate-evoked local cytosolic Ca(2+) signals. *The EMBO journal* **18**, 4999–5008 (1999).
- [64] Raraty, M. G. T., Murphy, J. a., Mcloughlin, E., Smith, D., Criddle, D. & Sutton, R. Mechanisms of acinar cell injury in acute pancreatitis. *Scandinavian journal of surgery* **94**, 89–96 (2005).
- [65] Petersen, O. H., Burdakov, D. & Tepikin, a. V. Polarity in intracellular calcium signaling. *BioEssays : news and reviews in molecular, cellular and developmental biology* **21**, 851–60 (1999).
- [66] Ashby, M. C. & Tepikin, A. V. Polarized calcium and calmodulin signaling in secretory epithelia. *Physiological reviews* **82**, 701–34 (2002).
- [67] Straub, S. V., Giovannucci, D. R. & Yule, D. I. Calcium wave propagation in pancreatic acinar cells: functional interaction of inositol 1,4,5-trisphosphate receptors, ryanodine receptors, and mitochondria. *The Journal of general physiology* **116**, 547–60 (2000).
- [68] Ito, K., Miyashita, Y. & Kasai, H. Kinetic control of multiple forms of Ca²⁺ spikes by inositol trisphosphate in pancreatic acinar cells. *The Journal of cell biology* **146**, 405–13 (1999).

- [69] Leite, M. F., Dranoff, J. a., Gao, L. & Nathanson, M. H. Expression and subcellular localization of the ryanodine receptor in rat pancreatic acinar cells. *The Biochemical journal* **337**, 305–9 (1999).
- [70] Giovannucci, D. R., Bruce, J. I. E., Straub, S. V., Arreola, J., Sneyd, J., Shuttleworth, T. J. & Yule, D. I. Cytosolic Ca^{2+} and Ca^{2+} -activated Cl^- current dynamics: insights from two functionally distinct mouse exocrine cells. *The Journal of Physiology* **540**, 469–484 (2002).
- [71] Petersen, O. H., Tepikin, A. & Park, M. K. The endoplasmic reticulum: one continuous or several separate Ca^{2+} stores? *Trends in neurosciences* **24**, 271–6 (2001).
- [72] Mogami, H., Nakano, K., Tepikin, a. V. & Petersen, O. H. Ca^{2+} flow via tunnels in polarized cells: recharging of apical Ca^{2+} stores by focal Ca^{2+} entry through basal membrane patch. *Cell* **88**, 49–55 (1997).
- [73] Petersen, O. H. Ca^{2+} signaling in pancreatic acinar cells: physiology and pathophysiology. *Brazilian journal of medical and biological research* **42**, 9–16 (2009).
- [74] Criddle, D. N., Raraty, M. G. T., Neoptolemos, J. P., Tepikin, A. V., Petersen, O. H. & Sutton, R. Ethanol toxicity in pancreatic acinar cells: mediation by nonoxidative fatty acid metabolites. *Proceedings of the National Academy of Sciences of the United States of America* **101**, 10738–43 (2004).
- [75] Barrow, S. L., Voronina, S. G., da Silva Xavier, G., Chvanov, M. a., Longbottom, R. E., Gerasimenko, O. V., Petersen, O. H., Rutter, G. a. & Tepikin, A. V. ATP depletion inhibits Ca^{2+} release, influx and extrusion in pancreatic acinar cells but not pathological Ca^{2+} responses induced by bile. *Pflügers Archiv : European journal of physiology* **455**, 1025–39 (2008).
- [76] Voronina, S. & Barrow, S. Dynamic changes in cytosolic and mitochondrial ATP levels in pancreatic acinar cells. *Gastroenterology* **138**, 1976–87 (2010).

- [77] Yano, K., Petersen, O. H. & Tepikin, A. V. Computational Models of Calcium Signaling in the Pancreas - Temporal and Spatial Regulations. *Genome Informatics* **14**, 603–604 (2003).
- [78] Yano, K., Petersen, O. H. & Tepikin, A. V. Dual sensitivity of sarcoplasmic/endoplasmic Ca^{2+} -ATPase to cytosolic and endoplasmic reticulum Ca^{2+} as a mechanism of modulating cytosolic Ca^{2+} oscillations. *The Biochemical journal* **383**, 353–60 (2004).
- [79] Tsaneva-Atanasova, K., Yule, D. I. & Sneyd, J. Calcium oscillations in a triplet of pancreatic acinar cells. *Biophysical journal* **88**, 1535–1551 (2005).
- [80] Talzhanov, Y. Computational modeling of the pancreas: lifelong simulations of pancreatitis (2012).
- [81] Raschi, E., Vasina, V., Poluzzi, E. & De Ponti, F. The hERG K^+ channel: target and antitarget strategies in drug development. *Pharmacological research : the official journal of the Italian Pharmacological Society* **57**, 181–95 (2008).
- [82] Magnus, G. & Keizer, J. Model of beta-cell mitochondrial calcium handling and electrical activity. I. Cytoplasmic variables. *The American journal of physiology* **274**, C1158–73 (1998).
- [83] Magnus, G. & Keizer, J. Model of beta-cell mitochondrial calcium handling and electrical activity. II. Mitochondrial variables. *The American journal of physiology* **274**, C1174–84 (1998).
- [84] Jafri, M. S., Dudycha, S. J. & O'Rourke, B. Cardiac energy metabolism: models of cellular respiration. *Annual review of biomedical engineering* **3**, 57–81 (2001).
- [85] Cortassa, S., Aon, M. a., O'Rourke, B., Jacques, R., Tseng, H.-J., Marbán, E. & Winslow, R. L. A computational model integrating electrophysiology, contraction, and mitochondrial bioenergetics in the ventricular myocyte. *Biophysical journal* **91**, 1564–89 (2006).

- [86] Cortassa, S., Aon, M. a., Marbán, E., Winslow, R. L. & O'Rourke, B. An integrated model of cardiac mitochondrial energy metabolism and calcium dynamics. *Biophysical journal* **84**, 2734–55 (2003).
- [87] Nguyen, M.-H. T. & Jafri, M. S. Mitochondrial calcium signaling and energy metabolism. *Annals of the New York Academy of Sciences* **1047**, 127–37 (2005).
- [88] Bertram, R., Gram Pedersen, M., Luciani, D. S. & Sherman, A. A simplified model for mitochondrial ATP production. *Journal of theoretical biology* **243**, 575–86 (2006).
- [89] Tilakaratne, H. K., Hunter, S. K. & Rodgers, V. G. J. Mathematical modeling of myoglobin facilitated transport of oxygen in devices containing myoglobin-expressing cells. *Mathematical biosciences* **176**, 253–67 (2002).
- [90] Husain, S. Z., Orabi, A. I., Muili, K. a., Luo, Y., Sarwar, S., Mahmood, S. M., Wang, D., Choo-Wing, R., Singh, V. P., Parness, J., Ananthanarayanan, M., Bhandari, V. & Perides, G. Ryanodine receptors contribute to bile acid-induced pathological calcium signaling and pancreatitis in mice. *American journal of physiology. Gastrointestinal and liver physiology* **302**, G1423–33 (2012).
- [91] Venglovecz, V. The effects of bile acids on pancreatic ductal cells. *The Pancreas: Exocrine Pancreas Knowledge Base* 1–8 (2012).
- [92] De Young, G. W. & Keizer, J. A single-pool inositol 1,4,5-trisphosphate-receptor-based model for agonist-stimulated oscillations in Ca^{2+} concentration. *Proceedings of the National Academy of Sciences of the United States of America* **89**, 9895–9 (1992).
- [93] Lu, S., Michailova, A., Saucerman, J., Cheng, Y., Yu, Z., Kaiser, T., Li, W., Bank, R., Holst, M., McCammon, J., Hayashi, T., Hoshijima, M., Arzberger, P. & McCulloch, A. Multiscale modeling in rodent ventricular myocytes. *IEEE engineering in medicine and biology magazine* **28**, 46–57 (2009).

- [94] Higgins, E. R., Goel, P., Puglisi, J. L., Bers, D. M., Cannell, M. & Sneyd, J. Modelling calcium microdomains using homogenisation. *Journal of theoretical biology* **247**, 623–644 (2007).
- [95] Dayel, M. J., Hom, E. F. & Verkman, a. S. Diffusion of green fluorescent protein in the aqueous-phase lumen of endoplasmic reticulum. *Biophysical journal* **76**, 2843–51 (1999).
- [96] Huber, H. J., Duesmann, H., Wenus, J., Kilbride, S. M. & Prehn, J. H. M. Mathematical modelling of the mitochondrial apoptosis pathway. *Biochimica et biophysica acta* **1813**, 608–15 (2011).